An Experimental Study of the Geometry and Kinematics of Caldera Collapse

Eoghan P. Holohan

Submitted for the degree of Doctor of Philosophy to the University of Dublin, Trinity College

September 2007

SUMMARY

Calderas are 1 - 100 km diameter, volcanic depressions that form primarily through m-scale to km–scale subsidence of a magma reservoir roof into an underlying magma reservoir. This study addresses several fundamental geometric and kinematic aspects of the structure of caldera volcanoes via a series of scaled physical (or analogue) modelling experiments. Results of these models are combined in detail with observations from natural calderas recorded in the literature, in order to provide as strong an element of 'ground-truthing' for the experimental results as possible.

The basic experimental materials and methods are common to all the results chapters (2-6), and so for convenience are summarised together in Chapter 1. An exception to some extent is the experiment set described is Chapter 5; these were made with different materials and apparatus, the particulars of which are described in that chapter. Each of the results chapters is otherwise self-contained, with its own specific introduction to the problems addressed, summary of data, discussion, and conclusions. The contents of Chapters 1, 5, and 6 have been published in two peer-reviewed articles. The remaining chapters are presently unpublished, although Chapter 3 and part of Chapter 4 have been submitted for peer review, whilst the rest of Chapter 4 and a part of Chapter 2 will be submitted for publication at a later date. Given the assistance of co-authors in the preparation of manuscripts now integrated into the thesis, my contribution to the individual chapters as presented here may be summarised as: Chapter 1: 85%, Chapter 2: 90%, Chapter 3: 75%, Chapter 4: 80%, Chapter 5: 50%, Chapter 5: 75%. The structure of the thesis, the major aspects of caldera evolution investigated, and the main results are as follows:

Chapter 1: Introduction and Methodology - outlines the current understanding of caldera structure as achieved to date by previous authors and supplies the rationale for using physical models to help unravel caldera evolution. This section also summarises the insights for how these. Details of the experimental methodology employed in this study, as well as scaling considerations for the application of small-scale models to the study of large-scale deformation associated with caldera subsidence in nature, are also provided.

Chapter 2: The Geometry and Evolution of Circular Caldera Collapse Structures - details the results of experimental subsidence of mechanically isotropic reservoir roofs that are circular in plan view. This baseline experiment set illustrates the generalised kinematic evolution of caldera subsidence. Structures resolving radial and concentric strains are documented, the latter for the first time. The control of the roof's thickness/diameter ratio upon these structures' development is also highlighted. The kinematics of caldera ring faults, the generation of polygonal caldera outlines and the development of piecemeal-type subsidence are also discussed in light of the evidence from experiment and nature.

Chapter 3: The Caldera Collapse Continuum - systematically integrates results of simple circular collapses in Chapter 2 with those from past experimental, numerical and field studies to

produce a 'state-of-the-art' synthesis of the mechanics and kinematics of caldera collapse. This synthesis sheds new light on the long-standing but poorly-defined continuum between end-member caldera collapse styles. Structural elements characteristic of each end-member are shown to reflect progressively overlapping structural sub-processes in a single collapse event. The continuum between end-member collapse styles is thus defined primarily as a progressive evolution related to increasing subsidence, although the regulatory role of roof thickness/diameter and caldera subsidence/diameter ratios in the development of structural elements of each collapse end-member is also highlighted.

Chapter 4: The Role of Magma Chamber Ellipticity in Caldera Collapse – documents the results of experimental collapse of mechanically isotropic reservoir roofs that are varyingly elliptical in plan view. Physical models demonstrate that an elliptical reservoir roof predictably fails first at the ends of its shorter principal axis, and show that lateral propagation ('unzipping') patterns vary systematically with ellipticity. The models also highlight a characteristic geometric arrangement of elliptical ring structures and provide a first comprehensive view of the elliptical caldera structural architecture in 3D.

Chapters 5 & 6: Regional tectonic influences on the evolution of caldera collapse – outlines the results of experimental collapse of reservoir roofs that contain pre-existing mechanical anisotropies in the form of regional-tectonic faults and collapse under regional tectonic stress. Although disregarded in most previous physical and numerical models of calderas, regional faults have long been thought to play a major role in caldera development, principally through their reactivation during collapse. In Chapter 5, caldera formation in areas of orthogonal regional deformation is examined; in Chapter 6, caldera collapse in strike-slip regimes is investigated. In physical models, regional faults reactivated during collapse where they coincided with and ran parallel to the magma reservoir margins. Here, where syn-collapse strain usually tends to localise, pre-collapse faults are optimally orientated for reactivation. Contrary to inferences from some previous field studies, differential movement on pre-collapse faults was not observed in central parts of the subsiding reservoir roof. Physical models thus confirm that regional fault reactivation is an important process, and help clarify conditions favouring it.

Chapter 7: Summary of Main Conclusions and Outlook - provides a brief overview of the main findings of this thesis, notes their general implications for our understanding of calderas, and outlines some potential avenues for future work.

An electronic appendix (DVD) is attached to the back of the thesis. This appendix contains photos of all experiments (in jpeg format), animations of the experiments (in MS PowerPoint files), and copies of the two published articles (in PDF format).

Acknowledgements

I would firstly like to thank my supervisor and mentor, Prof. Valentin Troll, for his unwavering encouragement, guidance, organisational energy, support (motivational and financial), and seemingly endless reserves of patience. He has taught me great deal about volcanoes, science, and life. Prof. Benjamin van Wyk de Vries was an ever generous host and inspirational supervisor at the Laboratoire Magmas et Volcans in Clermond-Ferrand, France. He also suggested the use of honey to model collapse calderas and designed the deformation rig for the strike-slip experiments. Dr. Thomas Walter designed and built an earlier version of the extensional deformation rig and provided much of the experimental data interpreted in Chapter 5, which represents early experimental work that also benefited from the contributions of Dr. Z. Shipton, A. Soden, S. Muenn, and S. McDonnell. Van Wyk de Vries and Walter also critically assessed and contributed toward several manuscripts subsequently incorporated into this work.

Conversations over the years with V. Acocella, T. Druitt, S. Jones, B. Kennedy, P. Lipman, P. Mouginis-Mark, O. Roche, and R. West were enlightening, challenging, and greatly appreciated. C. Childs, M. Schoepfer, and J. Walsh of the Fault Analysis Group in UCD generously gave time and advice on matters structural. I. Bindeman, W. Bosworth, F. Donnadieu, G. Girard, J. Marti, U. Riller, O. Roche, J. Wolff, and several anonymous reviewers constructively criticised and helped improve those parts of the thesis submitted for publication. Thanks are also due to A. Gudmundsson, C. Jaupart, and J. Stix for editorial assistance and encouragement. I am also very grateful to the thesis examiner Dr. Mike Branney for his very stimulating discussion of its contents, probing questions posed, and insights given from his experience.

J. Graham, P. Shannon and J. Walsh encouraged my development as a scientist and teacher by entrusting me with the invaluable opportunities of a Teaching Fellowship at TCD and an Assistant Lectureship at UCD. M. Duncan was always on hand to sort out problems. N. Kearney was ever helpful and resourceful, particularly regarding the VAMP lab. C. O'Donovan and G. McGranaghan of TCD Engineering re-designed and upgraded the early deformation rig. Technical assistance from F. Hendron and D. Burke over the years is also appreciated. Thanks also to A. Soden, P. Byrne, A. Baxter, F. Deegan, N. Finn, N. Martin, and L. Matthieu whose time undertaking (or enduring!) undergraduate laboratory projects under my supervision helped me explore many ideas, some of which were that subsequently expanded upon to form parts of this thesis.

Special thanks go to the VAMPs who helped bring the ship safely into port. F. Deegan, C. Flanagan, F. Sheehan and S. Wiesmeier greatly assisted with figure drafting and text editing. P. Byrne, J. Chadwick, E. Donoghue, and F. Meade, kindly proofed various chapters. M.-A. Longpré and G. Nicoll volunteered for late-night shifts to make sure everything got safely printed. The ladies of the URL – C. Duggan, J. Hellawell, A. O'Halloran, and E. Rogers - supplied sweets, biscuits, and patient reminders (polite but firm) to cease drumming my pens. Together with those named above, S. Bennett, F. Cassidy, B. O'Driscoll, and A. Lynch provided companionship, camaraderie, and great conversations throughout my postgraduate time at TCD.

My siblings Clare, Kevin, Enda, and Catherine, and especially my parents, Pat and Breda, gave support only family can. I am also especially grateful to Jeni Ringland for her essential, ever-present positivity and love.

Finally, financial support for my postgraduate studies was gratefully received from the TCD Broad Curriculum Initiative, Enterprise Ireland, the Volcanic and Magmatic Studies Group, the TCD Graduate Studies Office, the Trinity Trust, the Irish Geological Association, and the TCD Geology Department.

Contents

List of Figures and Tables

Chapter 1

Chapter 2

Chapter 3

Chapter 4

Chapter 5

Chapter 6

Figure 6.7: Results of experimental collapse in strike-slip regimes (Cal Mag 3 and 5) *215*

1 Introduction and Methodology

1.1 Caldera Volcanoes

'Caldera' is Spanish for 'cauldron', a word aptly reflecting this volcano type's typical basin-like morphology, fiery nature, and propensity for filling with water (**Figure 1.1a**). The geological meaning of 'caldera' has changed though time, however, as understanding of the formation of such large volcanic depressions has developed (see reviews of the history of caldera research by Williams, 1941; McBirney, 1990; and Cole et al., 2005). Calderas were initially thought to have formed as enormous explosion craters accompanied by subsidence at the apex of an area of up-doming caused by magma intrusion ("explosion craters" by von Buch 1820). In landmark studies of the 1300 B.P. Santorini eruption (Fouqué 1879) and of the 1883 A.D. Krakatoa eruption (Verbeek 1885), however, the volume of lithics from the pre-caldera edifice in the erupted syn-caldera deposits was calculated to be only a fraction of the volume of the caldera. These authors thus concluded that the bulk of the pre-caldera edifice had just not been obliterated by explosion, but that instead, the pre-caldera edifices must have subsided. Crustal subsidence has since been recognised as the characteristic structural process of caldera formation (cf. McBirney 1990).

The term 'caldera' is therefore increasingly confined to subsidence-related volcanic depressions of a diameter exceeding that of included explosive vents and craters (Williams, 1941; Lipman, 1997, Cole et al., 2005 – e.g. **Figure 1.1b,c**). Magmatic compositions associated with calderas are highly variable. With some notable exceptions (e.g. the 65 km diameter Olympus Mons caldera – Mouginis-Mark and Robinson 1992), mafic calderas are generally smaller (< 5km diameter) and therefore less catastrophic in origin than their more silicic counterparts (see Walker 1984). Large calderas may reach diameters of many tens of km, (e.g. Toba, Indonesia – Aldiss and Ghazali 1984; Bindeman 2006), attain structural subsidence of up to 5 km (e.g. Stillwater Complex, Nevada - John, 1995), and erupt magma volumes in excess of 5,000 km^3 (e.g. La Garita caldera, Colorado - Lipman, 1997). Such definition in terms of scale and process thus serves to distinguish calderas from other volcanic depressions, such as explosion craters and landslide amphitheatres. It should nonetheless be noted that during the evolution of small diameter (< 1 km) calderas, subsidence may occur in combination with significant contributions from explosion and landsliding (cf. Lipman 1997). In plan-view, caldera shape may be circular, or more commonly, ellipitcal, or even polygonal. In this thesis, calderas are thus considered to be 1 - 100 km diameter, volcanic depressions that form primarily through subsidence of a magma reservoir roof by several metres to several kilometers into an underlying magma reservoir.

For society, calderas present substantial benefits, but also significant challenges. On one hand, calderas host large economically-important mineral deposits (e.g. Ag, Au, Cu, Pb, U, Mo), and are key geothermal energy sources. On the other hand, past caldera collapses have occurred with enormous eruptions of over 1000 km^3 of magma (‘super-volcanoes’), which have obliterated areas > 100 km from their source (cf. Aldiss and Ghazali 1984) and potentially altered global climate (Rampino and Self 1992). The recurrence interval of such eruptions is much shorter than other major hazards to humanity (e.g. large meteorite impacts), and still-active calderas often lie adjacent to or under large population centres (e.g. Campi Flegrei caldera, Naples, Italy **– Figure 1.1c**). A crucial stepping-stone to better hazard prediction, and management of the impact of calderas on society, positive and negative, is the better understanding of caldera formation as a structural process.

1.2 General evolution of calderas:

The modern volcanological and structural outline of the evolution of caldera volcanoes was established in the mid-to-late 20th century, although in many respects this outline has close forebears originating as far back as the early 20th century (e.g. the study by Clough et al. (1909) of Glencoe caldera, Scotland,). The most direct evidence concerning caldera structure has come from detailed field studies of eroded calderas, particularly those in the Western USA (e.g. Smith and Bailey 1968; Varga and Smith 1984; Lipman 1984, 1997; Friedrich et al. 1991), Britain (Howells et al. 1986; Branney and Kokelaar 1994; Kokelaar and Moore 2006), and Japan (e.g. Aramaki 1984; Yoshida 1984). Geophysical evidence, particularly gravity data (e.g. Hallinan 1993), earthquake epicentre locations (e.g. Mori and McKee 1987), and seisimic tomography (e.g. Finlayson et al. 2003), has also yielded valuable insights in to the geometry of calderas, caldera fault systems and sub-caldera magma bodies where hidden at depth. Drawing heavily on field and geophysical evidence, several major syntheses of calderas and caldera structures have been published, including those by Williams 1941; Smith and Bailey 1968; Walker 1984; Lipman 1984, 1997; and Cole et al. 2005)

A generalised three-stage ‘caldera cycle’ characterises the evolution of many of these and other calderas around the world (cf. Smith and Bailey 1968, Lipman 1984). The caldera cycle begins with voluminous intrusion of less-evolved (typically basaltic-andesitic) magmas into the crust. This generates of a large volcanic field, below which a major batholith of more-evolved magma (typically dacite-rhyolite) eventually accumulates (**Figure 1.2a**). With voluminous and often violent eruption of the more evolved magma, the magma chamber roof catastrophically founders and generates a caldera. Collapse of the magma chamber roof is commonly accommodated along a major ring fault (**Figure 1.3a**), although sagging of the magma chamber roof may also be important (Walker 1984 - **Figure 1.3b**). The caldera is rapidly infilled by ponded ash-flow tuffs (ignimbrites) and landslide material from the depression’s walls (**Figure 1.2b and Figure 1.3a**). The latter generates a lateral enlargement of the caldera through the formation of topographic embayments in the calderas structural margin (see ‘collapse collar’ in **Figure 1.3a**) Finally, after some time has elapsed, rejuvenation of the magmatic system below the caldera leads to post-collapse intrusion and eruptions into the caldera. Voluminous post-collapse magmatism in some cases generates a new or ‘resurgent’ sub-caldera pluton, the intrusion of which can lead to up-warping of the caldera floor and infill and formation of a resurgent dome and uplift (inversion) of the caldera basin (**Figure 1.2c**).

This study focuses on Stage 2 of the caldera cycle – caldera subsidence. For simplicity, the effects of pre-collapse tumescence and post-collapse resurgence are thus ignored, although it is fully acknowledged that these effects will have impacted greatly on the structures seen at many calderas in nature. Evidence for the pre-collapse uplift is elusive at most calderas (Lipman 1984), although one notable exception is the Isle of Rum caldera, Scotland (cf. Emeleus et al 1985, Emeleus 1997, Troll et al. 2000). Many calderas are weakly or even-non resurgent (e.g. Sierra Negra, Galapagos Islands – Reynolds and Geist 1995). Those calderas that are resurgent have often reactivated structures previously generated during collapse (cf. Lipman 1976; Acocella et al. 2001). The collapse-related structures therefore often represent the major tectonic and geomorphologic features at many calderas.

1.3 Caldera collapse: uncertainties of initiation and structural accommodation

There is persistent uncertainty and debate about how caldera collapse is triggered and how it is structurally accommodated (Lipman 1997; Cole et al. 2005). This is because: a) no one has directly documented a large caldera collapse (and survived), and b) the structures produced during collapse of modern volcanoes are usually poorly-exposed and/or ill-preserved. Since calderas are wide, deep, and rapidly-formed holes in the ground, they quickly fill with erupted ash and/or lava, landslide debris from over-steepened caldera walls, and in many cases, lakes and associated sediments (**Figure 1.1a**). In addition, continued post-collapse magma intrusion and eruption (**Figures 1.1b-c & 1.2c**) commonly obliterates the earlier collapse structures. Also, the sheer complexity of structures and deposits generated during each part of the caldera cycle can be difficult to unravel from the static (and frequently incomplete) field exposures. Mapping eroded caldera complexes in sufficient detail to accurately constrain their volcanic, sedimentological, and structural histories is a time-consuming process. For example, detailed mapping of one of the best-constrained calderas, the ~ 13 km diameter Scafell caldera, England, took over 25 man-years (M. Branney, pers. comm.).

Uncertainty of how caldera collapse is triggered is seen in a debate in the literature over whether collapse is initiated as a result of conditions of over-pressure or under-pressure (relative to lithostatic pressure) in the magma reservoir. In the both cases, influx of fluid into the magma reservoir is assumed to cause reservoir pressure to exceed lithostatic pressure (i.e. to cause over-pressure). This leads to dyke intrusion from the reservoir to the surface and hence eruption. One school of thought (e.g. Druitt and Sparks 1984) has envisaged the eruption to then lead to reduction of the reservoir pressure to below lithostatic values (i.e. to cause under-pressure), which, with the resultant removal of magmatic support of the reservoir roof, promotes wholesale collapse along outward-dipping reverse faults (Anderson 1936). Another school of thought (e.g. Gudmundsson 1988, 1998) has argued that eruption should lead to reduction of reservoir pressure only back to lithostatic, at which point dykes opened during the over-pressure phase should close and eruptions should halt. In this view, the reservoir thus cannot be under-pressured; instead it is argued that caldera subsidence must occur along inward-dipping normal faults induced by apical tensile stresses acting whilst the reservoir remains over-pressured (and thus expanding).

Geological evidence favours the former argument. Volcanic rocks erupted during caldera-forming eruptions and deposited around the caldera often comprise basal Plinian fall deposits that are underlie, and in some cases remain interbedded with (e.g. Wilson & Hildreth 1997), wide-spread (several 1000 km^2) and thick (several 10's to 100's of m) ash flow deposits (ignimbrites). Such a sequence has been interpreted to represent the establishment of a tall pyroclastic column during the early, gas-charged over-pressure phase, followed by voluminous outpourings of pyroclastic material from ring fractures opening as the magma chamber roof catastrophically founders during the under-pressure phase (Druitt & Sparks 1984). Modelled accumulation rates for such deposits yield emplacement times of days to weeks (e.g. Wilson & Hildreth 1997). Moreover, whilst ignimbrite deposits outside the caldera may by up to a few hundred metres thick, equivalent ignimbrite units contemporaneously ponded within the caldera are often several kilometres thick, for example as revealed by borehole data at Valles caldera, New Mexico; (Fraser and Goff 1994) and Long Valley caldera, California (Hildreth and Mahood 1986; Wilson and Hildreth 1997). In addition, individual cooling units within ignimbrites exposed at deeply eroded calderas may be several hundred metres thick (e.g. at Lake City Caldera, Colorado – Lipman 1984). The rapid, clearly syn-collapse accumulation of such thicknesses of ignimbrite necessitates subsidence rates along ring faults of several 10's to 100's of m per week, or even per day. The mechanism of caldera collapse triggering by overpressure plus accommodation by resultant apical tensile faulting is directly connected to the influx rate of magma into the magma reservoir, however. Such influx rates and the general the timescales of voluminous intrusion-related deformation (e.g. resurgence) are respectively miniscule and lengthy compared to eruption and subsidence rates (cf. Francis 1993; Jellinek and DePaulo 2003). It is thus hard to see how sustained overpressure conditions can trigger and accommodate catastrophic caldera collapse. Moreover, analogue models (e.g. Marti et al. 1994; Walter and Troll 2001) show that to attain the observed magnitudes of caldera subsidence via magma chamber inflation would actually require a commensurate magnitude of uplift (km-scale) of the caldera's surrounds *over the same time-scale of collapse*, something for which there is scant evidence (Lipman 1984, 1997).

The question of whether eruption triggers collapse or vice versa has fed another such debate (McBirney 1990). Although the former view is supported in many cases, for reasons outlined above, the latter view reflects the observation that, in at least some cases, Plinian fall deposits do not underlie voluminous syn-collapse ignimbrites, e.g. the $1000m^3$ Cerro Galan Ignimbrite, NW Argentina, the 2.2 Ma eruption of which occurred during subsidence of the eponymous 35 x 25 km diameter caldera (Francis 1993 p. 301). Thus even the evidence for initial over-pressure at the beginning of caldera forming eruptions, as in the Druitt and Sparks (1984) model, seems to be absent at some calderas. Instead, in the case of Cerro Galan at least, catastrophic discharge rates of magma seem to have been achieved from the onset of eruption, which has been interpreted to signify that gaping syn-collapse ring fractures were on hand at the onset of eruption to act as sufficiently efficient vent systems.

One mechanism potentially resolving this conundrum is the lateral, rather than vertical, withdrawal of magma from the reservoir. Lateral withdrawal of magma leading to subsidence of small-diameter calderas or even smaller-diameter pit craters has been frequently observed at basaltic volcanoes, such as Kilauea, Hawaii (Newhall and Dzurisin 1988), Piton de la Fournaise, Reunion Island (Longpré et al., in press), and perhaps most spectacularly, at Miyakejima, Japan (Geshi et al. 2002). The 1912 collapse of the 3 x 4 km diameter Katmai caldera, Alaska, occurred during a rhyolitic eruption (the largest of the 20^{th} century) from a vent located over 7 km away from the volcano. Lateral withdrawal of magma leading to caldera collapse can thus occur regardless of magma composition. Moreover, in the case of Miyakejima, magma seems to have been transported laterally by several 10's of km (as tracked by migration of earthquake epicentres) without major precursory eruptions either within or at distance from the caldera (Geshi et al. 2002). Collapse in the analogue experiments of the present study, and those of several previous works, implicitly replicated such a scenario (see below).

Uncertainty of how caldera collapse is structurally accommodated is seen in debates in the literature over how to resolve the apparent 'space problem' of caldera subsidence The 'space problem' arose from many workers depicting calderas as having subsided en-bloc along a steeply inward-dipping fault with a normal sense of slip (see Lipman 1984 and references therein; Walker 1984 (**Figure 1.3b**) see also Gudmundsson 1988, 1998). The subsidence of a magma chamber roof as a coherent block along such an inward-dipping fault alone is geometrically unfeasible, however, since if the ring-fault dips inward on all sides of the block, the block cannot move downward. Moreover, this geometry apparently contradicted theoretical (e.g. Anderson 1936, 1951) and experimental predictions (Sanford 1959) of the accommodation of collapse along an outward-dipping fault with a reverse sense of slip. Further uncertainty in the structural accommodation of caldera collapse has been encapsulated in the debate over the style of collapse. Postulated alternative collapse styles have included a coherent, sag-like manner (e.g. Walker 1984); a coherent, piston-like manner (e.g Lipman 1997); or a non-coherent, piecemeal or chaotic manner (e.g. Aramaki 1984; Scandone 1990; Branney 1995). It is worth noting that caldera collapse need not always occur as a result of one or two catastrophic events, but can also occur incrementally over several relatively small magnitude eruption/subsidence events (see Walker 1984), which may or may not generate additional structural complexity.

To gain further insights into the initiation, development, and final geometry of caldera collapse structures, and in tandem with detailed field and geophysical studies of calderas, researchers have consequently turned to the study of physical models (natural subsidence analogues and scaled sand-box experiments) and numerical models of subsidence. The results and methodologies of the latter are not summarised or analysed in detail in this work, although some results of recent numerical models are discussed at relevant points in subsequent chapters (**Chapters 2, 3, & 4**).

1.4 Current picture of collapse caldera structure: recent insights from mining subsidence, ice-melt collapse, and sand-box models.

Analogue modelling is the scaled physical simulation of natural processes. It is highly complementary to field, geophysical and numerical caldera studies, as it: 1) helps overcome the limited structural exposure due to sedimentary and volcanic infill, lakes, and vegetation at many calderas; 2) seamlessly links structures from magma chamber to surface, and so relates lower-level structures at deeply eroded ancient calderas to higher-level structures and surface features of young calderas; 3) allows deformation of, for instance, the collapse phase to be decoupled from that of post-collapse resurgence, intrusions, and regional-tectonics; 4) allows the potential influence of many geometric and rheological parameters to be isolated and evaluated; and 5) helps constrain the geometry and kinematics of discontinuous structures (i.e. fractures) formed during progressive deformation beyond the elastic limit, the point at which the predictive power of most numerical models cannot reach.

Analogue studies of subsidence-related deformation have been conducted since the 1950's (e.g. Sanford 1959 – **Figure 1.4a**), with particular reference to mining-related subsidence (e.g. Whittaker and Reddish 1989 - **Figures 1.5a & 1.6**). Only since the mid-1980's, however, have volcanologists adopted physical models to specifically examine longstanding questions of how caldera collapse may be accommodated structurally. Many recent experimental studies of caldera formation since then sought to systematically examine the general development and interaction of structures formed during either two parts of, or the whole of, a caldera cycle. Komuro (1987); Marti et al. (1994) examined magma chamber inflation ('tumescence') and subsequent deflation (collapse). Acocella et al. (2000, 2001) considered collapse and resurgence only; Walter and Troll (2001) and Troll et al. (2002) simulated the structural evolution of a whole caldera cycle, as well as the superimposition of several caldera cycles. The results of these studies is not summarised in detail here, but those bearing upon the collapse process are outlined below.

A suite of studies focussed more on the process of collapse was initiated with Branney and Gilbert's (1995) detailed study of ice-melt collapse-pits (**Figure 1.5b**). Branney (1995) then highlighted the close similarity between subsidence structures in sand-box models, ice-melt collapse-pits, and mines and those structures seen at many calderas. This work was followed by a series of analogue experimental modelling studies (Roche et al. 2000, 2001; Kennedy et al. 2004; and Geyer et al. 2006), in which the thickness/diameter ratio of the magma chamber roof was varied under more controlled laboratory conditions. As previously known from mining subsidence (Whittaker and Reddish 1989) the thickness/diameter ratio exerts a critical influence upon the initiation, geometry and kinematics of collapse-related deformation (**Figures 1.6 & 1.7**). Since the present work began, other works published by Lavallee et al. (2004); Belousov et al. (2005); Acocella et al. (2004); and Holohan et al. (2005, in press, and this study) began to examine the impact upon collapse of other factors, such as pre-collapse topography, laterally sited pre-collapse stratovolcanoes, and pre-collapse regional tectonics.

From the study of mining subsidence, ice-melt pits and analogue subsidence models has apparent 'space-problem' has resolved in favour of initial subsidence along outward-dipping reverse faults, as predicted by Anderson (1936) and shown by Sanford (1959) (**Figure 1.4a**), with variable sagging (**Figure 1.5**) as suggested by Walker (1988). Outward-dipping fractures form initially because in a sufficiently thick roof (thickness/diameter ratio ~ > 0.15) above a cavity the principal stress trajectories are arched (e.g. Timoshenko & Woinowsky-Krieger 1959; Whittaker & Reddish 1989; Young & Budynas 2002) (**Figure 1.4b**) The development of outward-dipping reverse faults, either directly or from initial outward-dipping fractures, may be related to shear arising between material above the margin of the cavity and that in the subsiding roof centre (Roche et al 2000). In this view, the reverse faults form in the (preferred) orientation of a Riedel shear fracture within the shear zone above the cavity margin (**Figure 1.4c**). In reality, such outward-dipping faults may be of mixed mode (tensile and shear – e.g. Anderson 1936; Walter and Troll 2001). In most sand-box experiments, progressive deformation (continued subsidence) eventually also leads to formation of vertical or inward-dipping normal faults that are above or just outside the cavity/reservoir margins (**Figures 1.4a, & 1.7**).

In general therefore, these analogue studies conclude that a caldera subsidence resulting from magma chamber evacuation and withdrawal of magmatic roof support may possess two structural zones, a central zone of compression and a peripheral zone of extension (**Figures 1.4a, 1.5a-b, & 1.8)**. With sufficient subsidence, the outermost of one or more ring-faults of vertical to outward dip and reverse motion may therefore bound a *central caldera zone*. A concentric extensional *peripheral caldera zone* may stretch from the outermost reverse ring-fault to, and cryptically beyond, an outermost normal ring-fault of steep inward dip, the scarp of which forms the caldera's topographic margin (**Figures 1.4a & 1.5c)**. The peripheral zone is also characterised by crevasse opening, horst and graben formation, inward rotation of strata and structures, and mass movement of rock toward the caldera centre (**Figures 1.4a & 1.5b-c**).

The potential importance of roof thickness/diameter in the initiation, geometry and development of caldera subsidence structures (Whittaker and Reddish 1989; Roche et al. 2000; Kennedy et al. 2004; Geyer et al 2006) is illustrated in **Figures 1.6 and 1.7**. With low thickness/diameter ratios (supercritical geometry - **Figure 1.6c**), a more sagged, coherent style of collapse is favoured (**Figure 1.7a).** This is because the effects of stress arching are inhibited, which reduces the roof's stiffness and strength, but leaves a large portion of the roof centre relatively undeformed. With high thickness/diameter ratios (subcritical geometry - **Figure 1.6c**), a less sagged, non-coherent style of collapse is favoured (**Figure 1.7b).** This is because the effects of stress arching are enhanced, which increases the roof's stiffness and strength, but causes deformation due to the stress arching effect to be expressed across the whole roof. Roche et al. (2001) also showed the potential impact of the material properties of the roof in small-scale subsidence structures; with more cohesive materials, tensile and mixed mode fracturing is promoted. Moreover, at high thickness/diameter ratios, quasi-stable cavities may form at depth and act at depocentres for chaotically slumped overlying roof material. More recently Geyer et al. (2006) have shown, in agreement with theoretical predictions of Roche and Druitt (2001), that a greater volume of magma must be extracted to cause complete failure of high thickness/diameter roof than a low thickness/diameter roof (i.e. the latter are more unstable).

The past analogue studies and experimental models have thus not only refined our understanding of how and under what conditions caldera collapse structures may form (**Figures 1.5c, 1.7 & 1.8**), but they have also shed light on the debate over potential styles of caldera subsidence (e.g. **Figure 1.3**). As also noted for natural calderas (Walker 1984; Branney 1995; Lipman 1997) structural elements of various proposed styles of collapse (e.g. downsag, trapdoor, piston, piecemeal, and funnel) have all been noted to greater or lesser extent within individual analogue collapses. The thickness/diameter ratio of the roof is particularly important in regard to the exact suite of structures formed and therefore for the expression of such elements. A more detailed discussion of how analogue models, numerical models, field studies and geophysical evidence together give insight into the style of caldera subsidence is given in **Chapter 3**.

1.5 Outstanding Problems and Aims of this Work

This study seeks to shed new light on four previously unaddressed aspects concerning caldera collapse. Firstly, although it is clear from low-strain numerical and analogue models that subsidence requires structural accommodation of both radial and concentric components of strain (cf. Whittaker and Reddish 1989; Zuber and Mouginis-Mark 1992), the latter has not been previously addressed experimentally. It is thus unclear how concentric shortening may be accommodated at the high strains characteristic of caldera collapse. To gain further insights into how concentric strains are accommodated during caldera formation, the basic scenario of circular caldera collapse is revisited (**Chapter 2**). Also, the kinematics of caldera ring fault systems and the origin of polygonal calderas are further explored.

Secondly, a continuum between idealised structural end-members for caldera subsidence has been previously proposed (Walker 1984; Lipman 1997). Although this continuum is a fundamental concept related to caldera structure, it is rather vaguely defined. In light of data from recent field studies, analogue models (including data from this study described in **Chapter 2**) and numerical simulations, principles underpinning the caldera collapse continuum are critically assessed and illustrated (**Chapter 3**).

Thirdly, many granite batholiths (likely natural analogues for pre-caldera magma reservoirs) are actually highly elliptical in plan view, as are many calderas. Despite this, the vast majority of previous physical and numerical modelling studies of caldera formation have assumed a reservoir roof that is circular in plan view and have only examined in detail the effect of the roof's thickness/diameter ratio, or vertical aspect ratio, on subsidence. The influence of the plan-view 'ellipticity', or horizontal aspect ratio, of the pre-caldera reservoir roof on a caldera volcano's structural evolution and architecture is thus systematically examined here (**Chapter 4**).

Fourthly, an acknowledged limitation of most previous analogue and numerical studies of caldera formation prior to the start of this study was the absence of pre-collapse regional faults. Indeed, exceptionally detailed field studies in ancient, well-exposed calderas (e.g. Glencoe, Scotland - Moore and Kokelaar 1998) highlight several potential influences of regional-tectonic structures in caldera evolution. Calderas occur in various tectono-magmatic environments, such as along volcanic arcs at destructive plate margins (Hildreth and Fierstein 2000), along oceanic and continental rift zones (Bosworth et al., 2003), or along major transform (i.e. strike-slip) faults (Bellier and Sebrier, 1994; Lecuyer et al. 1997; Riller et al., 2001), as well as oceanic islands (e.g. Troll et al. 2002). Many caldera volcanoes have thus formed in areas that experienced contemporaneous regional tectonic deformation of extensional, compressive or strike-slip type. Despite this observation, no systematic experimental evaluation of how regional structures and stresses influence caldera development had been undertaken before this study commenced. These influences are explored in **Chapters 5 and 6**.

Investigation of the role(s) of regional-tectonic setting and structures in caldera development remains at an embryonic stage (cf. Lipman 1997; Cole et al. 2005), however. A symptom of this is the ambiguity around the term 'volcano-tectonic'. This term has variously described structures or structural depressions that are: a) generated solely by regional-tectonic processes, but host volcanic deposits (Lipman 1997 and references therein); b) generated by regional-tectonic processes, but with some displacement related to magmatic/volcanic activity (Nappi et al. 1991); and c) generated solely by magmatic/volcanic activity (Branney and Kokelaar 1994). In this work, 'volcano-tectonic' refers to faults or fault motions generated by local magmatic/volcanic processes only. Likewise, 'regional-tectonic' refers to faults or fault motions generated by regional-scale deformation processes.

A fault of hybrid regional-tectonic/volcano-tectonic history may be possible - e.g. generated due to interaction of regional and local deformations, or generated by regional deformation and reactivated during local deformation. The former case may be resolved by judging which deformation regime (regional-tectonic or volcano-tectonic) has had must influence. The latter case may be resolved by separating a regional-tectonic origin of the fault from a volcano-tectonic displacement on it. Outside the controlled bounds of a model, however, reality may of course render awkward the application of such terminology.

1.6 Basic experimental set-up in this study

Past studies have used various materials to simulate the brittle behaviour of upper crustal rocks in a magma chamber roof and the ductile behaviour of a magma chamber. Material used for the brittle crust included: clay (Komuro 1987), alumina powder (Marti et al. 1994), sand (Acocella et al. 2000; Roche et al. 2000; Troll et al. 2002; Kennedy et al. 2004), flour or sand/flour mixtures (Walter and Troll 2001; Geyer et al. 2006) and sand/gypsum mixtures (Roche et al. 2001). To simulate a pre-collapse magma chamber most workers have used either fluid silicone (Acocella et al. 2000; Roche et al. 2000) or air/water in a rubber balloon (e.g. Marti et al. 1994; Walter and Troll 2001; Troll et al. 2002; Kennedy et al. 2004; and Geyer et al. 2006). An exception was Komuro's (1987) dry ice sphere. These analogue materials present advantages and disadvantages in terms of practicality of use, boundary effects and scaling accuracy (see below).

For most of the experiments in this study, fine-grained (0.09-0.25 mm diameter), well-sorted Fontainebleau sand mixed at 4:1 by volume with gypsum powder (cf. Donnadieu and Merle 1998; Girard and van Wyk de Vries 2005) was used as an analogue to rock at shallow crustal levels (**Figure 1.9**). Creamed honey, which has a surface tension and viscosity high enough to retard significant permeation into the sand, was used to simulate granitic magma in the majority of experiments. The basic experimental set-up for most caldera collapse experiments (**Chapters 2, 3, 4 & 6**) comprised a fixed table, on which lay a 5 –8 cm thick sand-gypsum pack. As caldera collapse is regarded as a high-level deformation above the brittle-ductile transition in the Earth's upper crust (Lipman 1984), a ductile lower crust component was excluded from the models. Within the sand/gypsum pile was an inclusion of honey of laccolithic or tabular geometry (thought to be the most common form for natural granitic plutons - Cruden 1998). A 0.8 cm diameter honey conduit allowed evacuation of the honey from the reservoir base (**Figure 1.9**).

To construct this set-up, and create the conduit for honey evacuation, a vertical hole of 1 cm diameter was first drilled through the table and lined with a pipe of 1 mm wall thickness (**Figure**

1.10a). The pipe was plugged at its lower end and a honey-filled syringe was fixed upright in its upper end (**Figure 1.10b**). The sand pile was then levelled off around the syringe at a height corresponding to the desired depth of the chamber base. To fill the pipe and link it to the chamber base, the syringe was withdrawn upward to the levelled sand surface, while simultaneously squeezing out more honey (**Figure 1.10c**). A cylindrical mould was placed on the sand surface and filled with honey to the scaled chamber thickness (1 - 2.5 cm) (**Figure 1.10d-f**). The sand pile was then built up around the mould to the honey level, and the mould was slowly extracted. After sufficient time elapsed to ensure a flat honey surface (no wrinkles or ridges **- Figure 1.10g**), sand was carefully and evenly placed over the chamber to make the roof (**Figure 1.10h**). The sand-pile was then levelled off at a desired total height (**Figure 1.10i**). Constructing the sand-pile with marker layers of alternating colour allowed fault offsets to be detected and measured in model cross-sections (see below).

If any roof subsidence occurred during this procedure, the experiment was aborted. Unplugging the lower end of the pipe caused evacuation of the honey chamber via the conduit, destabilisation of the roof, and onset of caldera collapse. Although collapse was thus in response to fluid outflow, rather than vice versa (see Roche et al. 2000), resultant structures closely matched those of past analogue studies (e.g. Roche et al. 2000; Kennedy et al. 2004), and so any deformation imposed by fluid flow was negligible.

Experimental evolution in plan view was recorded by time-lapse photography from a camera overhead. Photograph quality was later enhanced with image processing software. Model surfaces were illuminated with low-angle lighting to accentuate relief and contrast to aid the recognition of structures and improve appearance of photographs. After models were run, they were soaked with soapy water and serially sectioned (**Figure 1.11a-d**) to reveal the geometry of structures in 3D.

The experiments in **Chapter 5**, which formed part of a preliminary study on regional tectonic influences in caldera collapse, were run with 12:1 or 3:1 mixtures sand/flour (cf. Walter and Troll 2001) and an air-filled rubber balloon to simulate brittle crust and a pre-collapse magma chamber respectively. During the course of the project, creamed honey was identified as an analogue for magma best suited for resolution of some of the problems that the study aimed to address, however. In particular, the creamed honey chambers allowed regional tectonic deformation to be expressed in the chamber and so permitted investigation of the influence of regional-fault-defined pluton boundaries on caldera collapse (see **Chapter 6**). Also, tests showed that collapse was more sensitive to subtle variations in roof loading than the rubber balloons. The latter feature was particularly important in unravelling patterns of fault nucleation and propagation in **Chapters 2 and 4**. Flour and sand, and combinations thereof, were thus only used for the experiments described in **Chapter 5**. For immediacy, properties of these materials and their scaling are thus described separately in **Chapter 5**.

Chapters 5 and 6 also contain the results of more complex experiments simulating regional tectonic deformation in addition to caldera collapse. For convenience and immediacy, descriptions of experiment methodologies and set-ups for the simulation of regional tectonic deformation are included in the relevant chapter.

1.7 Scaling of experimental parameters to those in nature

Analogue models should obey the Principle of Similarity (Hubbert 1951), whereby lengths, deformation rates, material properties, and forces in experiment should scale to those in nature. A scaling ratio for any given physical property is $X^* = X_{Model}/X_{Nature}$ and relates to scaling ratios for other properties through standard physical equations. In **Chapters 2, 3 and 4**, only deformation related to the caldera collapse phase is considered, and so scaling calculations are relatively straightforward. In **Chapters 5 & 6** pre-collapse regional tectonics and syn-collapse caldera formation are addressed together, however, and as the timeframes of these processes differ greatly in nature, they must be scaled as two separate deformation phases in experiment (**Table 1.1**).

Brittle failure of sand and rock approximates a Coulomb criterion defined by the material cohesion and angle of internal friction (Hubbert 1951; Schellart 2000). The length ratio, $l^* = l_{Model}/l_{Nature}$ (geometric scaling factor) was 5×10^{-6}, so that 1 cm in the model corresponds to ~ 2 km in nature. The stress and cohesion ratio, $\sigma^* = \sigma_{Model}/\sigma_{Nature}$ (dynamic scaling factor) is calculated from the equation $\sigma^* = \rho^* g^* l^*$. The angle of internal friction of the sand/gypsum mix (ϕ_{SG} ~ 37° from maximum sand/gypsum cone slope) matches that of natural rocks (ϕ_{Nature} = 30-45° – Goodman 1989). The sand/gypsum mixture's density was around 1400 kg m^{-3}, whereas that of most natural rock types (granites, basalts, hard limestones, etc.) lies between 2600 – 3000 kg m^{-3} (Goodman 1989). As the analogue material density is half that of natural rocks (i.e. $\rho^* = 0.5$) and gravitational acceleration is the same in both model and nature (i.e. $g^* = 1$), the required stress ratio for a geometric scaling factor of 5×10^{-6} is $\sigma^* = 2.5 \times 10^{-6}$. Cohesion of natural rocks lies in the range of 10^5-10^8 Pa (Schellart 2000 and references therein), although mechanical anisotropies (fractures, etc.) will result in cohesions less than the range maximum – perhaps around 10^6 Pa (Schultz 1996). When the above natural cohesion range is scaled down by 2.5×10^{-6}, the required analogue material cohesion is 0.25 – 250 Pa (**Table 1.1**). At normal stresses applied in the models, cohesion of dry, fine-grained sand is 0 – 250 Pa (Schellart 2000); addition of finer material like gypsum or flour raises this value only slightly (e.g. $\sigma_{Model} \approx 200$ Pa in Donnadieu and Merle 1998). Resolution of fractures is consequently enhanced, but effects on overall geometries and kinematics in the models are actually minimal (Belousov et al. 2005).

Scaling of brittle material behaviour is theoretically time-independent, and is thus the same for the regional and caldera deformation phases. Scaling of ductile behaviour is time-dependent, however, as viscosity (η) ratios relate to stress (σ^*) and time (T^*) ratios through the equation $\eta^* = \sigma^* T^*$. The time ratio $T^* = l^*/V^*$, where V is velocity (**Table 1.1**).

For the regional deformation phase (**Chapter 6**), slip rates along major strike-slip faults can exceed 2.5 cm y^{-1} (e.g. the Great Sumatran Fault – Bellier et al. 1999), which for a model strike-slip rate of 1 cm h^{-1} gives velocity and time ratios of $V_r^* = 3.5 \times 10^3$ and $T_r^* = 1.4 \times 10^{-9}$. Durations of 1.5 – 4 hours typical for the model regional deformation phase thus scale to 1.2 – 3.2 x 10^5 years in nature (**Table 1.1**). This range is within that of $10^5 - 10^6$ years, over which large caldera-forming magmatic centres are believed to accumulate and reside in the Earth's crust (Jellinek and DePaolo 2003). Measured before each experiment with a rotary viscometer, creamed honey viscosity was ~ 200 – 600 Pa.s (**Figure 1.9**), which through the viscosity equation, scales to $\eta_{nr} = 5.7 \times 10^{16} - 1.7 \times 10^{17}$ Pa.s for the regional deformation phase. Depending on temperature and water content, experimentally derived viscosities for granitic melts range from $10^4 - 10^{12}$ Pa.s (Dingwell 1999). As cooling, degassing, and crystallisation occur, however, viscosities in assembling granite plutons possibly approach values up to 10^{18} Pa.s (Scaillet et al. 1997) – particularly around the pluton margins. Past analogue studies of syn-tectonic granite emplacement into strike-slip or transpressive regimes (Benn et al. 1998; Roman-Berdiel 1999; Corti et al. 2005) assume similar or higher natural granite viscosities to those in the regional deformation phase here.

The caldera deformation phase occurs on geologically instantaneous timescales relative to the time-spans of large-scale regional tectonics and batholith construction. Catastrophic collapse over hours to days (e.g. Long Valley caldera – Hildreth and Mahood 1986) can result in subsidence of ~100 m to 5 km (e.g. Stillwater caldera complex – John, 1995). A natural subsidence rate of ~ 3 km over ~ 48 hours, i.e. $V_{nc} = 1.7 \times 10^{-2}$ ms^{-1}, was replicated in our models as 1 cm in 5 hours (on average), i.e. $V_{mc} = 5.6 \times 10^{-7}$ ms^{-1}. This gives $V^* = 3.2 \times 10^{-5}$, which with $l^* = 5 \times 10^{-6}$, yields $T^* = 1.5 \times 10^{-1}$. Through the viscosity equation, the honey thus scales to a natural viscosity of $\eta_{nc} = 5.1 \times 10^8 - 1.5 \times 10^9$ Pa.s for the caldera collapse deformation phase (**Table 1.1**). Such viscosities are at the higher end of the experimentally-defined range for a pure melt, but are lower than the bulk viscosity of a semi-crystallised pluton (Scaillet et al. 1997). They may thus characterise a mobile, eruptible granitic magma fraction that is crystal-rich (20-50% phenocrysts - e.g. the Youngest Toba Tuff – Chesner 1998), and has relatively low temperatures (700-800º C) and water contents (2-3 wt. %).

For experiments with caldera collapse following regional deformation (**Chapters 5 and 6**), caldera slip rate and regional slip rate must be scaled directly within the caldera collapse phase. Since caldera collapse velocity, $V_{nc} = 1.7 \times 10^{-2}$ ms^{-1} and regional strike-slip velocity, $V_{nr} = 7.9 \times 10^{-10}$ ms^{-1}, natural caldera collapse rate is about 20 million times faster than contemporaneous regional deformation rate. This relationship was replicated in most experiments in **Chapter 6** by switching off the motor (i.e. $V_{mr} = 0$) whilst the honey chamber evacuated. In **Chapter 5**, maintaining an extremely slow regional deformation rate during caldera collapse approximated this relationship.

1.8 Limitations of analogue models past and present

Edge effects were minimised by using a sufficiently large sand pile such that the width of the area of interest was around on third that of the sand-pile. Whereas caldera formation is commonly related to eruption of magma from the chamber to the surface, this is not simulated in experiments. Withdrawal of magma is instead from the analogue reservoir base, although this procedure may approximate caldera collapse triggered by lateral withdrawal - as inferred Katmai caldera, Alaska (Hildreth and Fierstein 2000) and Miyakejima caldera, Japan (Geshi et al. 2000). Where a fluid (honey) analogue reservoir was employed, the low-cohesive nature of the sand and sand/gypsum materials inhibited tensile fracture propagation by magmatic pressures (hydrofracturing). Moreover, the honey viscosity was too high to allow its intrusion into dilating faults; where a balloon was used, such intrusion was anyway impossible. Therefore, whilst the syn-collapse intrusion of caldera faults, and accumulation of syn-collapse deposits within the caldera may have some influence on the structural development of calderas, their effects could not be examined or accounted for here.

Realistic rhyolite viscosities, especially in water-rich explosive eruptions, are probably around 10^4 -10^8 Pa s (Dingwell 1999). Creamed honey therefore scales to relatively high natural viscosities, although these are still lower than those scaled to by the silicone used in previous experiments (e.g. Acocella et al. 2000; Roche et al. 2000). As a consequence, intrusion of honey along ring fractures was prohibited. Although air may be of low enough viscosity to simulate rhyolitic and even basaltic magmas, its confinement within an elastic balloon greatly limits the fluid's mobility (although this also depends on the wall thickness and diameter of the balloon). The rubber balloon walls and ability to intrude also impede the penetration of fault blocks into the chamber. Another potential disadvantage of balloons, as detected in tests, is that they may have inherent elastic deformation bias – i.e. contract on one side more or faster than the other.

The lack of a temperature gradient in both the magma chamber and the crust is a potentially important limitation. A thermally and rheologically graded (locally ductile) envelope of crust surrounding the magma chamber is therefore neglected, and as a result, caldera collapse was simulated as a system consisting of two thermo-mechanically homogeneous and sharply defined components. Since caldera collapse strain rates are so high (up to several km in hours to days – Wilson and Hildreth 1997), however, rheological behaviour of this heated envelope may anyway shift into the brittle field (cf. Twiss and Moores 1992; Park 1997) during caldera formation.

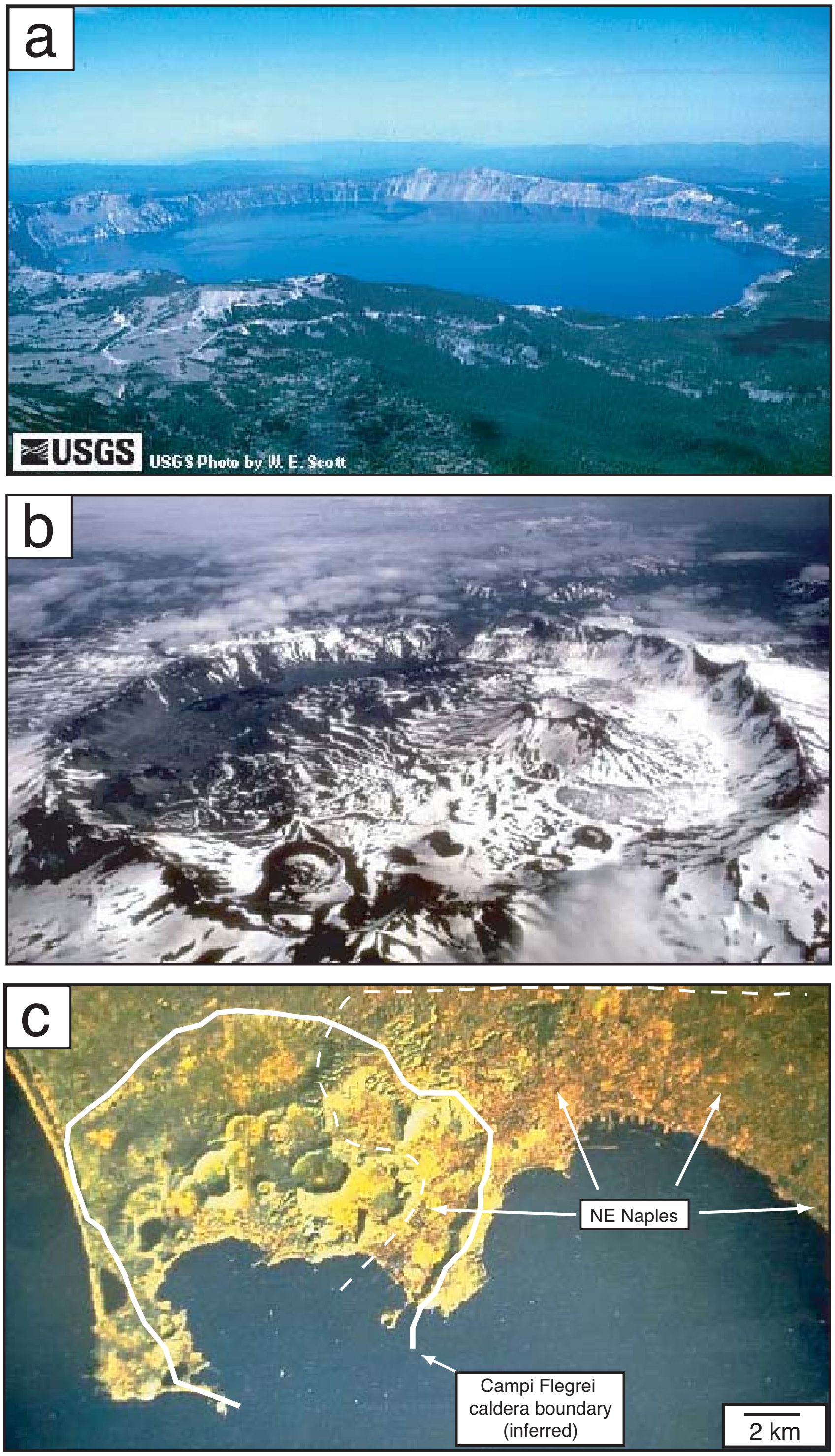

Figure 1.1: Photos of some modern calderas
a) Photo of Crater Lake caldera, Oregon (diameter ~ 8 km). USGS photo.

b) Aniachak caldera, Alaska (diameter ~10 km), shows the typical post-collapse morphology and poor structural exposure of an infilled caldera. Note the post-collapse volcanoes inside the caldera; magma intrusions feeding these can destroy the collapse structures buried far below the surface (USGS photo).

c) The still-active Campi Flegrei caldera, Italy, with Naples (pop. 3 million) adjacent. The caldera-forming eruption 37,000 yrs ago obliterated an area of 30,000 sq. km around the caldera. The 'resurgent' magma reservoir has since replenished and is now actively growing (ESA photo).

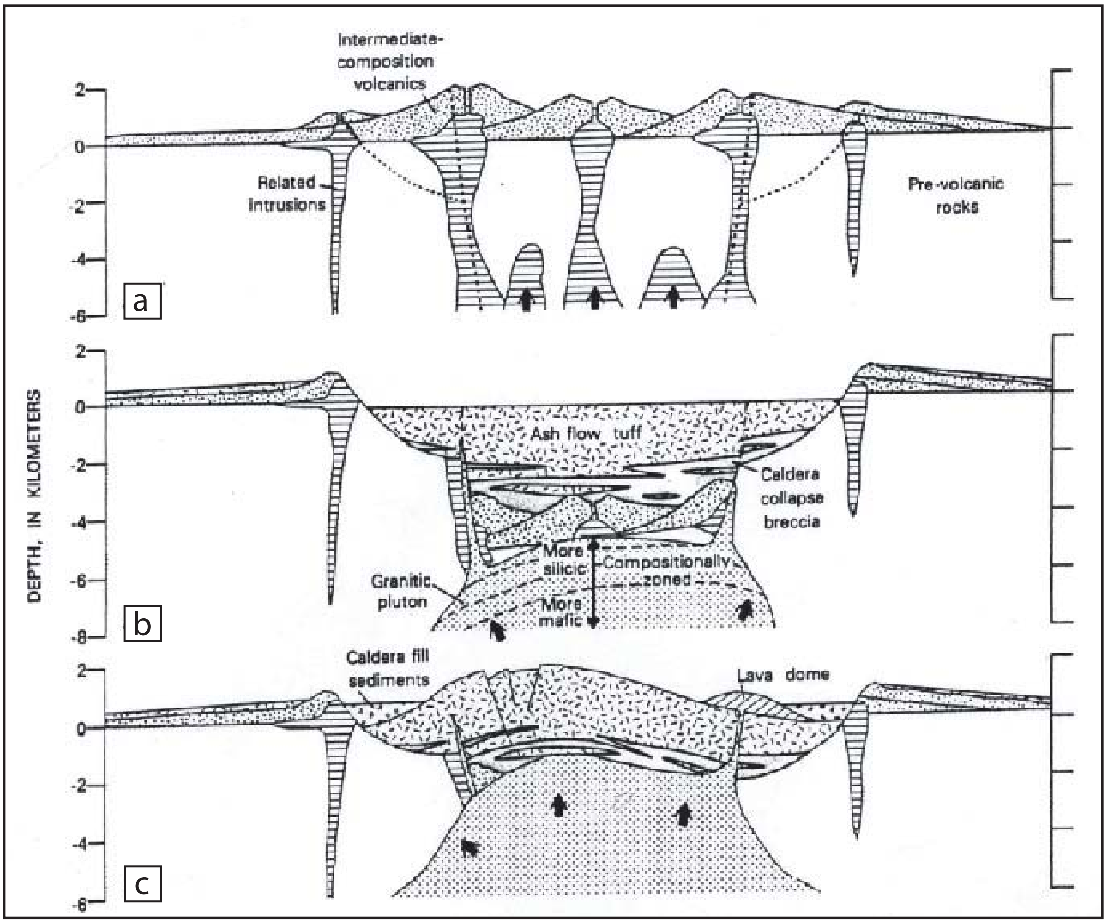

Figure 1.2 : Schematic evolution of a caldera cycle, as initially proposed by Smith and Bailey 1968, and modified by Lipman 1984). The diagram incorporates many common elements of ash flow calderas as revealed principally by field studies in the Western USA (from Lipman 1984).

a) Pre-collapse volcanism: Intermediate-composition stratovolcanoes grow over small high-level plutons. The plutons are precursors (and facilitators?) of a batholithic-size silicic magma body that will feed later ash flow eruptions. Uplift related to emplacement of plutons potentially leads to the development of arcuate ring fractures (indicated by dotted lines): these may guide subsequent caldera collapse. Heavy arrows indicate upward movement of magma.

b) Caldera collapse during ash flow eruptions: The magma chamber roof, including earlier volcanoes and the palaeo-landsurface (caldera floor), subsides (asymmetrically in this case; tilted to the left side of diagram). Intracaldera tuff, an order of magnitude thicker than cogenetic outflow ignimbrite sheet, ponds in the developing caldera. Ring faults guiding initial collapse over-steepen and their scarps collapse; voluminous landslide breccias accumulate and interfinger with intracaldera tuff.

c) Postcaldera volcanism, resurgence, and sedimentation: Magma intrudes caldera infill and cogeneic intracaldera tuff, and almost entirely obliterates the original caldera floor. Resurgent doming and uplift, perhaps accommodated by inverted movement along the subsidence ring faults, also results. A caldera moat and an apical graben form at the dome margins and dome crest respectively. Caldera moat is parly filled by lava domes and volcaniclastic sediments. Hydrothermal activity and mineralisation become dominant late in this part of the cycle.

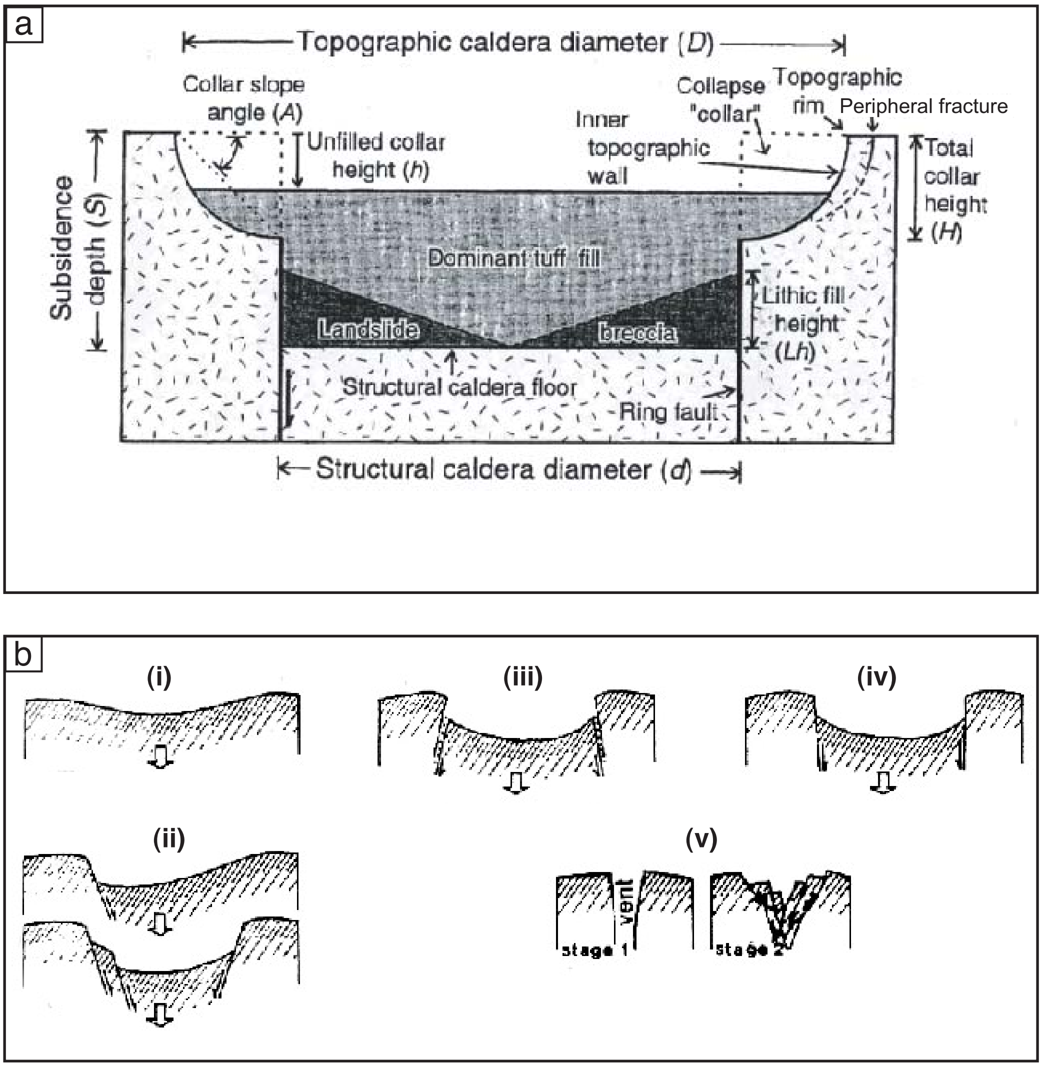

Figure 1.3:
(a) Simplified model of plate (piston) caldera subsidence (after Lipman 1997). Ring faults, which typically dip steeply, are arbitrarily shown as verical. The land-slide breccia is schematically shown as a wedge at the base of caldera fill, rather than as a more realistic complex interfingering with the fill. Omitted are the sub-caldera magma chamber, any resurgence stuctures, and any post-collapse volcanic constructs.

(b) Potential alternative styles of caldera subsidence (from Walker 1988). These include subsidence by: **(i)** pure downsag; **(ii)** downsag plus inward-dipping normal fault (with asymmetric subsidence progressing to symmetric subsidence); **(iii)** downsag plus outward dipping reverse fault (Andersonian-type ring fault); **(iv)** block subsidence along vertical ring fault or steeply inward-dipping ring fault with marginal strata upwarped bynormal drag; **(v)** collapse into a cored-out explosive vent.

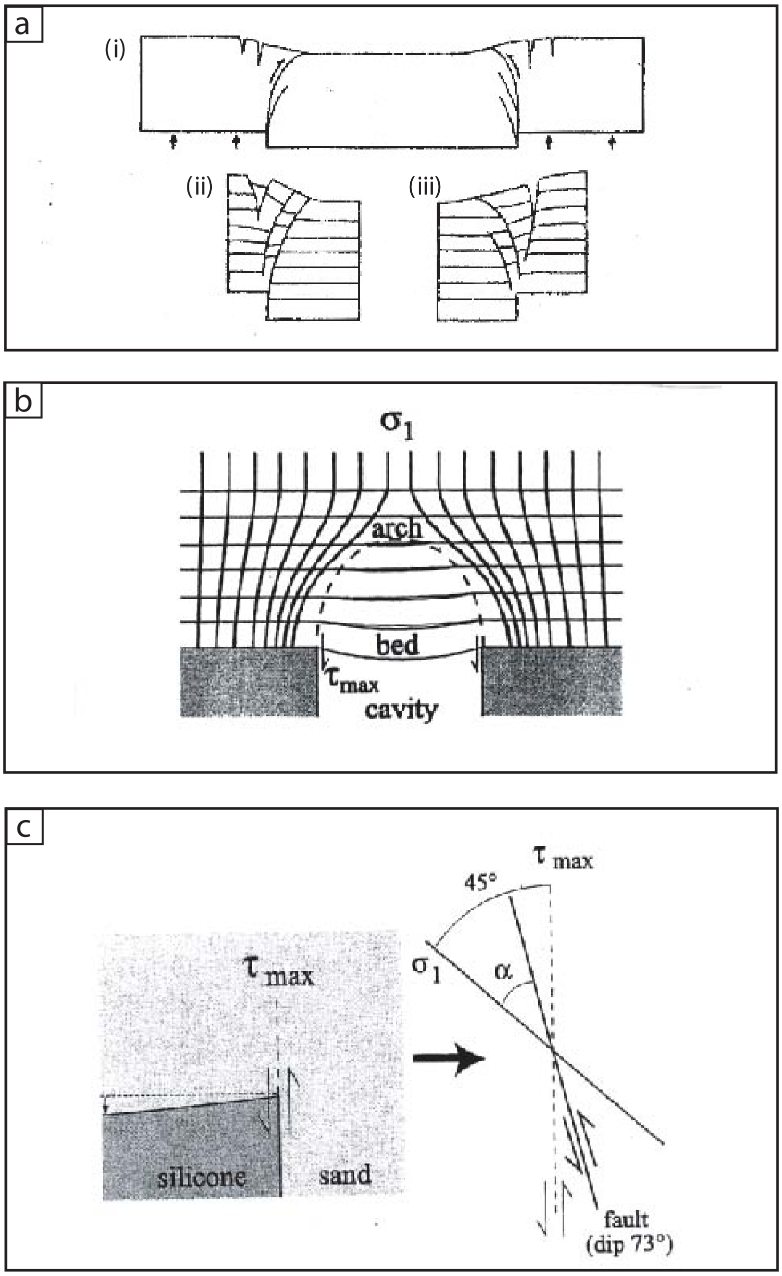

Figure 1.4: Stress arching and the formation of outward-dipping reverse faults
a) Cross-sections through sand-box experiments simulating subsidence (from Sanford 1959, via Branney 1995). (i) Sand collapses due to downward movement of base plate below sand-pile. Outward-dipping reverse faults form first at depth and in the centre. Reverse fault dip varies from very gentle near surface to near vertical above the base plate. (ii-iii) Crevasse, graben and inward-dipping normal faults from near surface in the inward-tilted (and slightly sagged) margins. Reverse fault propagate upward, normal faults propagate downward.

b) Sketch of maximum principal stress (σ_1) trajectory in a layered roof overlying a cavity (from Roche et al. 2000 - see also Whittaker and Reddish 1989). The stress trajectories define an arch, below which material is unsupported and so subsides. Shear stresses are maximum at the edge of the cavity (τ_{max}).

c) Close up sketch of experimental reservoir edge, showing the local subvertical shear zone between the down-going roof and unaffected surrounds (from Roche et al. 2000). The arched σ_1 trajectory lies at an angle of ~ 45^o to the shear zone.The reverse fault forms at an angle, α, of 45^o - $\varphi/2$ to σ_1, where φ is the angle of internal friction, ~ 34^o. The reverse fault is thus roughly in Riedel shear orientation and dips outward at ~ $73^{o.}$

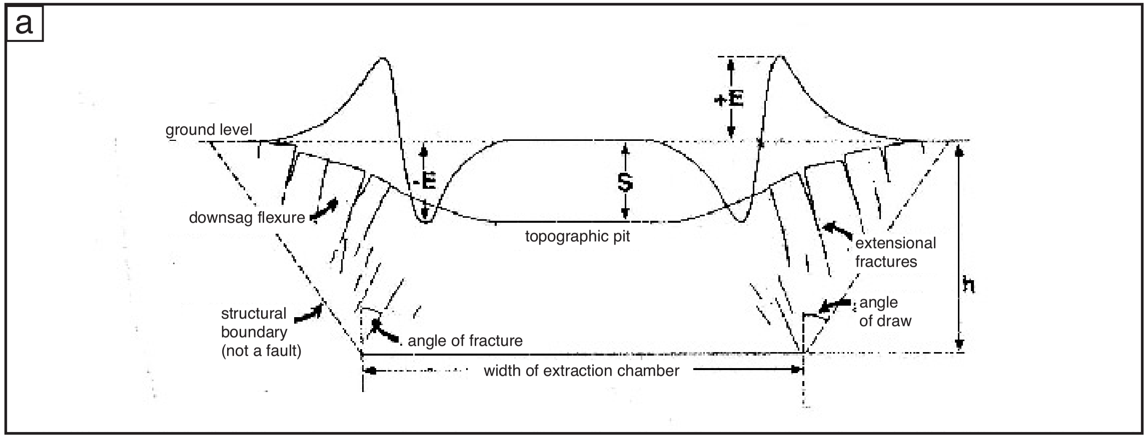

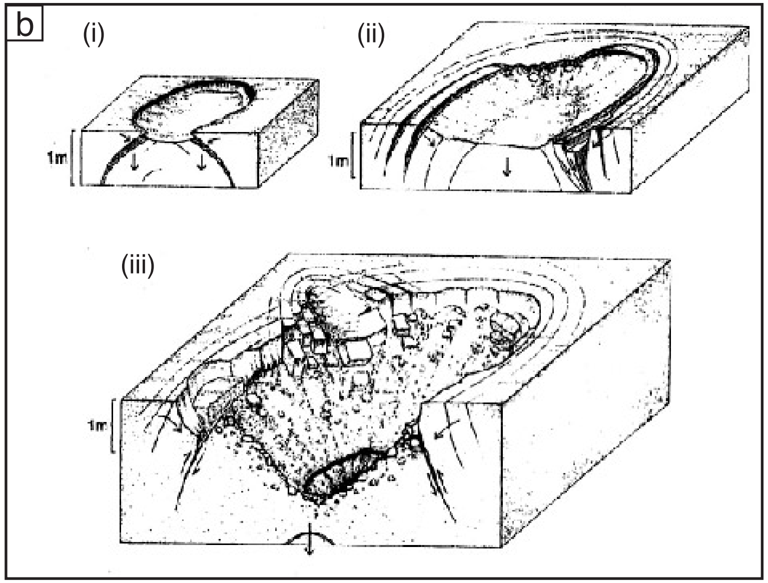

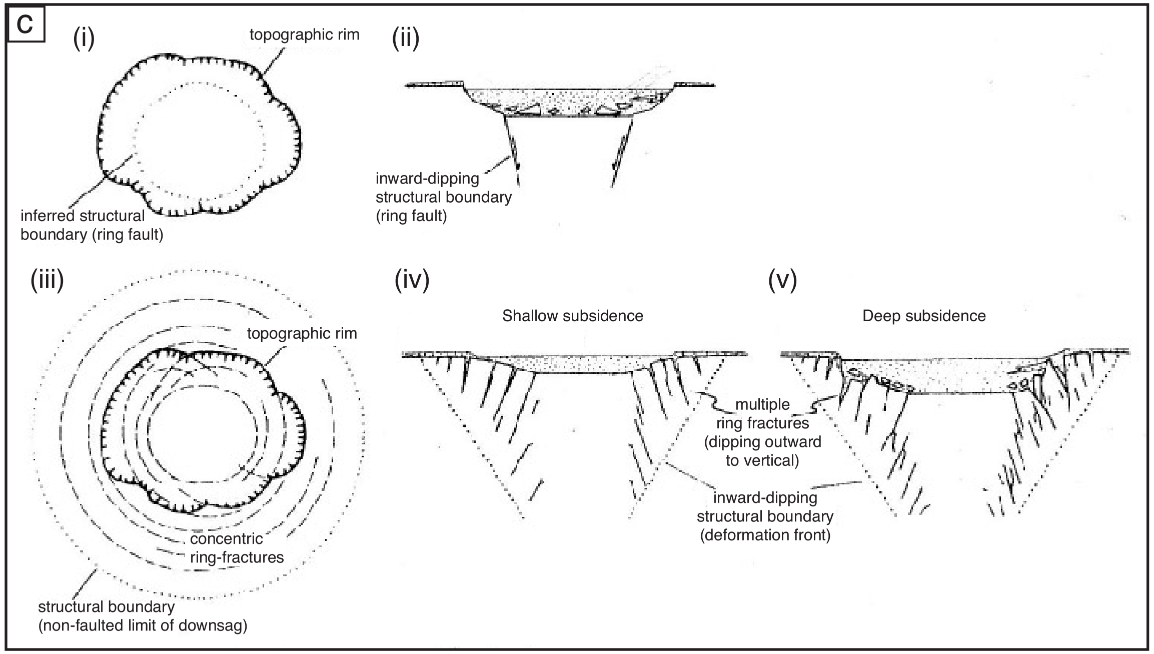

Figure 1.5: Application of mining subsidence theory to ice-melt collapse pits and calderas (from Branney 1995)

(a) Cross-section of generalised mining subsidence structure (based on Whittaker and Reddish 1989), showing surface strain and subsidence profiles. -E and +E are maximum extension and contraction respectively. Note limit of influence defined by angle of draw.

(b) Structures formed in ice-melt collapse pits. (i) small immature pit with outward-dipping fracture; (ii) larger, more mature pit with central compressional zone and peripheral extensional zone (iii) Still more mature and deeply-subsided pit (now has funnel shape, and overhanging walls have extensively collapsed to form debris aprons).

(c) Suggested alternative caldera stucture, based on mining and ice-melt pit evidence. Above: previously accepted ring-fracture-orientated caldera structural model in (i) plan-view and (ii) cross-section (see also Fig. 1.3a). Below: alternative downsag-orientated caldera structural model (iii) in plan-view with (iv) early stage and (v) late stage cross-sections. Note the non-faulted, cryptic structural boundary (limit of influence) lies outside (rather than inside) the topographic rim and dips inward in cross section. Note also the early-formed outward-dipping fractures; the central fractures may develop into reverse faults. The peripheral fractures form crevasse and graben. Note finally the collapse of peripheral extension zone as debris during late stage development.

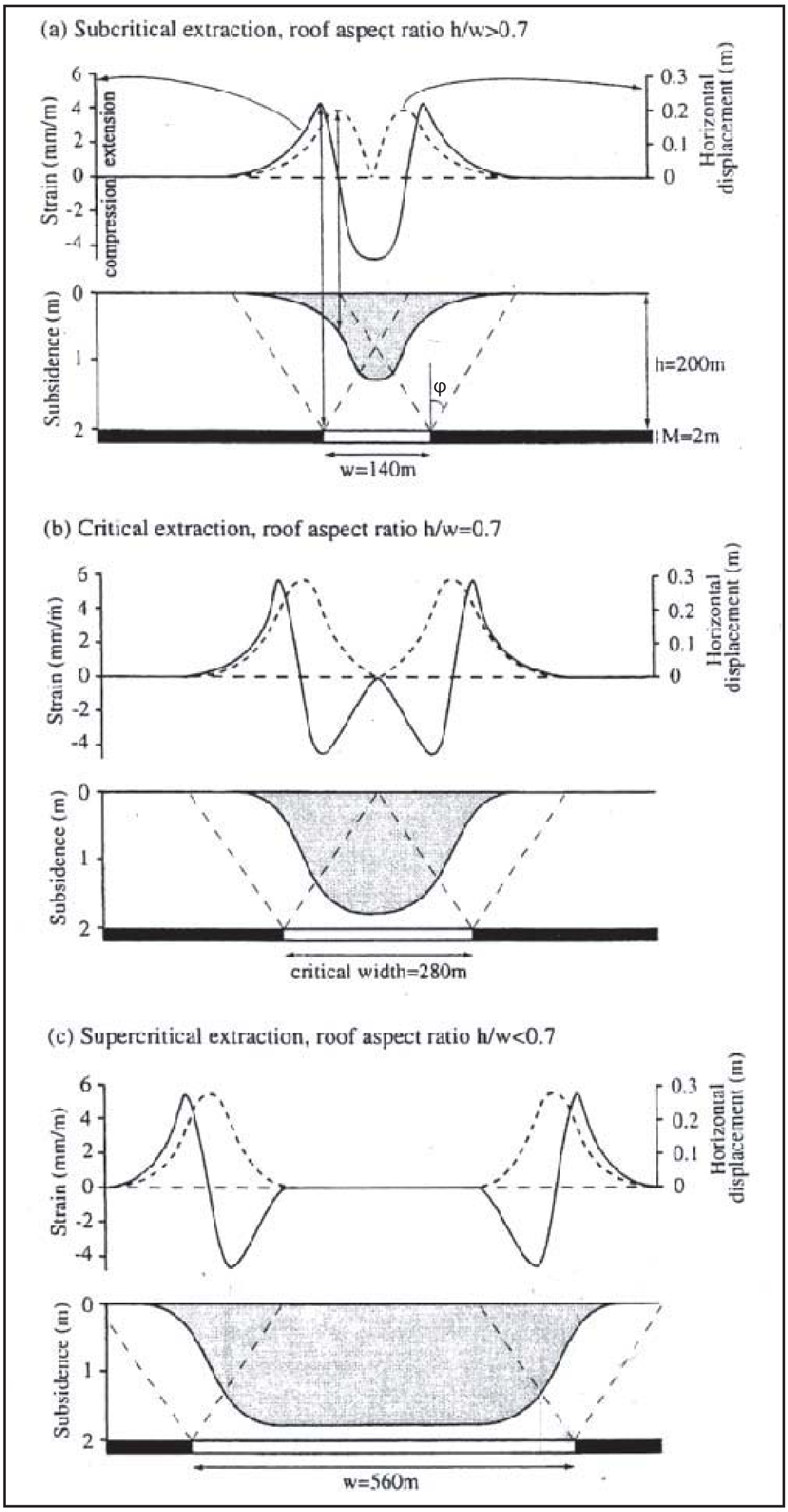

Figure 1.6: Effect of the ratio of roof thickness (h) to roof diameter (w) on mining subsidence profiles (from Whitaker and Reddish 1989 via Roche et al. 2000). M = extracted seam thickness (i.e. mine cavity height). φ = angle of draw (defines outer limit of the subsidence profile). Note that maximum surface extension occurs above, but maximum horizontal displacement (inward) occurs slightly further inside, the cavity margins. It is assumed that subsidence cannot exceed seam height (= 2 m here). Thus strains are relatively low here, and subsidence is accomodated via downwarping or distributed fracturing (Whittaker and Reddish 1989).
(a) Subcritical case (h/w > 0.7): full potential subsidence (downwarping) is inhbited by a degree of natural arching of the strata across the roof. Note that the whole width of the roof is deformed (see strain profiles).
(b) Critical case (h/w = 0.7): full potential subsidence just about permitted. Whole roof width is deformed.
(c) Supercritical case (h/w < 0.7): full potential subsidence is permitted as extraction width is too great to allow natual arching across the whole roof. Note that in this case the central part of the roof is undeformed.

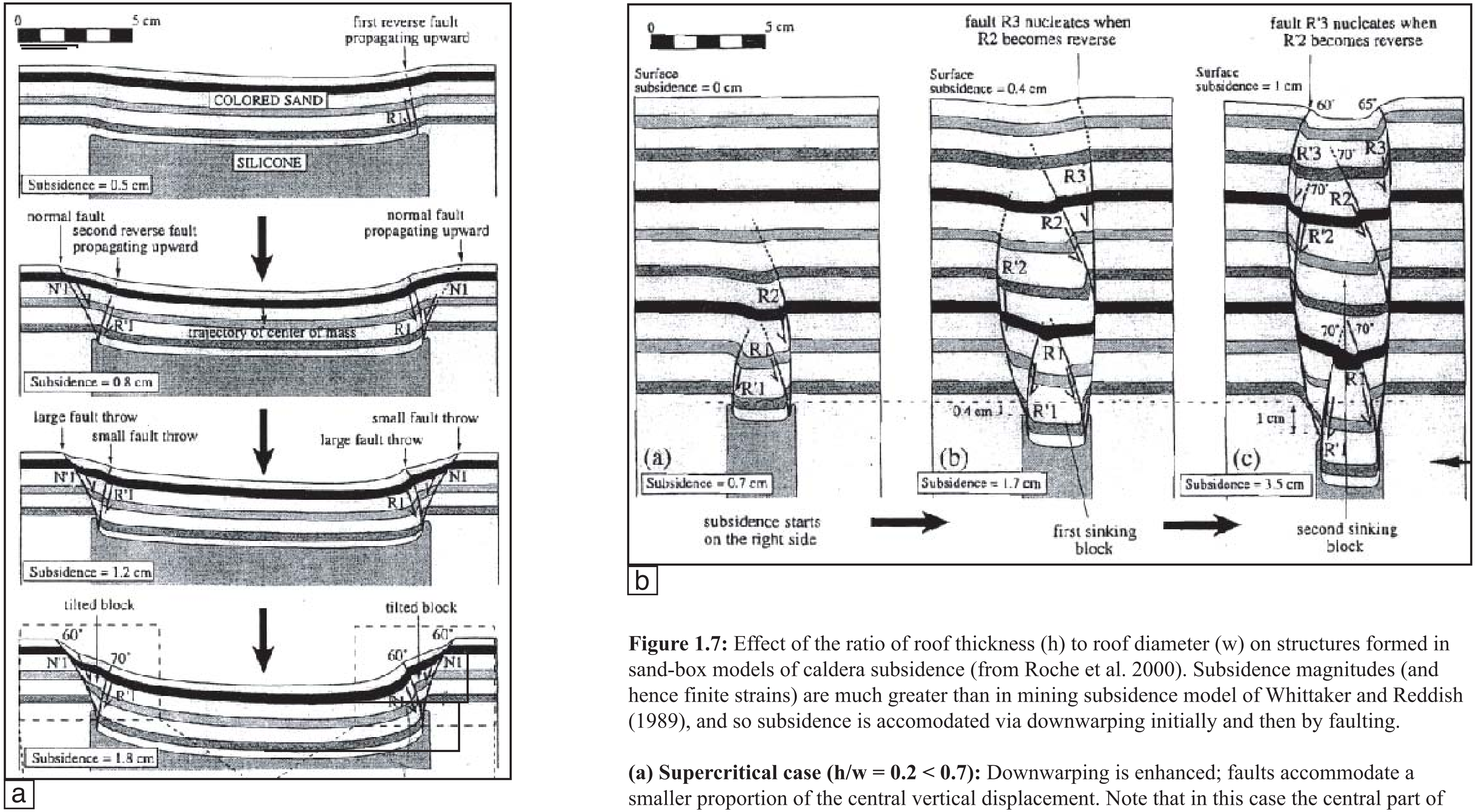

Figure 1.7: Effect of the ratio of roof thickness (h) to roof diameter (w) on structures formed in sand-box models of caldera subsidence (from Roche et al. 2000). Subsidence magnitudes (and hence finite strains) are much greater than in mining subsidence model of Whittaker and Reddish (1989), and so subsidence is accomodated via downwarping initially and then by faulting.

(a) Supercritical case (h/w = 0.2 < 0.7): Downwarping is enhanced; faults accommodate a smaller proportion of the central vertical displacement. Note that in this case the central part of the roof is undeformed by faulting.

(b) Subcritical case (h/w = 4.5 > 0.7): Downwarping is inhibited; faults accommodate a greater proportion of the central vertical displacement. Note that the whole width of the roof is deformed

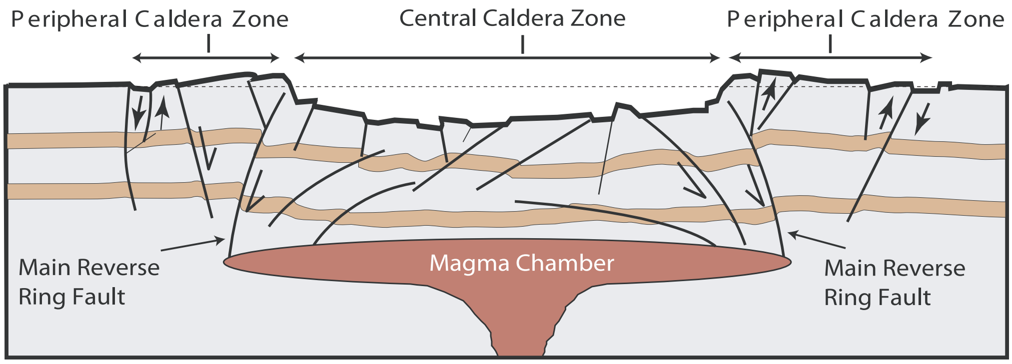

Figure 1.8: Sketch of model structures generated by tumescence followed by caldera collapse (simultaed via balloon inflation and deflation). Adapted from Walter and Troll (2001).

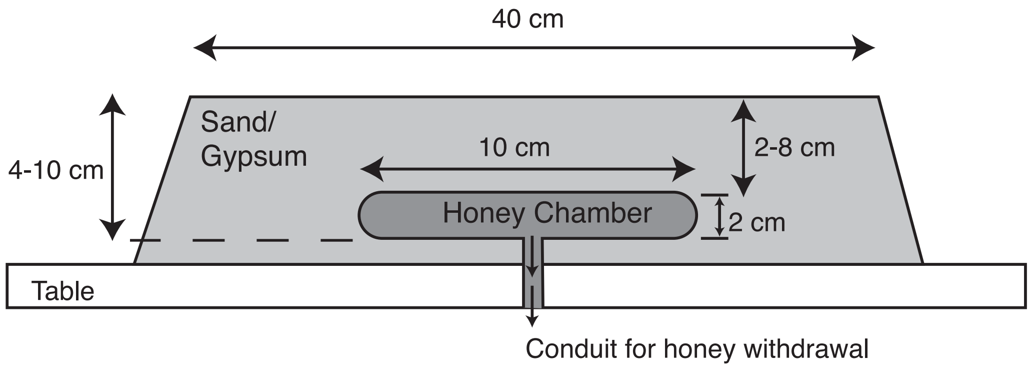

Figure 1.9: Cross-section of basic experimental set up used in this study for simulation of caldera collapse.

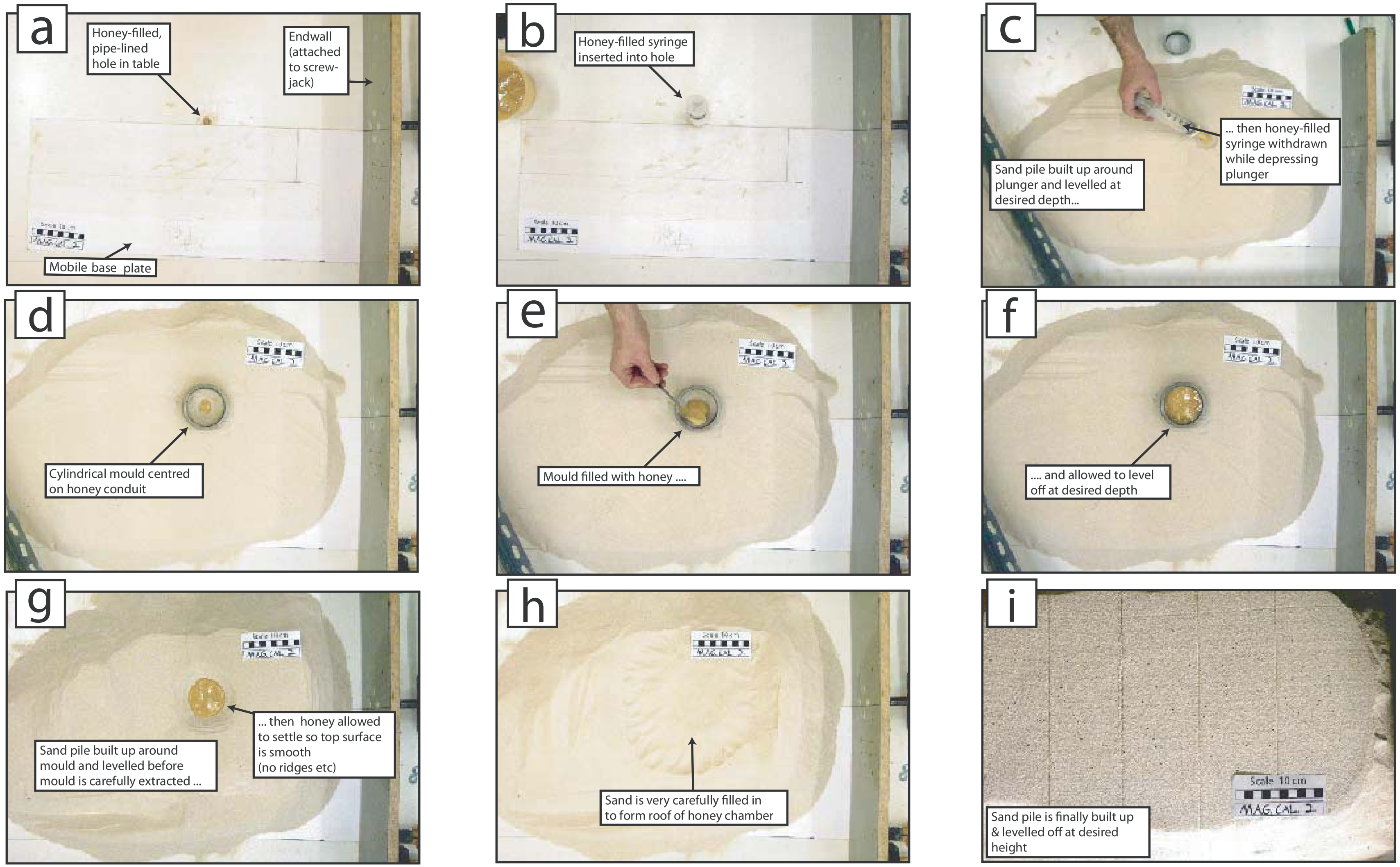

Figure 1.10: Sequential plan-view photos of honey chamber emplacement procedure for caldera collapse experiment series (in this case the MagCal set - see Chapter 6) .

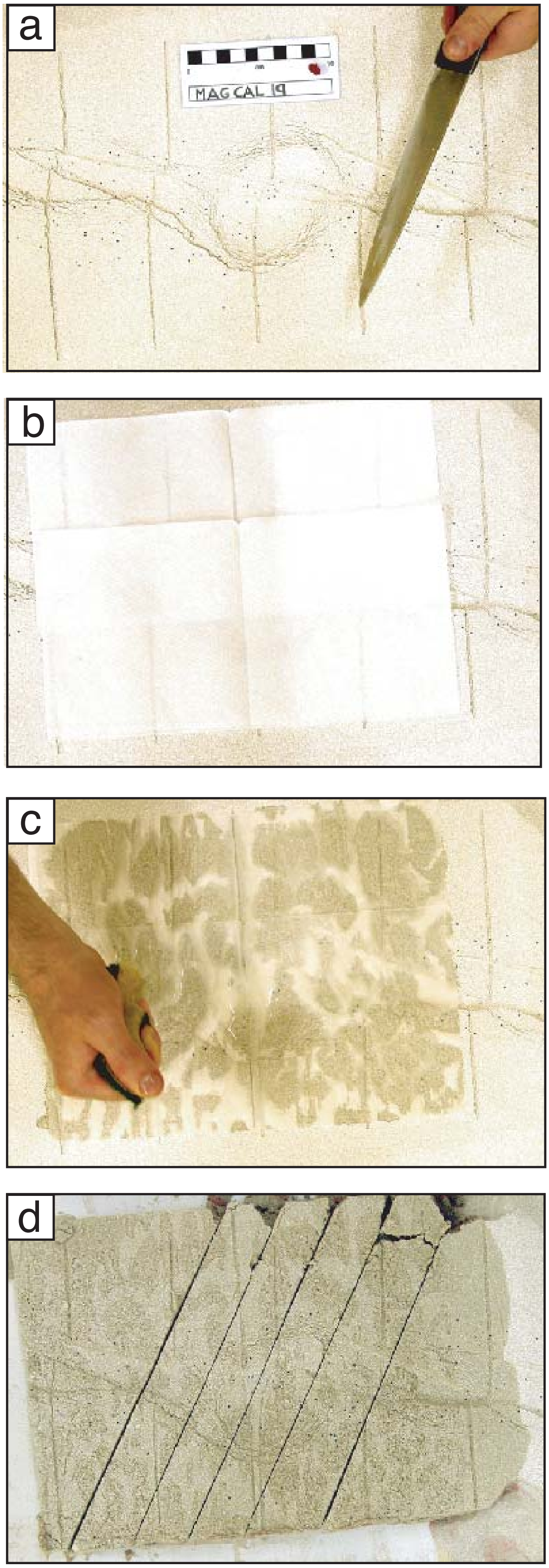

Figure 1.11: Plan-view photos of model cross-sectioning process.

a) Model run complete.

b) One or more paper towels is placed carefully on model surface. Usually only the area of most interest is covered.

c) Warm soapy water, applied gently from a sponge, soaks through the paper towel and into the model. Enough water is applied (typically 1-2 litres) until the area of interest in the model is wetted through to the base. Care must be taken not to over-saturate the model or it will disintegrate.

d) Once the model is wet through, unwetted areas and wetted areas of little importance are removed. The model may now be cut. With a sand-gypsum model, sections should be cut rapidly before the gypsum sets. Once cut, however, a sand-gypsum model can be allowed set, after which the slices are more robust. Smearing from the knife on the section face can be carefully scraped off - e.g. with a knife edge.

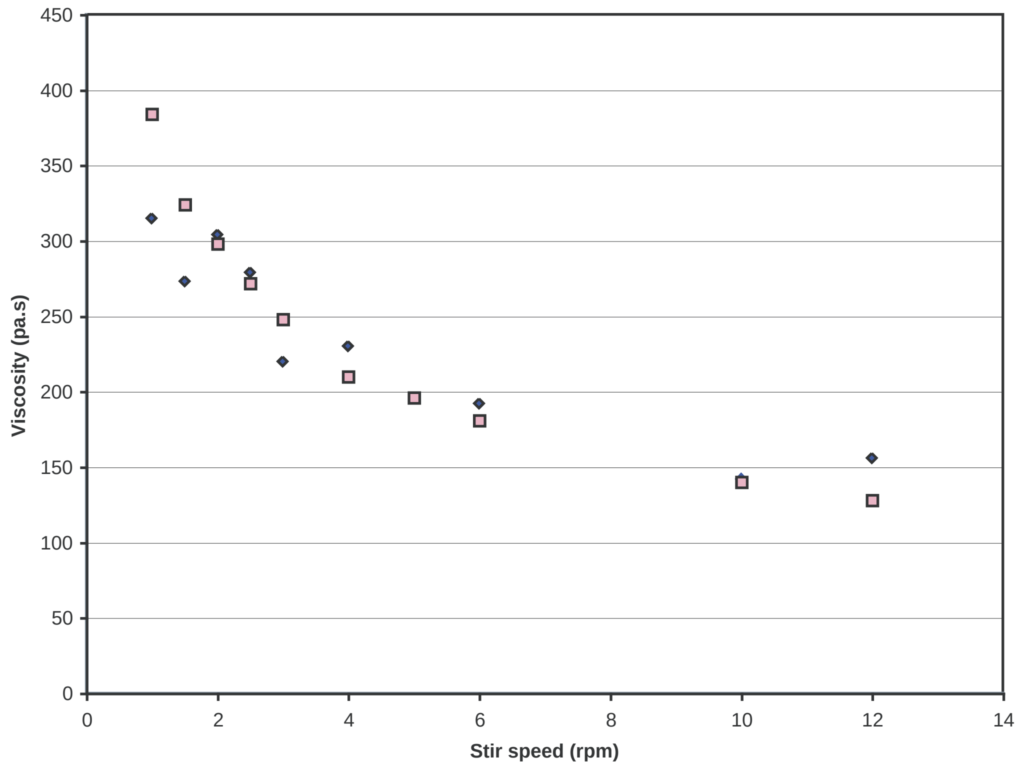

Figure 1.12: Viscosities of creamed Auvergne honey at room temperature, 20^{o} C. Diamonds and squares correspond to viscosity values measured for the representative honey sample, but with slightly different diameter spindles (or stirrers). The decrease in honey viscosity with increasing stirring speed indicates a departure from idealised Newtonian behaviour, but the plot shows the potential range of honey viscosities for different evacuation rates in experiment (10 - 50 cm^3 per hour).

Physical properties	Deformation Phase 1: Regional strike-slip	Deformation Phase 2: Caldera collapse
Length (l), Density (ρ), Gravity (g), & Stress/Cohesion (σ) [Geometric & Dynamic Similarity]	$l^* = l_m/l_n = 5 \times 10^{-6}$; $\rho^* = \rho_m/\rho_n = 0.5$; $g^* = g_m/g_n = 1$	As for Phase 1
	$\sigma^* = \rho^* g^* l^* = (0.5)(1)(5 \times 10^{-6}) = 2.5 \times 10^{-6} = \sigma_m/\sigma_n$	As for Phase 1
	$\Rightarrow$ If $\sigma_n = 10^5 – 10^8$ Pa, $\sigma_m = 0.25 – 250$ Pa	
Velocity (V) & Time (T) [Kinematic Similarity]	$V_r^* = V_{mr}/V_{nr} = 3.5 \times 10^3$	$V_c^* = V_{mc}/V_{nc} = 3.2 \times 10^{-5}$
	$T_r^* = l^*/V_r^* = (5 \times 10^{-6})(3.5 \times 10^3) = 1.4 \times 10^{-9} = T_m/T_n$	$T_c^* = l^*/V_c^* = (5 \times 10^{-6})(3.2 \times 10^{-5}) = 1.5 \times 10^{-1}$
	$\Rightarrow$ If $T_{mr} = 5.4 \times 10^3 – 1.4 \times 10^4$ s, $T_{nr} = 3.9 \times 10^{12} – 1 \times 10^{13}$ s	
Viscosity (η)	$\eta_r^* = \sigma^* T_r^* = (2.5 \times 10^{-6})(1.4 \times 10^{-9}) = 3.5 \times 10^{-15} = \eta_m/\eta_n$	$\eta_c^* = \sigma^* T_c^* = (2.5 \times 10^{-6})(1.5 \times 10^{-1}) = 3.9 \times 10^{-7} = \eta_m/\eta_n$
	$\Rightarrow$ If $\eta_{mr} = 200 - 600$ Pas, $\eta_{nr} = 5.7 \times 10^{16} - 1.7 \times 10^{17}$ - Pas	$\Rightarrow$ If $\eta_{mc} = 200 - 600$ Pas, $\eta_{nc} = 5.1 \times 10^8 – 1.5 \times 10^9$ Pas

Model Parameters	**Natural Parameters**	**References**
Length (l_n) = 1 cm = 10^{-2} m	Length (l_n) = 2 km = 2×10^3 m	
Density of Sand + Gypsum (ρ_m) = 1400 kg m^{-3}	Density of Crustal Rocks (ρ_n) = 2600 – 3000 kg m^{-3}	Goodman 1989
Gravity (g_m) = 9.8 m s^{-2}	Gravity (g_n) = 9.8 m s^{-2}	
Cohesion of sand (σ_m) = 0-250 Pa	Cohesion of Crustal Rocks (ρ_n) =10^5–10^8 Pa	Schellart 2000
Angle of internal friction (ϕ_m) = 37°	Angle of internal friction (ϕ_n) = 30-45°	Goodman 1989
Strike-slip velocity (V_{mr}) = 1 cm hr^{-1} = 2.8×10^{-6} m s^{-1}	Strike-slip velocity (V_{nr}) = 2.5 cm yr^{-1} = 7.9×10^{-10} m s^{-1}	Bellier et al. 1999
Chamber residence time (T_{mr}) = 1.5-4 hr = $5.4 \times 10^3 – 1.4 \times 10^4$ s	Chamber residence time (T_{nr}) = 10^5–10^6 yr = $3.2 \times 10^{12} – 3.2 \times 10^{13}$ s	Jellinek & DePaolo 2003
Caldera-collapse velocity (V_{mc}) = 0.2 cm hr^{-1} = 5.6×10^{-7} m s^{-1}	Caldera collapse velocity (V_{nc}) = 1.7×10^{-2} m s^{-1}	
Viscosity of creamed honey (η_m) = 200 - 600 Pa.s	Viscosity of granitic magma (η_n)= 10^4-10^{12} Pa.s	Dingwell 1999

Table 1.1 Outline of scaling adopted for two deformation phases, regional tectonic strike-slip and volcano-tectonic caldera subsidence. Values of parameters in model and nature are also given.

2 Caldera Collapse into Circular Reservoirs: Kinematics and Geometry of Associated Structures

2.1 Introduction

As outlined in **Chapter 1**, a major motivation for the suite of analogue studies and numerical models of caldera subsidence since the 1990's to present was initially to resolve the structural mechanisms by which subsidence might be accommodated in light of a perceived 'space problem'. This 'space problem' arose from many workers concluding or depicting caldera subsidence as having involved en-bloc subsidence of a magma chamber roof along a steeply inward-dipping ring fault with a normal sense of slip (see Lipman 1984 and references therein; see also Gudmundsson 1988, 1998). Indeed at many calderas, and potentially due to incomplete exposure, an inward-dipping, arcuate or ring-like fault (or fault scarp) was observed or inferred to be the main subsidence structure (e.g. Ischizuchi caldera – Yoshida 1984; Long Valley caldera – Newhall & Dzurisin 1988; Suswa caldera Kenya – Skilling 1993). The subsidence of a magma chamber roof as a coherent block along such an inward-dipping fault alone has long been thought to be geometrically unfeasible, however, since if the ring-fault dips inward on all sides of the block, the block cannot move downward. The block can only move downward within an inward-dipping ring fault if the block's diameter is somehow shortened (**Figure 2.1**).

One solution to this apparent space problem involves the downward bending (folding or sagging) of the strata inside the ring fault. Bending of strata reduces the radius of the down-going magma chamber roof and so allows the roof to slide down along the inward-dipping ring fault. This bending has been envisaged to occur either as a kind of localised friction-induced normal drag along the down-going side the ring fault, with the rest of the roof more or less undeformed (cf. Reynolds in Lipman 1984; Roberts 1974 in Moore and Kokelaar 1998), or as a more wholesale down-sag of strata inside the ring fault (e.g. Walker 1984 – **Figure 2.1a**). Indeed, the dips of caldera infill rocks are commonly inward (i.e. are centroclinal), particularly adjacent to what was found (or regarded to be) an inward-dipping ring fault (cf. Lipman 1984). In well-exposed calderas, strata of the pre-collapse caldera floor also show evidence of sagging, such as at Scafell caldera, England (Branney and Kokelaar 1994) and the Gross Brukkaros Depression, Namibia (Stachel et al. 1994). The normal drag visualisation has since fallen out of favour, since it requires the area immediately inside the normal ring fault to undergo horizontal shortening, whereas field evidence indicates these areas to undergo horizontal extension. At Scafell caldera, for instance, marginal graben and syn-eruptive normal faulting occurred just inside a main normal fault system. At Rotorua caldera, New Zealand (Milner et al. 2002) and Glencoe caldera, Scotland (Moore and Kokelaar 1998), sagged strata occur in conjunction with tensile fissures near the caldera margins. These field observations are compatible with wholesale sagging of the roof, however, and would relate to outer-arc extension about the margins of the down-flexure.

An alternative solution the apparent space problem involves the initial formation of outward-dipping faults with a reverse sense of slip, as per theoretical (e.g. Anderson 1951) and experimental predictions (Sanford 1959), followed by formation of an inward-dipping normal fault. Shortening across the reverse fault again solves the apparent 'space problem' by decreasing magma chamber roof's diameter (**Figure 2.1b)**. Further evidence for this solution has stemmed from analogue studies of caldera subsidence (e.g. Marti et al. 1994; Branney and Gilbert 1995; Branney 1995; Roche et al. 2000; Acocella et al. 2000; Walter and Troll 2001; Kennedy et al. 2004), which have also shown that the precursory development of one or more outward-dipping and reverse faults almost invariably leads to caldera subsidence along an inward-dipping and normal fault. Indeed, most analogue modelling studies have inferred that the formation of both outward-dipping and inward-dipping ring faults is an integral part of the caldera-collapse process on all scales (cf. Roche et al. 2000, 2001). Moreover, at the 'restless' Rabaul caldera, Papua New Guinea, an outward-dipping main ring fault has been imaged from the location of earthquake epicentres (Mori and McKee 1985), refinement of which has led to the suggestion of marginal inward-dipping structures also (Saunders 2001). Even more recently, during the closely monitored collapse of Miyakejima caldera, Japan, in 2000, workers documented strong evidence for both a central outward-dipping reverse fault and a peripheral inward-dipping normal fault compatible with experimental predictions (Geshi et al. 2002).

In reality, and in agreement with observations and predictions by (Walker 1984), most of these experimental studies have reported a combination of both of these end-member solutions acting to accommodate radial shortening (**Figure 2.1c)**. Furthermore, experiments by Roche et al. (2000) and Kennedy et al. (2004) indicate that sagging and reverse faulting are respectively more prominent in the hybrid solution at low and high thickness/diameter ratios of the roof. As will be shown below, the experiments of this study agree with this result.

Another kind of 'space problem' not considered in previous experimental studies of caldera formation, is that arising from the radial inward movement of material toward the caldera centre. Such inward radial motion has been observed during surface subsidence above depleted hydrocarbon reservoirs (cf. Odonne et al. 1999 and references therein), above mines and other sub-surface excavations (Whittaker and Reddish 1989), and during deflation episodes at restless calderas (e.g. Sierra Negra, Galapagos Islands – Geist et al. 2006). If the roof material moves inward along all radial directions toward a central point, it not only undergoes radial shortening (as discussed above), but it must also undergo some concentric shortening. Indeed, numerical studies of caldera subsidence (e.g. Zuber and Mouginis-Mark 1992) calculate compressive concentric stresses that at initiation of subsidence can be of greater magnitude than radial stresses. In some cases, the concentric stresses are thought to relieved by the generation of so-called wrinkle ridges that trend radially from the centre of the caldera – e.g. in Olympus Mons caldera, Mars (Mouginis-Mark and Robinson 1992). Such features, or alternative mechanisms to accommodate concentric shortening, have not as yet been documented experimentally, however, and so it is as yet unclear what these may be, and how key parameters such as the thickness/diameter ratio of the roof may influence their development.

The experimental simulation of caldera collapse into circular reservoirs was thus revisited to shed new light on the accommodation of concentric shortening during caldera collapse, and also to examine other general aspects of the geometry and kinematics of caldera-related structures. These general aspects include the propagation and interaction of subsidence related faulting, polygonality of caldera outlines in plan view, and the development of incoherent caldera floor (piecemeal-like subsidence). Experiments simulating caldera collapse into circular reservoirs also served two other purposes. First, these 'simple' collapses served as the baseline or control against which the evolution of more complex experiments (detailed in **Chapters 4, 5 and 6**) could be compared. Secondly, since previous experimental and numerical studies of caldera collapse mostly assumed a magma reservoir that is circular in plan view, past analogue and numerical data may be most readily compared and contrasted with new data from this part of the present study.

2.2 Experiment Set-up

The experimental setup comprised a sand/gypsum pack, in which resided a two cm-thick and 10 cm diameter, tabular (sill-like) reservoir of creamed honey (see **Figure 1.6**). Evacuation of the reservoir could be achieved via a honey conduit, which extended from the reservoir base through the sand/gypsum pack to a 0.8 cm diameter pipe-lined hole in the table.

The main parameter varied was the thickness/diameter ratio of the roof, which previous studies (e.g. Whittaker and Reddish 1989, Roche et al 2000, Kennedy et al 2004) previously identified as having a decisive influence on the geometry and structural development of subsidence. 'Thin roof' models were therefore run with a roof thickness of 2 cm (Cal Stat A3) or 3 cm (Cal Stat A1, A2, A4 &A5) and 'thick roof' models were run with a roof thickness of 8.0 cm (Cal Stat H1-H2). 'Thin roof' thickness/diameter ratio was thus 0.20 - 0.33 and 'thick-roof' thickness/diameter ratio was 0.80. To further evaluate the kinematic development of collapse structures in 3D, and in line with previous work (Roche et al 2000; Walter and Troll 2001), a number of 'thin-roof' experiments were conducted against a glass pane, through which the structural development in cross-section could be directly monitored. A detailed description of the construction procedures and scaling considerations of the models is given in **Chapter 1**.

2.3 Experimental Results

2.3.1 Collapse into circular reservoirs with 'thin' roofs

Collapse above circular model reservoirs with thin roofs was always asymmetric and always occurred via sagging and ring faulting. Since collapses varied from almost symmetric (e.g. CalStat

A5 - **Figures 2.2 & 2.3**) to very asymmetric (e.g. Cal Stat A1 - **Figure 2.2**), both ends of a spectrum collapse symmetry were encompassed. In addition, the floors of some thin-roof models were noticeably more sagged (particularly the thinnest-roofed model - Cal Stat A3 - **Figure 2.5**) than others. Though structural development in all experiments was very similar, the degree of collapse symmetry and the amount of sagging produced some subtle variations on that development. This had consequences for the types and geometries of structures formed, and for the relative importance of different structures in accommodating subsidence-related deformation.

Early subsidence was always accommodated by sagging above the reservoir centre and a network of tensional fractures around the reservoir margins (**Figure 2.2a, 2.4a, & 2.5a**). Early sagging during experiment Cal Stat A5 (**Figure 2.2a**) remained symmetric, although in ultimately highly asymmetric experiments like Cal Stat A1 (**Figure 2.4a**), sagging commonly became slightly asymmetric. In this case, marginal tensional fractures adjacent the area of greatest subsidence often became more prominent. The outermost limit of marginal tension fractures defined a macroscopic ‘limit of collapse influence’. The exact limit of collapse influence was probably microscopic or ‘cryptic’ (cf. Branney 1995), and so may have lain a little further outside the macroscopic limit. In all experiments, the early sagging phase was also associated with inward horizontal movement of material along radial paths toward the developing caldera’s centre, as revealed by the motions of sand or calcium carbide grains on the model surface.

After initial sagging, a reverse fault trace composed of one or more near-linear facets appeared inside the projected outline of the reservoir margin (**Figures 2.2b, 2.4b & 2.5c**). That this fault was reverse and dipped outward was later verified in cross-section for several models – (e.g. **Figure 2.3**), but it could also be inferred from its characteristic ‘snubbed’ scarp morphology and from the horizontal shortening observed across the fault trace, where material outside moved across and over the subsiding material inside (e.g. **Figures 2.2c, 2.4c**). In the near-symmetrically sagged Cal Stat A5, the reverse fault formed instantaneously all around the reservoir’s circumference as a polygonal ‘ring’ (**Figure 2.2b**). In the asymmetrically sagged Cal Stat A1, the reverse fault initially localised along a discrete arc near or at the area of greatest sagging (**Figure 2.4b**). The exact position of initial reverse fault localisation on the reservoir circumference during asymmetric collapse varied between experiments. In the very thin-roofed and markedly sagged Cal Stat A3, reverse fault localisation was delayed (**Figure 2.5b,c**). Instead, sagging was sufficiently pronounced to firstly generate compressive ‘wrinkle ridges’ (cf. Plescia and Golombek, 1986) at the roof centre. With further subsidence, collapse ultimately became asymmetric and a reverse fault localised near the area of greatest subsidence. Compared to Cal Stat A1 and A5, however, the reverse fault in Cal Stat A3 was less sharply defined and did not appear to accumulate as much displacement. Also unlike Cal Stat A1 and A5, central sagging in Cal Stat A3 persisted after reverse fault formation, as seen by the progressive development of the wrinkle ridges into a pronounced radial array (**Figure 2.5d,e**).

In all highly asymmetric collapses, the reverse fault propagated bi-directionally around the reservoir margins from its single localisation point toward the flexured area of least subsidence ('hinge zone') on the side opposite (**Figure 2.4c**). In the down-going central block, asymmetric subsidence along the outward-dipping reverse fault induced a component of horizontal motion that was directed away from the hinge zone and toward the point of most subsidence (see also Roche et al. 2000). From this point, where all slip was down-dip, the reverse fault therefore displayed an increasing component of oblique-slip. Oblique slip reached a maximum near the hinge zone, where motion on the reverse fault was initially predominantly strike-slip (**Figure 2.4c**). Within the hinge zone, extension related to the horizontal motion of the central block commonly caused the reverse fault to eventually link with or further propagate as a normal fault (**Figure 2.5c,d)** - similar to an extensional 'horse-tail' termination of a strike-slip fault (cf. Twiss and Moores 1992). In Cal Stat A5, slight asymmetry to subsidence appeared *after* the reverse fault formed, and induced a similar, but less pronounced, horizontal component to the central zone motion (**Figure 2.2c**). The circumferential variation in vertical displacement and oblique slip on the reverse faults in asymmetric collapse indicates that they were mixed-mode fractures (Modes 2 and 3, and possibly also Mode 1 – Walter and Troll 2001), rather than truly dip-slip Mode 2 fractures.

Once the reverse fault began to propagate laterally around the reservoir margin, surface deformation in the zone peripheral to the central block changed from tension fracturing to normal faulting (**Figures 2.2c & 2.4c**). In greatly sagged collapses, this transition occurred just before the delayed appearance of the reverse fault trace (e.g. Cal Stat A3 - **Figure 2.5b,c**). With asymmetric collapse, even slightly, the component of horizontal motion in the down-going central zone block usually induced normal faulting in the hinge zone first (**Figure 2.2c, 2.4c & 2.5c**), where eventually a well-defined graben formed (e.g. **Figures 2.2d, 2.4d & 2.5d**). With more subsidence, the main normal fault systems rapidly developed from the hinge zones to the points of maximum subsidence (e.g. **Figure 2.2d,e**). The final normal 'ring'-fault system comprised a single subtly polygonal fault and/or a more complex array of faceted and sub-concentric fault strands (**Figures 2.2d & 2.4d**). In the second case, lateral (along-strike) displacement transfer occurred between adjacent faults strands - analogous to 'soft-linkage' of normal faults via relay ramps in rift zones. This arrangement gave rise to benches and 'step-faulting' around the margins of the model caldera (e.g. **Figure 2.2d**). The trace of the main normal fault or normal fault system was located outside both the reverse fault and the projected outline of the reservoir margin (**Figures 2.2d, 2.4d, 2.5d & Figure 2.3**). The main normal fault trace was also usually located slightly inside, or at, the macroscopic 'limit of collapse influence', as defined in the sagging phase by the outermost limit of marginal tension fractures. Indeed, many facets of the main normal fault traces coincided with tension cracks formed during the earlier sagging phase.

Whilst the outer normal fault system developed, material in the peripheral zone subsided, underwent further inward rotation, and moved bodily inward from the limit of collapse influence toward the caldera centre (e.g. **Figures 2.2c & 2.4c**). As the peripheral zone floor moved inward along the reverse fault, the plan-view diameter of the central zone floor decreased somewhat. This inward motion also resulted in two structural sub-zones within the peripheral zone - an outer sub-zone in which horizontal inward motion was less pronounced, and an inner sub-zone in which horizontal inward motion was more pronounced. The boundary between the two sub-zones was in some cases cryptic, but in others it was coincident with a well-developed outward-dipping normal fault (see northern sector of **Figures 2.2d,e & C-end of Figure 2.3**). This normal fault was always antithetic to the main outer normal fault and defined the inner boundary to a complexly-faulted marginal graben (e.g. **Figures 2.2d,e & 2.3**). Both sub-zones displayed a contrasting assemblage of structures.

The outer-sub-zone was primarily characterised by radial extension, which was taken up along a complex network of sub-concentrically trending fissures and normal to oblique-normal faults (**Figures 2.2d 2.4d & 2.5d**). As with the main normal 'ring'-fault system, many of the minor fault strands and crevasse comprising this complex network of fractures were faceted, and many of their traces coincided with tension cracks formed during the earlier sagging phase (**Figures 2.2b-d 2.4b-d & 2.5b-d**). Usually, several faults, facets, and/or cracks defined a set of parallel fractures. The intersection of several sets of parallel or near-parallel fractures defines the complex network of fissures, oblique-normal faults, rhombic fault blocks and step-faults in the outer sub-zone. Additionally, many of the fracture sets were parallel or near-parallel to facets in the outer normal ring-fault system (**Figures 2.2c-d & 2.4c-d**).

The inner-sub-zone was primarily characterised by concentric shortening, which was taken up along radially trending 'wrinkle ridges', sub-concentrically trending strike-slip faults, and/or obliquely trending oblique-reverse faults (**Figure 2.2d**). The strike-slip faults were commonly continuations of fractures that curved in from the outer sub-zone toward the reverse fault trace (**Figures 2.2d & 2.4d, 2.5d**), and they locally acted as tear-faults at the termination of the radial wrinkle ridges (**Figure 2.2e)**. The oblique-reverse faults usually formed as splays from the reverse 'ring'-fault section nearest the area of most subsidence. As these splays cut across the peripheral zone, they obliquely thrust one section of the peripheral zone over the other (e.g. Cal Stat A5 - **Figure 2.2d, e**). The inner sub-zone and its associated deformation was most noticeable when an inner reverse ring fault was well developed (e.g. Cal Stat A5 – **Figure 2.2**), but some of its characteristics (mainly the strike slip faults) could also be seen in collapses dominated by sagging (e.g. Cal Stat A3 – **Figure 2.5c,e**).

With further subsidence, major vertical displacements, at least at shallow structural levels, transferred from the reverse fault to the outer normal fault system. As evidenced by continued inward movement of the peripheral zone across the central zone, displacement continued on the reverse fault system, but at a slower rate than previously (**Figures 2.2d-e & 2.4d-e**). Further displacement also accrued on the minor normal fault and graben systems in the peripheral zone. In the highly asymmetric Cal Stat A1 experiment, a new reverse fault strand formed adjacent to the trapdoor-like hinge zone and linked with the existing reverse fault system to form a completed 'ring' (**Figure 2.4d**). As displacement on the now complete reverse 'ring'-fault equalised, horizontal motion in the central block sharply reduced and subsidence became increasingly less asymmetric. Consequently, slip kinematics on the reverse fault changed to become more dip-slip all around.

The scarps of the main reverse and normal ring faults and the peripheral zone faults eventually oversteepened, and decayed to produce grain flow deposits (**Figure 2.2e & 2.4e)**. Most material stemmed from the main outer normal fault system. Embayments into the normal fault scarp produced outward migration of the topographic margin and lateral enlargement of the caldera, but also decoupled the structural and topographic caldera margins. Decay of the main normal ring-fault system also buried the adjacent peripheral zones (and the hinge zone) in debris (**Figures 2.2e & 2.4e**), and slightly reduced the 'polygonality' of the caldera outline (e.g. in Cal Stat 5 – **Figure 2.3e**).

In a cross section through Cal Stat A5 (**Figure 2.3**), sagging or bending of pre-collapse strata is gentle in the roof centre and at a maximum above the reservoir edges, where the outward-dipping reverse ring fault cuts through. Here inward dips were usually 20-35°, but adjacent the reverse faults can locally be up to 70°. Reverse fault dip steepens with depth from ~ 35° near surface (shallow angle thrust) to ~ 70° just above the reservoir, but overall is about 62-68°. The reverse fault is shallowest in the part of the roof toward which the compressive horizontal motion of the central block was directed - i.e. at the D end of the C-D cross section. This relationship was also seen in the cross-sections of Cal Stat A4, and was very commonly found in the experiments of Roche et al. (2000).

The inward dip of the outer normal fault system varies from 75° to 86°, and is steepest at the D end of the C-D cross section (**Figure 2.3**). The effect of the compressive horizontal motion due to the slight asymmetry of subsidence is reflected in the slightly poorer development of peripheral extensional faults at the D end of the C-D line of section. Extension of the inward-rotated peripheral zone is mostly expressed in cross section as a marginal 'key-stone' graben, which internally is complexly faulted and fractured near surface. Whilst the keystone graben and complex extensional faults in the peripheral zone affect only the caldera floor and upper levels of the reservoir roof, the main outer normal ring-fault seems to penetrate all the way to the reservoir. Displacements on the outer normal ring fault system and keystone graben faults typically decrease downward. In contrast, displacement on the reverse fault system typically decreases upward (see also Kennedy et al. 2004).

2.3.2 Collapse into circular reservoirs with 'thick' roofs

In general, the structure and evolution of the 'thick roof' experimental collapses (Cal Stat H1-H2) resembled the 'thin roof' counterparts, particularly Cal Stat A5. Thick roofs again sagged and then failed along an inner, outward-dipping, and reverse ring-fault (**Figure 2.6a**). Subsidence again became slightly asymmetric once this reverse ring-fault had formed, and the central zone block moved slightly horizontally toward the area of maximum subsidence (**Figure 2.6b**). As before, an outer, inward-dipping, and normal ring-fault subsequently formed. Because of the slight horizontal component to subsidence, the normal ring-fault first localised opposite, and then propagated around to, the area of maximum subsidence (**Figure 2.6b-c**). The peripheral zone between the main ring faults again moved toward the caldera centre and underwent inward rotation and complex faulting (**Figure 2.6b-e**). Toward the experiment end, displacement seemed to shift outward onto the outer normal fault, and over-steepened fault scarps - particularly the outer normal fault system - again decayed to form grain flows (**Figure 2.6d-e**).

In detail, the 'thick roof' collapses displayed some pronounced geometric and developmental differences to the 'thin roof' collapses. Firstly, pre-failure sagging and marginal tension fracturing was much less pronounced in 'thick-roof' collapses than in 'thin-roof' collapses (see **Figure 2.6a vs. 2.2a**). Secondly, the reverse ring-fault trace localised almost instantaneously as a complete ring in both Cal Stat H1 and H2, unlike the arcuate initial localisation in most of the Cal Stat A experiments. Thirdly, subsidence asymmetry in Cal Stat H1-H2 was not as pronounced as in Cal Stat A1-A4. Indeed compared to thin-roof equivalents, less asymmetric subsidence was a characteristic of all thick-roof collapses regardless of whether the magma chamber was circular or elliptical in plan view (at least those with a centred conduit – see **Chapter 4**). Fourthly, the trace of the reverse ring-fault had a smaller initial diameter (by ~ 1 cm) in Cal Stat H1 and H2 than in Cal Stat A5. This resulted from the conical shape of the outward-dipping reverse ring fault, the trace of which must decrease in diameter as the distance from the magma chamber top (base of the cone) to the surface increases (cf. Roche et al. 2000; Walter and Troll 2001). The overall diameter of the collapse zone (macroscopic limit of influence) in 'thick roof' collapses was conversely slightly greater than in 'thin roof' collapses, although the diameter of the main normal ring-fault was roughly similar (see **Figure 2.6e vs. 2.2e**). The peripheral zones of 'thick-roof' experiments thus initially comprised a proportionally greater part of the overall collapse area than in equivalent 'thin-roof' experiments, though this changed as subsidence progressed. The outer sub-zone of oblique-normal faulting in the peripheral zone was similarly wide regardless of roof thickness, so the inner sub zone of strike-slip and oblique-reverse faulting was initially wider than in thin roof experiments, though again this changed as subsidence proceeded (see below).

A marked feature of all 'thick roof' experiments was the synchronous formation of new reverse faults that cut through the caldera floor *outside* the first-formed reverse ring-fault system (**Figure 2.6c-d** - see also Branney and Gilbert 1995; Roche et al. 2000; Kennedy et al. 2004).

These new faults formed with or after localisation of the outer normal ring-fault system. From surface observations, they originated in two ways: 1) as obliquely-trending splays from the first-formed reverse fault - most common and similar to those in thin-roof experiments (**Figure 2.6c)**, or 2) as seemingly-independent, concentrically-trending, faults or fault strands (e.g. **Figure 2.6c-e**). From cross-section observations, however, the new reverse faults were usually all tightly linked at depth to either the first-formed reverse fault, or the outer normal fault, or both. Indeed, most faults could be regarded as splays of the same single shear zone at depth (see **Figure 2.7**).

As in 'thin-roof' experiments (e.g. Cal Stat A5 - **Figure 2.2d-e**), new reverse faults usually nucleated around the area of maximum subsidence, and cut across the peripheral zone, sections of which were obliquely thrust over each other. Formation of new reverse faults or reverse fault splays also caused deactivation of the first-formed reverse ring-fault, either partially or completely, as displacement transferred from it to the newly forming faults. Though the simple outward migration of activity previously described by e.g. Roche et al. (2000) was observed in Cal Stat H1, Cal Stat H2 shows more complex temporal and spatial interactions between active reverse faults (**Figure 2.6**). With formation of new reverse faults, the earlier reverse fault only partly deactivated. Then, whilst sections of the new-formed reverse faults deactivated, still-active sections of the new-formed reverse faults linked laterally with still-active sections of the earlier-formed reverse faults. Such temporal and spatial intricacy of fault growth and death greatly increased complexity of syn-collapse disruption of the caldera floor.

The less pronounced surface sagging noted in thick-roof collapses is reflected in the straighter (less sagged) strata in between the main ring faults in cross sections through CalStat H2 (**Figure 2.7**). Peripheral zone faulting in the thick roof experiments was not generally as intense as seen in the experiments with thinner roofs. Peripheral extension seems to have almost completely localized on the outer normal fault system; the complex fracturing seen on the surface inside it does not penetrate to any appreciable depth, and key stone graben are very small or absent (**Figure 2.7**).

The slight variation in fault patterns on either cross-section through Cal Stat H2 is similar to Cal Stat A5 (**Figure 2.3**), and seems similarly relatable to the effects of asymmetric central zone subsidence and the associated component of horizontal motion. Unlike in Cal Stat A5, however, the direction of this horizontal motion component varied through the course of the experiment, so the exact relationships are more complex. Early in the experiment, just before the first reverse ring-fault trace appeared, horizontal motion was directed toward the NNE – i.e. toward the A-end of the model (**Figure 2.6a**). Thereafter, the direction of horizontal motion shifted rapidly away from the A-end, first to the SE and then to the SSW, toward the point of maximum subsidence near the B-end of the model (**Figure 2.6b-d**). Deformation is consequently of a more compressive nature at the B-end overall, in that much more displacement is accommodated reverse faults compared to at the A-end. The faulting pattern on the C-D section is more or less identical at either end (i.e. symmetric), and so reflects a parity of horizontal motion and associated compression.

At the ends the cross-section, the structure typically comprises a steep shear zone, from which reverse faults splay at depth and the normal ring fault system splays nearer the surface. In agreement with observations of Odonne et al. (1999) and Kennedy et al. (2004), reverse faults are overall steeper in the 'thick roof' experiments relative to 'thin-roof' experiments (see **Figure 2.7 vs. Figure 2.3**). As seen in thin-roof experiments, however, displacement on reverse faults typically decreases upward, whilst displacement on normal faults usually decreases downward.

2.3.3 Collapse against a glass pane

The evolution of collapse against a glass pane closely matched that described above for 'thin roof' collapses without a glass pane. This is taken to mean that edge effects from the glass were insufficient to cause significant deviation in structural development of collapse (see also Roche et al. 2000; Walter and Troll 2001). These experiments may thus provide further insight into the collapse processes in 3D. Again subsidence in all experiments was asymmetric; the evolution of a representative collapse is illustrated in **Figure 2.8**. Observations of most importance concern the propagation and interaction of the reverse and normal ring-faults. For this reason, a close up of the development of inner reverse fault and outer normal fault is also shown in **Figure 2.9**.

After onset of sagging, tension fractures (fissures) can be seen to propagate downward from the surface to accommodate marginal stretching of the uppermost pre-collapse strata, which lie on the outer arc of a monocline that forms just above the edge of the reservoir (**Figures 2.8a & 2.9a)**. These tension fractures do not penetrate the roof as a whole, and so do not accommodate complete roof failure (contra Pinel and Jaupart 2005). As inferred from plan-view observations of the above experiments, complete roof failure first occurs along the outward-dipping reverse fault, which cuts through the tilted limb of the monocline (**Figures 2.8b-c & 2.9b-c;** Branney 1995).

In agreement with both Roche et al. (2000) and Kennedy et al. (2004), localisation of this reverse fault tended to occur with an upward sense of propagation. The speed of this propagation was much more rapid than observed by Roche et al. (2000), however. Whereas, propagation from chamber to surface occurred over c. 3-5mm of surface subsidence in the experiments of Roche et al (2000), it typically occurred over less than 1mm of surface subsidence in the experiments of this study (**Figures 2.8b & 2.9b)**. This rapid fracture propagation is difficult to detect with still photos. Most of the fractures detected in this study were noted in animation, where by crack propagation could be seen a subtle relative change in the movement of material either side of a narrow line. This line was frequently invisible or cryptic, but was sometimes visible as a 'hairline' crack (e.g. **Figure 2.9b**). Many normal ring faults in this study showed a similarly rapid propagation as 'hairline' fractures (**Figures 2.8b,d & 2.9c)**. This propagation usually occurred with a downward sense, however, in agreement with Kennedy et al's (2004) inference, rather than an upward-sense as observed by Roche et al. (2000).

In most cases, propagation of reverse and normal faults was accompanied by accumulation of displacement, such that a very slight displacement gradient existed along the fault upon completion of fracture propagation (e.g. **Figure 2.9b-c)**. This slight displacement gradient was usually amplified by subsequent post-propagation displacement on the fault, however (**Figures 2.8b,d & 2.9c**), such that by the experiment's end the reverse faults and normal faults had the well-defined upward-deceasing and down-decreasing displacement profiles respectively. These displacement profiles matched those seen in cross sections of collapses without a glass pane **(see Figures 2.3 and 2.7).**

Analysis of the cross-sections shows that the sum of all vertical displacements of a horizon across the ring fault systems equalled (or nearly equalled) the total vertical displacement at the model centre, regardless of whatever combination of faults are present at that level in the roof (**Figure 2.10**). This indicates an overriding geometric and kinematic coherence between the faults in the caldera fault systems as they evolve, similar to that documented for faults in extensional basins and thrust sheets (Walsh and Watterson 1991). The vertical displacements of a horizon comprised brittle offsets along a sharply defined fault traces, as well as more ductile tilting and bending (locally related to drag along the faults). The proportion of vertical displacement accommodated by ductile tilting and bending was far greater in thin roof models than in thick-roof models (**Figure 2.10**).

2.4 Discussion

2.4.1 The kinematics of caldera collapse: solving space problems

The results of this study primarily agree with those of earlier works regarding the role of reverse faulting in accommodating radial shortening and hence resolving the old 'space-problem' of caldera subsidence. It is also worthwhile noting that in some instances in this study, particularly with 'thin roofs' (e.g. Cal Stat A4), asymmetric subsidence led to resolution of the 'space problem' by a ring fault with an outward dip along one side of the caldera and an inward dip along the other side (e.g. Cal_2D_3 – **Figure 2.8**). A similar structure is seen at the well-exposed and asymmetrically subsided Glencoe caldera, Scotland (Kokelaar and Moore 2006), where the ring fault dips steeply inward along the NE side of the caldera and steeply outward along SW side.

Previous analogue studies of caldera collapse (e.g. Branney 1995; Roche et al. 2000; Kennedy et al. 2004), have also pointed out the potential importance of sagging in solving this perceived 'space problem'. In agreement with these works, the results of the present study also show that sagging may indeed act in conjunction with and complement reverse faulting in accommodating radial shortening, albeit under certain conditions. Sagging was most pronounced in experimental roofs of low thickness/diameter ratio (i.e. relatively thin roofs – e.g. **Figure 2.3**), where it accounted for a significant proportion (up to half) of the net subsidence (**Figure 2.10**). In contrast, sagging was a minor feature of experiments with a high thickness/diameter ratio (i.e.

relatively thick roofs - **Figure 2.7**), where it accounted for a very small proportion of the net subsidence (**Figure 2.10**).

Roche et al. (2000) and Kennedy et al. (2004) reported a very similar relationship between sagging and roof thickness. Sagging is likely to be less important in a relatively thick roof because the influence of the stress arching is enhanced relative to that in a relatively thin roof (cf. Roche et al. 2000 and references therein). Stress arching tends to increase the roof's rigidity and so inhibit sagging (cf. Jones et al. 1990). This leads to the greater role of reverse faulting in accommodating subsidence of a thick roof and in producing the radial shortening required to solve the space problem. Although stress arching is present in thin roofs (note reverse ring faults form even in the thin roof experiments), its influence is reduced, the roof is less rigid, and so sagging accommodates more subsidence.

In summary, the experimental evidence here agrees with that of previous studies in showing that the apparent 'space problem' of caldera subsidence, which was to a large extent an historical artefact of poor structural control on and unrealistic depiction of caldera structure (see Branney 1995 for further discussion), is resolved by radial shortening via a combination of either of two end-member mechanisms (Walker 1984): ductile sagging or brittle reverse faulting (**Figure 2.1**). In agreement with previous analogue and field studies of caldera formation, and with some numerical studies (e.g. Folch and Marti 2004), the experimental evidence presented here also supports the view that ductile sagging may be more prominent at low roof thickness/diameter ratios and brittle reverse faulting may be prominent at high roof thickness diameter ratios (**Figure 2.10**).

Another, but previously underappreciated, kinematic aspect of caldera subsidence is that of how to accommodate the concentric shortening arising from the radially-inward movement of subsiding material. The present study highlights several structural mechanisms by which concentric shortening is accommodated during experimental collapses; these structures and those accommodating radial shortening/extension are summarised in **Figure 2.11**. For an ideally symmetric subsidence, three structural zones may be distinguished (**Figure 2.11a**). An inner Zone 1 is dominated by compressive structures, typically concentrically-trending reverse faults and/or radially-trending wrinkle ridges (**Figure 2.11b**). An outer Zone 3 is dominated by extensional structures, such as: concentrically- to slightly obliquely-trending normal faults, oblique-normal faults, and fissures; graben and half-graben; faceted fault blocks and 'step faults' (**Figure 2.11b**). An intermediate Zone 2 displays predominantly strike-slip to compressive structures: obliquely-trending to concentrically-trending strike-slip faults; radially-trending folds or 'wrinkle ridges' (often associated with strike-slip faults); and obliquely-trending faults with oblique-reverse slip (**Figure 2.11b**). Though rare, oblique-normal faults also locally form in Zone 2. Zone 1 thus undergoes strong radial lengthening and a relatively weak concentric shortening (**Figure 2.11c**). Zone 2 undergoes slight radial lengthening, sometimes then followed by slight radial shortening (especially in thick roof collapses), but principally undergoes strong concentric shortening (**Figure 2.11c**). Zone 3 undergoes both strong radial and concentric shortening (**Figure 2.11c**).

The expression of some of the structures in Zones 1 and 2 depended on the extent to which experimental deformation was ultimately taken up by sagging or faulting. This was in turn linked to roof thickness (see above). Where central sagging was overall more pronounced, and reverse faulting took up a relatively small amount of the subsidence, radial wrinkle ridges were prominent in the central part of Zone 1 (e.g. the very thin-roofed Cal Stat A3 – **Figure 2.5**). Here the radial wrinkle ridges accommodated concentric shortening, whilst sagged floor and the concentric reverse fault accommodated radial shortening. In this case, concentric strain was distributed between Zones 1 and 2 and so radial wrinkle ridges form in the more deformed central floor and strike-slip faults formed in the periphery. In contrast, where reverse faulting accommodated much of the subsidence and sagging was overall less pronounced, the central part of Zone 1 inside the reverse ring fault was relatively undeformed. In this case, most of the radial shortening was taken up on the reverse ring fault, and most of the concentric shortening was partitioned into Zone 2 (e.g. the slightly thicker-roofed Cal Stat A5 - **Figure 2.2**), where it was taken up along radial wrinkle ridges, obliquely- to concentrically-trending strike-slip faults, and obliquely-trending oblique reverse faults. In very thick-roofed collapses, where sagging was very minor, accommodation of the concentric shortening was partitioned almost exclusively onto oblique reverse faults (see Cal Stat H2 – **Figure 2.6**) in Zone 2.

Many close natural parallels to the experimental structures and the zonation described here are found in the calderas of Biblis Patera and Olympus Mons on Mars (Branney 1995). The 2.5 km deep and 53 km diameter caldera of Biblis Patera (**Figure 2.12**), although a single caldera, is also thought to have had a history of multiple collapses (Plescia 1994) and burial (‘resurfacing’) of the caldera floor by lava lakes. The multiple collapses presumably developed above a similarly positioned chamber; however, one should note that such a history was primarily inferred from the structural complexity of faulting in the periphery of the caldera (Plescia 1994), which the experiments show can be generated in a single collapse. The caldera of Olympus Mons (**Figure 2.13a**) is a 3 km deep nested caldera complex with a history multiple collapses into differently positioned magma chambers and episodic burial (‘resurfacing’) of the caldera floor by basaltic lava lakes (Mouginis-Mark and Robinson 1992). The oldest of the nested calderas (caldera 1) is also the largest; its diameter measures some 64 km.

In its central parts, caldera 1 on Olympus Mons displays a sagged floor (and/or fill), a set of roughly radially-orientated wrinkle ridges, and a set of concentric to obliquely-trending ridges (**Figure 2.13a-b(i))**. Though they are often superimposed upon them, the concentric ridges are morphologically distinct from the wrinkle ridges. The concentric ridges are narrow (<1 km) and have minor topographic relief (<40m), whereas the wrinkle ridges are typically ~ 2km wide and have a topographic amplitude of ~300m (Mouginis-Mark and Robinson 1992). Mouginis-Mark and

Robinson (1992) suggested that both features nonetheless resulted from compression - the wrinkle ridges by concentric compression and the concentric ridges by radial compression. There is no clear indication of an inner reverse ring fault in crater 1 of Olympus Mons; a ring-like feature resembling a hanging wall to a reverse fault in the centre of the caldera is presently interpreted as the line of on-lap of a lava lake rather than the trace of an inner reverse fault (Mouginis-Mark and Robinson 1992; Mouginis-Mark 2006 Pers. Com.). In its outer parts, caldera 1 displays a well-developed system of peripheral gräben lying a just inside the scarp of a main, steeply inward-dipping, normal ring-fault (**Figure 2.13a-b(ii)** - Mouginis-Mark and Robinson 1992). Just outside the scarp of the main normal fault is a set of relatively minor normal faults defining steps in the main normal fault's footwall (**Figure 2.13a-b(iii)** - Mouginis-Mark and Robinson 1992). As in experiment, these peripheral gräben and step-faults are delineated by intersecting sets of parallel fractures, which are locally parallel to nearby facets in the polygonal trace of the main normal ring-fault (**Figure 2.13b)**. The structures at Olympus Mons caldera thus most closely approximate experimental collapse formed with very thin roof (Cal Stat A3 – **Figure 2.5**)

Biblis Patera's caldera exhibits a less obviously sagged floor (and/or fill) than at Olympus Mons, although there are wrinkle ridges in the central zone that radiate from the point of maximum subsidence in the SW (Plescia 1994), in a manner very similar to that seen in Cal Stat A3 (**Figure 2.5e**). There is also an inner scarp with a snubbed morphology characteristic of reverse faults in experiment, and the caldera floor immediately outside and adjacent the inner scarp is tilted steeply inward to form what closely resembles a hanging wall anticline above a reverse fault (**Figure 2.12a-b**). There also seems to be an oblique splay from this reverse fault from the caldera centre toward the periphery. Biblis Patera also exhibits a well-developed peripheral zone of gräben and stepped fault blocks that mostly lie inside a main, laterally-segmented, normal ring-fault system. Again, the faults bounding these graben and stepped fault-blocks are faceted, with facets comprising numerous intersecting sets of parallel fractures, many of which are sub-parallel or parallel to the facets in the main outer normal fault (**Figure 2.12b)**. On the whole therefore, the caldera of Biblis Patera displays structural elements reflecting the experiments with very thin and moderately thin-roofs (CalStat A3 and CalStat A5). This suggests that Biblis Patera's caldera formed above a deeper magma chamber than the crater 1 of Olympus Mons.

Zuber and Mouginis-Mark (1992) tried to constrain the position and dimensions of the magma chamber that might have produced the observed distribution of compressional and extensional structures seen in crater 1 of Olympus Mons. They did so by numerically modelling the distribution of stresses associated with an instantaneous deflation of an ellipsoidal magma chamber. These authors focused on the location of the transition between compressive and extensional radial stress at the free surface of the model (**Figure 2.14)**, which they believed was reflected in a sharp transition (over a few hundred m) between concentric ridges and concentric gräben on the surface of the caldera (**Figure 2.13c**). A radial distance from the centre caldera 1 for this location of this transition corresponds to the outermost limit of the concentric ridges (**Figure 2.13c**) and is given as 0.53Rc, where Rc is the caldera radius (Zuber and Mouginis-Mark (1992).

These authors' best-fit plot of the principal stresses acting at the surface above a deflating reservoir roof, shown in **Figure 2.14**, was achieved with an oblate ellipsoidal magma reservoir of the same radius as the caldera and at a depth of 0.25Rc. In addition to a transition from compressive radial stress to extensional radial stress at 0.53Rc, the plot shows a compressive concentric stress across the caldera floor. This compressive concentric stress is a maximum in the centre of the downwarped caldera floor and decays to zero somewhere beyond the projected edge of the reservoir (at the limit of influence). Where the radial stress is also compressive (i.e. negative) toward the centre of the roof and, the magnitude of the concentric stress is at almost always greater than that of the radial stress. As noted by Zuber and Mouginis-Mark (1992), this implies the formation first of radial wrinkle ridges in the central part of the downwarped roof. This is in agreement with experimental observations in in the highly sagged Cal Stat A3 (**Figure 2.5b**).

In light of the experimental observations from the present study, the structural relationships in crater 1 of Olympus Mons and the numerical data of Zuber and Mouginis-Mark (1992) may be interpreted somewhat differently. It is first worth noting that the transition between all these structures is not as sharp as idealised by Zuber and Mouginis-Mark (1992). The radial wrinkle ridges, concentric ridges and sporadic concentric graben actually overlap within a circumferential zone several tens of km long and five to eight km wide. Although the radial wrinkle ridges are thought to mainly pre-date the concentric ridges, several of the wrinkle ridges show apparent sinistral strike-slip offsets along concentric ridges (Zuber and Mouginis-Mark 1992 - **Figure 2.13c**). This raises the possibility that the two sets of ridges are effectively coeval (implicitly assumed by Zuber and Mouginis-Mark 1992), and that the concentric ridges formed as strike-slip faults in response to concentric shortening – as seen in experiment (**Figure 2.2d-e**) - rather than in response to radial shortening. There are no clear crosscutting relationships between the concentric graben and concentric ridges; in places, one structure seems to pass laterally into the other (**Figure 2.13c)** as seen between strike-slip faults and graben in experiment**.** Therefore, and although some wrinkle ridges appear to pre-date the concentric graben (**Figure 2.13c**), all these tectonic features could thus be essentially coeval and kinematically-linked, with the wrinkle ridges and concentric ridges together helping to take up the component of concentric shortening around the transition to the zone of radial extension (**Figures 2.11c, 2.13c & 2.14**).

On the plot in **Figure 2.14**, the outward changeover from negative (i.e. compressive) radial stress to positive (i.e. extensional) radial stress at a radius from the centre of r/Rc = 0.53 is regarded by Mouginis-Mark and Robinson (1992) as the changeover from compressive ridges to extensional graben. However, the magnitude of the concentric stress at this transition is far greater than the radial stress, and the concentric stress is compressive. As the numerical model assumes elastic behaviour, i.e. the magnitudes of the stresses are proportional to the magnitudes of associated strains, circumferential shortening should predominate at this point. The stress/strain conditions here are therefore more conducive to strike-slip faulting than simple graben formation (Anderson 1951) – i.e. this point may represent the boundary between Zones 1 and 2 as seen in experiment (**Figure 2.11)**. The magnitude of extensional radial stress/strain only exceeds that of the concentric stress/strain at a radial distance of r/Rc = 0.68. This is likely be the point at which extensional faulting predominates over strike-slip faulting (Anderson 1951) – i.e. the boundary between Zones 2 and 3 in experiment (**Figure 2.11)**. The radial width of the zone 2 as determined from this re-evaluation and drawn on the plot in **Figure 2.11** is r/Rc = 0.17. This is in close agreement with the width of Zone 2, r/Rc = 0.16, in the experimental structural zonation in **Figure 2.11**.

These observations from the calderas of Biblis Patera and Olympus Mons, together with data from numerical subsidence simulations, thus provide grounds to infer that the experimentally identified mechanisms for accommodating subsidence-related concentric shortening may well be more common in nature than hitherto recognised.

2.4.2 The propagation and interaction of main ring fractures

Experiments in this study provide evidence that following local ductile 'forced folding' above the magma chamber edge, reverse faults may localise almost instantaneously through the whole roof from magma chamber to surface – i.e. vertical propagation is very rapid – once sufficient vertical shear strain has been accumulated. Lateral propagation may be less rapid, as initial failure at any section of the reservoir circumference depends on whether sufficient subsidence (i.e. vertical shear strain) has occurred there. This will be to some extent affected by subsidence symmetry. This difference in speed of reverse fault (and normal fault) propagation compared to that observed by Roche et al. (2000) is ascribed to the different materials used - the more cohesive and brittle behaviour of the sand/gypsum mix used in this study vs. the slightly less cohesive and less brittle pure-sand used in Roche et al's (2000) experiments.

The observations here regarding directions of propagation contrast with those of Roche et al. (2000), who reported upward propagation of both reverse faults and normal ring faults in their experiments against a glass pane. The upward-decreasing displacement on reverse ring-faults and corresponding downward-decreasing displacement on the main normal ring-faults was interpreted by Kennedy et al. (2004) to reflect the respective upward and downward propagation of the reverse and normal ring faults.

Displacement gradients along a ring fault in cross-section may not directly relate to the propagation of the ring fault, as assumed by e.g. Kennedy et al. (2004), however. Experiments in this study provide evidence that the vertical length of the ring fault may be established very rapidly (**Figures 2.8 & 2.9)**. Once propagated, a ring fault then accumulates most of its displacement. The displacement gradient seen along a fault's vertical trace at the end of experiment tends to form post-propagation, as one part of the fault accumulates more displacement than the other. Reverse faults accumulated more displacement along their lower parts, whereas normal faults tended to accumulate more displacement along their upper parts. This differential accumulation of displacement may thus mainly reflect and be controlled by a type of geometric and kinematic coherence (cf. Walsh and Watterson 1991) between the reverse fault(s) and normal fault(s) (**Figure 2.10)**.

Fracture propagation is difficult to detect with still photos, as the low strains that characterise the initial formation of the hairline cracks are very difficult to see. Also the smear effect of the honey against the glass often retarded the offset of the lowermost marker layer adjacent the glass (**Figure 2.8**). Measurement of the true offset of this layer is therefore underestimated. More quantitative constraints on the relationships between the propagation and accumulation of displacement on ring-faults in experiment, particularly at low initial strains, may be achieved by the use of image analysis software that enables high-resolution image correlation, e.g. by techniques like Particle Imaging Velocimetry (PIV). For example, Adam et al. (2005) use PIV to show that the pattern of localised deformation (i.e. faulting) in convergent thrust wedges is established much earlier than may be detected by eye. Such rapid fault localisation may occur with a sense of propagation, but before substantial offset of layering – i.e. offset of layering may not record propagation. Use of techniques such as PIV in the experimental study of caldera collapse mechanisms is thus recommended as further work. Indeed, at the time of writing, initial PIV analyses of analogue collapse against a glass pane reveal very similar patterns of fault propagation and kinematic evolution to those described from the experiments in this study (Dr. T. R. Walter pers. comm).

2.4.3 Complex slip kinematics of reverse ring faults

Most experimental collapses were asymmetric, and so even where subsidence asymmetry was slight, a component of horizontal motion of the central zone toward the point of maximum subsidence resulted (also noted by Roche et al. 2000). This horizontal motion induced systematically varying down-dip to oblique slip kinematics on the main reverse ring fault. That subsidence asymmetry may produce similar horizontal motion and ring fault kinematics in nature is evidenced at Kumano caldera, Japan (Miura 1999). Here, the southern section of the caldera initially subsided as an independent elliptical block along an almost continuous, inward-dipping to locally outward-dipping ring fault. From stratigraphic correlations between the pre-caldera sedimentary rocks inside and outside the caldera, displacement on the ring fault comprises 1 km of sinistral offset and a several hundred metre westerly increase in throw (**Figure 2.15**). Miura (1999) thus deduced an oblique westward subsidence of the caldera floor, a conclusion also supported by an oblique-to-dip rake of striations in cataclasites along the ring fault there. Changes in subsidence symmetry during the course of collapse evolution resulted in an even more complicated variation of kinematics on the model reverse fault system. Kumano caldera, Japan also displays kinematic indicators for motions in very different directions on its ring fault system (Miura 1999). Though possibly also reflecting later processes such as resurgence and/or later collapse, such very complex and multiply overprinted sets of kinematic indicators in ring fault zones could therefore just record a single collapse evolution.

2.4.4 Polygonality of 'ring' structures and peripheral zone fractures

A feature of all analogue calderas produced in this study was the segmented or 'faceted' character of the main ring fault systems and the minor peripheral zone fault systems. The only other experimental study in which similarly 'polygonal' ring structures have been noted is that of Kennedy et al. (2004), where they were attributed to the particular length scale, time scale, and analogue materials used. Kennedy and Stix (2003) also noted that several deeply-eroded calderas, or 'cauldrons', display a polygonal outline that is mostly preserved in the form of ring dykes that encompass a downthrown central block (e.g. Ichizuchi, Japan – **Figure 2.16**). These authors suggested that such 'polygonal piston' calderas might be considered a variant of a 'Piston-type' caldera and that they might be difficult to recognise from their surface morphology because of rounding of their edges by erosion and/or mass movement.

The preservation of a faceted outline to calderas in nature is nonetheless, demonstrable not only in deeply eroded cauldrons, but also in the higher-level probably topographic outlines of many very young calderas (e.g. Ambrym, Vanuatu - **Figure 2.16b**). Just the second volume of Newhall and Dzusrisin's (1988) extensive database of Quaternary calderas contains numerous calderas with markedly polygonal topographic outlines similar to those produced in experiment. Since the wholesale destruction of fault scarps occurred only after a large amount of subsidence relative to the caldera width in experiments and at Miyakejima, the preservation of the faceted outlines at many of the above examples may relate to small overall subsidences relative to caldera diameters. The observations reported here thus show that polygonal ring faults are not just seen at deeply eroded cauldrons, but occur in calderas of all ages and erosion levels.

This study supports Kennedy and Stix's (2003) suggestion that erosion/mass movement may help reduce or obscure the polygonal nature of natural caldera ring structures (see also Branney and Gilbert 1995). Some reduction in the linearity of faceted ring-fault traces occurred with the decay of over-steepened reverse and normal faults scarps toward the ends of most experiments (e.g. **Figures 2.2, 2.4, 2.6**). Also, the traces of the early-formed collapse structure at Miyakejima caldera, which comprised two clearly faceted ring fault systems (**Figure 2.17**), were completely obscured by landsliding (Geshi et al. 2002). However, this landsliding still produced a subtly polygonal topographic outline (**Figure 2.18**), albeit one that did not at all match the initial geometry of the ring faults.

On balance, therefore, the experimental and field evidence does not provide a basis for a separate 'polygonal piston' category of caldera classification (Kennedy and Stix 2003). First, the characteristic structural elements of caldera end-members other than the piston end-member demonstrably also form during the course of a 'polygonal' subsidence event in both experiment and nature (see also **Chapter 3**). Exposure in most calderas, especially the proposed 'polygonal piston' type-localities of Ossipee and Ichizuchi (Kennedy and Stix 2003), is far too poor to determine whether elements of other end-members formed or not - i.e. if collapse was indeed entirely coherent. Faceted or polygonal ring faults are thus probably not particular to any type of collapse, but seem an inherent feature of subsidence on any scale. Second, the polygonality of a caldera particularly at higher structural levels may be stem from degradation of, and be geometrically different from, the ring faults. A sub-classification of calderas on the basis of the polygonality of ring faults or outline is therefore probably not significant genetically.

2.4.5 Geological significance of peripheral zone faulting

In experiment, the faceting of caldera ring faults is strongly reflected in the pattern of parallel fracture sets that define the complex array of differentially-subsided blocks, graben and half graben in the peripheral caldera zone. This extensional peripheral zone fault pattern particularly reflects the segmentation of the main normal ring fault system in that most fracture sets form parallel to one of the normal ring fault's facets. As for the facets of the normal fault system, the peripheral zone fracture sets are to a large extent pre-defined by the pattern of tensional fracturing during the sagging phase. The relationship between the segmented ring fault systems and the complex array of peripheral zone faults, and a better understanding of the underlying mechanics behind their formation, are important for at least two reasons.

Firstly, the intersecting fracture sets control the break up the marginal peripheral zone floor during experimental subsidence. According to Branney and Kokelaar (1994) and Branney (1995), the floor of the piecemeal type-locality caldera of Scafell, England, which is mainly exposed around the caldera margins, comprises many differentially-subsided, "arcuate and multifaceted fault blocks" (**Figure 2.19**). The margins of Scafell caldera also display arcuate keystone graben, which separate almost horizontal pre-caldera rocks outside the caldera from inward-tilted pre-caldera rocks inside the caldera. The arcuate key stone graben are up to 2 km wide, and contain upward-flaring crevasses up to 200m wide, 300 m deep and 3km long (Branney and Kokelaar 1994; Branney 1995) (**Figure 2.19**). These descriptions of the marginal floor at Scafell closely fit the intricate array of crevasses, faceted fault-blocks, half-graben, and graben that characterises the differentially subsided floor in the model caldera peripheral zones (see also Branney 1995). Moreover, the dimensions and throws of the crevasse, normal faults, and graben in the peripheral zones of the analogue models scale well to these dimensions in nature.

Like the model peripheral zones, the complex subsidence structures seen at Scafell are thought to mostly relate to radial extension and sagging of the caldera floor due to central collapse (Branney 1995). Many faults moved during eruption (as shown by rheomorphic drag of ignimbrites against the fault surfaces) and are thus interpreted as volcano-tectonic in origin. By comparison with the models presented here, the linear and curvilinear faults defining the complex fault-blocks at Scafell may be related to the syn-collapse disruption of the pre-caldera basement along systematic intersecting sets of peripheral zone faults (see also Branney 1995). Indeed, many of the faults defining the blocks in the Scafell floor are parallel or sub-parallel to segments of the bounding normal ring fault system there (**Figure 2.19**). Extension of this logic is that peripheral faulting, perhaps augmented by formation of multiple reverse faults, may account for much of Piecemeal-style break-up of calderas floors generally. This is supported by similar observations of peripheral faulting during the collapse of Miyakejima caldera, Japan (Geshi et al. 2002). Here, the peripheral zone floor was also dissected by a multitude of normal faults and crevasse. As in experiment, these fracture systems were locally defined by intersecting fracture sets orientated parallel to the linear segments of the outer normal ring fault (**Figure 2.17**). Similarly complex relationships, very like those in experiment and at Scafell, are seen in the extensional peripheral fault zone at the basaltic Sierra Negra caldera in the Galapagos Islands (**Figure 2.20** - Reynolds et al. 1995).

Secondly, these peripheral zone fracture and fault systems may have a hitherto unrecognised importance for the localisation of mineral deposits in calderas. In a review of the roles and interactions of volcano-tectonic and regional-tectonic structures in the localisation on mineral deposits at calderas, Rytuba (1994) noted that mineral exploration at calderas has primarily focussed on collapse-associated ring fractures and resurgence-related radial fractures. However, Rytuba (1994) also notes that in some calderas, economically important mineralization has occurred along inward-dipping normal faults that lie outside of, but trend concentrically to, the caldera's main ring fault. Rytuba (1994) suggests that such peripheral zones may represent an important new target for mineral exploration. These normal faults are interpreted as generated by pre-caldera tumescence (Rytuba 1994), but the analogue collapses indicate that they may also relate to peripheral extension during subsidence.

An example of the localisation of voluminous precious metal deposits (mainly silver) in similar fracture systems outside a main ring fault zone is the southern part of Silverton caldera, Colorado (**Figure 2.21a –** Varnes 1963). From Varnes's (1963) cross-section (**Figure 2.21a**) these fractures occupy the same structural position as the peripheral fractures formed in experiment. These fractures comprise (1) a concentric system of fissures and other tensional fractures, (2) a well-constrained Western Shear system of mainly inward-dipping and primarily dextral oblique-normal faults, and (3) a poorly-constrained Eastern Shear system of mainly inward-dipping sinistral oblique-normal faults and arcuate dykes (Varnes 1963). The latter two systems were mostly considered to be roughly radial to the caldera centre, and so the mineral hosting fractures systems (though not necessarily the mineralization itself) were thought to relate to radial compression, perhaps due to magma intrusion and doming (Burbank in Varnes 1963). Varnes (1963) pointed out that the Western and Eastern shear systems are not radial to the caldera, however. He also noted that if they were doming related, the fractures should converge inwards toward the caldera centre, but instead they converge outwards from the caldera centre. Varnes (1963) regarded the shear fracture systems as conjugate shear zones related to initial radial compression, and thought the dominantly normal displacements on the inward-dipping shear fractures occurred after a phase of oblique reverse faulting. The age relationships between the two shear fracture systems and the tensional concentric fracture system is unclear (Varnes 1963).

A noticeable feature of the south Silverton area is that the ring fault zone trace is not curved, but comprises three main linear segments (**Figure 2.21a-b**). Moreover, the three main mineralised fracture systems are each segment roughly parallel to one of these segments. An experimentally derived alternative interpretation of the Silverton fracture systems is therefore that they formed as sets of extensional and shear fractures parallel to the segments of main ring fault system, and relate to the break up of the peripheral zone during caldera subsidence. This hypothesis requires further testing to see if the dextral and sinistral slip motions observed in the field would be consistent with it, however. In many experiments, the sense of shear on peripheral zone fractures adjacent a three-segment reverse ring fault (similar in trace to that at Silverton) is opposite to that observed in the field. In Cal Stat C5 (**Figure 4.6 – Chapter 4**), however, the intersecting peripheral fracture pattern has very similar kinematics and arrangement the Silverton fracture systems. More detailed work to determine under what circumstances fracture systems akin to those at Silverton might be generated is required. A higher resolution of the slip kinematics of experimental peripheral fracture systems with image analysis software may be illuminating. If the syn-collapse fracture generation hypothesis is correct, then it may not be coincidence that the South Silverton fracture systems, which host the some of the most productive veins of silver, gold, copper, lead, and zinc ores in Colorado (Varnes 1963), are located near the short axis ends of the elliptical Silverton caldera (**Figure 2.21a**). This where the analogue models predict such intersecting sets of extensional faults and fractures should be best developed after an elliptical collapse, and it is where the similar slip kinematics in Cal Stat C5 are seen (see **Chapter 4**).

2.5 Summary and Conclusions

From the experimental results reported in this chapter, four interlinked themes from previous experimental studies of the structure of calderas are further developed: 1) The influence of the reservoir roof's thickness/diameter ratio on the kinematics of the collapse process and on the nature and geometry of collapse structures produced in resolving the space problem of caldera subsidence; 2) The propagation, interaction, and slip sense of faults in the main ring-fault systems; 3) The 'polygonality' of calderas in plan-view; and 4) The generation of structural complexity and non-coherent or 'piecemeal'-like collapse. Relative to previously published experimental studies, however, a more detailed 3D analysis of the geometry and kinematics of collapse structures is presented, and some more detailed links between experimental and natural calderas are also provided.

Previous analogue studies of caldera structure have helped solve the long-debated ‘space problem’, which arose from a perception that caldera subsidence occurs primarily along inward-inclined ring faults with a normal sense of slip. Indeed, the past experiments have shown that subsidence occurs along inward-inclined normal faults, but that it does so secondarily to initial formation of outward-dipping ring faults with an ideally reverse sense of slip and/or central sagging of roof strata. The latter two mechanisms resolve the ‘space problem’ by accommodating a radial shortening of the down-going magma chamber roof. The experiments of this study agree with those of the past in this regard, and it is also emphasised here, as noted by previous workers, that with relatively thinner chamber roofs (i.e. low thickness/diameter ratios) distributed (ductile) sagging may accommodate a more substantial proportion of subsidence, and hence accommodate more of the required radial shortening, than localised (brittle) reverse faulting.

The results of this study also highlight several structural mechanisms for accommodating concentric shortening during caldera subsidence, a hitherto neglected kinematic aspect of the collapse process. These structures include radial wrinkle ridges, obliquely to sub-concentrically trending strike-slip faults (sometimes conjugate) and obliquely trending oblique-reverse faults. The models also show that, like those accommodating the radial shortening, the relative development of these structures is strongly dependent of the ratio of roof thickness/diameter. Wrinkle ridges are more prominent at low thickness/diameter ratios; oblique reverse faults are more prominent at high thickness/diameter ratios. Also, structures accommodating concentric shortening are more distributed across the caldera with low thickness diameter ratios, whereas they are localised within the peripheral zone (via a kind of strain partitioning) at high thickness/diameter ratios. Combined with existing numerical observations and with evidence from Biblis Patera and Olympus Mons caldera on Mars, the experimental evidence of this study leads to the prediction that the experimentally identified structures accommodating concentric shortening may be more widespread in nature than previously recognised.

Observations in this study also indicates that reverse ring faults propagate upward and normal ring faults propagate downward, as inferred by Kennedy et al. (2004) and Walter and Troll (2001), but that the displacement profiles seen on the faults may not always directly reflect their propagation. Furthermore, this study demonstrates that the reverse and normal ring faults accommodating caldera collapse form a complexly interacting but geometrically coherent system, which may regulate the accumulation of displacement along the faults during caldera development.

Deviations from ‘ideal’ dip slip senses were commonly observed on reverse ring faults, even along the same ring structure. Usually such deviations involved a component of oblique-slip resulting from the influence of asymmetric collapse and changes in the location of the point of maximum subsidence as collapse proceeded. These results imply that slip kinematics observed on caldera ring faults in the field may be complex, even if there has only been one volcano-tectonic episode (i.e. just collapse).

For the third and fourth of the above themes, this work expands further than previous studies and presents several new insights. This study shows that the polygonality of calderas noted by previous workers is seen regardless of exposure level or scale, and reveals how both collapse faulting and landsliding may act in concert to produce a caldera with a polygonal outline. In agreement with previous studies (in particular Roche et al. 2000 and Kennedy et al. 2004), the results herein also show that a relatively thick chamber roof - i.e. one with a high thickness/diameter ratio, will develop a more structurally-complex and less coherent collapse style compared to a relatively thin chamber roof. This point is allied to the observation that peripheral subsidence faulting along intersecting fracture sets produced structurally-complex model caldera floors very similar to those at many calderas, including Scafell caldera, the type-locality for piecemeal subsidence style. Implications of these last points for the much-debated continuum between caldera collapse styles are further developed in **Chapter 3**.

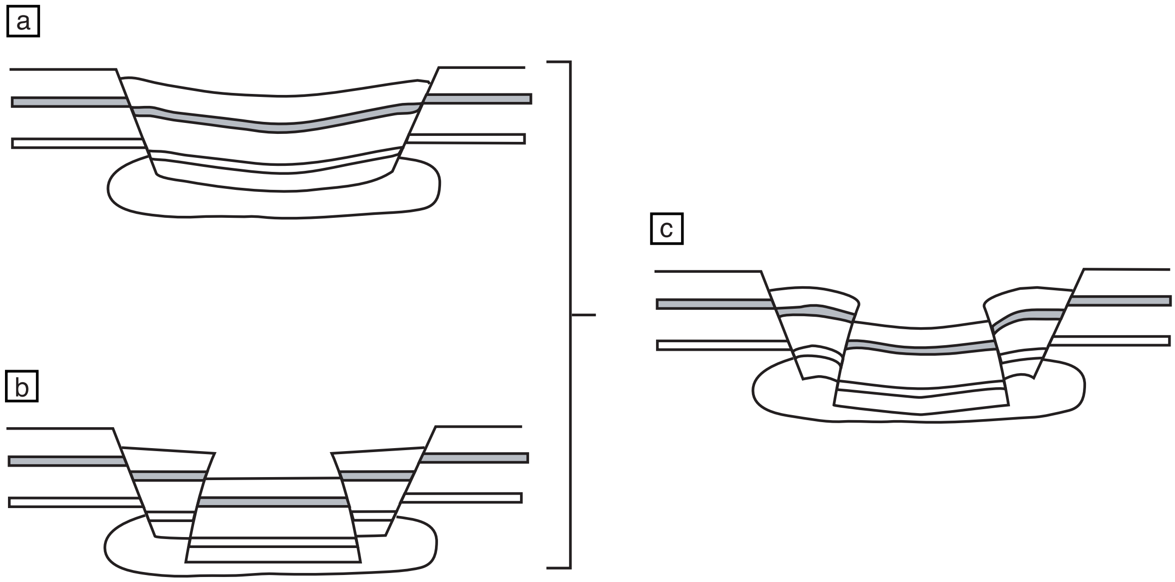

Figure 2.1: Cross-section sketches of end-member and hybrid solutions to the apparent problem of accomodating subsidence along an inward-dipping ring-fault (the so-called 'space problem'). The problem is solved by radial shortening, which is acheived either by **a)** ductile sag (distributed), or **b)** brittle reverse faulting (localised). The solution in analogue models and probably in reality is hybrid, i.e. both brittle and ductile **c)**. Past modelling results (Roche et al. 2000; Kennedy et al. 2004), and those of this study, indicate that the ductile end-member is favoured more by a 'thin' (relatively weak/flexible) roof, whilst the brittle end-member is favoured more by a 'thick' (relatively strong/rigid) roof.

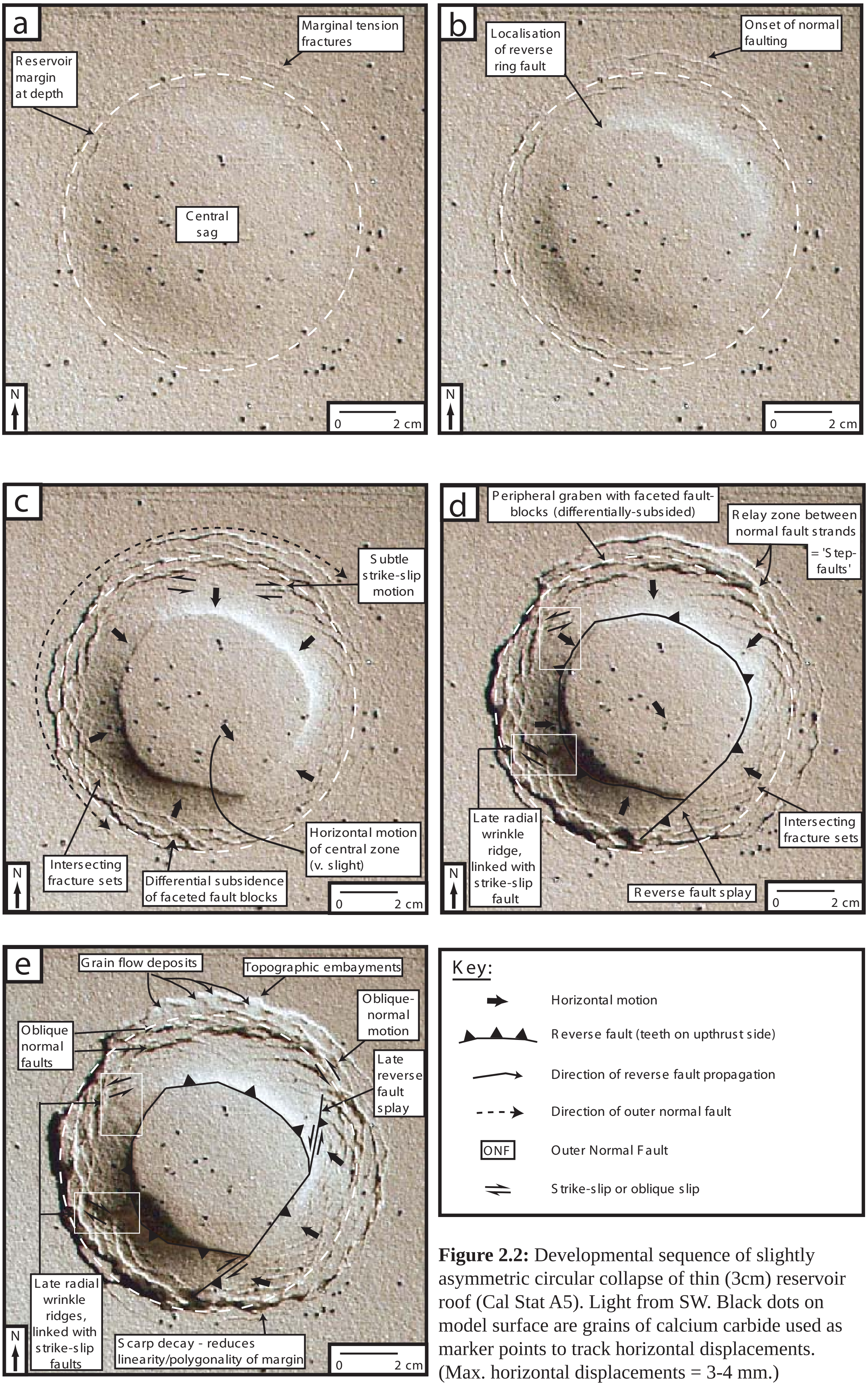

Figure 2.2: Developmental sequence of slightly asymmetric circular collapse of thin (3cm) reservoir roof (Cal Stat A5). Light from SW. Black dots on model surface are grains of calcium carbide used as marker points to track horizontal displacements. (Max. horizontal displacements = 3-4 mm.)

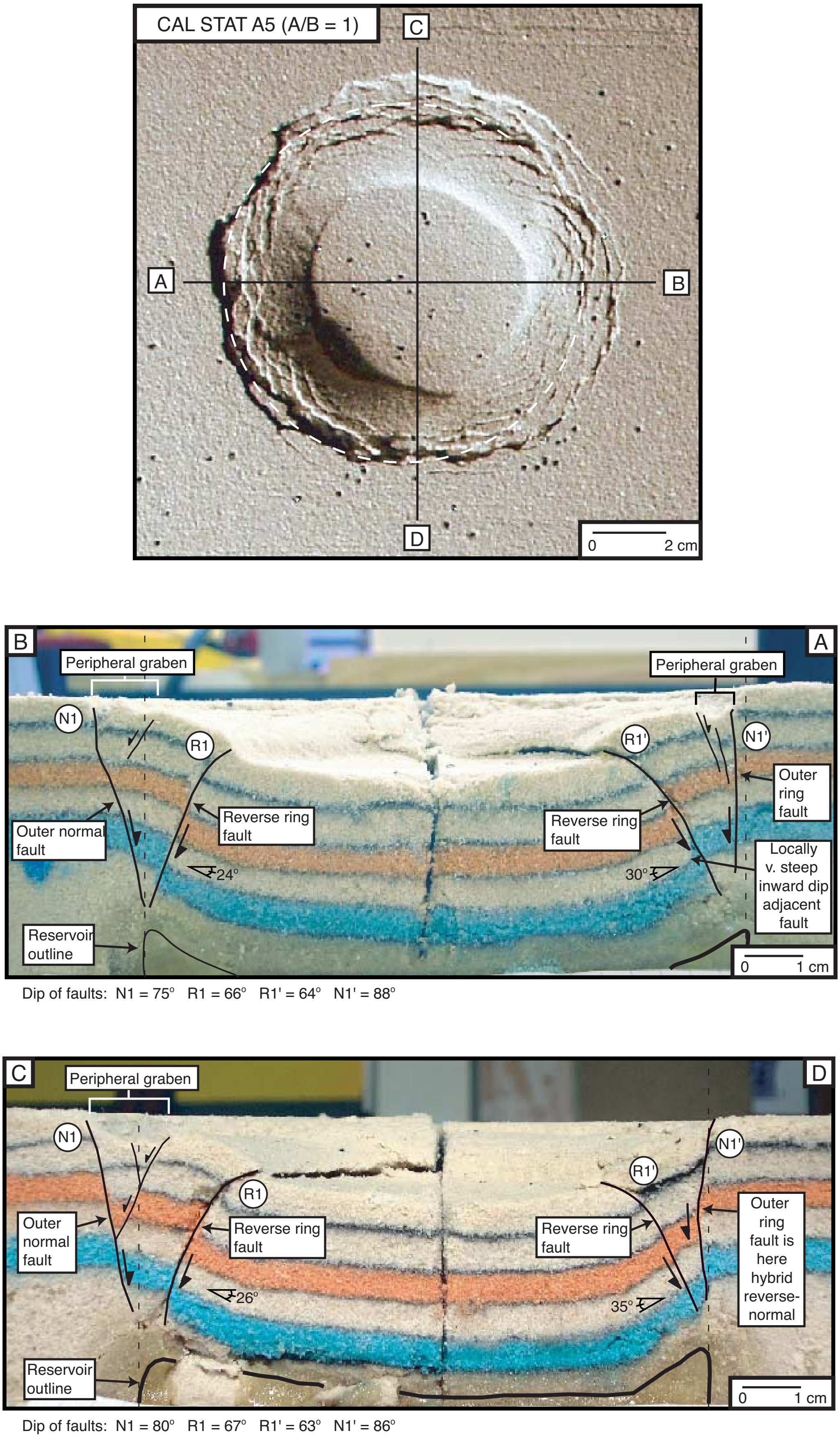

Figure 2.3: Cross-sections through a thin-roofed (3 cm), nearly-symmetric, circular caldera collapse (Cal Stat A5). Top picture is final subsidence structure in plan-view (Figure 2.2e), with lines of section indicated. Overall fault dips in sections are measured as the inclination of a chord that best connects the cut-off points of the uppermost and lowermost laters in the model. Dashed black lines are upward projections of reservoir margins, whihc are also marked by the dashed white line in the top picture.

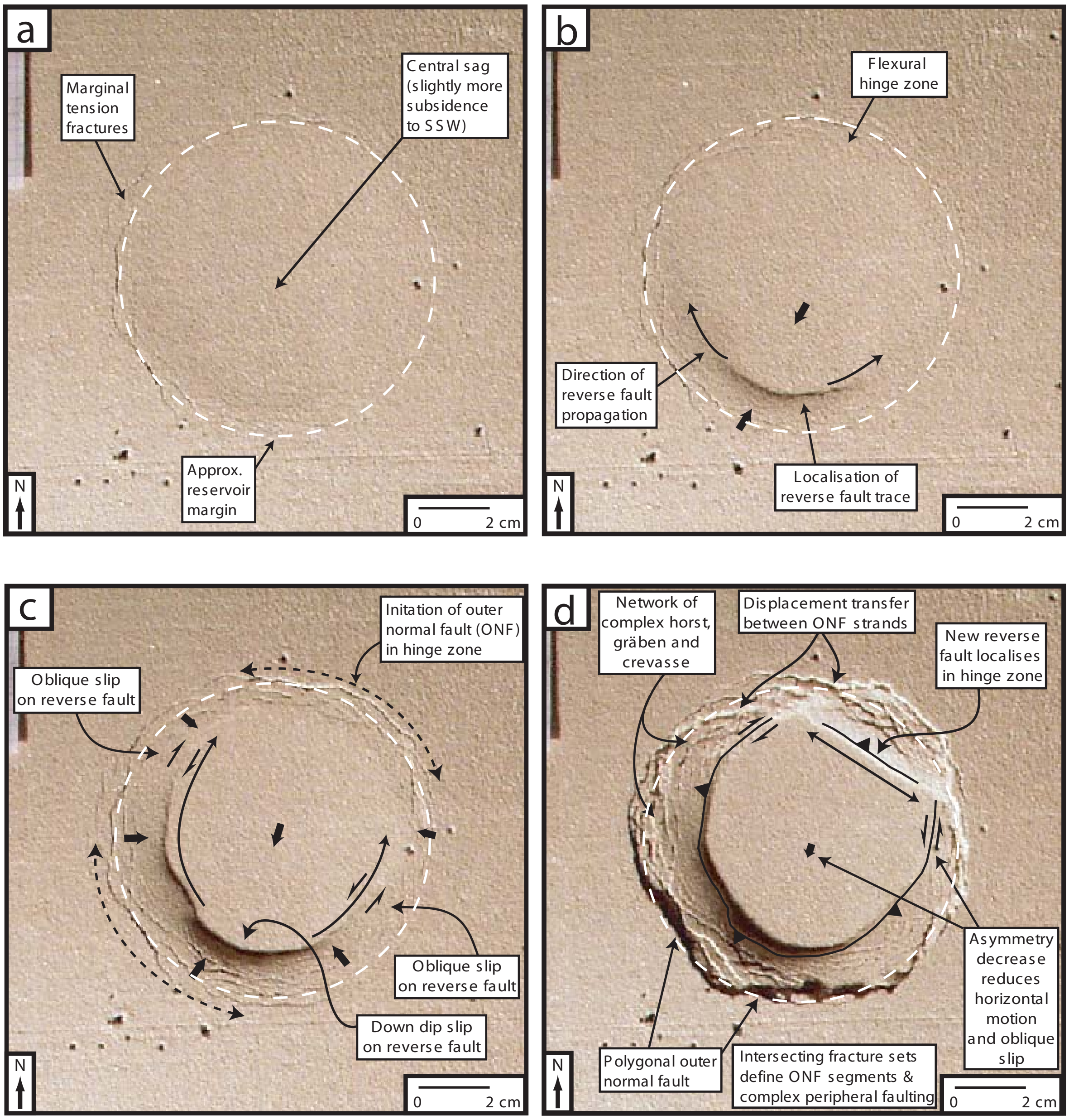

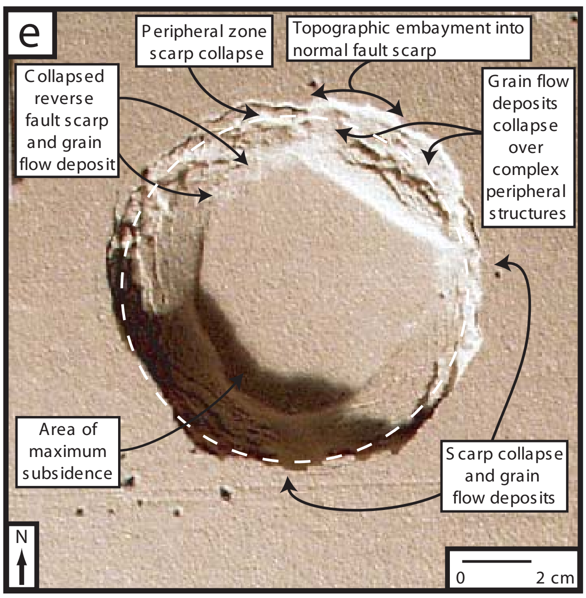

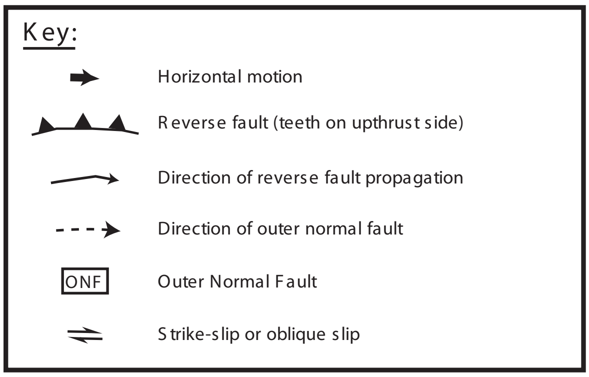

Figure 2.4: Developmental sequence of highly asymmetric collapse of a thin (3 cm) circular reservoir roof (Cal Stat A1). Light is from SW. Note initial localistaion of arcuate reverse fault in zone of most subsidence, then bidirectional propagation to hinge to form a complete ring-fault.

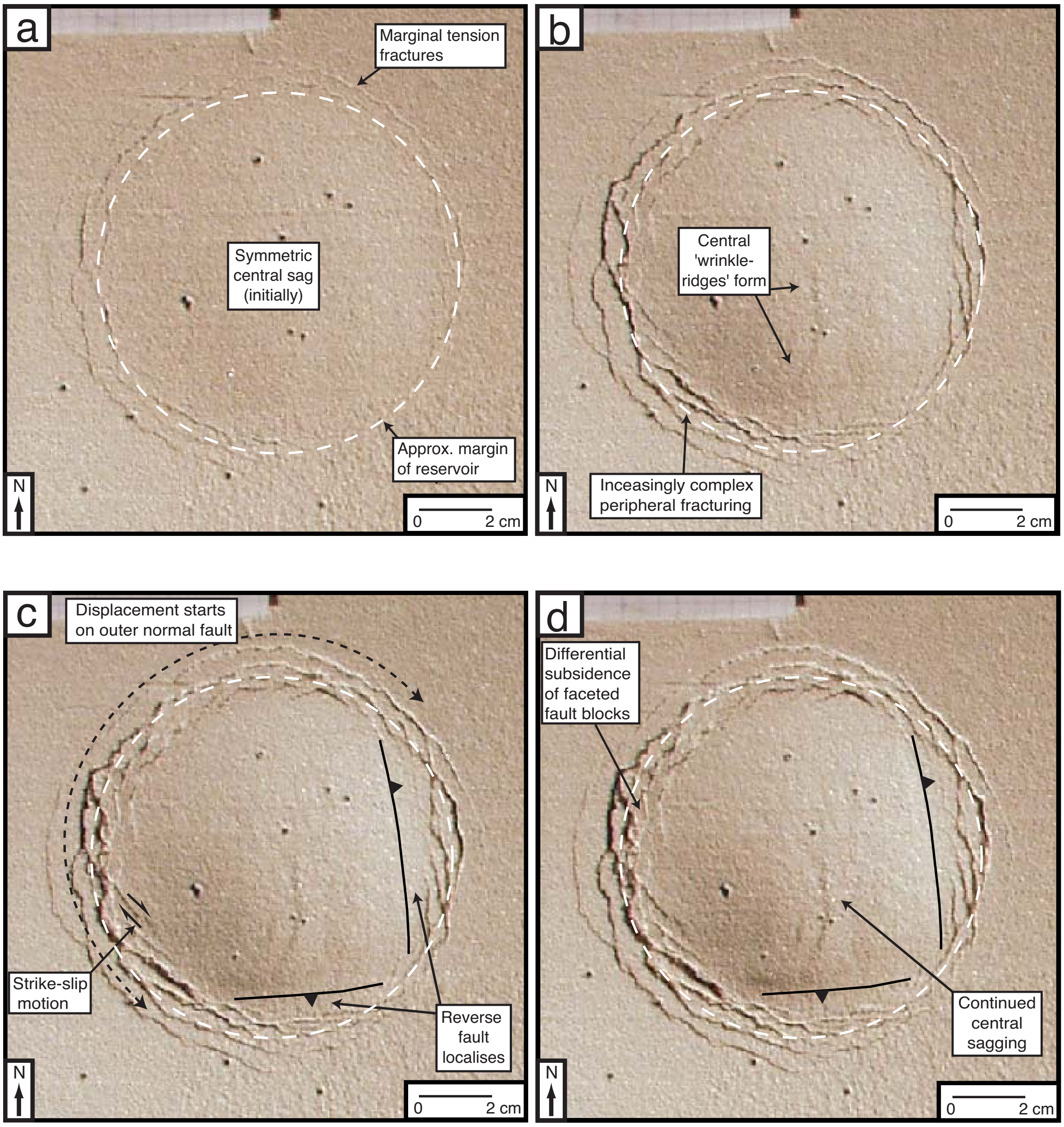

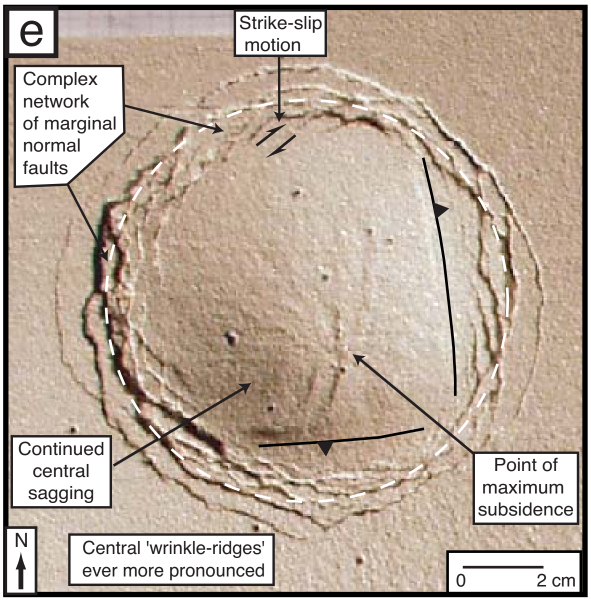

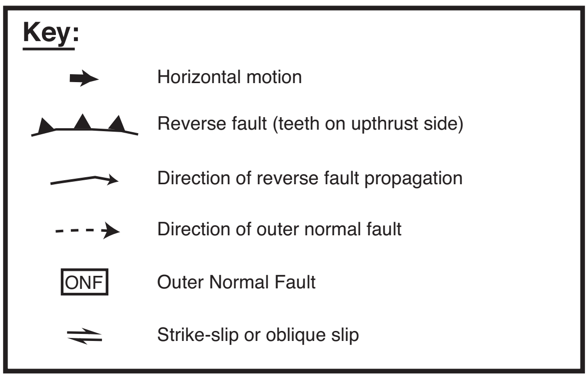

Figure 2.5: Evolution of an asymmetric collapse of a 'very thin' (2 cm) circular reservoir roof (Cal Stat A3). Light is from the SW. Note more pronounced sagging of floor, formation of central wrinkle ridges, and more subdued reverse faulting, compared to experiments with 'thin' (3 cm) roofs.

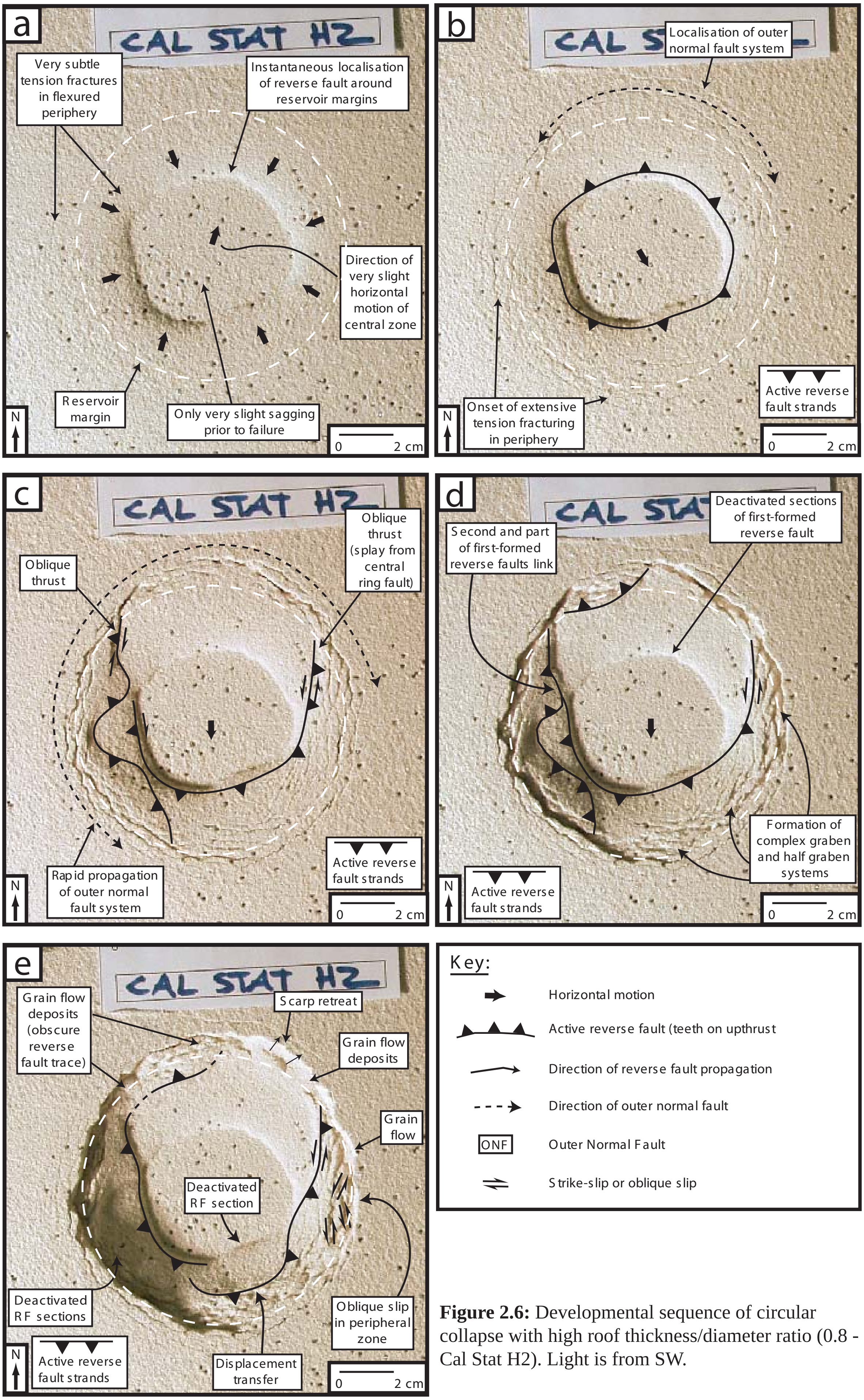

Figure 2.6: Developmental sequence of circular collapse with high roof thickness/diameter ratio (0.8 - Cal Stat H2). Light is from SW.

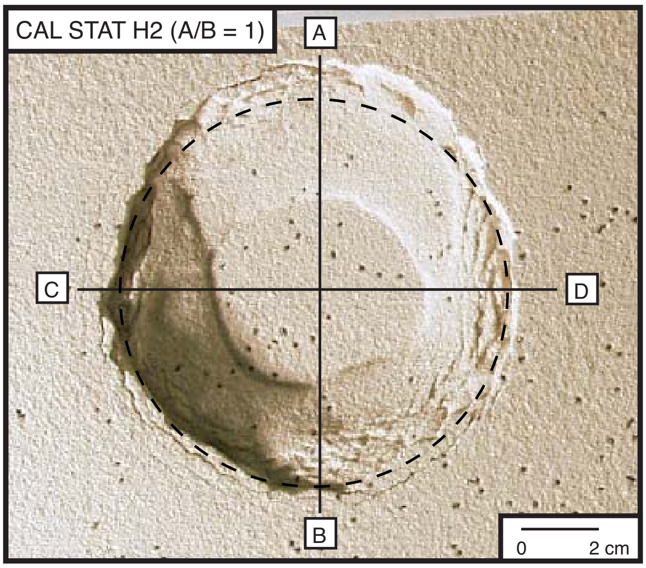

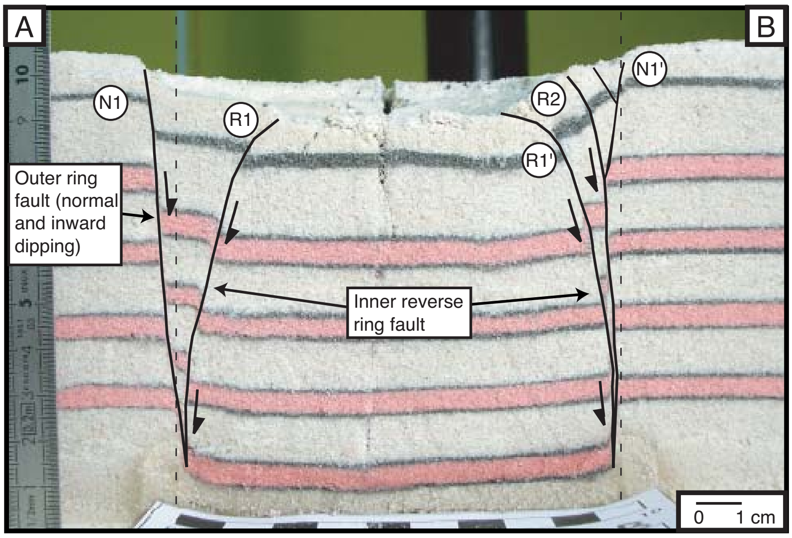

Dip of faults: N1 = 86° R1 = 75° R1' = 79° R2 = 85° N1' = 79°

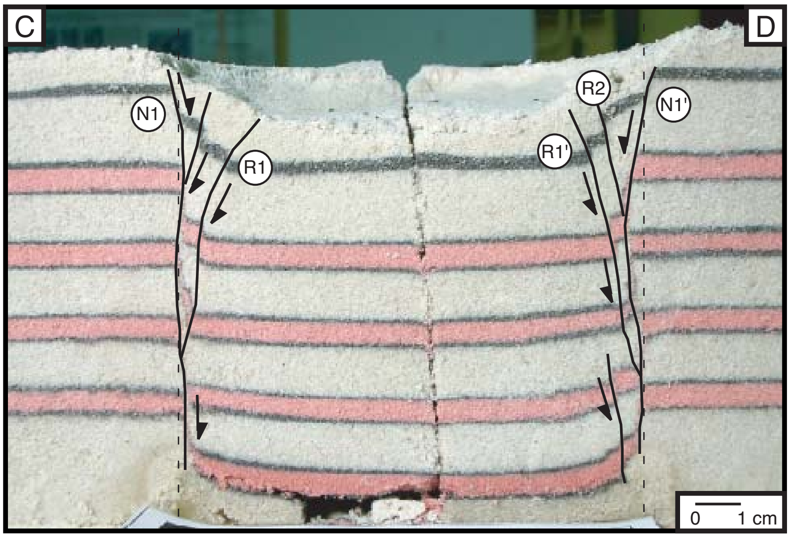

Dip of faults: N1 = 85° R2 = 86° R1 = 78° R1' = 78° R2' = 83° N1' = 83°

Figure 2.7: Cross-sections through a 'thick-roof' (8 cm) circular collapse model (Cal Stat H2) (thickness/diameter ratio = 0.8). Top picture is final collapse structure as shown in Figure 2.6e. Vertical dashed lines on cross sections are upward projections of the reservoir margins, which are also marked by dashed black circle in top picture.

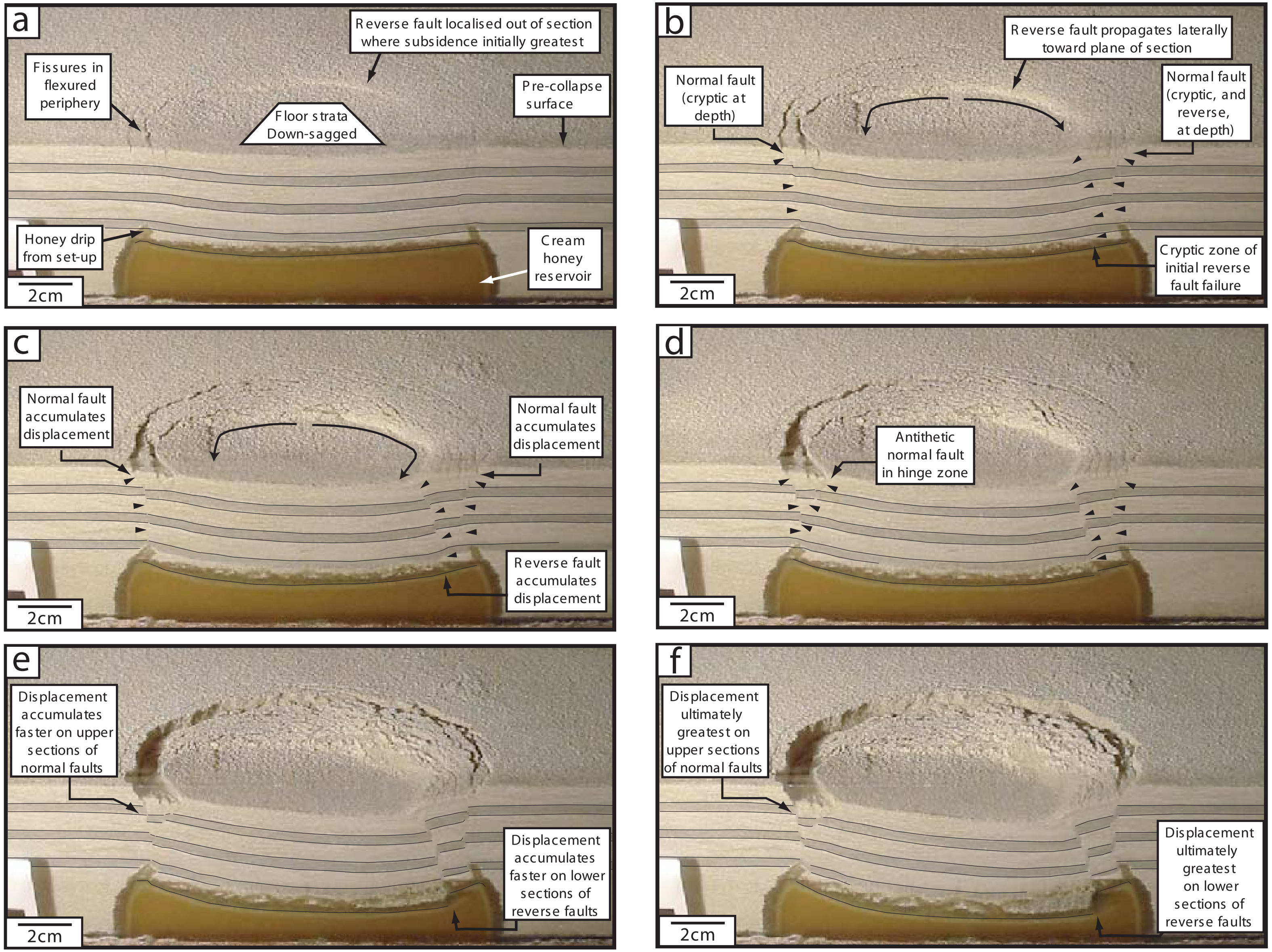

Figure 2.8: Caldera collapse simulated against a glass pane (Cal_2D_3), to see evolution of faulting at depth.

Magma chamber is emplaced as a half-cylinder adjacent the glass pane, but otherwise the set-up is constructed in the same way as for the other 3D experiments, and is similarly drained via a basal honey conduit (c. 1 cm inside the glass). Light is from left hand side.

In these experiments, faults are often seen first as hairline fractures that propagate very rapidly first, then accumulate displacement.

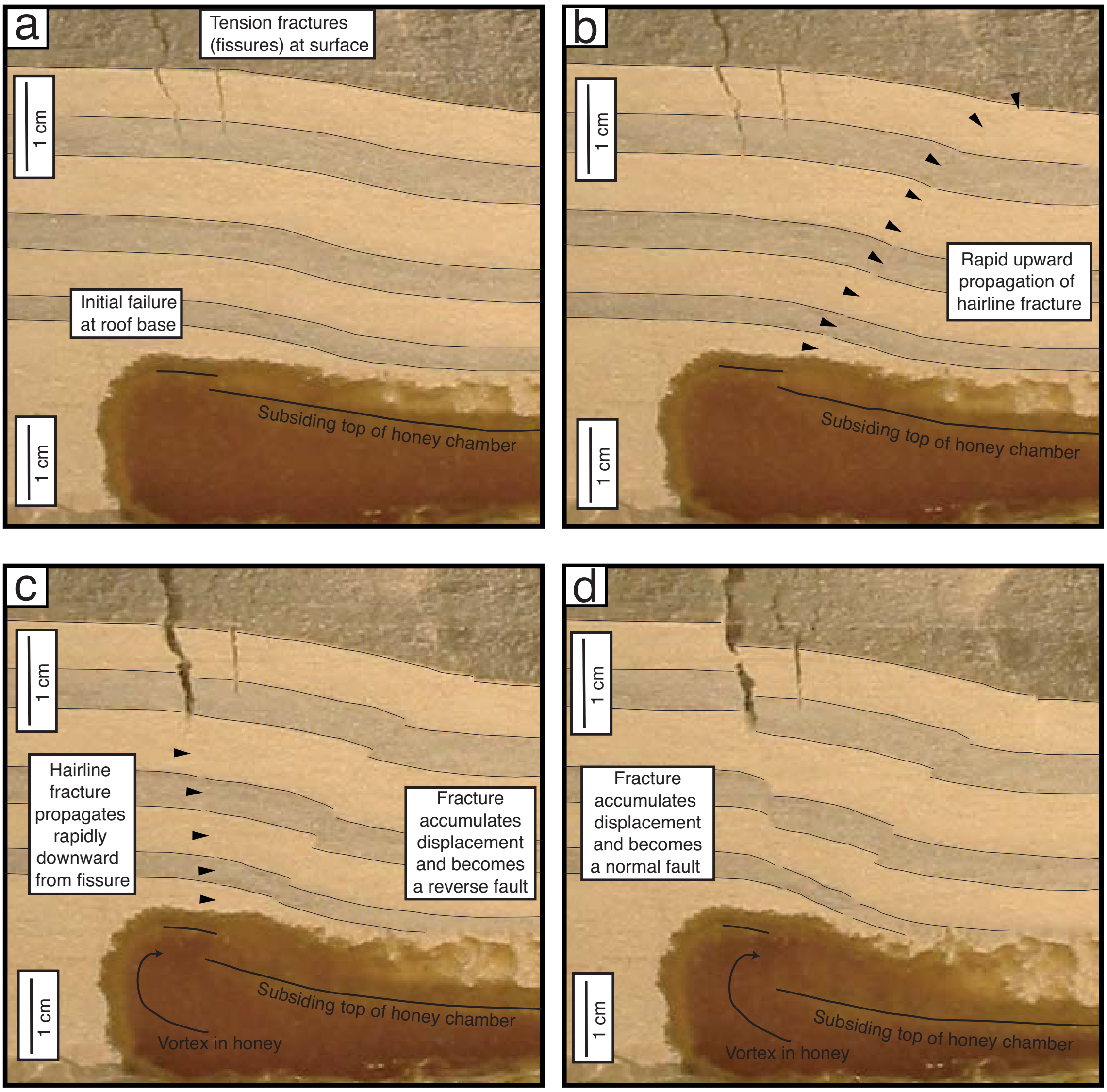

Figure 2.9: Close-up of the evolution of inner reverse and outer normal faults during caldera collapse simulated against a glass pane (Cal_2D-2). Light is again from the left hand side. Note that, due to the oblique angle of view, the vertical scale changes slightly up section.

In this model, one can see the failure of the roof along a hairline fracture, which subsequently accumulates displacement to become a reverse fault. Also shown is how a hairline fracture propagates downward from a tensile fracture at the surface, and then accumulates displacement to become the main normal fault.

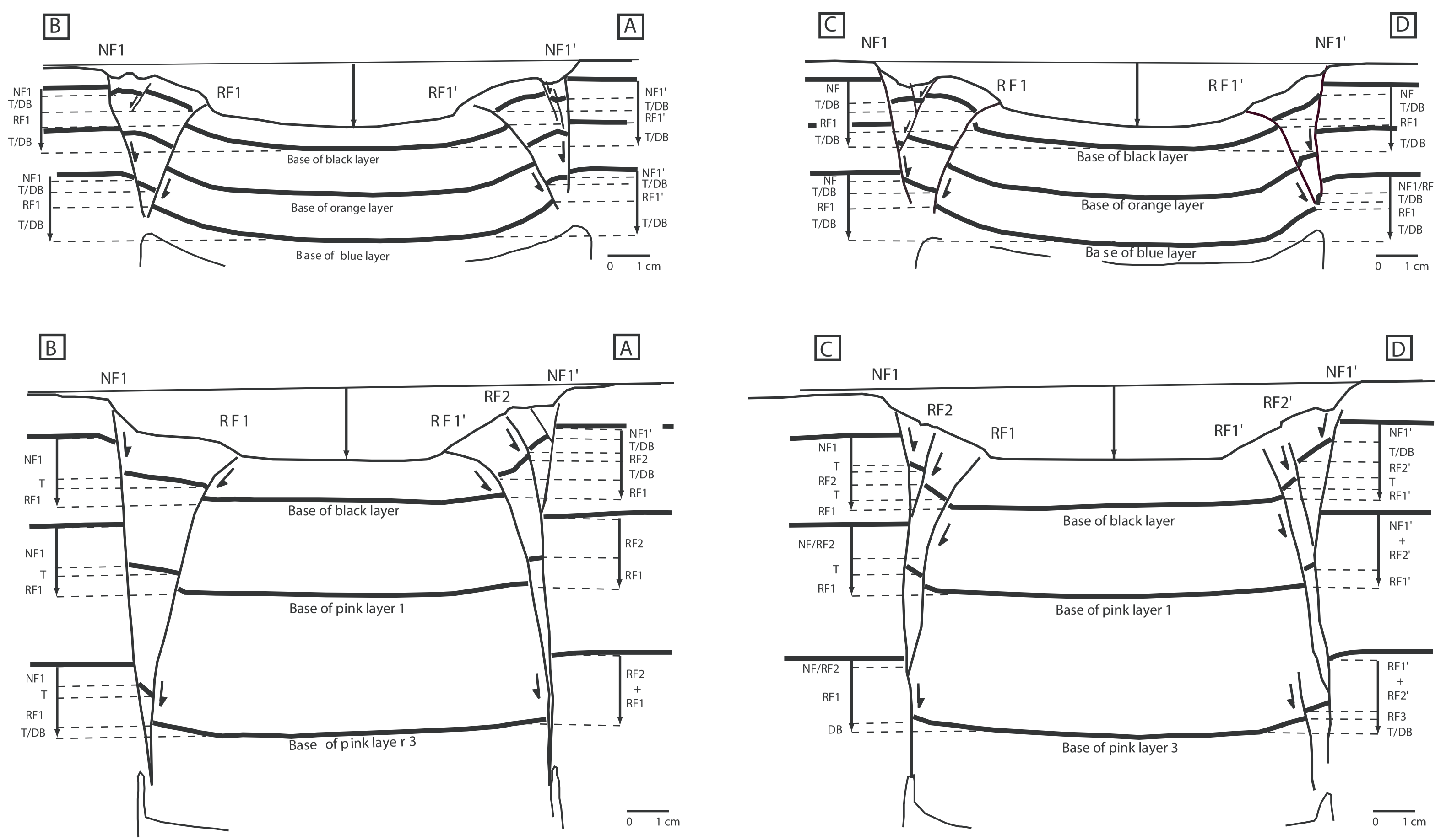

Figure 2.10: Cross-section sketches of the offsets along selected model horizons in 'thin' (Cal Stat A5 - above) and 'thick' (Cal Stat H2 - below) reservoir roofs.

The central vertical black arrow in each sketch shows the net central subsidence along each cross section.

The peripheral vertical black arrows show the proprotion of that central displacement taken up along various structures for each selected horizon.

Stuctures include: NF = main normal ring fault and associated antithetic faults in marginal graben; RF = reverse ring faults and oblique reverse splays; DB = monoclines formed by ductile bending; T = tilted segments.

Note that at each side of each cross-section, the vertical displacements of each horizon across all these structures sums to the net central subsidence. Thus at each side and at any level of the caldera, the structures present maintain a type of geometric coherence in their accomodatation of the net central subsidence. Although displacement on a normal fault deceases downward and displacement on a reverse fault dceases upward, at each level in the roof the sum of the displacments on both ring faults is equal. Note also that, by taking up nearly 50% of the vertical displacement. ductile bending (i.e. sagging) plays a significant role in maintainng this geometric coherence in the 'thin' roof. In the 'thick' roof, however, ductile bending is much less importatnt, although tilting is locally still prominent.

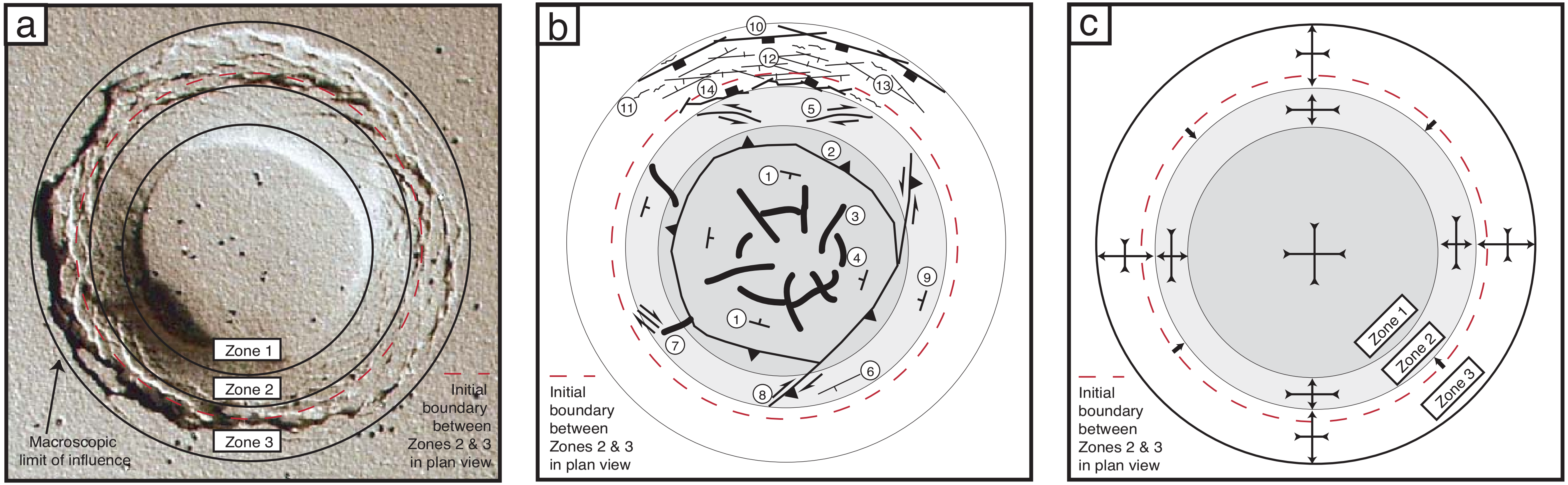

Figure 2.11: Structural zonation of calderas in plan view

(a) Outline of three structural zones observed in plan view in collapse experiments (here shown for near-symmetric collapse of Cal Stat A5). Zone 1 corresponds to the 'central caldera zone' of Chapters 1, 5 and 6; Zones 2 and 3 correspond to the 'peripheral caldera zone' in these chapters.

(b) Generalised sketch of structures observed in different plan view zones (based on 'thin roof' collapses Cal Stat A5 and Cal Stat A3)
Zone 1 structures: (1) centroclinally-sagged floor strata; (2) concentrically-trending reverse faults; (3) radially-trending wrinkle ridges; (4*) concentrically-trending wrinkle ridges. *seen in nature only - Figure 2.13
Zone 2 structures: (5) obliquely-to concentrically-trending strike-slip faults (locally conjugate); (6) occasional oblique-normal faults, (7) radially-trending wrinkle ridges (often associated with strike-slip faults), (8) obliquely-trending oblique-reverse faults (splay from inner concentric ring fault), (9) high inward tilts
Zone 3 structures: (10) roughly concentrically-trending, normal- to oblique-normal faults (11) fissures, (12) graben, (13) step-faults, (14) faceted fault-blocks (rhombic).

(c) Interpretation of orientation and relative magnitudes of plan-view principal strains in the three zones from observed horizontal displacements and the above structures.
Zone 1: radial and concentric shortening, plus vertical extension (constrictional strain)
Zone 2: slight radial extension or shortening; concentric shortening, plus slight to no vertical extension
Zone 3: Large radial extension and slight concentric shortening, plus vertical shortening

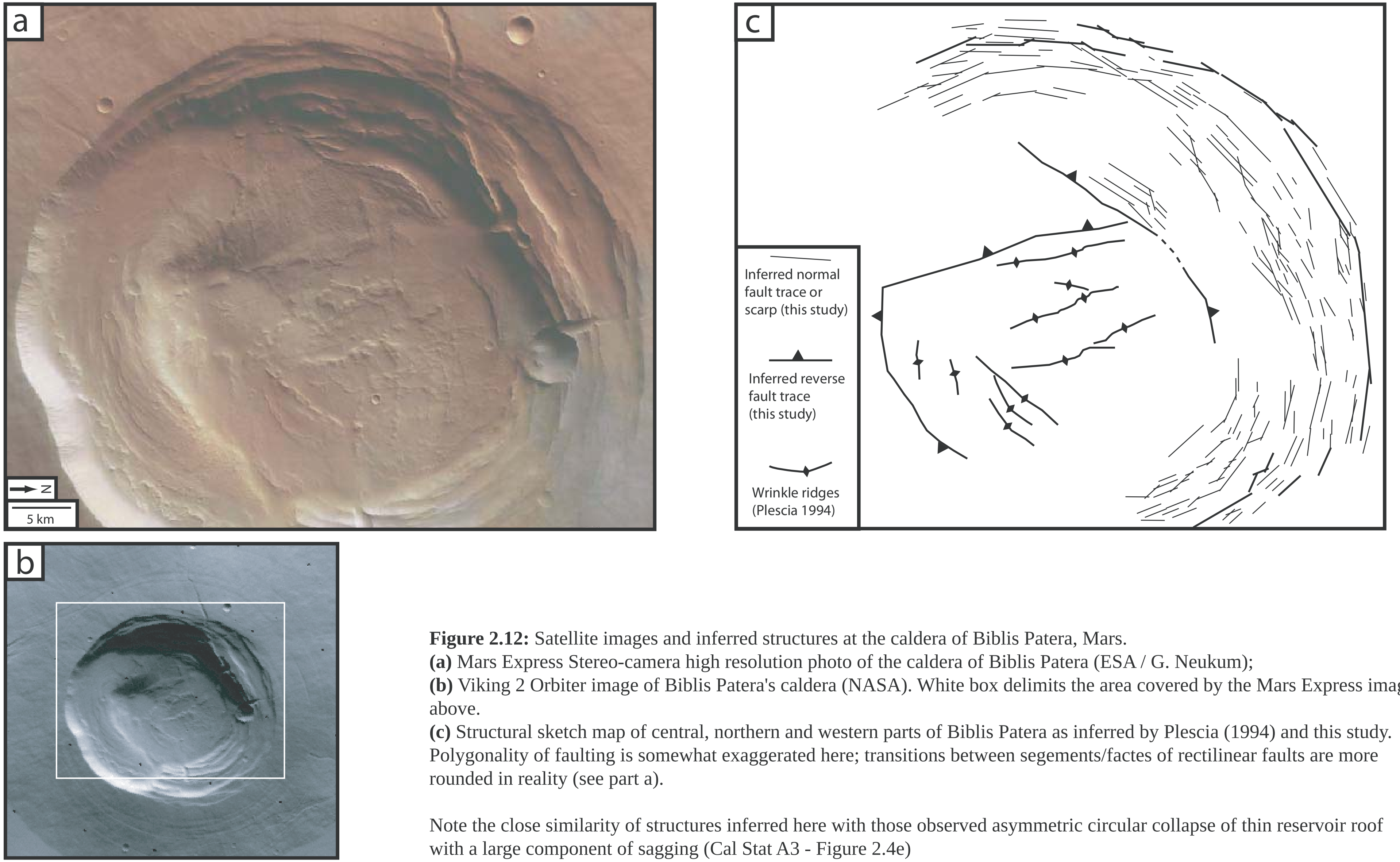

Figure 2.12: Satellite images and inferred structures at the caldera of Biblis Patera, Mars.
(a) Mars Express Stereo-camera high resolution photo of the caldera of Biblis Patera (ESA / G. Neukum);
(b) Viking 2 Orbiter image of Biblis Patera's caldera (NASA). White box delimits the area covered by the Mars Express image above.
(c) Structural sketch map of central, northern and western parts of Biblis Patera as inferred by Plescia (1994) and this study. Polygonality of faulting is somewhat exaggerated here; transitions between segements/factes of rectilinear faults are more rounded in reality (see part a).

Note the close similarity of structures inferred here with those observed asymmetric circular collapse of thin reservoir roof with a large component of sagging (Cal Stat A3 - Figure 2.4e)

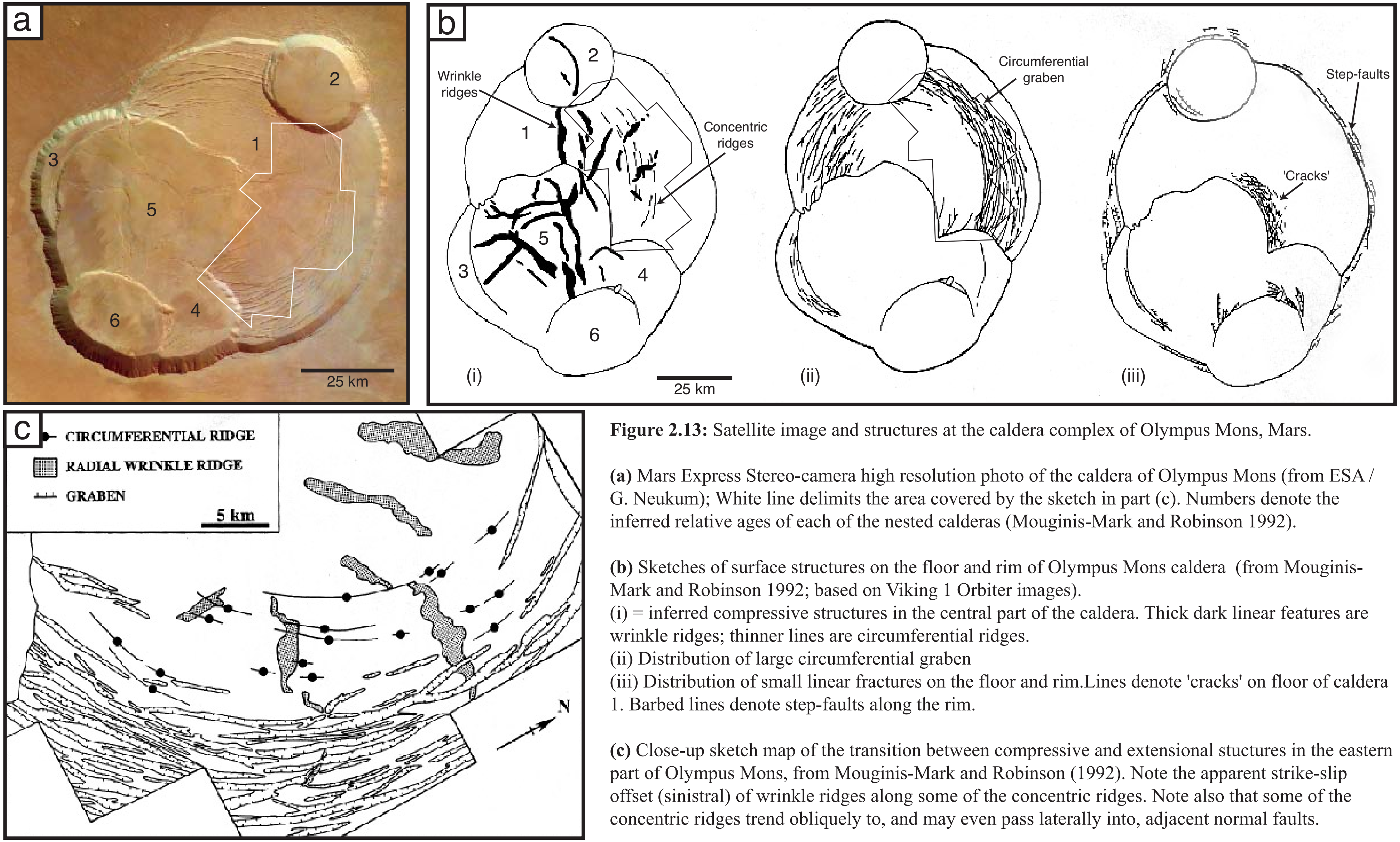

Figure 2.13: Satellite image and structures at the caldera complex of Olympus Mons, Mars.

(a) Mars Express Stereo-camera high resolution photo of the caldera of Olympus Mons (from ESA / G. Neukum); White line delimits the area covered by the sketch in part (c). Numbers denote the inferred relative ages of each of the nested calderas (Mouginis-Mark and Robinson 1992).

(b) Sketches of surface structures on the floor and rim of Olympus Mons caldera (from Mouginis-Mark and Robinson 1992; based on Viking 1 Orbiter images).
(i) = inferred compressive structures in the central part of the caldera. Thick dark linear features are wrinkle ridges; thinner lines are circumferential ridges.
(ii) Distribution of large circumferential graben
(iii) Distribution of small linear fractures on the floor and rim.Lines denote 'cracks' on floor of caldera 1. Barbed lines denote step-faults along the rim.

(c) Close-up sketch map of the transition between compressive and extensional stuctures in the eastern part of Olympus Mons, from Mouginis-Mark and Robinson (1992). Note the apparent strike-slip offset (sinistral) of wrinkle ridges along some of the concentric ridges. Note also that some of the concentric ridges trend obliquely to, and may even pass laterally into, adjacent normal faults.

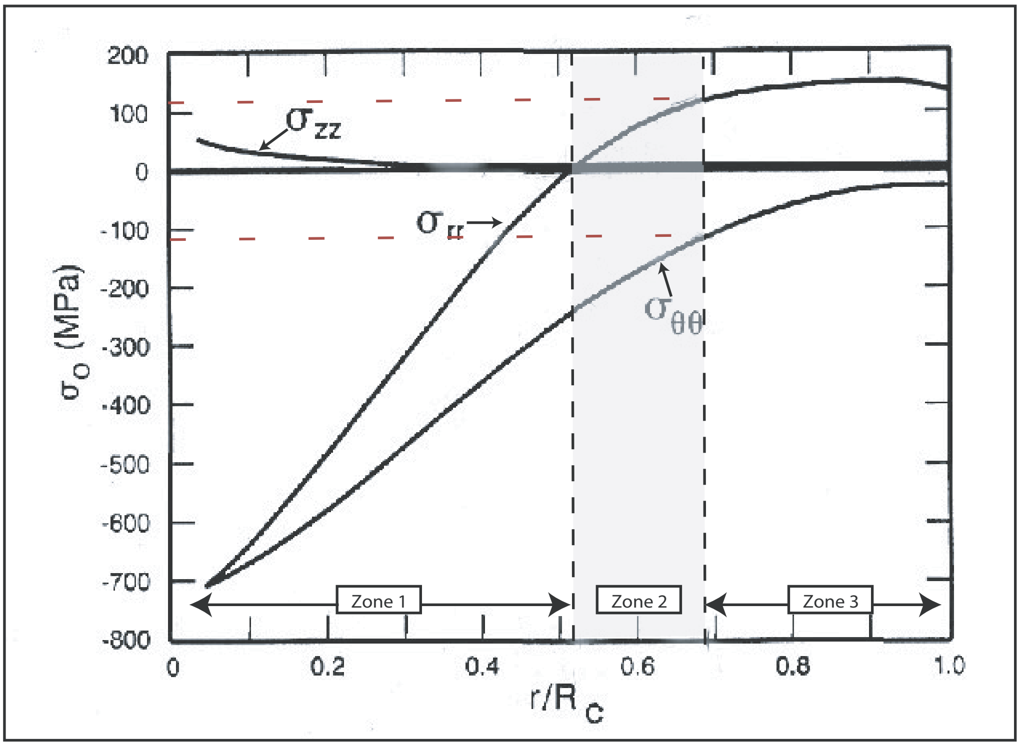

Figure 2.14: Surface stresses arising in a caldera floor from elastic deformation of the roof above an instantaneously depressurised ellipsoidal chamber. The stress magnitudes are plotted against radial distance from the caldera centre (r/Rc, where Rc is the caldera radius). The chamber has radius a = Rc and height c = 0.5Rc, and lies at a depth beneath the surface of d = 0.25 Rc. σ_{rr} = radial principal stress, $\sigma_{\theta\theta}$ = concentric principal stress (or "hoop stress"), σ_{zz} = vertical principal stress. Negative stresses are compressional and positive stresses are extensional. Modified from Zuber and Mouginis-Mark (1992).

Drawn on this plot are the tentative positions of the boundaries between the three deformation zones observed in experiment. The boundary between Zones 1 and 2 is therefore located where radial contraction changes to radial extension. The boundary between Zones 2 and 3 is positioned where radial extension and concentric contraction are equal in magnitude. Inside this boundary strike slip faulting should predominate, whereas outside the boundary normal faulting should predominate. The resultant width of Zone 2 (0.17Rc) in the plot is in close agreement with the observed width of Zone 2 in experiment (~ 0.16Rc - see Figure 2.11) and approximates that in nature on Olympus Mons (width of zone of concentric ridges ~ 0.16 - 0.25Rc - see Figure 2.13).

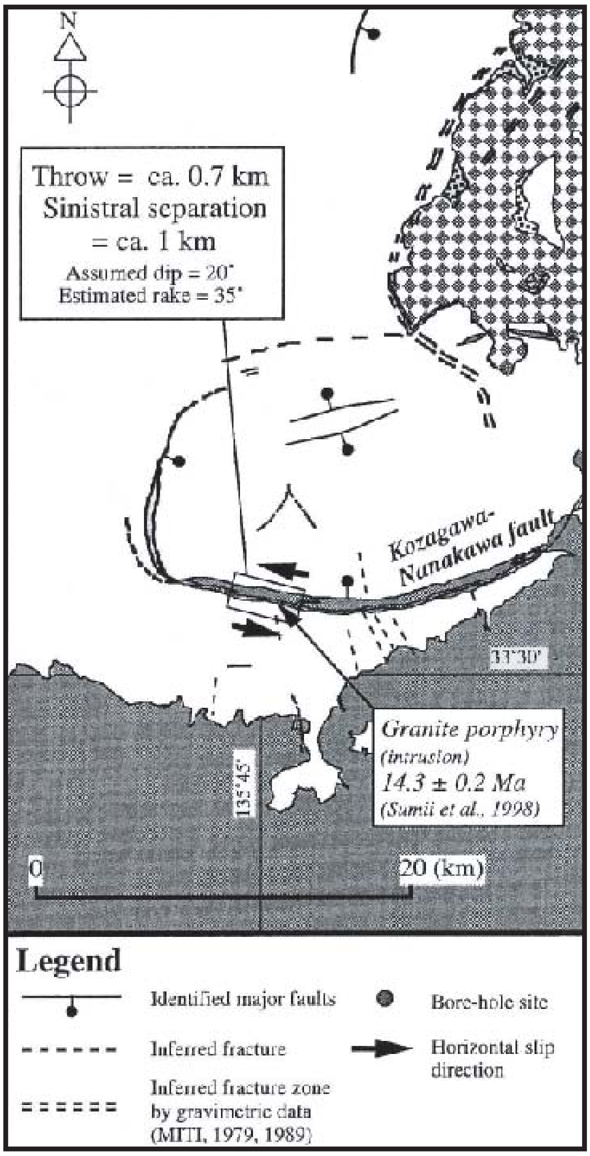

Figure 2.15: Map of the southernmost part of Kumano caldera, Japan (from Miura 1999). This elliptical part aparently subsided independently of the rest of the caldera. Note the strong oblique slip component on the ring fault. This is compatible with asymmetric collapse of the caldera along a reverse fault, with maximum subsidence to the west.

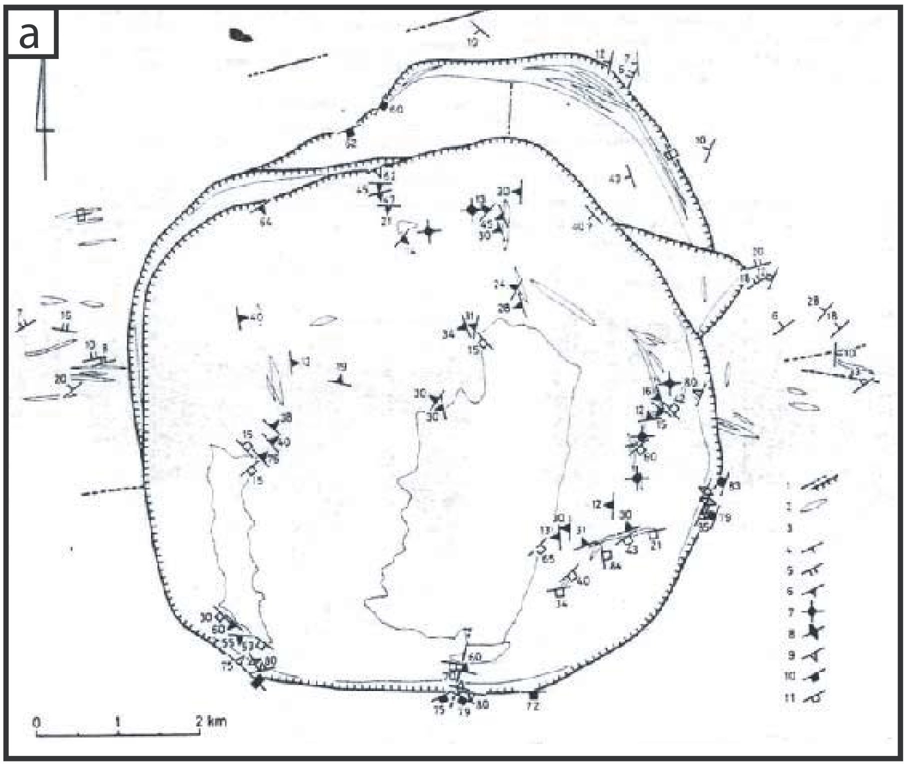

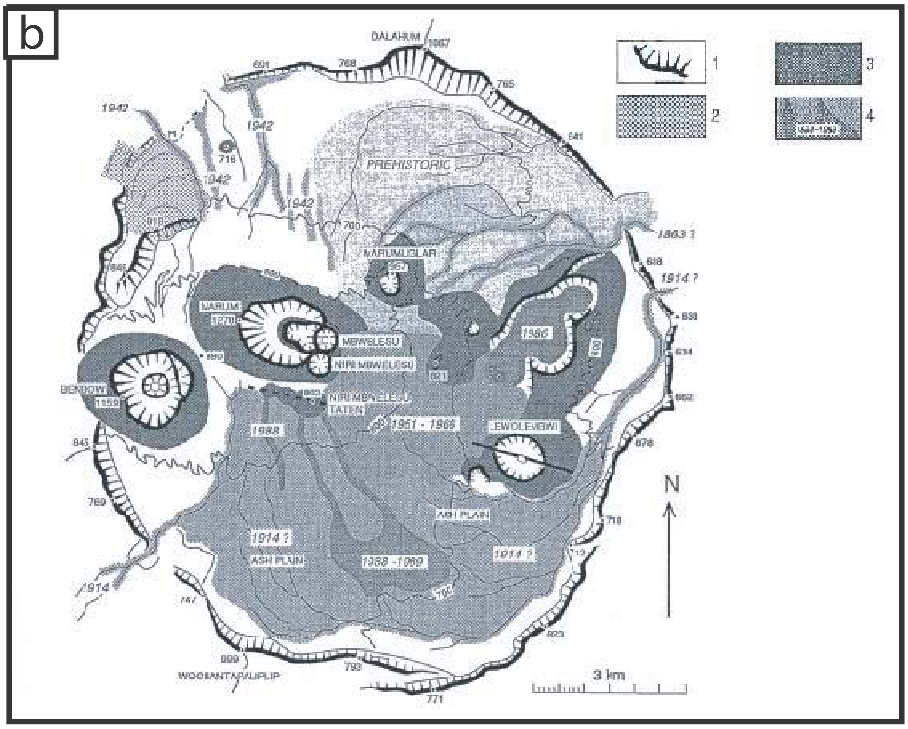

Figure 2.16: a) Structural sketch map of Ishizuchi caldera, Japan (from Yoshida 1984). Ishizuchi is Palaeogene in age and deeply eroded. 1= faults and ring faults; 2= dikes and intrusions; 3 = lithological boundaries; 4 = bedding plane; 5 & 6 = inclination of essential lenses (fiamme?) in pyroclastic flow deposits; 7 = horizontal dip; 8 = vertical dip; 9 = inclination of essential lens in intrusive breccias; 10 = plane of ring fracture; 11 = contact plane of intrusive rocks.

b) Volcanological sketch map of Ambrym caldera, Vanatu (from Robin et al. 1993). Ambrym is Quaternary in age (still active) and not deeply eroded. 1= caldera scarp; 2 = andesite lava flow; 3 = volcanic cones; 4 = pre-historic and historic lava flows.

Note that regardless of erosion level, the structural (Ishizuchi) and topographic (Ambrym) caldera boundaries are subtly polygonal.

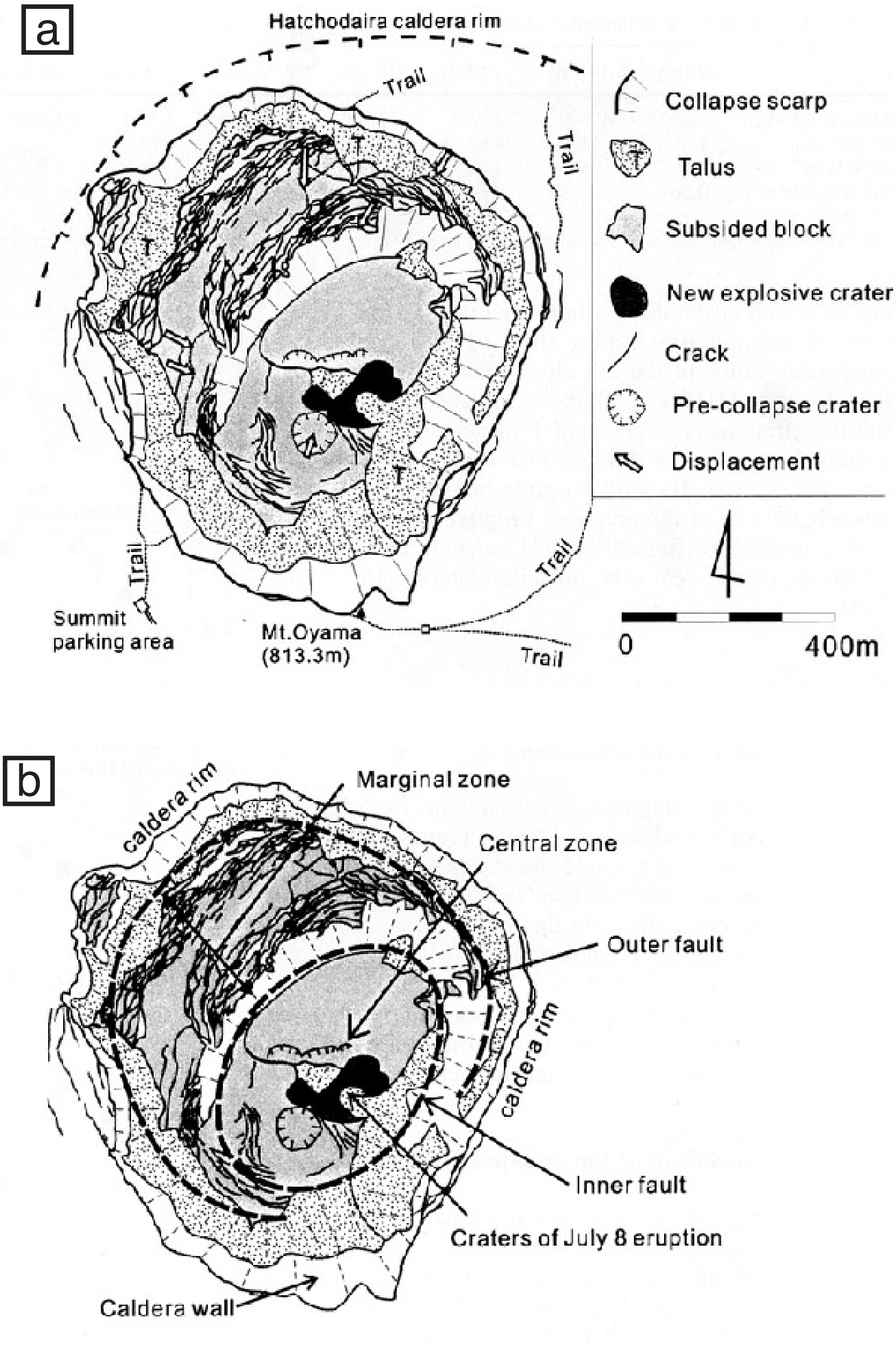

Figure 2.17:
a) Surface structure, geomorphological and volcanological features of Miyakejima caldera, as sketched from aerial photographs on the 8th of July 2000 (just after the first summit eruption and c. 100m surface subsidence). From Geshi et al. (2002).

b) Classification of caldera structures. From Geshi et al. (2002). Note the pattern of marginal zone fracturing (normal faults and fissures), the trends of which parallel the facets in the caldera's rim. The rim is the, as yet, only slightly decayed scarp of an outer normal ring-fault. These structural relationships are very similar to those produced in experiment.

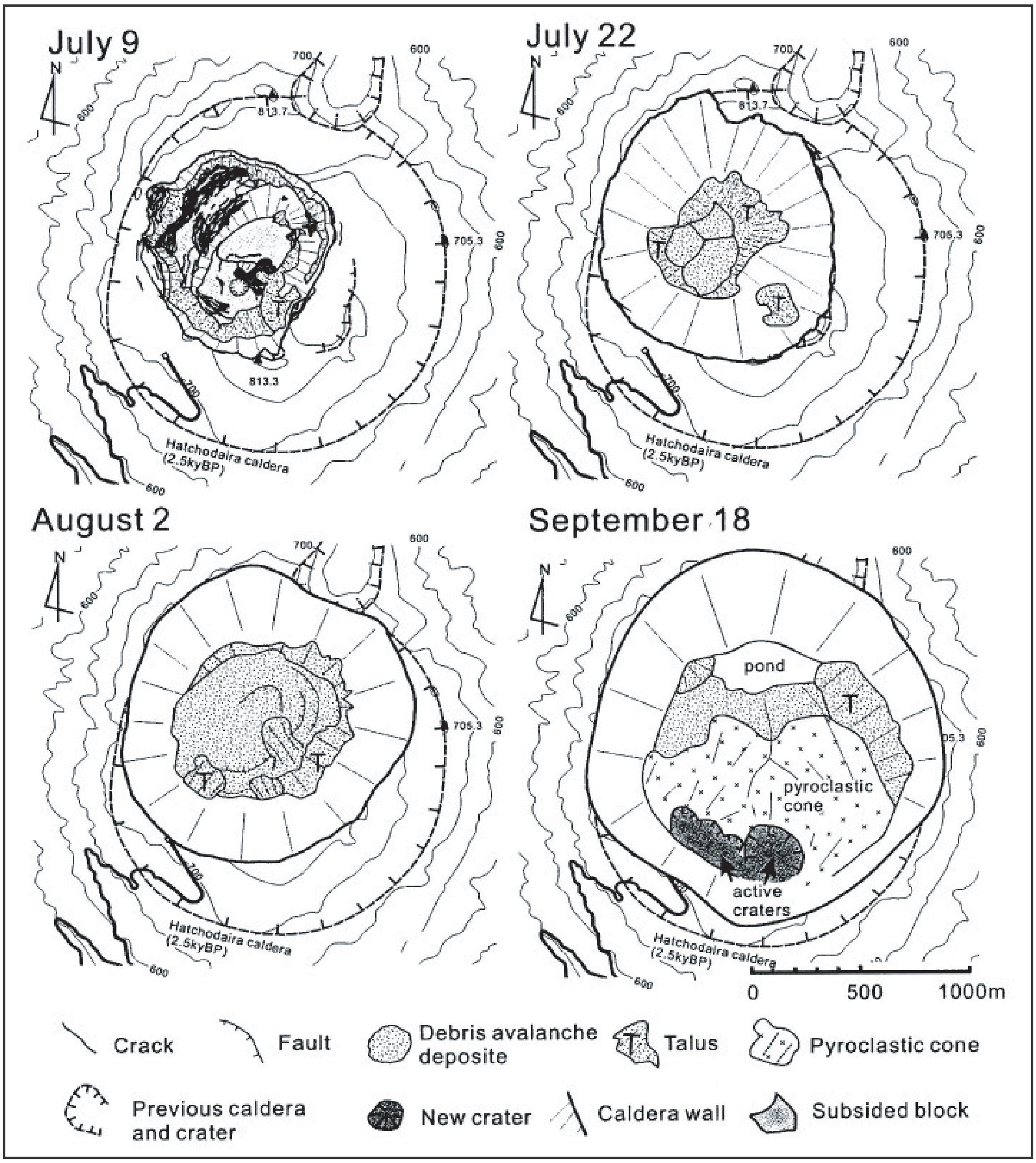

Figure 2.18: Structural, geomorphological and volcanological evolution of Miyakejima caldera from the 9th of July 2000 to the 18th of September 2000, as sketched from aerial photographs. From Geshi et al. (2002).

July 9th: shortly after the caldera formed, the polygonal ring fault scarps are still fresh and well-defined (compare with Figure 2.19). The polygonality of the caldera is thus initially defined by the strongly polygonal shape of the structural margin.

July 22nd - Sept 18th: With continuous subsidence (up to 2.1 km), the initial scarps become oversteepened and progressively degrade. The outer normal fault scarp retreats outward and so the caldera diameter, as defined by the topographic margin, increases.

Less pronounced and geometrically rather different to the initial structural margin, the polygonality of the caldera is ultimately defined by the more weakly polygonal shape of the topographic margin.

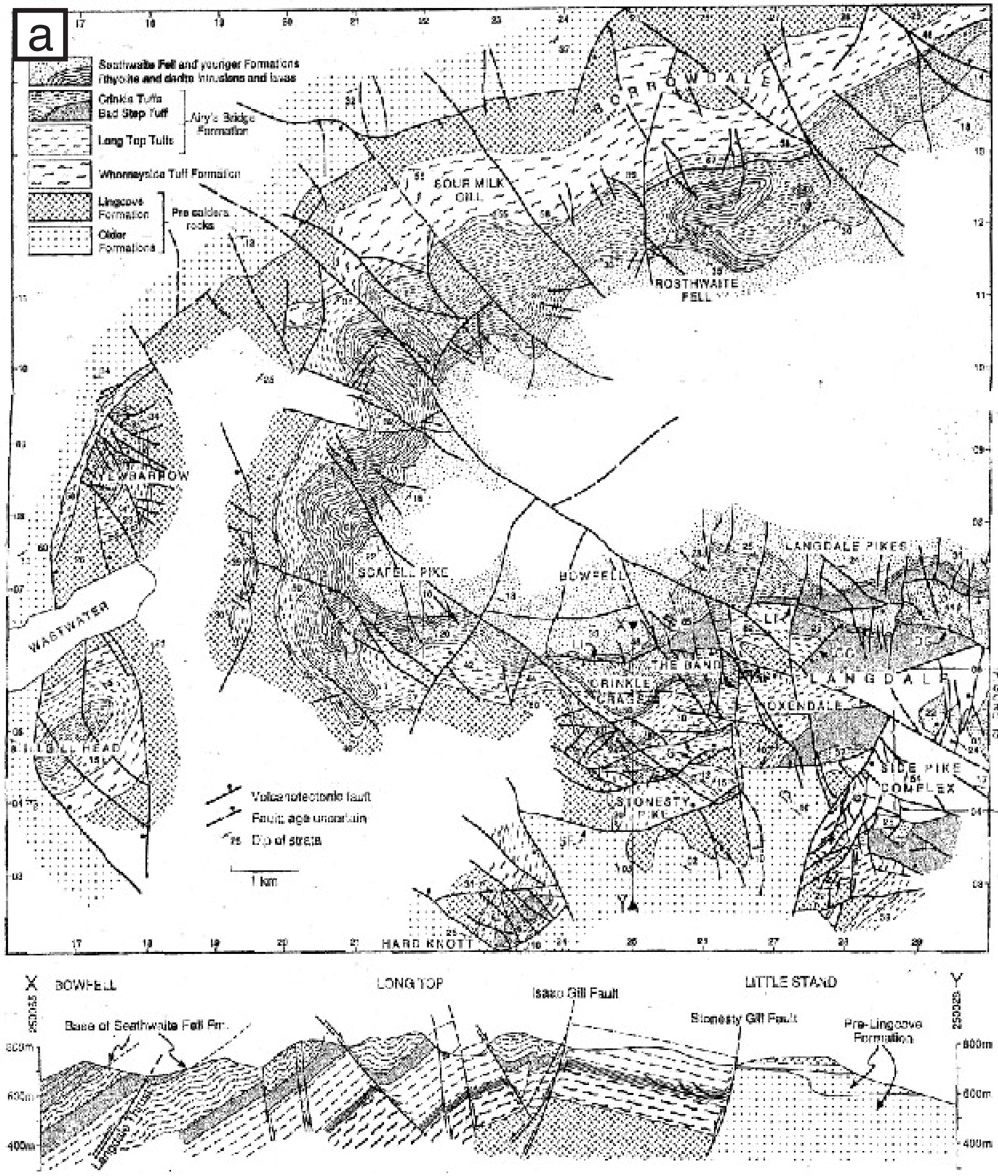

Figure 2.19:

a) Simplied geologic map of part of the Scafell caldera, England.

Volcano-tectonic faults are represented by solid lines; faults for which a volcano-tectonic origin is unproven are marked as dashed lines. IG = Isaac Gill fault; SF = Stonesty fault; DG = Dungeon Gill fault; GG = Grave Gill fault; LT = Langdale Thrust.

Cross section shows the structure of the south side of the caldera (note line of section X-Y).From Branney and Kokelaar (1994).

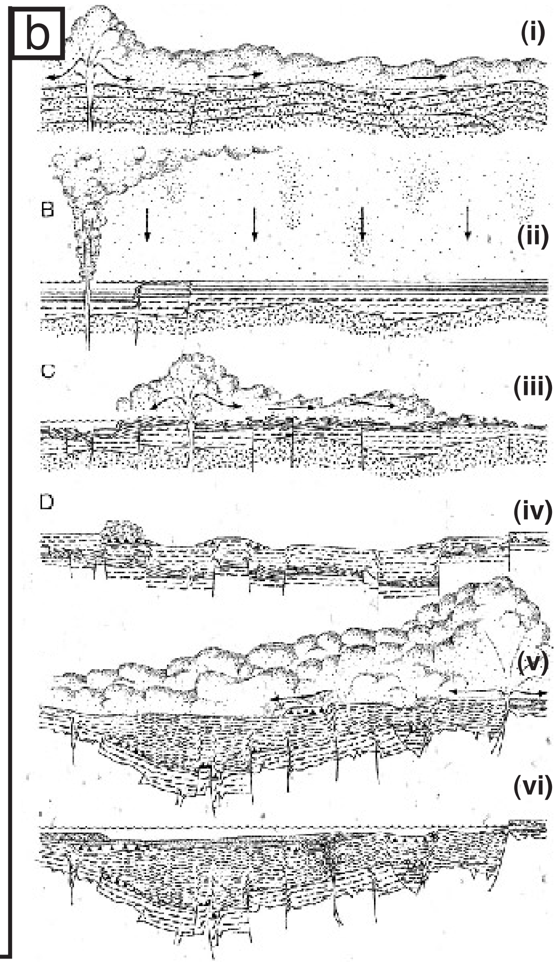

b) Schematic summary of piecemeal collapse in the Scafell area, from Branney and Kokelaar (1994). Not a cross-section or to scale.

(i - iii) Emplacement of Whorneyside Ignimbrite; (iv) Emplacement of the Long Top Tuffs; (v) Emplacement of paroxysmal Crinkle Tuffs; (vi) Post-collapse lacustrine sedimentation and intrusion

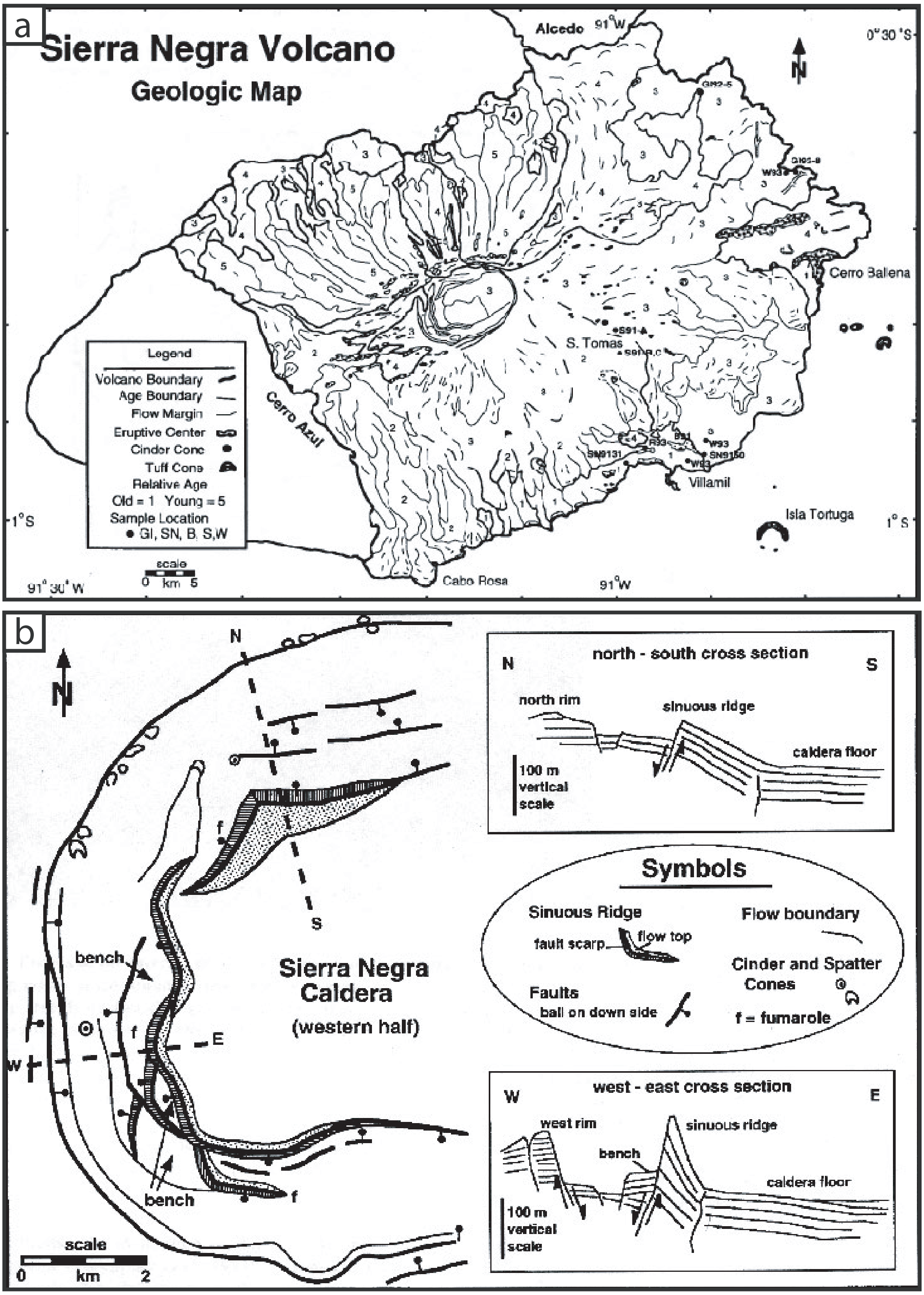

Figure 2.20:
a) Geologic map of Sierra Negra volcano on Isabela Island in the Galapogos Archipelago. Map shows outlines and relative ages of the main lava flows, ENE-trending rift related eruptive centres, cinder cones and tuff cones, and the summit caldera. From Reynolds et al. (1995).

b) Structural map of the western part of Sierra Negra's summit caldera. Faults are indicated by heavy lines with a ball on the downthrown side. These faults define a structurally-complex graben system in the peripheral caldera floor. The inner boundary of the graben system is marked by a prominent 'sinuous' ridge defined by a number of faceted normal faults. Cross-sections are schematic - note the great vertical exaggeration. From Reynolds et al. (1995).

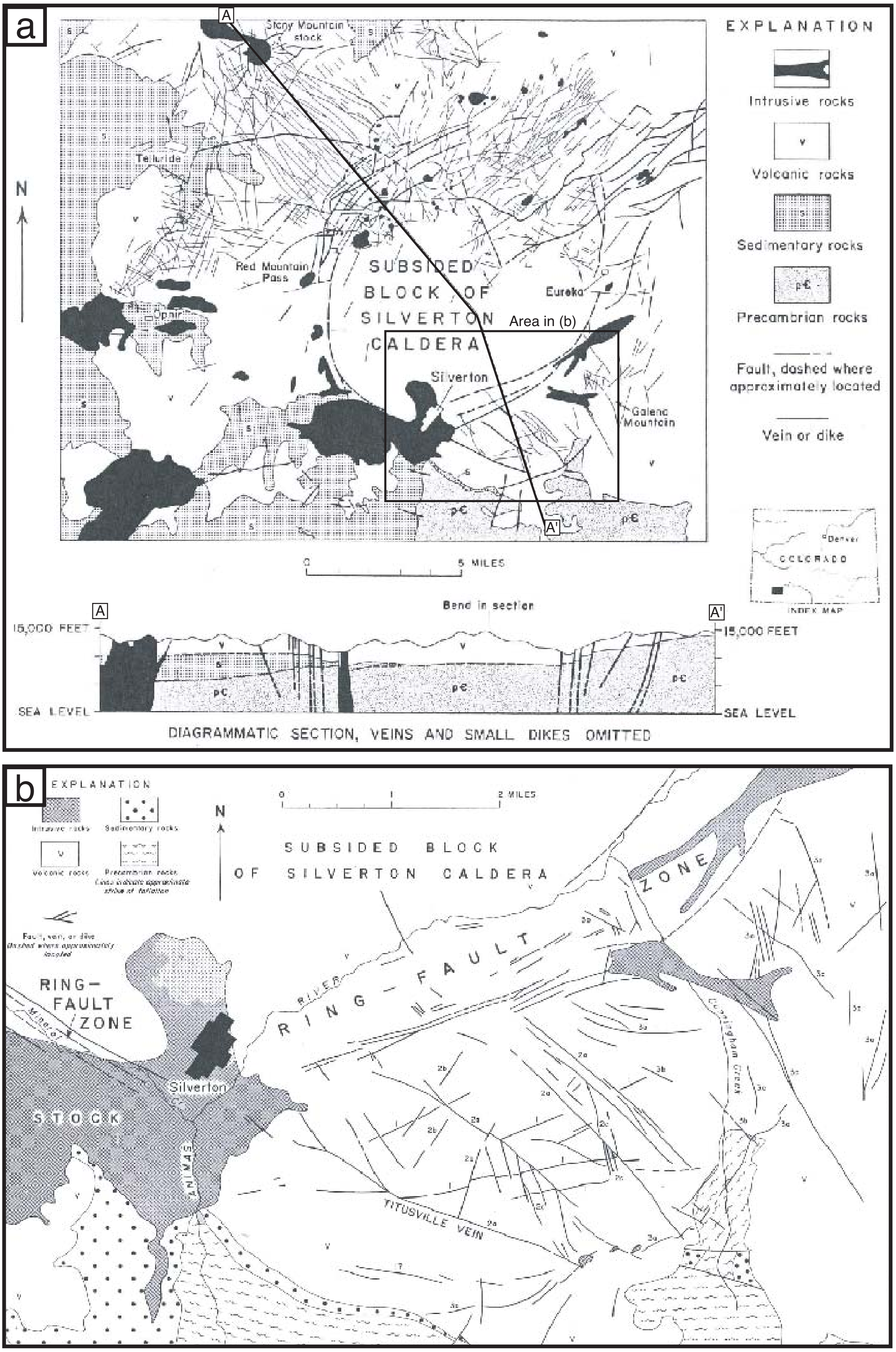

Figure 2.21:
a) Generalised geologic map of Silverton caldera, from Varnes (1963).
b) Map of principal fracture systems of the South Silverton mining area, from Varnes (1963). Fracture sets are by Varnes (1963) considered as three main groups (1) Concentric system, (2) Western shear system and (3) Eastern shear system. The fractures are predominantly oblique-normal faults, veins and dykes. Note the strong parellelism, similar to that in the experiments, between ring fault segments and the fracture sets.

3 The Caldera Collapse Continuum: Insights from recent Field, Experimental, and Numerical Evidence

3.1 Introduction

A first step toward a systematic understanding caldera structure has been to define various caldera types with distinct geometric, developmental, and eruptive characteristics - see reviews by Williams (1941); Smith and Bailey (1968); Walker (1984); Lipman (1984, 1997, 2000); Kennedy and Stix (2003); Cole et al. (2005). Over the course of several subsidence-focussed reviews, five idealised end-member styles of caldera collapse, each with characteristic structural elements and/or subsidence mechanisms (**Figure 3.1),** were outlined from the then available field and geophysical data and (Walker 1988; Lipman 1997, 2000) . Previous authors (e.g. Walker 1984; Branney 1995; Kennedy and Stix 2003; Lipman 1997, 2000; Cole et al. 2005) have noted from the outset that natural calderas rarely, if ever, unequivocally conform to one end-member collapse style, however, and stressed that natural calderas most often include structural elements of several collapse end-members. A continuum between the end-member caldera subsidence styles was thus inferred (Lipman, 1997). The occurrence and relative importance of each end-member has since been intensely debated (e.g. Branney 1995 vs. Lipman 1997), however. In addition, the continuum's exact nature, i.e. how end-member collapse styles interrelate and what controls this inter-relationship, has remained vaguely defined.

This chapter aims to illustrate how the idealised collapse end-members may interrelate and hence to shed light on the nature of the caldera collapse continuum. It is readily acknowledged that many ideas underpinning this re-evaluation of the continuum concept are adopted or modified from earlier work (notably Branney and Gilbert 1995; Branney 1995, Lipman 1997, Roche et al. 2000, and Kennedy et al. 2004). The focus here is on the occurrence within the collapse process of structural elements characteristic of each end-member, and on what parameters regulate the expression of these elements. To this end, results of the systematic experimental collapse studies, in which the effects of different parameters can be constrained, are here synthesised and integrated with representative data from this work (**Chapter 2**). The experimental evidence is then examined in light of existing and more recent field observations, as well as some recent numerical studies.

From this synthesis, it is argued (contra Acocella 2006) that the structural elements characteristic of all five idealised caldera collapse end-members can accumulate sequentially in gradational phases of a single collapse evolution (Branney 1995; Holohan et al. 2006). The continuum between all the end-member styles of caldera collapse can thus, for the most part, be viewed in terms of a progressive accumulation of their characteristic structural elements with increasing structural maturity. However, it is also explained here how analogue and numerical models can show that the relative importance of these structural elements is strongly controlled by ratios of magma chamber depth/diameter and caldera subsidence/diameter.

3.2 End-member styles of caldera subsidence: previous views of the continuum

In their idealised state, each end-member collapse style is associated with certain characteristic structural elements (**Figure 3.1**), and was tentatively related to a distinct geometry of the pre-collapse magma reservoir roof and/or a particular eruptive history.

1) Piston (or Plate) end-member collapse style produces a caldera with a well-defined, large-displacement ring-fault that encloses a coherently-subsided caldera floor (Lipman 1997) (caldera floor = subsided pre-collapse Earth's surface). The ring-fault's dip and slip has been much debated; it may be: a) inward-dipping and normal, b) outward-dipping and reverse, or c) vertical (cf. Kennedy and Stix 2003). Ideally, the caldera floor should be non-sagged, and any marginal deformation related to central subsidence should occur as large landslides that form megabreccia deposits. Piston collapse has been suggested to reflect a single voluminous eruption from a large-diameter, but shallow magma chamber (i.e. low thickness/diameter ratio of the magma chamber roof) (Lipman 1997).

2) Piecemeal end-member collapse style produces a caldera defined by an irregular or fragmented caldera floor that comprises multiple, differentially-subsided fault blocks (Walker 1984; Branney and Kokelaar, 1994, Branney 1995). Such differential subsidence is characterised by syn-collapse growth faulting (Branney and Kokelaar, 1994; Lipman 1997), and may relate to reactivation of pre-collapse regional-tectonic faults during subsidence (Moore and Kokelaar 1998) and/or pre-collapse volcano-tectonic doming (Marti et al. 1994; Troll et al. 2002), or by generation of several new volcano-tectonic faults (Branney and Kokelaar 1994). Piecemeal subsidence style has also been attributed to a multi-cyclic eruptive and subsidence history (Lipman 1997; Troll et al. 2002).

3) Trapdoor end-member collapse style produces a coherent, but asymmetrically-subsided caldera floor, which is delimited by a laterally-incomplete, arcuate ('horseshoe-shaped') fault on the side of most subsidence and a flexured hinge-zone in the area of least subsidence (Walker 1984). Trapdoor collapse has been suggested to relate to: a) a combination of early sagging and incipient piston collapse generated by small-sized eruptions (Lipman 1997), b) regional tectonic influences (Lipman 1997; Ramelow et al. 2006), and/or c) an initially asymmetric magma chamber roof (Lipman 1997; Kennedy et al. 2004) (**Figure 3.1**) .

4) Downsag end-member collapse style produces coherently-subsided floor strata that dip gently and radially toward the caldera centre (i.e. centroclinally - **Figure 3.1**). This down-flexured floor lacks large-displacement ring-faults (Walker 1984). Downsag collapse has been ascribed to down-flexure prior to localisation of a major ring fault, and suggested to be characteristic of small eruptions and/or a deep magma chamber (i.e. high thickness/diameter ratio of the magma chamber roof) (Walker 1984; Lipman 1997).

5) Funnel end-member collapse style produces a caldera with a 'funnel' morphology, with a highly brecciated, incoherent to chaotic floor, and without clear ring-faults (Aramaki 1984). Calderas thought to have formed by end-member funnel collapse are supposedly of small (<5 km) diameter (Lipman 1997), are breccia-filled and are apparently chaotic in nature. These observations have led to suggestions that the funnel end-member's characteristic elements may result from explosive reaming and/or slumping of material into an areally restricted depression, perhaps formed above a relatively narrow and deep magma chamber (Lipman 1997) (**Figure 3.1**). In terms of process, 'funnel collapse' was thus envisaged to merge with the formation of large explosive vents and diatremes (Lipman 1997).

Lipman (1997) stressed that the most useful approach to further understanding the relationship between structural and eruptive processes and pre-collapse magma chamber geometry would be to interpret caldera structures in terms of a continuum between these subsidence styles, rather than attempting to sub-classify a caldera in terms of one end-member collapse type (e.g. Acocella 2006). How to exactly envisage that continuum remains unclear, however. On one hand, Lipman (1997) suggested that the continuum is essentially one of size, with small-diameter funnel-style collapses grading into larger-diameter piston-style collapses, and that the presence of elements of other collapse styles depending on other factors, such as the geometry of the magma reservoir roof and the eruptive history of the caldera. On the other hand, a sense of progression or gradation between subsidence styles within an individual collapse - from downsag to trapdoor to piston - has also been proposed (Lipman 1997; Acocella 2006), again with elements of other collapse styles depending on other factors outside of the basic collapse mechanism. Questions remain, however: Is one of these views more pertinent, or are both valid, and to what extent? How can these two views be reconciled? Can any revised view incorporate all five end-member collapse styles and their structural elements?

Recent physical and numerical models of collapse, allied to existing and recent field data, provide evidence that both such views of the caldera continuum are indeed pertinent, and moreover, are reconcilable. In addition, this reconciliation can encompass the structural elements of all five end-members of collapse style, even for a single collapse event.

3.3 Evidence from physical models (analogue experiments)

Of the many recent experimental studies of caldera formation, those by Komuro (1987); Marti et al. (1994); Acocella et al. (2000); Roche et al. (2000); Walter and Troll (2001); Troll et al. (2002); Kennedy et al. (2004); and Geyer et al. (2006) systematically examined the basic dynamics of the caldera cycle (Smith and Bailey 1968; Lipman 1984) - magma chamber inflation, deflation, and/or re-inflation ('resurgence') - within brittle crust. The main model parameters varied included: *the thickness/diameter of the magma chamber roof* (= depth to diameter ratio of the magma chamber), the *shape of the chamber top surface* (concave-upward vs. flat), the *3-D chamber geometry* (sphere, cylinder, ellipsoid, cuboid). Other studies by Lavallee et al. (2004); Belousov et al. (2005); Acocella et al. (2004); and Holohan et al. (2005 and in press) examined factors, such as pre-collapse topography, laterally sited pre-collapse stratovolcanoes, and pre-collapse regional tectonics.

Chapter 1 contains a summary of the scaling procedures and limitations of all these experiments, in which various analogues for the magma chamber (dry ice, silicone, air/water in a balloon) and the crust (clay, alumina powder, sand, flour, sand/flour mixtures) were used. Different scaling ratios (length, viscosity, stress, time, velocity) were also applied. All the experimental approaches scaled appropriately for brittle crustal deformation, and to varying degrees of accuracy for a ductile magma body. Firstly, a synthesis of the results is presented for the above studies for single collapse event of a uniformly loaded roof into a deflating (evacuating) magma chamber that is circular in plan view, has a flat top surface, and a low depth to diameter ratio (see representative experiments in **Figures 3.2 and 3.3)**. Then, their results are considered for higher magma chamber depth to diameter ratios (see representative experiments in **Figures 3.4 & 3.5**).

Regardless of materials, scaling, boundary conditions, and other geometric parameters, the subsidence evolution of past experiments is in general similar to these representative cases. Except where specified, the observations made below are thus common to all the studies cited above. Since past studies employed various length scales, however, this synthesis of their results and its later application to nature is necessarily qualitative rather than quantitative. As the boundary between the pre-caldera rocks and the caldera infill is geologically the most important structural level for identifying the characteristic elements of the collapse end-members (Walker 1984; Lipman 1984, 1997; Branney and Kokelaar 1994), focus is given to the deformation pattern of the pre-collapse model surface (i.e. the caldera floor).

3.3.1 Progressive subsidence

With increasing subsidence, collapse in the experiments evolves through four inter-gradational phases (subtly distinct from those of Geyer et al. 2006 and Acocella 2006):

Phase 1 is characterised by sagging of the chamber roof and caldera floor (**Figure 3.2a, 3.3a**). The surface and upper structural levels comprise a gently inward-dipping flexure with marginal tension fractures (fissures). At the lowermost structural levels, a ring-fault with outward-dip and reverse motion eventually propagates upwards from the magma chamber.

Phase 2 is reached when the scarp of an outward-dipping arcuate fault or ring fault with reverse slip cuts the sagged surface to signal complete magma chamber roof failure. This scarp defines a coherent and fault-bound central zone that lies inside a flexured peripheral zone (**Figures 3.2b, 3.3b**). Such outward-dipping reverse faults form as a response to the arching of principal stress trajectories within a reservoir roof (Roche et al. 2000). Upon asymmetric collapse (common), the reverse fault cuts the area of greatest floor subsidence and occurs opposite a flexural hinge (**Figure 3.3b**). In this case, the reverse fault is initially arcuate (horseshoe-shaped), but with a little more subsidence, the fault may become a complete ring and asymmetry may decrease (Roche et al. 2000).

Phase 3 is reached when the scarp of a major inward-dipping fault with normal slip cuts the edge of the flexured peripheral zone and forms an outer topographic rim (**Figures 3.2c, 3.3c**). Roughly concentric development of a reverse-fault-bound central zone and a normal fault bound peripheral zone thus results. With yet more central subsidence, the flexured peripheral zone undergoes further inward rotation and extension, to form numerous fissures, and complexly-faulted horst and graben systems (Marti et al. 1994; Branney 1995; Roche et al. 2000; Walter and Troll 2001; Kennedy et al. 2004); (**Figures 3.2c, 3.3c**). On asymmetric collapse, the reverse and normal ring-fault systems may be complete rings or not. If incomplete, the normal and reverse fault systems develop best at the most subsided part, opposite a flexured or normal faulted hinge zone in the least subsided part. Changes in collapse symmetry, usually from asymmetric to symmetric (**Figure 3.3d;** Roche et al. 2000), but sometimes vice versa (Holohan et al. in press), may occur at any stage.

In Phase 4, subsidence proceeds mainly on the existing ring structures (**Figures 3.2d, 3.3d)**. Over-steepened ring fault scarps eventually fail, and material moves into the caldera interior as lumps and grain flows (cf. Branney 1995; Roche et al. 2000; Walter and Troll 2001; Kennedy et al. 2004; Belousov et al. 2005). The two main source areas for this material (**Figures 3.3d, 3.2d)** are: 1) the footwall scarp of the outer normal ring-fault, and 2) the hanging wall scarp of the inner reverse fault (i.e. the innermost part of the peripheral zone). Decay of the outer normal ring fault scarp results in lateral morphological enlargement through creation of topographic embayments (‘scalloping’; see Branney and Gilbert 1995) (**Figure 3.3d**).

3.3.2 The role of increasing magma chamber depth/diameter ratio

Several important variations upon this scheme are seen at higher magma chamber depth/diameter ratios. Firstly, flexure of the floor at Phase 1 is initially less pronounced and is more constrained to above the chamber centre (Acocella 2000) – **Figure 3.4a**. Secondly, multiple reverse faults form in Phases 3 and 4 (**Figures 3.4c,d**) (Roche et al. 2000; Walter and Troll 2001; Kennedy et al. 2004). These reverse faults sequentially cut the floor surface outward from the caldera centre and so break up the central zone floor and the peripheral zone into differentially subsided sections. Such generation of multiple reverse faults related to the increased effects of stress arching in the thicker roof (cf. Roche et al. 2000), and seems to be enhanced by a convex-up (arch-like) chamber top surface (Roche et al. 2000; Walter and Troll 2001; Kennedy et al. 2004). Thirdly, with magma chamber roof of very high thickness/diameter ratios (i.e. very deep and/or narrow chambers), these reverse faults may, at the deepest levels, form as hybrid reverse-normal faults and enclose a series of 'stoped' blocks. These blocks that form in an upward-migrating sequence, before one reverse fault eventually cuts the surface to cause complete roof failure (**Figure 3.5**) (Roche et al. 2000; Geyer et al. 2006). Fourthly, whilst the area of the peripheral zone generally tends to increase relative to the area of the central zone (Branney 1995; Roche et al. 2000; Acocella et al. 2001; Walter and Troll 2001), the prominence of (i.e. the displacements on) peripheral extensional faults and gräben diminishes (**Figures 3.2d vs. 3.4d**).

3.4 Evidence from Field Studies

Structural elements that accumulate through each experimental phase all occur in nature, and many are found in concert at individual well-studied calderas (Branney 1995; Lipman 1997; Kennedy and Stix 2003; Cole et al. 2005). These elements include: a) caldera floors that are sagged, coherent, variously incoherent, and symmetrically to asymmetrically subsided; b) major arcuate faults or ring-fault systems that are outward-dipping and reverse or are inward-dipping and normal; c) multiple subsidiary ring-faults, or arcuate faults, that are reverse or normal; d) complex peripheral zones of fissures, normal faults, and horst and gräben; and e) slumped (mega-)blocks and mass movement deposits from over-steepened and decayed fault scarps, as well as corresponding topographic embayments.

For instance, the carbonatitic Gross Brukkaros depression, Namibia (Stachel 1994) displays sagged a floor and infill (Phase 1 - **Figure 3.6a**). Ignimbrite- and breccia-filled fissures that are several hundred metres deep, and demonstrably related to inward rotation of basal strata, are found at Glencoe caldera, Scotland (Moore and Kokelaar 1998). Although the caldera floor is not visible, young calderas with inward-inclined syn-collapse strata and extensional fissures that occur marginal to an inferred principal inner ring-fault (Phases 1-2) include Bolsena, Italy (Walker 1984), and Rotorua, New Zealand (Milner et al. 2002). Reports of ring-faults with outward-dip and reverse motion (Phase 2) are rare, possibly due to the scarcity of exposed vertical sections through caldera floors, but occur at Rabaul caldera, Papua New Guinea (Mori and McKee 1987, Nairn et al. 1995) (**Figure 3.6b**); Glencoe caldera, Scotland (Kokelaar and Moore 2006); and possibly Gross Brukkaros (**Figure 3.6a)**. Ancient calderas with demonstrably sagged floors later enclosed by vertical to inward-dipping ring-faults (Phases 1-3) include Sabaloka, Sudan (Almond 1977); Grizzly Peak, Colorado (Fridrich et al. 1991); and Scafell, England (Branney and Kokelaar 1994, – **Figure 3.6c**). Arcuate faults or ring-faults with inward-dip and normal displacement (Phase 3) are commonly reported, such as at Lake City, Colorado (Lipman 1984); Ishizuchi, Japan (Yoshida 1984); and Bolsena, Italy (Nappi et al. 1991).

Peripheral horst and graben systems of several kilometres width and with syn-collapse differential block faulting (late Phase 3) occur at the calderas of Scafell, England (Branney and Kokelaar 1994) (**Figure 3.6c**); Sabaloka, Sudan (Almond 1977); and Tejeda, Gran Canaria (Troll et al. 2002). Landslide megabreccias derived from oversteepened caldera faults (Phase 4) are commonly found near the caldera margins inside a bounding normal ring-fault, for instance at Lake City caldera, Colorado (Lipman 1976) (**Figure 3.6d** - note also the topographic embayments outside the normal ring fault), Grizzly Peak caldera (Fridrich et al. 1991), and Scafell caldera (Branney and Kokelaar 1994). Onset of extensive land sliding and mesobreccia/megabreccia formation at Scafell and Glencoe calderas occurred late in the subsidence evolution of these calderas (Branney and Kokelaar 1994; Moore and Kokelaar 1998). Asymmetric subsidence is common, for instance at Organ caldera, New Mexico (Seager in Lipman 1984), Snowdon caldera, Wales (Howells et al. 1986) as well as Grizzly Peak, Rotorua, and Bolsena calderas. Syn-collapse symmetry changes (e.g**. Figures 3.3c-d**) occurred during the evolution of Timber Mountain caldera, Nevada (Carr and Quinlivan in Lipman 1984). The giant Martian calderas (Mouginis-Mark & Robinson 1992; Crumpler et al. 1996) also display many of these structural elements (**Figure 3.7**), which, although formed under lower gravitation, show a close geometric correspondence to those seen in experiment (cf. Branney 1995).

Understanding the static and frequently fragmental exposures at such natural calderas depends on correct identification and interpretation of such structural elements and their inter-relationships. The experiments' principle value is to contextualise the genesis, evolution, and interrelation of these different structural elements, and hence to show how they define the structure, subsidence style(s), and overall geometry of calderas seen in nature.

The only eye-witnessed natural collapse evolution, at Miyakejima caldera in Japan (Geshi et al. 2002), is also especially instructive here (**Figure 3.8**). Shortly after onset of subsidence, an inner ring structure formed around a central coherent block (Phase 1-2), outside which formed a concentric normal fault and a complexly fissured and normal-faulted peripheral zone **(Figure 3.8b)**. As seen in experiment (cf. **Figures 3.2, 3.3, 3.4**), the peripheral zone rotated inward and extended across the vertically subsiding central zone (Phase 3), a motion that implies an outward-dipping reverse fault between central and peripheral zones (Geshi et al. 2002). With progressive subsidence, increasingly prolific mass movement from the peripheral zone and especially the outer normal fault scarp (Phase 4) buried the whole caldera floor and all the ring structures under voluminous chaotic debris. This landsliding also caused substantial lateral enlargement of Miyakejima caldera (Geshi et al. 2002) via rapid retreat of the outer normal fault scarp, and so imparted a pronounced 'funnel' or 'flared' morphology to the final depression (**Figure 3.8c**).

3.5 *Evidence from analytical studies and numerical models*

Comparable numerical simulations of caldera collapse, i.e. those replicating subsidence via an 'underpressured' reservoir have mostly used the Finite Element or Boundary Element methods (e.g. Zuber and Mouginis Mark 1992; Gudmundsson 1998; Folch and Marti 2004; Pinel and Jaupart 2005). Unlike analogue models, such numerical models cannot reproduce fracturing as they assume fully recoverable elastic strain. Instead, they resolve stress orientations and magnitudes, from which initial fracture locations and orientations may be inferred. Their results are nonetheless complementary to, and broadly agree with, many aspects of the above physical modelling.

A representative model is shown in **Figure 3.9**, which shows deflation of an oblate sill-like magma chamber at depth-diameter ratios comparable to those in the representative analogue models (**Figures 3.2, 3.3, & 3.4**). Deflation of the thin-roofed magma chamber produces pronounced surface sag, a wide near-surface zone of high tensile stress above and extending outward beyond the magma chamber margins, and high differential stresses in the roof (**Figure 3.9a**). In contrast, the same deflation (same under-pressure value) of the thick-roofed magma chamber produces more limited surface sag, weaker near-surface tensile stresses, and lower differential stresses in the roof (**Figure 3.9b**).

According to elastic theory, stress arching (also termed 'membrane stress') in a vertically loaded elastic plate results if plate thickness/diameter ratio is sufficiently high (~ > 1/8 - cf. Timoshenko and Weinowsky-Krieger 1959; Young and Budynas 2002). The influence of stress arching increases with increased plate thickness (Jones et al. 1990), which for calderas equates to increased thickness/diameter ratio of the magma chamber roof. The effect of stress arching is twofold. Firstly, the plate (or roof) is strengthened and made more rigid (cf. Jones et al. 1990). Secondly the orientation of the maximum principle stress assumes the shape of an arch above the magma chamber (cf. Roche et al. 2000 and refs therein), which promotes ultimate through-going failure along outward-dipping reverse faults.

Postulated roof failure only along tensile fractures and/or an inward-dipping normal ring fault (e.g. Gudmundsson 1998 - **Figure 3.9a inset**) is also possible, but is consistent with theoretical and observed failure modes of <u>very</u> thin plates only (thickness/diameter ratios of ~ < 1/8 - Young and Budynas 2002), where stress arching is negligible. In both the 'thin-roofed' and 'thick-roofed' models of **Figure 3.9**, for instance, the zone of high pre-failure differential stresses, i.e. where faulting is most likely to occur, is arched. This is consistent with arching of the maximum principal stress trajectories and hence initial failure in both cases along outward-dipping reverse faults (**Figure 3.9a inset** - see also Patton and Fletcher 1995). The lower values of differential stresses in the thicker roof in **Figure 3.9b** for the same value of under-pressure are also compatible with the initial strengthening of the thicker roof via arching. A greater under-pressure (~ volume percentage of magma extracted from the reservoir) is thus required to generate the differential stress necessary to cause failure of a thicker magma chamber roof. This agrees with analytical calculations of Roche and Druitt (2001) and experimental observations of Geyer et al. (2006).

Rare numerical studies that can reproduce fractures and have simulated under-pressure (e.g. Burov and Guilliou-Frottier 1999), produce very similar fracture patterns to analogue models – i.e. an inner ring fault that is vertical to outward-dipping and reverse plus an outer normal ring fault. These also predict an inhibition of ring fracture formation, again compatible with the increased effects of stress arching, at higher thickness/diameter ratios of the magma chamber roof.

3.6 A new view of the continuum of end-member caldera collapse styles

From the sequential accumulation of their characteristic structural elements during a single collapse event in experiment and nature, the inter-relationship between all the idealised end-member caldera subsidence styles can be primarily viewed as one of evolving structural maturity (Figure 3.10). As noted in experiment and numerical studies, however, the relative predominance of these elements within any collapse is also regulated by chamber depth/width aspect ratio (Figure 3.11) and caldera subsidence/diameter ratio. **Elements of the Downsag end-member** - sagged pre-collapse strata and marginal tensional fissures - predominate in Phase 1 **(Figure 3.10)**. Though such elements are common to many calderas in nature, pure 'end-member' downsag calderas have not been convincingly documented (cf. Lipman 1997; Cole et al. 2005). As observed in experiment, most natural subsidences will probably therefore quickly pass through this initial phase of flexure (Milner et al. 2002). However, it is worth noting that inward rotation and bending of the caldera floor in association with, and locally controlled by, faulting may continue to occur throughout later stages of the subsidence evolution (e.g. Branney 1995; Acocella 2006 – see **Figure 3.3**).

Collapse accommodated by sagging is greater with low thickness/diameter ratios of the chamber roof (**Figure 3.11**). This relationship is supported by experimental (Kennedy et al. 2004; Geyer et al. 2006; and this study) and numerical simulations of subsidence (e.g. Jones et al. 1990, Folch and Marti 2004) and is a consequence of decreased influence of stress arching, which reduces the roof's effective rigidity (cf. Jones et al. 1990).

Elements of the Trapdoor end-member - asymmetrically subsided floor and flexured hinge zone - can appear at the onset of Phase 2 **(Figure 3.10)** as a transitional step between sagging and complete lateral propagation of a ring-fault (Lipman 1997; Roche et al. 2000). If subsidence remains asymmetric after ring-fault completion (e.g. at Grizzly Peak caldera- Fridrich et al. 1991), however, then this Trapdoor element will be retained throughout subsequent evolutionary phases. Then again, changes in subsidence symmetry (e.g. as in **Figure 3.2d** and as inferred at Timber Mountain caldera (Lipman 1984)), can also cause Trapdoor elements to be lost and/or gained in subsequent phases. Such symmetry changes may relate to lateral variations in roof loading/support as ring-faults propagate laterally (Roche et al. 2000), or as the subsiding roof meets the chamber floor and 'bottoms-out' (e.g. **Figure 3.3d**).

Asymmetric collapse also seems more pronounced at low roof thickness/diameter ratios (**Figure 3.11),** i.e. with thin reservoir roofs, (cf. Kennedy et al. 2004), possibly because a thinner roof is laterally less tightly constrained by its surrounds and so can tilt more as it subsides.

Elements of the Piston end-member – steeply dipping, large-displacement ring faults and a largely coherently subsided floor – usually appear in Phases 2 and 3 **(Figure 3.10)**. An outward-dipping reverse ring-fault enclosing a relatively coherent and often symmetrically-subsided subsided central floor zone appears in Phase 2. An inward-dipping normal ring-fault then develops early in Phase 3 within the peripheral zone. Inheriting elements from Phase 1, subsidence style is now a fusion of idealised Downsag and Piston (and possibly Trapdoor) end-members.

Major ring faults and a relatively coherently subsided central zone occur regardless of thickness/diameter ratio (**Figure 3.11**). Nonetheless, relative to other elements, a coherently subsided central floor zone is overall more prominent at low thickness/diameter ratios (Roche et al. 2000, Kennedy et al. 2004, this study).

Elements of the Piecemeal end-member - non-coherent subsidence of the magma chamber roof and/or an irregular, differentially-subsided caldera floor of multiple fault blocks - may develop late in Phases 2 and 3 **(Figure 3.10)**. In the simplified collapse scenarios modelled, two mechanisms may cause such piecemeal behaviour. Firstly, the increased influence of stress arching within a relatively thick roof (Roche et al. 2000), perhaps further enhanced by a curved magma chamber top-surface, can cause localisation of multiple reverse ring faults. These reverse faults break up both the magma chamber roof and, if cutting the surface, the caldera floor into separate differentially-subsided fault blocks (Roche et al. 2000; Kennedy et al. 2004). Secondly, radially-directed peripheral extension can localise as complexly-intersecting extensional fault systems that dissect the peripheral zone of the caldera floor (**Figures 3.2c, 3.3c, 3.4c, 3.6c, 3.7, 3.8**). Unlike the reverse faults, these peripheral fissures and normal faults do not penetrate through the roof as a whole, but only affect the floor and uppermost levels of the roof. With elements inherited from Phases 1, 2 and 3, collapse style is thus a fusion of Downsag, Piston, and Piecemeal end-members **(Figure 3.10)**. Again any asymmetry to subsidence will add transient or persistent elements of the Trapdoor end-member.

Overall, the predominance of Piecemeal elements increases as the thickness/diameter ratio of the magma chamber roof increases (**Figure 3.11**), although the relationship is not straight-forward. On one hand, the complex extensional faulting within the peripheral zone in experiment seems better developed with lower to intermediate roof thickness/diameter ratios (cf. **Figures 3.2, 3.4 & 3.5**). This may relate to greater marginal bending and tension associated with more pronounced sagging at lower thickness/diameter ratios (Folch and Martt 2004 – **Figure 3.9)**. On the other hand, the peripheral zone's width in experiment falls into a relatively constrained range (Roche et al. 2000; Troll and Walter 2001) that is possibly defined by the angle of draw from above the reservoir edge (cf. Branney 1995, Roche et al. 2000). The width, and hence area, of the more-coherent central zone in experiment can greatly exceed that of the peripheral zone at low thickness/diameter ratios (Roche et al. 2000). As thickness/diameter ratio increases, however, the area of central zone decreases relative to that of the peripheral zone (Roche et al. 2000; Troll and Walter 2001). In addition, increased depth/diameter ratio causes the caldera floor and magma chamber roof to be increasingly broken up by multiple reverse faults.

Elements of the Funnel end-member - *apparently* chaotic floor, *apparent* absence of ring-faults, and flared funnel-like morphology - form in Phase 4 **(Figure 3.10)**. Continued subsidence after Phase 3 in experiments mainly results in decay of over-steepened ring-fault scarps and the peripheral zone (Roche et al. 2000; Kennedy et al. 2004 - **Figures 3.2d, 3.4d**). If subsidence is taken to an extreme, inward-slumped material completely buries the structural elements (ring faults, etc.) inherited from Phases 1-3, and a funnel-shaped hole infilled with 'chaotic' debris results. This is exactly what occurred at Miyakejima caldera (**Figure 3.8)**, which subsided ~ 2.1 km relative to its diameter of just over 1 km (Geshi et al. 2002). Whilst generating a 'false-floor' of chaotic debris, landsliding also creates a distinct topographic margin outside the commonly obscured structural margin (outer normal ring fault), either through uniform scarp retreat or through creation of pronounced topographic embayments (**Figures 3.3d, 3.4b & c** – see also the 'collapse collar' of Lipman (1997)). This landslide-related topographic margin imparts or enhances the overall 'flared' funnel-like shape to the caldera. With elements inherited from Phases 1, 2 and 3, the resultant collapse style will thus be a fusion of Downsag, Piston, and Piecemeal and Funnel collapse end-members.

The prominence of a flared topographic margin and landslide-related debris burying the caldera floor increases as subsidence/diameter ratio increases (**Figure 3.11**) - either through increasing subsidence for a given diameter (e.g. Miyakejima – **Figure 3.8**) or by a decreased diameter for a given subsidence (see analysis of Lipman (1997). At large diameter (>10 km) calderas, collapse debris from over-steepened outer walls and/or the peripheral zone will concentrate toward the caldera margin and diminish (wedge out) toward the caldera centre (Lipman 1997) – as seen from megabreccia distributions, e.g. San Juan calderas, Colorado (cf. Lipman 1976, 1984; Hon 1987; **Figure 3.6d**). In contrast, and for the same subsidence, smaller diameter calderas are more likely to evolve to the completely and deeply debris-covered floors characteristic of what might *appear* to be a true Funnel end-member collapse (e.g. Miyakejima - Geshi et al. 2002, **Figure 3.8**).

3.7 Discussion and Comparison of Old and New Views

The experimental and field evidence shows that the structural processes and elements characteristic of the five 'end-member' caldera subsidence styles can accumulate progressively over a single subsidence evolution. Although other sequences may be possible, elements of the Downsag, Trapdoor, Piston, Piecemeal, and Funnel end-members can accumulate in that order during a single collapse event (**Figure 3.10**). From this perspective, the idealised end-member collapse styles and their characteristic structural elements do not so much reflect individual or localised particularities of pre-collapse magma chamber roof geometry, regional tectonic structure, or eruptive history (see **Section 3.2**). Instead, the structural elements characteristic of the collapse end-members primarily relate to systematically-evolved and kinematically-linked structural sub-processes that occur within a fundamentally very similar developmental scheme of crustal subsidence.

As outlined above, however, the extent to which these elements develop depends on 'priming' factors such as thickness/diameter ratio of the magma chamber roof and 'developmental' factors such as caldera subsidence/diameter ratio. The evidence also shows that elements of Trapdoor and Piecemeal end-members (as denoted here) may be ephemeral in any collapse evolution. In this sense, the continuum of caldera collapse styles may be considered to be somewhat similar to that invoked for mass movement (Summerfield 1991). For instance, a particular end-member mass movement style (creep, slide, fall, avalanche, flow) may predominate in an individual mass-movement event, depending on initial 'priming' factors, such as clay content and 'developmental' factors such as water uptake during run-out (cf. Vallance 2000). However, progressive gradational transitions or transformations between end-member mass movement styles may also occur as an individual mass movement event evolves – e.g. creep → slide → avalanche → flow (e.g. Mt St Helens 1980 – Voight et al. 1981).

In contrast to initial suggestions (Lipman 1997), experimental and numerical evidence shows that down-sag should be more prominent with thin, rather than thick, reservoir roofs, but supports the idea that down-sag and trapdoor collapse may represent precursory phases to the formation of elements of the piston end-member. Lipman's (1997) postulation that an initially asymmetric magma chamber roof could drive asymmetric collapse (**Figure 3.1**) has also been borne out experimentally (Lavallee et al. 2003; Kennedy et al. 2004), albeit with maximum subsidence where the roof is thickest. It is also worth noting here that experiments in this study (**see Chapter 4**), as well as some interpretations of field evidence (e.g. at Snowdon caldera Wales, Howells et al. 1986; Bonanza caldera, USA – Varga and Smith 1984), suggest a link between asymmetric subsidence and asymmetric withdrawal (via laterally sited eruptive vents). Asymmetric experimental collapse often occurs even with apparently symmetric magma chamber roofs (Roche et al. 2000, Kennedy et al. 2004), however, in which case it may be more prominent at low thickness/diameter ratios.

The suggestion that piston collapse reflects a single voluminous eruption from a large-diameter and shallow magma chamber (Lipman 1997) is compatible with the greater prominence of elements of the Piston end-member in experimental collapses with low roof thickness/diameter ratios. Due to rapid decay of their overhanging scarps, reverse ring-faults formed may commonly be obscured or misidentified as normal faults. As preservation potential of the outer normal ring-fault is higher than that of inner reverse ring-faults, many calderas in nature may thus *appear* to have subsided along a single inward dipping ring-fault only.

Although piecemeal subsidence is often envisaged as the wholesale and through-going differential break up of the magma chamber roof from reservoir top through to caldera floor (cf. **Figure 3.1**), this is very difficult to prove in the field. Establishing piecemeal subsidence in the field has thus far entailed demonstration of syn-eruptive volcano-tectonic offsets along faults in the caldera floor and overlying infill (Branney and Kokelaar 1994; Lipman 1997). It is usually difficult or impossible to determine if such offsets observed at that level characterise the reservoir roof as a whole, however. As seen in experiment, differential block faulting can occur near surface in the peripheral zone and/or at depth in the central zone, and it may or may not reflect through-going differential break up of the roof as a whole. The characteristic element of piecemeal (non-coherent – Roche et al. 2000) subsidence was thus here considered to be the break up of the *caldera floor and/or the magma chamber roof* into differentially-subsiding blocks.

Exposures of differential block faulting of the caldera floor at the ‘type’ locality for piecemeal collapse, Scafell caldera, are mostly located around the caldera periphery (Branney and Kokelaar 1994) (**Figure 3.6c – note line of section**), where they comprise complex horst and graben systems that are ascribed to radial extension (Branney 1995). The central 20% of Scafell caldera is unexposed (Branney 1995); it may have subsided coherently, or not. Similar complexly-faulted peripheral zones are described from many other calderas (see Branney 1995 for overview), where in many cases they comprise a series of stepped terraces rather than gräben (e.g. **Figure 3.7a**). Such complex peripheral floor zones may be several km to >10 km in radial extent - e.g. (**Figures 3.6 & 3.7**), although fault displacements within them are usually relatively small (a few 10’s to 100’s of m) compared to those seen on major ring-faults (100’s of m to > 2 km) (Branney and Kokelaar 1994; Lipman 1997; Geshi et al. 2002). These relationships are reflected in the experimental data (Marti et al. 1994; Roche et al. 2000; Walter and Troll 2001; Kennedy et al. 2004) (**Figure 3.2c**). At Miyakejima caldera, an upward-migrating pattern of micro-earthquakes recorded prior to surface appearance of caldera faults (Geshi et al. 2002) is compatible with the upward-migrating failure pattern characteristic of the generation of multiple reverse faults and differential break-up of the chamber roof at very high thickness/diameter ratios (Roche et al. 2000, 2001; Geshi et al. 2002) (**Figure 3.5b**).

Although not treated here, reactivation of pre-collapse faults (Marti et al. 1994; Moore and Kokelaar 1998; Troll et al. 2002) may also produce multiple differentially-subsided fault blocks - i.e. elements of the Piecemeal end-member. Pre-collapse faults reactivated during volcano-tectonic subsidence may have been originally related to doming of the magma chamber roof (Marti et al. 1994; Troll et al. 2002) and/or regional tectonism (Moore and Kokelaar 1998). Reactivation of such pre-collapse faults may thus induce a greater degree of piecemeal behaviour in nature.

Lipman (1997) suggested that a 'multicyclic' eruptive and subsidence history might account for piecemeal caldera subsidence. This implies temporally distinct eruption/subsidence events, however, between which important aspects such as magma chamber geometry and position could have changed. A history of several eruption/subsidence events will create superimposed or 'nested' collapses, which may accumulate in any combination of arrangements including: 1) concentrically overlapping collapses - e.g. Campi Flegrei caldera (Orsi et al. 1996); 2) non-concentrically overlapping collapses - e.g. Latera-Vepe calderas (Nappi et al. 1991); 3) partially overlapping and intersecting collapses - e.g. Olympus Mons (Mouginis-Mark and Robinson 1992 – **Figure 3.7**). Differential offsets of the caldera floor could thus represent reactivation or inversion of earlier-formed faults (e.g. at Scafell – Branney and Kokelaar 1994), or signify the boundary between two discrete collapse structures. It is thus fully acknowledged that this form of multi-collapse subsidence history may produce caldera floor complexities additional to those possible in a single collapse event.

In agreement with other studies (Lipman 1997; Branney 1995; Roche et al. 2000, 2001), experimental and natural evidence presented here shows that its structural/morphological elements characteristic of the funnel collapse end-member principally result from syn-collapse land-sliding, the deposits of which may be misinterpreted as chaotic 'floors'. By analogy with Miyakejima and experiments (**Figures 3.3, 3.4, & 3.8**), such deposits are primarily sourced from the scarp of the outer normal ring-fault in agreement with Lipman's (1997) 'collapse collar' concept. By further analogy with Miyakejima, however, these deposits may also result from decay of the inner reverse fault scarp(s) and, in some cases, from the destabilisation and wholesale inward collapse of the peripheral zone (cf. Geshi et al. 2002). As noted above, the characteristic elements of the funnel collapse end-member should, for the same subsidence values, be more pronounced at smaller diameter calderas than at larger diameter calderas (Lipman 1997; Roche et al. 2000). Although not an essential prerequisite, a deep reservoir <u>may</u> be associated with more pronounced elements of the funnel end-member (**Figure 3.1**), on the potentially often violated premise that small-diameter calderas and large-diameter calderas are respectively likely to have had relatively high and low thickness/diameter ratios of the magma chamber roof (Lipman 1997).

The view that all calderas are to some extent 'funnels' (Branney 1995; Lipman 1997) is supported, not just geometrically, but also in the sense that all calderas to some extent undergo the landsliding processes that lead to the elements characteristic of the funnel end-member collapse style. This is because calderas on all scales probably share very similar underlying collapse mechanics (Lipman 1997; Roche et al. 2000). Indeed, ice-melt pits (10s of m in diameter - Branney 1995), volcanic pit craters (10-100s of m in diameter (Rymer et al. 1998; Roche et al. 2001)) and depleted oil reservoirs (100s of m to several km in diameter (Odonne et al. 1999)) constitute intermediate scale analogues for caldera subsidence. They show extremely similar structural patterns and evolutions to those of the above experimental and natural calderas, which may indicate a gross scale-independence of subsidence mechanisms in the brittle upper crust.

3.8 Summary and Conclusions

From examining where, when, and to what extent their characteristic structural elements appear during a single caldera collapse evolution, a new picture of the theoretical continuum between all five idealised end-member styles of caldera collapse is provided (**Figure 3.11**). This revised continuum concept is supported by recent physical models, numerical simulations, and field observations of caldera collapse. These show that structural elements characteristic of the five 'end-member' subsidence styles in the literature can progressively accumulate over one collapse evolution, with elements of the Downsag, Trapdoor, Piston, Piecemeal, and Funnel end-members appearing and accumulating in that sequence. The combined experimental data further show that two parameters, the initial thickness/diameter ratio of the magma chamber roof and the final subsidence/diameter ratio of the caldera, play a key role in regulating the expression and relative predominance of each end-member's structural elements. At lower ratios, elements of downsag, trapdoor, and piston end-members are more clearly developed. At higher ratios, elements characteristic of the funnel end-member and, to some extent, the piecemeal end-member are more pronounced.

In nature, other factors particular to any one caldera collapse, such as strain rates, anisotropies in roof geometry, magma chamber geometry, thermal history, pre-collapse faulting, syn-collapse infilling, multicyclic eruption and collapse, etc., may cause some variation on this idealisation. The revised view of the continuum here should nonetheless serve as a generalised conceptual model that provides a first-order explanation of 1) the genesis of caldera structures, 2) the structural complexity seen at calderas, and 3) the likely architecture of calderas where hidden by syn- and post-collapse infill. This reappraisal of caldera collapse and its structural development may thus serve as a useful guide for future numerical, geodetic, and geophysical modelling of these enigmatic and highly complex volcanoes.

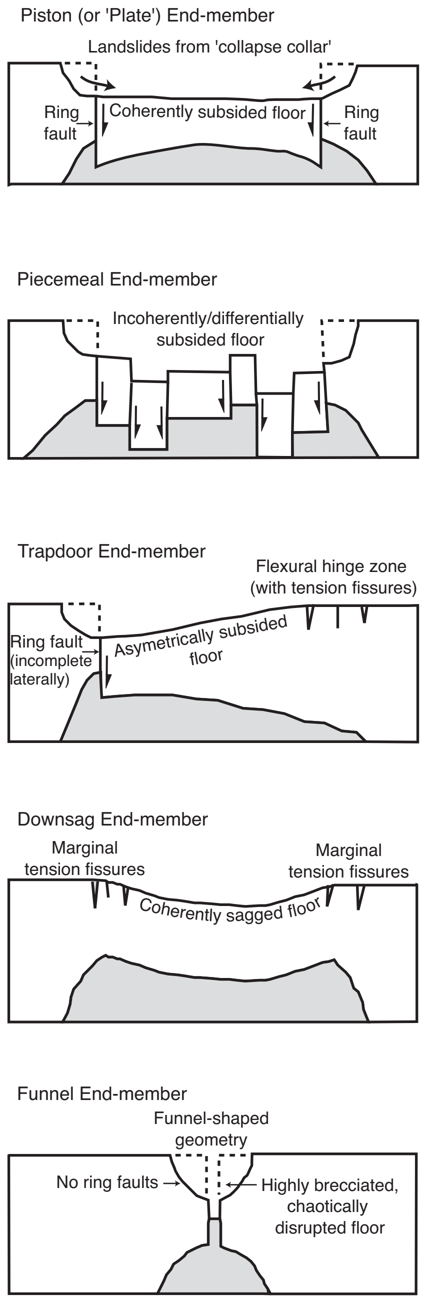

Figure 3.1: Highly idealised sketches that schematically portray the main structural elements of end-member caldera subsidence styles proposed in the literature from field, borehole, and geophysical data (Walker 1984, Lipman 1997). It is important to note that these sketches may not accurately represent the actual structural geometry of natural collapse calderas (Sketches adapted from Lipman 1997). See Section 3.2 for further explanation.

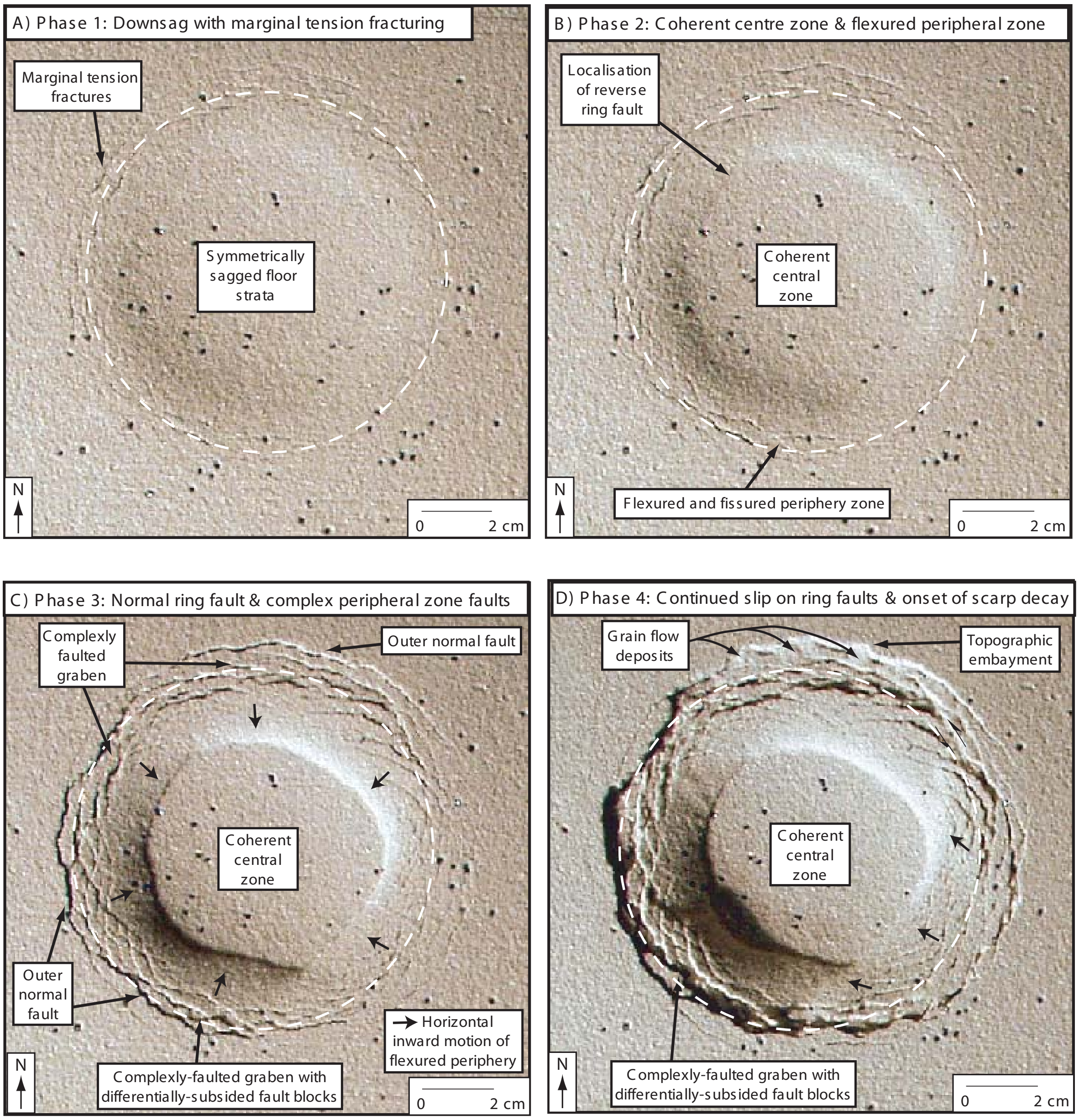

Figure 3.2: Plan view sequential development of a representative collapse model with a magma chamber roof of low thickness/diameter ratio. The 10 cm diameter cream honey chamber (outline is dashed white line) is sill-like and has 3.5 cm thick roof with a flat ceiling.

Experimental collapse generally evolve through four phases: **a)** Sagging of pre-collapse strata with formation of tensional fractures above the reservoir margins, **b)** failure of the chamber roof along an outward-dipping ring fault with reverse sense of motion, **c)** Formation of an inward-dipping ring fault with normal sense of motion, together with highly complex extensional faulting of the inward-rotating peripheral floor zone between the two main ring faults, **d)** Collapse of over-steepened fault scarps to produce grain flows and partially bury earlier formed structures.

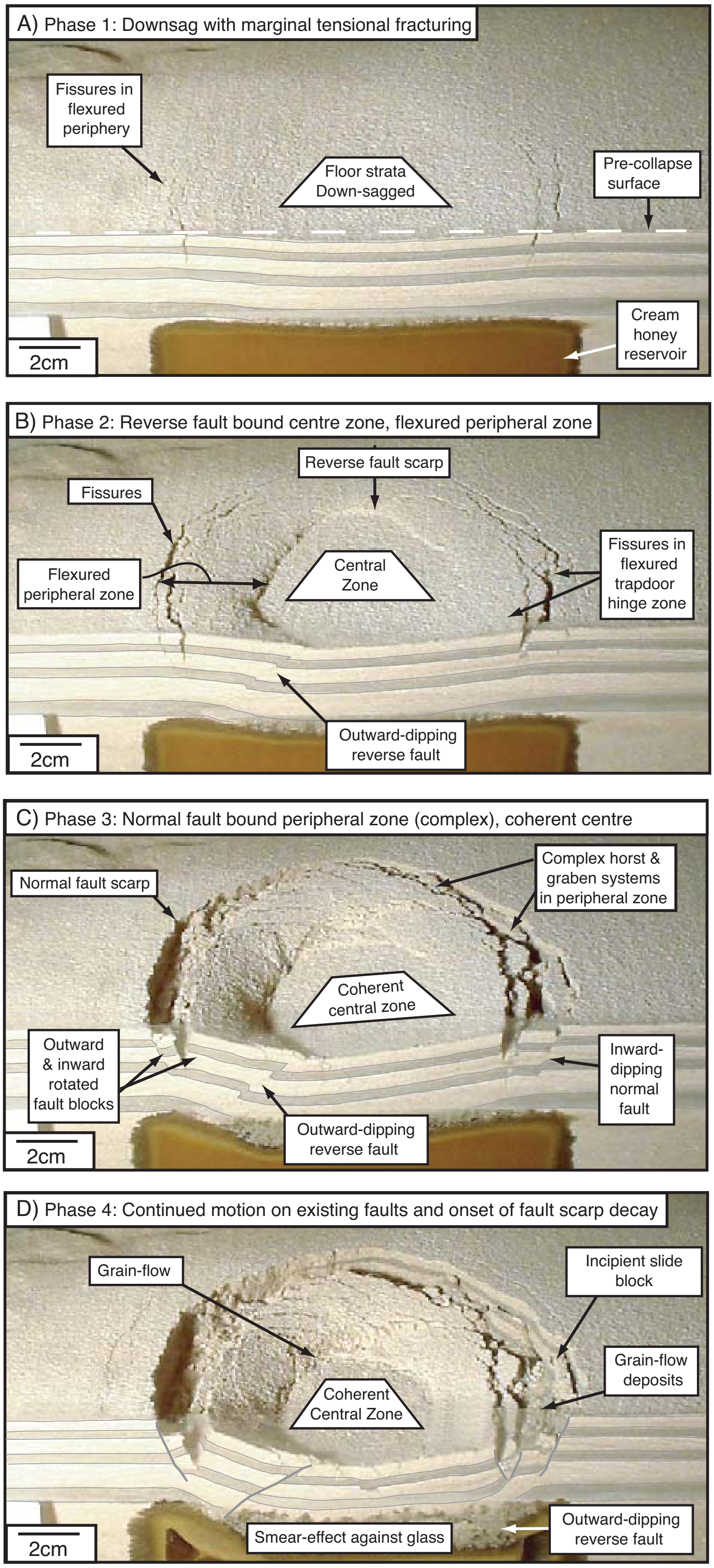

Figure 3.3: A 3D view of the structural evolution of a representative experimental collapse model with thickness/diameter ratio of the magma chamber roof as for **Figure 3.2**. The sand/gypsum cohesion is a little higher than ideal here (for illustration), and so marginal tensile fracturing is a slightly exaggerated. However, the geometry, kinematics, and complexity of structures are overall very similar to most past analogue studies (cf. Marti et al. 1994; Branney 1995; Roche et al. 2000; Walter and Troll 2001; Kennedy et al. 2004). Note also that in this example, the sense of subsidence asymmetry has reversed in later subsidence phases.

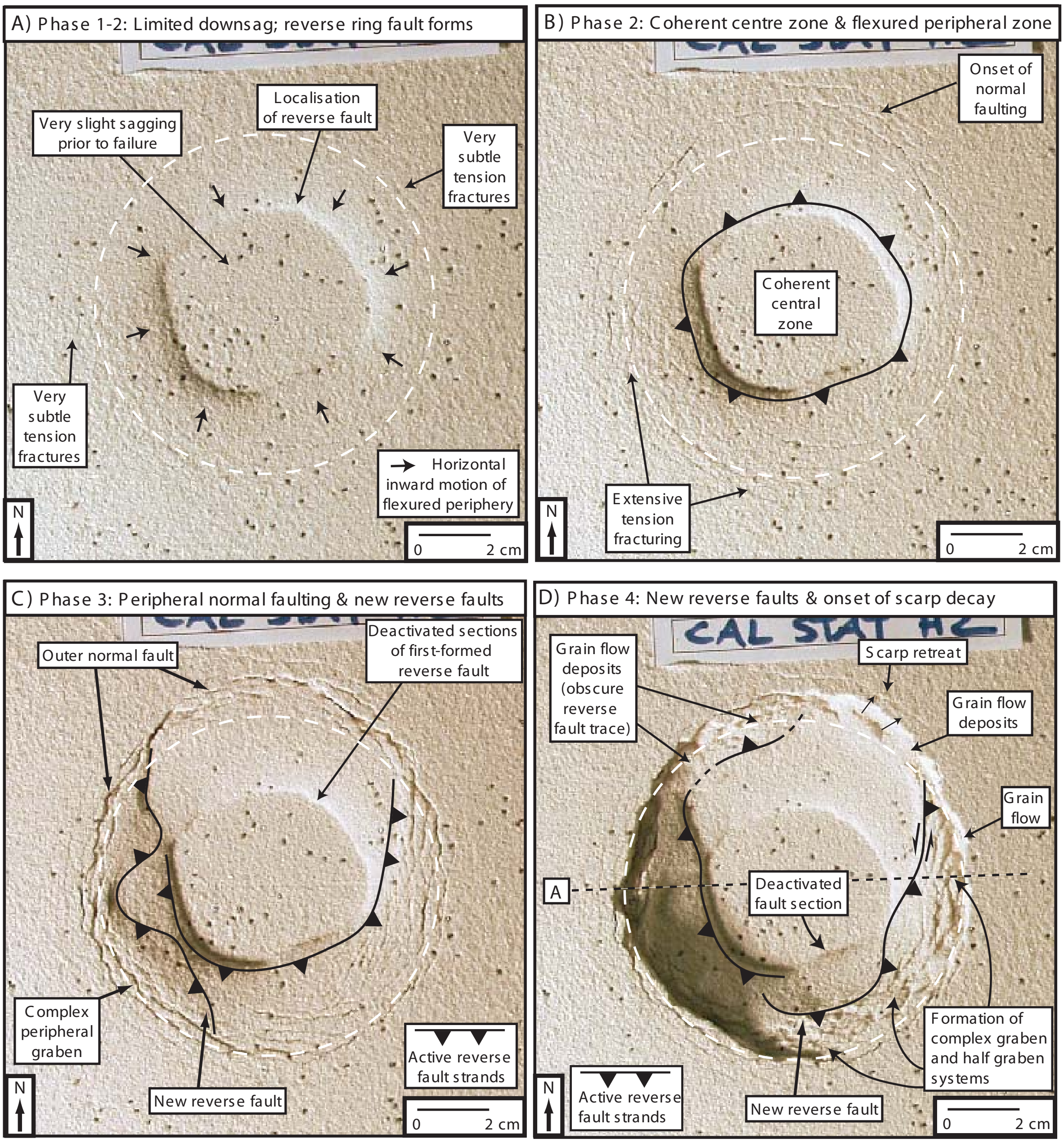

Figure 3.4: Plan view sequential development of a representative collapse model with magma chamber roof of high thickness/diameter ratio (dashed white line = outline of reservoir at depth). Experimental collapses generally evolve through the same four phases as low depth/diameter ratios, but with some important modifications:
a) The chamber roof again fails along an outward-dipping reverse fault, but central sagging and marginal tensional fracturing of the pre-collapse surface prior to failure is much more limited;
b) central zone subsidence induces extension and inward-tilting of the peripheral zone;
c) An inward-dipping ring fault with normal sense of motion forms, together with local onset of highly complex extensional faulting of the inward-rotating peripheral floor zone. However, new reverse faults form outward from the earlier reverse fault, which is partially deactivated.
d) Over-steepened fault scarps collapse to produce grain flows and partially bury earlier formed structures. Again, new reverse faults form to add to the structural complexity in the caldera.

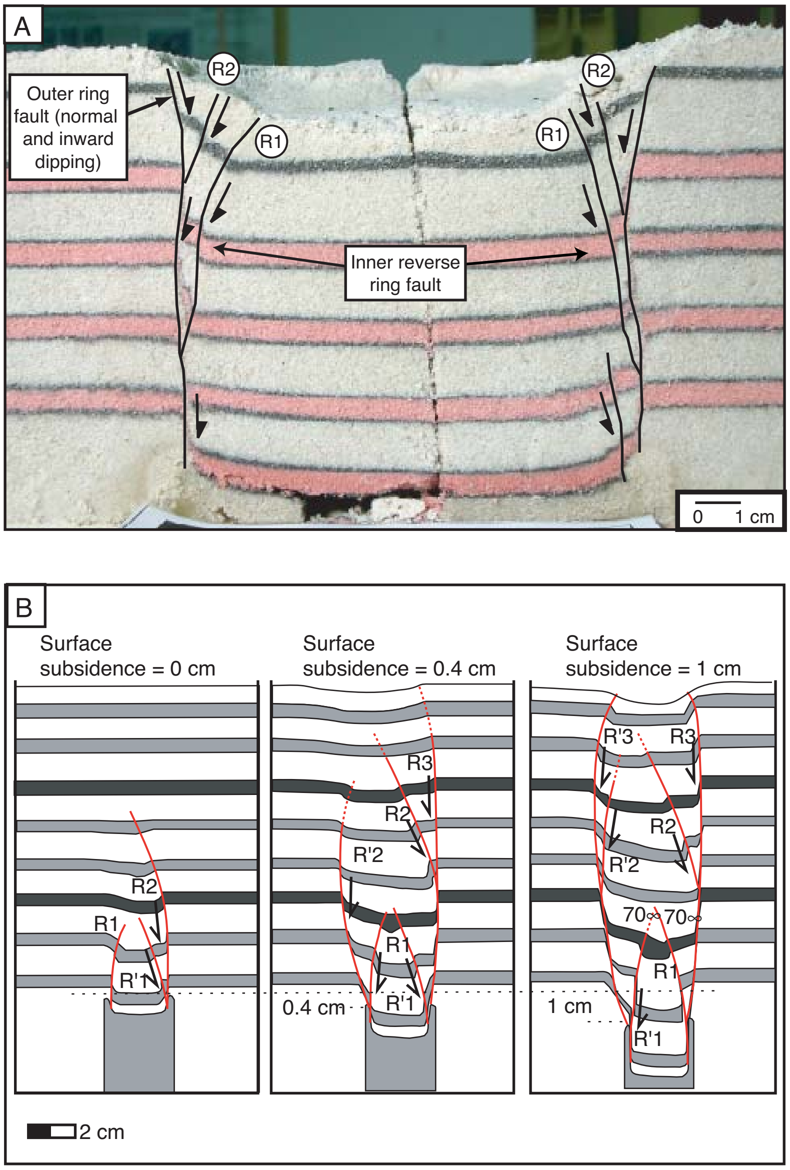

Figure 3.5:
a) Cross-section along section line in **Figure 3.4d** through the model with high roof thickness/diameter ratio. Note multiple reverse faults (numbered in order of formation) breaking up the magma chamber roof and caldera floor. With a flat chamber top, these reverse faults tend to splay from a single shear zone at depth. In experiments with curved magma chamber tops, however, such multiple reverse faults can remain separated all the way down through the magma chamber roof. Note also that strata in the magma chamber roof are less sagged than in the 'thin-roofed' models in **Figures 3.2 & 3.3**;

b) Sequential cross-section sketches of collapse development above a magma chamber of extremely high depth/diameter ratio. In this case, the influence of stress arching is sufficiently pronounced that the multiple reverse faults, although not intersecting the surface, break the chamber roof up into a set of sequentially-formed blocks (modified from Roche et al. 2000).

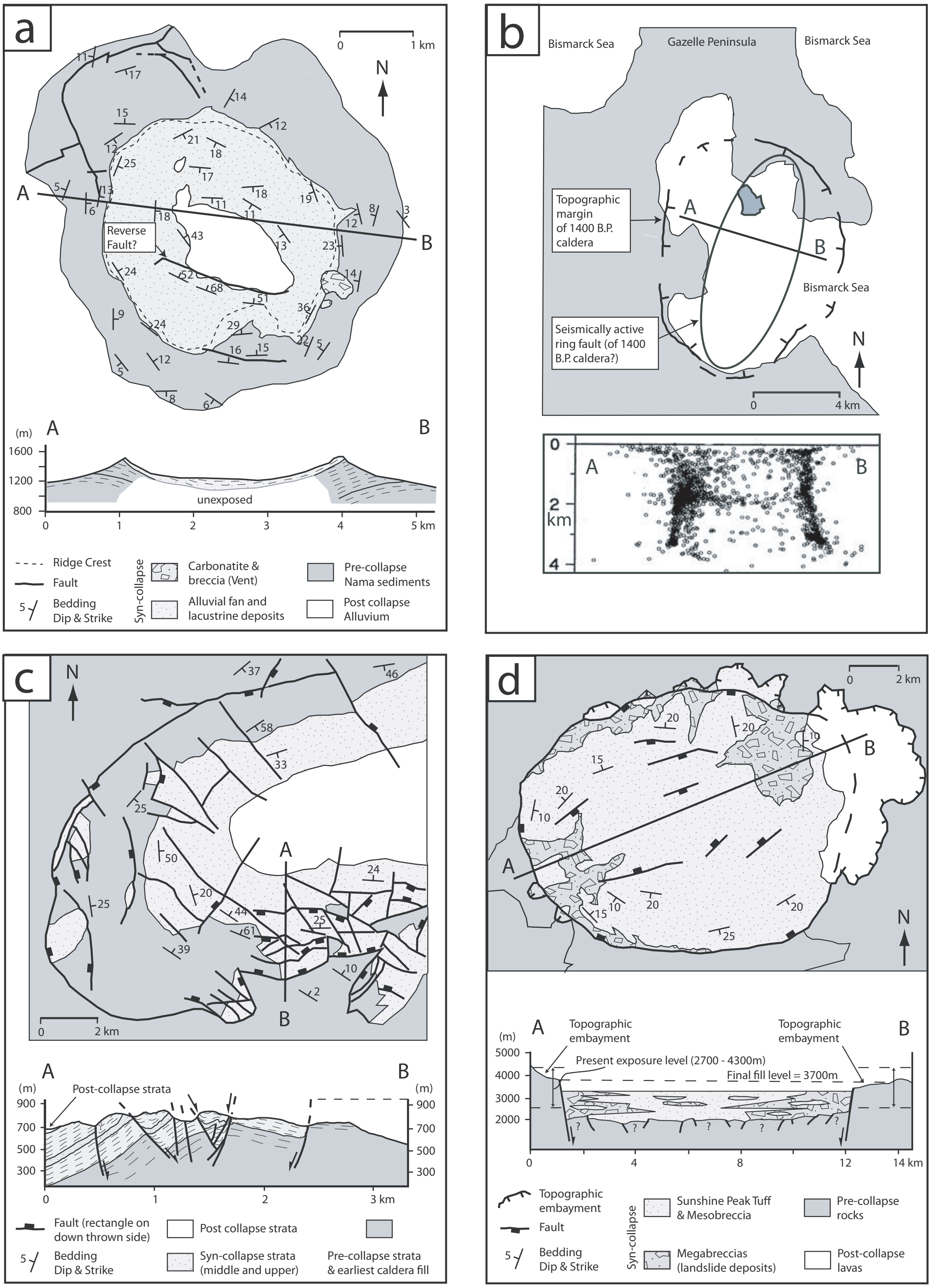

Figure 3.6: **a)** The Gross Brukkaros depression, Namibia, shows down-sagged pre- and syn-collapse strata (after Stachel et al. 1994). Note that toward the fault in the south-centre, dips in the infill steepen greatly, as in the hanging wall above an outward-dipping reverse fault (see **Figures 3.2 & 3.3**); **b)** Rabaul caldera, Papua New Guinea (after Nairn et al. 1995). Inset is a plot of 1983-85 earthquake epicentres (along section A-B) defining an outward-dipping inner ring-fault; **c)** Map and cross section of Scafell caldera, England (from Branney 1995). Note the inward tilted basement, bounding outer normal fault, and complex keystone graben in the periphery. The caldera centre is not exposed; **d)** Map of the resurgent Lake City caldera, Colorado (after Lipman 1984), and schematic pre-resurgence cross-section, showing structure and infill (after Hon 1987). Note the distribution of megabreccia deposits, the topographic embayments marginal to the inward-dipping ring fault, and the funnel-shape imparted to the caldera and its infill.

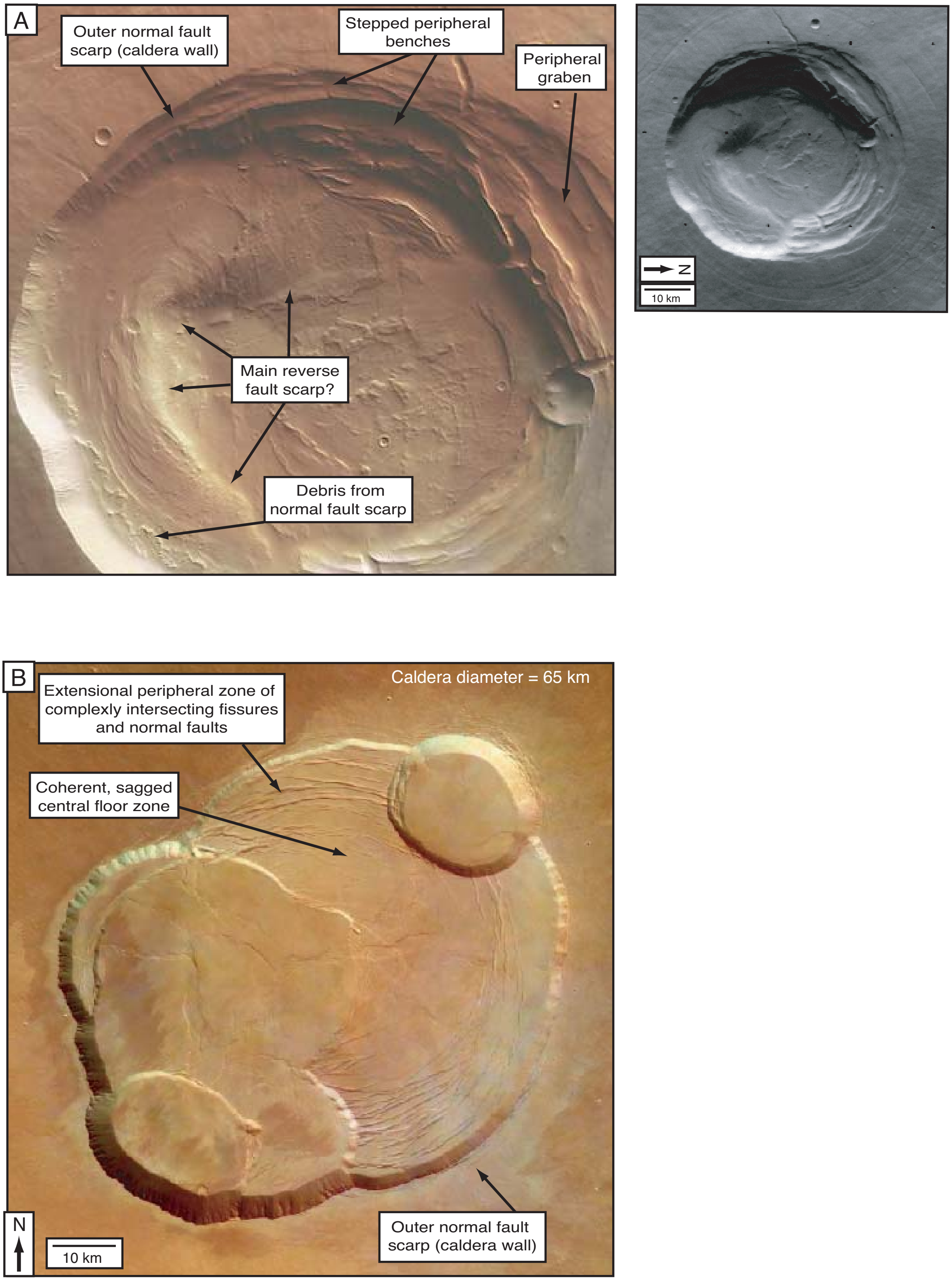

Figure 3.7: **a)** ESA Mars Express satellite image of the ~53 km diameter and ~1.7-2.0 km deep caldera of Biblis Patera, Mars, and outline of inferred structures (Plescia 1994; this study); **b)** ESA Mars Express satellite image of the nested collapse structures of Olympus Mons caldera, Mars (European Space Agency). Structures outlined are those thought to have been created during the first and largest collapse event (Mouginis-Mark and Robinson 1992), in which the magma chamber depth/diameter ratio was very small < 0.25. In both of these large-diameter calderas, land-slide deposits occur locally below the fault scarps, but are seem overall limited compared to those on Earth. Lower gravitation on Mars possibly reduces the instability of the outer normal fault scarp and so limits the generation of voluminous landslide debris.

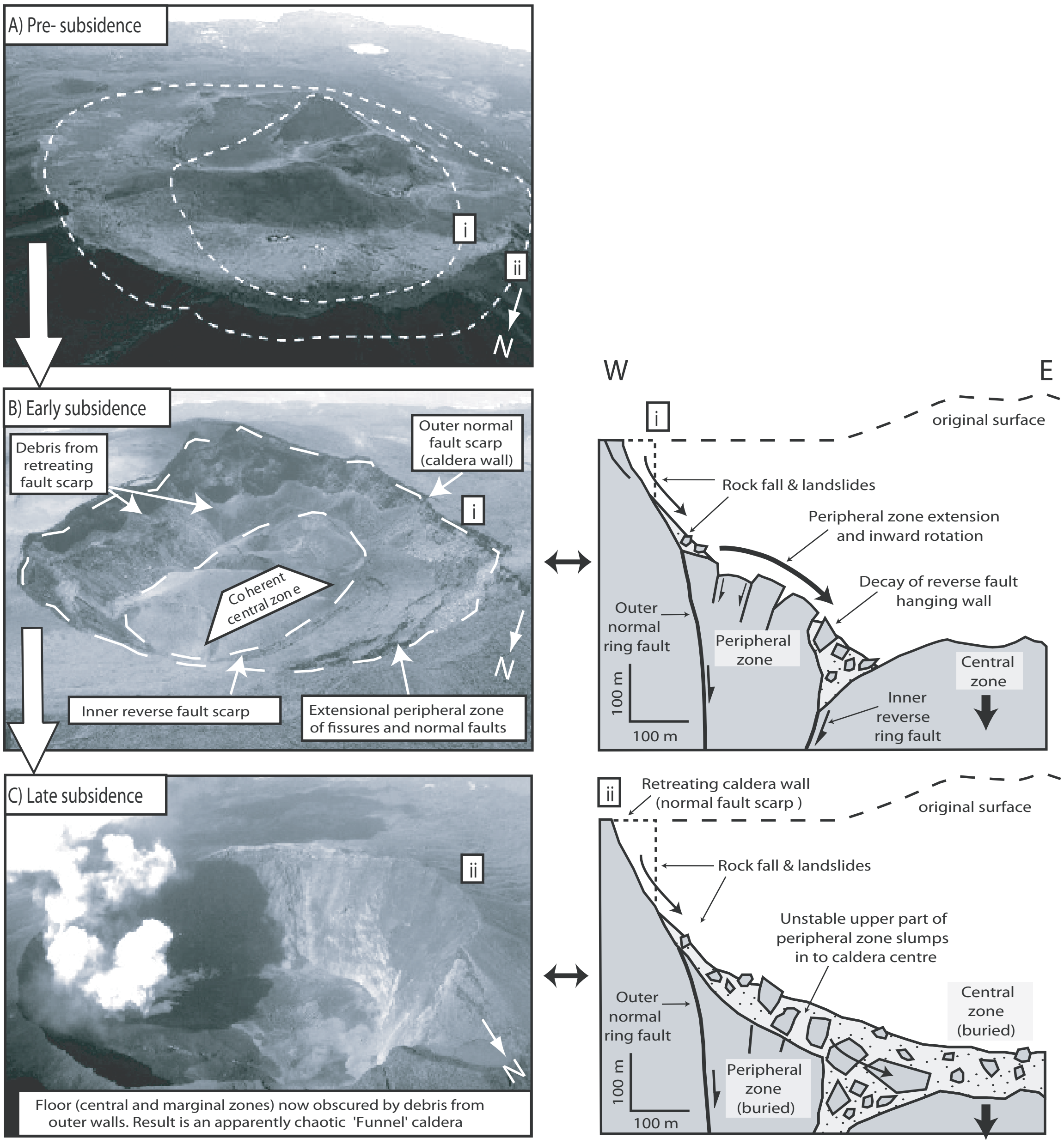

Figure 3.8: Structural and morphological evolution of Miyakejima caldera, Japan (adapted from Geshi et al. 2002): **a)** Pre-collapse view of Miyakejima summit area. i = Early subsidence caldera wall position, ii = Late subsidence caldera wall position. Outward migration of the caldera wall between i and ii occurred through landsliding from the oversteepened outer normal fault scarp; **b)** Early-mid subsidence view some 18 hours after initially rapid (~ 100 m per day) surface subsidence began. Caldera diameter = ~ 0.8 km; **c)** Late subsidence view almost 2 months after onset of surface subsidence. The central zone is by now deeply buried in debris from the peripheral zone and especially the retreating outer normal fault scarp. Part of the peripheral zone has slid into the caldera centre; the rest lies buried beneath landslide debris from the outer normal fault scarp. Caldera diameter = ~ 1.5 km.

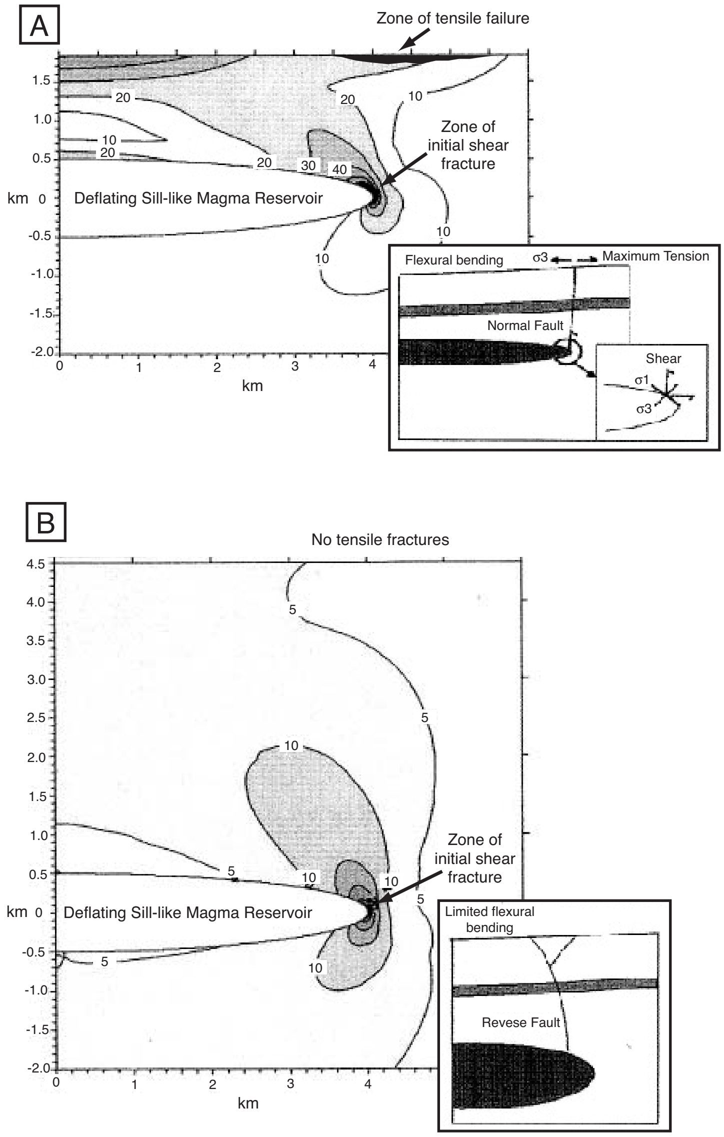

Figure 3.9: Results of representative Finite Element Models of caldera collapse with magma chamber roofs of **a)** low thickness/diameter ratio, and **b)** high thickness/diameter ratio (modified from Folch & Marti 2004). These ratios are very similar to these in the representative analogue experiments (see **Figures 3.2 - 3.5**). Insets illustrate idealised 'end-member' failure modes for relatively thin (via normal fault) and relatively thick (via reverse fault) magma chamber roofs (from Folch and Marti 2004).

In both cases, the magma chamber is under-pressured by 10 MPa with respect to lithostatic stress, and the resultant distribution of differential stress generated in the roof is plotted. Also included are zones of probable tensile failure and shear failure (the latter based on a Von Mises criterion for shear fracturing). In both models, differential stress reaches an absolute maximum near the magma chamber edge, from where a zone of high differential stresses arches upward toward the roof centre. This is suggestive of stress arching in both models, which favours shear failure along an outward dipping fault (rather than normal) - as in the analogue models.

In contrast to the 'thick-roofed' model, the 'thin-roofed' model also exhibits a near-surface zone of high differential stress over the magma chamber centre and a wide near-surface zone of high tensile stress over the magma chamber margins. These zones are compatible with substantial sagging of the magma chamber roof. The thick-roofed model exhibits neither such zones. This observation, together with the much lower differential stresses for the same under-pressure in the magma chamber, suggests that the thicker roof is much stronger and more rigid than the thin roof. This is in turn compatible with a greater influence of stress arching in the thick roof - as seen in the analogue models.

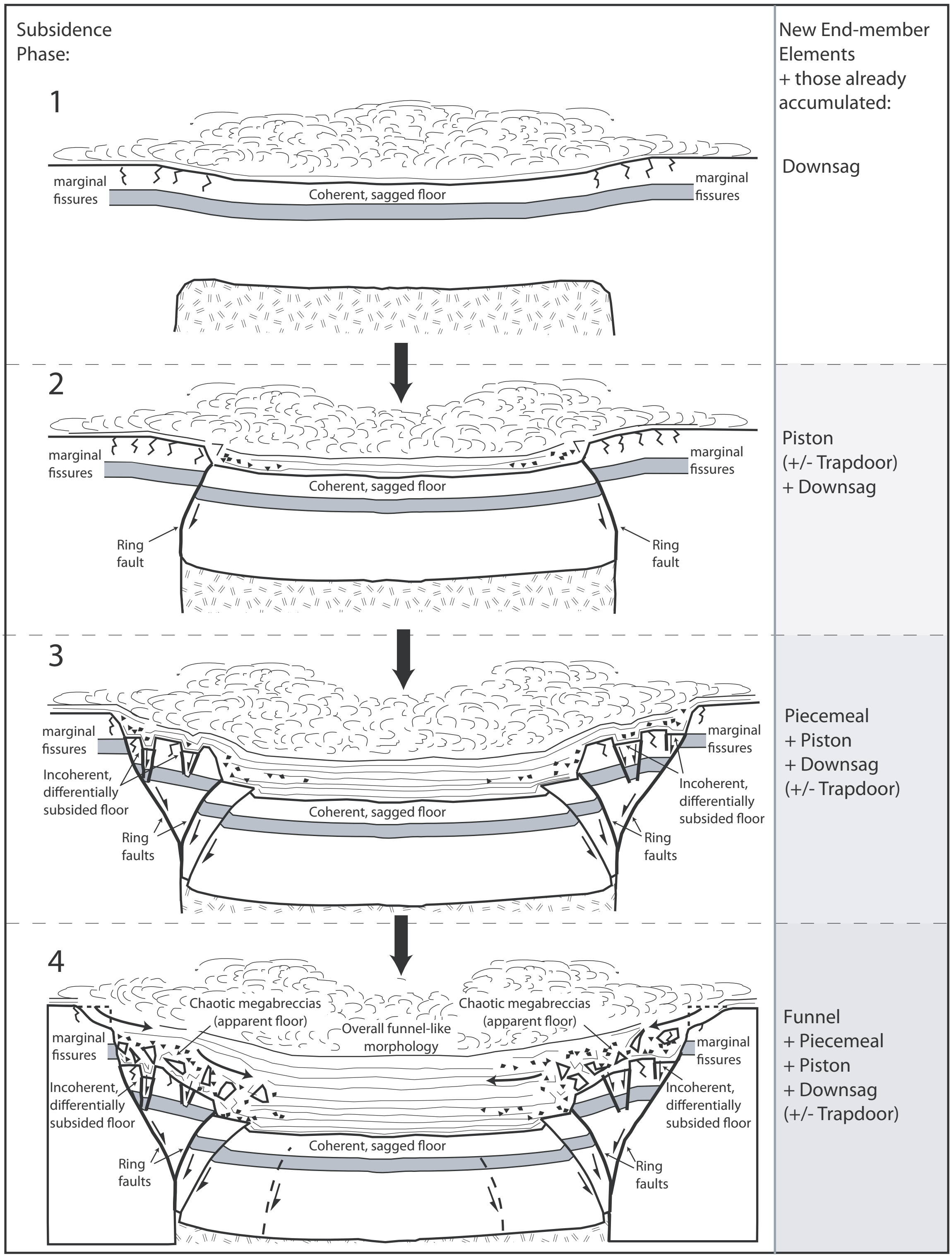

Figure 3.10: A generalised evolutionary path for sequential development of the structural elements characteristic of each idealised caldera 'end-member' (cf. **Figure 3.1**). No scale is implied. Note that the subsidence phases are gradational and overlap somewhat. This evolution may be achieved either in a single eruptive/collapse event or possibly over several events (i.e. incrementally). Subsidence is here symmetric for simplicity; asymmetric subsidence is also common, and may be permanent or transient through the course of caldera development.

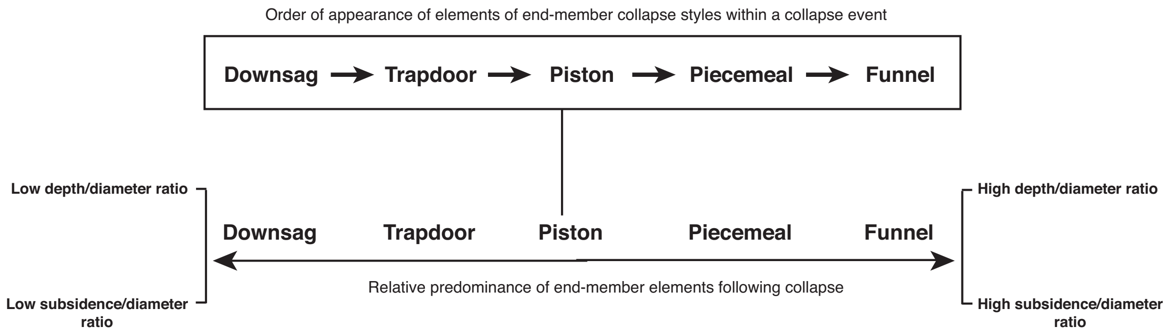

Figure 3.11: Revised outline of caldera continuum as envisaged from this synthesis. The upper part describes the progressive acumulation of the structural elements characteristic of all five end-member collapse styles during a collapse event. The lower part schematically describes how the initial thickness/diameter of the magma chamber roof and final subsidence-diameter ratio of the caldera regulate the extent to which each end-member's structural elements are expressed in the final caldera structure. See text for explanation and discussion.

4 The Role of Magma Chamber Ellipticity in the Evolution of Caldera Structures and Eruptions

4.1 Introduction

4.1.1 Potential factors in producing an elliptical caldera

Most caldera volcanoes are slightly or highly elliptical in plan view (e.g. the 30 x 20 km diameter Cerro Galan, Argentina - **Figure 4.1a**). A number of factors may explain why calderas have an elliptical surface expression. These include:

1) Asymmetric subsidence into a circular magma chamber (Lavallee et al. 2004; Kennedy et al. 2004).

2) Regional tectonic influences, such as (a) ‘distortion’ of caldera faults due to interaction of volcanic and regional stress fields during caldera formation (Mandl 1988; Holohan et al. 2005), or (b) elongation of the caldera structure by progressive post-collapse regional deformation, or (c) syn-collapse deflection of caldera faults along pre-existing or syn-volcanic structures (Acocella et al. 2004).

3) Non-concentric overlap of several calderas, each of which is related to an individual collapse event and possibly also associated with a discrete magma chamber. The overlapping collapse structures form a composite or ‘nested’ caldera structure with elongate geometry (e.g. Marti et al. 1994).

4) A pre-caldera magma chamber that is horizontally elongated or elliptical in plan view. Plutons likely represent the frozen remnants of or un-erupted equivalents to pre-caldera magma chambers, and are often highly elliptical or elongate in plan-view (**Figure 4.1b**). One cause of lateral elongation of a magma chamber is preferential lateral growth along crustal anisotropies, such as pre-existing or syn-tectonic fault trends (cf. Acocella et al. 2002; Jacques and Reavy 1994 - **Figure 4.1b**). Alternatively, a mechanism analogous to borehole breakout, whereby regional stresses cause differential spalling of a magma chamber’s walls, has also been considered (cf. Bosworth et al. 2003).

The influence on caldera collapse of a magma chamber that is elliptical in plan view is the subject of this chapter.

4.1.2 Previous experimental and numerical findings

Although likely to be fundamental pre-collapse geometric variable, the influence of plan-view ellipticity of a pre-caldera magma reservoir and its roof on caldera collapse has not previously been subjected to detailed experimental evaluation. Of numerous analogue experimental and numerical studies of caldera formation, only a few (Marti et al. 1994; Roche et al. 2000; Roche at al. 2001) considered subsidence into a horizontally elongated (elliptical or rectangular) reservoir. All other theoretical, numerical, and analogue studies of calderas, from which we derive much of our current understanding of these volcanoes, have thus far assumed circular plan-view geometries for the magma reservoir. Distinct influences from a horizontally elongated reservoir on the geometry and development of caldera structures were nonetheless noted (**Figure 4.2**).

Marti et al. (1994) concluded that an inflating or deflating elongated balloon (magma chamber analogue) imposes an anisotropic stress field and deformation pattern on its surroundings. These authors noted that during inflation of an elongate balloon, extensional faulting was better developed above the balloon's long axis. Descriptions of anisotropies generated by collapse are restricted to remarks that minor or no faulting occurred at the "termini of the elongate depression" and that "accommodation of the collapse depression at such termini was by gentle down-warping" (Marti et al. 1994). Photographs of experimental collapse into an elliptical balloon (**Figure 4.2a**; Figure 6 in Marti et al. 1994) seem to show a greater abundance of fracturing above the balloon's long sides.

Photographs of collapse into elongated silicone reservoirs in Figures 16, 17 & 18 of Roche et al. (2000) similarly show greater fracturing along the 'long sides' of the model caldera (**Figure 4.2b)**. Roche et al. (2000) also noted that outward-dipping reverse faults consistently first nucleated along the 'long sides' of the elongate silicone reservoir. Such patterns in elliptical caldera faulting were apparently unaffected by the thickness/diameter ratio of the reservoir roof – the principle factor investigated in that study. Intriguingly, Roche et al. (2000) observed that the pattern of experimental reverse fault nucleation and propagation matched the vent migration and ring fracture propagation proposed by Wilson and Hildreth (1997) for the highly elliptical Long Valley caldera, USA.

In an analytical study of caldera collapse initiation, Roche and Druitt (2001) calculated the critical volumetric fraction of magma that must be erupted to cause failure of a reservoir roof along a vertical to outward-dipping ring fault. One of the variables found to influence this critical volumetric fraction was the plan-view ellipticity of the magma reservoir. For a fixed ratio of roof thickness to roof short axis length, the critical volumetric fraction of magma that must be erupted to cause roof failure decreased with increasing roof ellipticity (Roche and Druitt, 2001). In other words, the more elliptical a magma chamber roof is, the more inherently unstable it appears to be when magmatic support is removed from under it.

Previous modelling observations thus suggest a profound control by an elongate magma chamber on kinematics and geometry caldera collapse structures, with potentially major implications for hazard assessment at restless elliptical calderas and the mineral resource potential of extinct examples. However, neither Marti et al. (1994) nor Roche et al. (2000) provide any detailed description of the geometric variations in faulting around the elliptical caldera models, and three-dimensional constraints from cross-sections are entirely lacking. Though the reservoir shape is inferred to control the anisotropies in overall deformation pattern, no mechanical explanations were given of why it should. The consistent nucleation and propagation pattern of reverse faulting observed by Roche et al. (2000) was unexplained. Reasons for the apparently lower stability of an elongate magma chamber are also somewhat uncertain (mainly since roof area, and hence total roof load, was not constant - cf. Roche and Druitt 2001).

4.1.3 Investigations of elliptical caldera collapse in this study

The structural development of caldera collapse into elliptical reservoirs is further explored in this chapter. Analogue experiments of caldera collapse were run to systematically examine the effects of a range of plan-view magma chamber ellipticities on the geometry and kinematics of caldera fault systems. Experimental observations are combined with existing analytical solutions and numerical models, as well as observations of subsidence above elliptical hydrocarbon reservoirs, to help explain the geometric and developmental patterns of elliptical caldera faulting in nature.

The experiments confirm the systematic location and lateral propagation of initial elliptical roof failure noted by Roche et al. (2000), but they also show that this may vary between several styles over a range of magma chamber ellipticities. A basic mechanical rationale for the systematic location of initial elliptical roof failure is provided. This rationale relates the failure pattern to the distribution of pre-failure shear strain in a magma chamber roof as it initially down-warps during reservoir depressurisation. In addition, the rationale provides a possible explanation for the apparently lower stability of an elliptical reservoir (Roche and Druitt 2001), may also account for the location and migration of caldera ring fracture vents at several natural elliptical calderas.

This chapter also documents an orderly circumferential variation in the geometry of final experimental elliptical caldera structures not only at the surface, but also in 3D. The surface variations are shown to closely match the structural geometry of several elliptical calderas in nature. From extrapolation of the model results of this study, a new view of the 3D structure of these calderas may thus be inferred.

4.2 Experiment Set-up and Design

Three experiment sets were designed to examine the geometric and kinematic development of structures formed by collapse into elliptical magma chambers (**Table 4.1**). The first set tested the effect of various plan-view ellipticities on the evolution of ‘thin-roof’ collapses. The second set assessed the sensitivity of elliptical ‘thin-roof’ collapse to the lateral position (centred or non-centred) of the conduit. The third set examined the effect of a ‘thick-roof’ on elliptical collapse.

The experimental setup for all sets again comprised a sand/gypsum pack (mixed 4:1 by volume) containing a two cm-thick, tabular (sill-like) reservoir of creamed honey (**Figure 4.3**). A honey conduit of 0.8 cm diameter extended from the reservoir base through the table and allowed evacuation of the reservoir. The ratio of the reservoir's horizontal long axis to its short axis, A/B, defines the roof's plan-view ellipticity (or 'horizontal roof aspect ratio'). This geometric variable was systematically altered by emplacing the honey with cylindrical to sub-cylindrical moulds of the same cross-sectional area, but varying cross-sectional ellipticity. A detailed description of the construction procedures and scaling considerations of the models is given in **Chapter 1**.

In the first set of experiments (Cal Stat A-D), four plan-view ellipticies were considered (**Figure 4.3**): A/B = 1.0 (circular), A/B = 1.3, A/B = 1.5 and A/B = 2.0 (highly elliptical). Although 2 cm in few models (Cal Stat A3, B3, C3, and D3 – **Table 4.1**), roof thickness was set to 3 cm in most experiments. Depending on ellipticity and cross-section, the roof's thickness/diameter ratio (or 'vertical roof aspect ratio') ranged from 0.16-0.45. To ensure reproducibility of results, each model type was run five times.

In the second set, an intermediate A/B = 1.5 was chosen, and the conduit was sited at one of three locations along the reservoir's long axis: 3.4–3.9 cm west of the centre (Cal Stat E1-E4), 4.2 – 4.5cm east of the centre (Cal Stat F1-F4), or 4.2 – 4.5cm west of the centre (Cal Stat F5-F8). Roof thickness was set to 3 cm. To ensure reproducibility of results, each model type was run four times.

In the third set, an intermediate A/B = 1.5 was again chosen, but roof thickness was set to 6.0 cm. Depending on diameter chosen, the roof's thickness/diameter ratio thus ranged from 0.50-0.80. For one model type, the conduit was centred (Cal Stat G1 and G2), whilst for the other type, the conduit was sited 4.2 – 4.5cm east of the reservoir centre (Cal Stat G1 and G2).

The results of the circular 'thin roof' Cal Stat A subset and circular 'thick-roof' Cal Stat H subset are described in detail in **Chapter 2**, but again some relevant points are noted here for purposes of comparison.

4.3 Experimental Results

The experimental results are conveyed in six parts, which in turn describe the kinematic evolution and final geometry of collapses produced in the three experimental sets outlined above.

4.3.1 Collapse of 'thin' elliptical roofs with centred conduits: Kinematics

The developments of Cal Stat B5 (**Figures 4.4 & 4.5**), Cal Stat C5 (**Figures 4.6 & 4.7**), and Cal Stat D5 (**Figures 4.8 & 4.9**) are broadly representative of collapse into reservoirs with plan-view ellipticies (A/B) of 1.33, 1.5, and 2.0 respectively. The general structural evolution of collapse in these experiment subsets closely resembled that of collapse into circular reservoirs (**Chapters 2 & 3**). In addition, most collapses were again asymmetric, which again produced slight variations in structural development. As reservoir ellipticity increased, however, asymmetric collapse became less common; collapse into the most elliptical reservoirs (Cal Stat D1-D5) was mostly symmetric.

In detail, the geometry and kinematics of faulting in elliptical collapses exhibited some marked differences from that in circular collapses. Subtle ellipticity-dependent differences were also noted between the experimental subsets, particularly regarding the lateral propagation of reverse faults (summarised in **Figure 4.10**). Development of faulting also varied slightly within each experiment subset (**Figure 4.11**), but was most consistent above the least and most elliptical reservoirs (Cal Stat A1-A5 and D1-D5).

Subsidence in nearly all elliptical collapses again began with more or less symmetric sagging of the sand above the reservoir and development of tension cracks (fissures) above the honey chamber margins (**Figures 4.4a, 4.6a & 4.8a**), The latter were commonly more pronounced above the long sides of the reservoir. Localisation of one or more steeply outward-dipping reverse faults again marked complete roof failure (**Figures 4.4a, 4.6a, 4.8a, & Figure 4.10 Aii-Dii**).

Ellipticity affected the exact nature of both localisation and lateral propagation of reverse faults around the reservoir, to produce three main 'unzipping' patterns (**Figure 4.10**). Experiments against a glass pane (**Chapter 2**) show that upward propagation of reverse faults was very rapid (nearly instantaneously), such that reverse fault's appearance at the surface occurs almost synchronously with its localisation at depth. The lateral propagation ('unzipping') patterns comprised a continuum bound by end-members characteristic of the A/B = 1 (circular) and A/B = 2 (highly elliptical) roof geometries (**Figure 4.10, Aii-Dii, Aiii-Diii)**. Only once, with a circular roof, did a reverse ring-fault localise instantaneously all around a reservoir circumference (*Pattern 0,* 'no unzipping' **- see Figure 4.11**). Circular reservoir roofs usually displayed unzipping *Pattern 1*, whereby the reverse fault first localised at one side of the reservoir and then propagated bi-directionally around to a 'hinge zone' on the opposite side. For circular roofs, the site of first reverse fault localisation was apparently random, but for elliptical roofs, reverse faults *always* first localised around the ends of the reservoir's short axis (**Figures 4.4a, 4.6a, & Figure 4.10, Aii-Dii**). In an experiment with slightly asymmetric pre-failure sagging (Cal Stat D1), the reverse fault localized around the end of the short axis closest to the area of most pre-failure subsidence.

After reverse fault localisation near one end of their short axis, slightly elliptical roofs (A/B = 1.25) often displayed unzipping Pattern 1, like the circular case (**Figure 4.10 Bi-iv)**. These roofs otherwise displayed *Pattern 2*, whereby the reverse fault propagated mainly uni-directionally from one end of the roof's short axis, around the long axis, and then on past the other end of the short axis (e.g. **Figures 4.4a-c & 4.11**). Moderately elliptical roofs (A/B = 1.5) also displayed unzipping Pattern 2 **(Figure 4.10 Ci-iv)** or else *Pattern 3*, where two discrete reverse faults localised simultaneously or in quick succession, one around each end of the roof's short axis (e.g. **Figures 4.6b-c & 4.11**). These reverse faults then propagated bi-directionally toward the ends of the roof's long axis, at which the reverse faults linked. Highly elliptical roofs (A/B = 2.0) displayed unzipping Pattern 3 only (e.g. **Figures 4.8b-c, 4.10 Di-iv, & 4.11**).

Subsidence of the central zone commonly became asymmetric once the reverse faults formed (though, as noted, less frequently so at the highest ellipticities). As in the circular collapses, the asymmetrically subsiding central zones displayed a component of horizontal motion directed toward the maximum point of subsidence with consequent lateral variation in reverse fault slip. Indeed, as the reverse fault propagated from a short axis end to (or around) a long axis end, the maximum point of subsidence and the direction of the horizontal motion component of the central zone sometimes changed within a single evolving collapse (e.g. Cal Stat B5 - **Figure 4.4b-d**). Most commonly, the maximum point of subsidence was finally located near one end of either the long axis or short axis, with a flexural or extensional hinge zone at the opposite end. A normal fault or a graben usually formed at this hinge zone. As in the circular experiments, reverse faults mostly linked into the hinge zone, though some hinge zones located along the reservoir's short axis were broken through by later reverse faults (e.g. Cal Stat C3, C4, D4).

New (second generation) inner reverse faults formed near the end of some experiments. The reverse fault traces again first appeared around the end of the elliptical reservoir roof's short axis (e.g. Cal Stat B5 & D5 – **Figures 4.4e & 4.8e**). In Cal Stat B5, the new inner reverse fault appeared on the side of the roof opposite where the earlier, outer reverse fault first localised. In addition, the point maximum subsidence and the associated horizontal motion shifted to the vicinity of the new inner reverse fault (**Figure 4.4b-e)**. This shift marked a 180° switch or 'reversal' in the subsidence asymmetry from one short axis end to the other through the course of the experiment.

After the first reverse fault(s) had localised, material in the peripheral zone began to thrust across the central zone. Once the reverse fault(s) had propagated to the long axis ends or had passed around them, the outer normal fault system began to form. As in the circular collapses, many segments of the outer normal fault trace in elliptical collapses were originally marginal tension fractures formed during the earlier sagging phase (**Figures 4.4b-d, 4.6b-d & 4.8b-d**). Also as in asymmetric circular collapses, the outer normal fault in asymmetric elliptical collapses tended to first develop at the hinge zone (e.g. Cal Stat B5 – **Figure 4.4d**), which was usually at one end of either the long or short axis. Regardless of hinge position and collapse symmetry, however, and particularly at higher ellipticities, the outer normal fault system also commonly first localised around the ends of the roof's short axis, and then propagated from there to the long axis ends (e.g. Cal Stat D5 – **Figure 4.8c-d**, Cal Stat C2 **– Figure 4.10 row 3**).

Concurrent with formation of the main normal ring-fault system, an intricate network of crevasse, faceted normal to oblique-normal normal faults, fault blocks, step-faults and complex marginal gräben formed in response to a predominant radial extension across the outer part of the peripheral zone (Zone 3 in **Chapter 2**). This complex network was again defined by intersecting sets of parallel fractures, many of which were also parallel to segments of the main outer normal fault system (**Figures 4.4d-e, 4.6d-e, & 4.8c-d**). Many of the peripheral fault traces coincided with tension fractures formed during the earlier sagging phase. Such extensional faulting was most pronounced around the short axis of the model calderas (or along the long sides), as seen in results of Marti et al. (1994) and Roche et al. (2000) (**Figure 4.2**).

As in the circular collapses, the peripheral zone incorporated an inner sub-zone, in which deformation was characterised primarily by strike-slip faults and oblique reverse faults that formed in response to circumferential contraction (Zone 2 in **Chapter 2**). Although not shown here, it is also worth noting that in experiments with the thinnest roofs (2cm thick - Cal Stat C3 and D3), wrinkle ridges were well developed in the central zone of the caldera, as in the equivalent circular experiment Cal Stat A3 (see **Chapter 2**). Wrinkle ridges in elliptical collapses were orientated either radially, as in Cal Stat A3, or predominantly parallel to the short axis and perpendicular to the long axis of the caldera.

Finally, as in the circular collapses, oversteepened fault scarps, particularly those of the outer normal ring-fault system, began to decay in the final stage of the elliptical experiments and produce grain flow deposits that partly buried earlier formed structures in the peripheral zone (**Figures 4.4e, 4.6e & 4.8e**).

4.3.2 Collapse of 'thin' elliptical roofs with centred conduits: geometric features

In the final plan-view structure of all model elliptical calderas, the outer limit of the peripheral zone was always less elliptical than the reservoir, whereas the central zone was always more elliptical than the reservoir (**Table 4.2; Figure 4.12**). This basic geometric characteristic was not greatly altered by asymmetric subsidence. Average peripheral zone and central zone ellipticities were respectively 1.17 and 1.56 for reservoir A/B = 1.33; 1.26 and 2.06 for reservoir A/B = 1.5; and 1.54 and 2.73 for reservoir A/B = 2.0, (**Table 4.2**). The differences between the average ellipticities of the peripheral zone, central zone, and reservoir were thus more pronounced as initial reservoir ellipticity increased (**Table 4.2**).

Geometric differences are further found in cross sections through the model calderas' long and short axes (**Figures 4.5, 4.7, & 4.9**). Along the long axes, the outer limit of peripheral zone fracturing at the surface coincided with or extended only slightly outside the projected edge of the honey reservoir (by < 0.5 cm). On the short axes, by contrast, the outer limit of peripheral zone fracturing at the surface always extended much further outside the projected edge of the honey reservoir (in most cases by 1-1.3 cm). The surface limit of the central zone, as defined by the outermost concentric reverse fault trace, occurs at a much greater distance inward from the projected reservoir edge along the short axis (1.0 – 1.7 cm) than along the ling axis (0.8 – 1.3 cm).

The appearance of peripheral surface fracturing further outward from the reservoir edge on the short axis reflects the upward divergence of reverse and normal faults from a low structural level (just above the reservoir edge). In contrast, upward divergence of reverse and normal faults on the long axis typically occurs from a higher structural level (far above the reservoir edge) (**Figures 4.5, 4.7, & 4.9**). Average normal fault dip was the same on long and short axes (**Table**

4.3). On the other hand, the appearance of reverse fault traces further inward from the reservoir edge on the short axis is reflected in a generally shallower dip of reverse faults on the short axis compared with those on the long axis (on average 66° vs. 77° respectively for all 'thin roof' elliptical experiments –**Table 4.3**).

The peripheral zone's final width, as measured on the model surface from the outermost tension fracture to the trace of the outermost reverse fault, was consequently greatest along the short axis and least along the long axis (**Figures 4.4e, 4.6e & 4.8e**). Two factors contributed to the final width of the peripheral zone over the course of the experiment, however. The first was the distance between the outermost tensional fracture (~ macroscopic limit of collapse influence) and the point of nucleation of the reverse fault trace. The second was the magnitude of the peripheral zone's horizontal inward motion. In most experiments, the distance between the outermost tension fracture and the nucleation point of the reverse fault trace was greater on the short axis than on the long axis. In all experiments, horizontal inward motion of the peripheral zone was equal on both axes or, more usually, greater on the short axis. For 12 out of the 15 experiments in this set, the distance from outermost tension fracture to reverse fault trace was substantially greater on the short axis and exceeded any contribution from the inward motion of the peripheral zone. Therefore, though circumferentially uneven inward motion of the peripheral zone may complement it, the main factor determining the greater width of the peripheral zone along the short axis was the greater distance between the outermost tension fracture and the reverse fault trace's initial nucleation point.

The style of peripheral deformation on and near the model surface reflected these circumferential geometric variations between the long and short axes in cross section. Shallow level normal faults were much more numerous and better developed on the short axis and commonly penetrated to deeper levels of the roof than on the long axis (**Figures 4.4e, 4.5, 4.6e, 4.7, 4.8e & 4.9**). These shallow level normal faults defined a main keystone graben or a more complex graben system of multiple differentially-subsided blocks or slivers (half gräben and gräben). Though narrow keystone gräben also formed on the long axis, particularly in hinge zones (e.g. **Figure 4.7, section A-B**), development of similarly complex extensional fault systems was weak. Extension on the long axis was instead almost entirely focussed on a single normal fault (**Figures 4.5, 4.7, & 4.9**).

The final inward-tilt of layers did not consistently differ between the long axes and the short axes. For example, whilst inward tilting is greater on the short axis in Cal Stat B5 (**Figure 4.5**), it is greater on the long axis in Cal Stat C5 and D5 (**Figures 4.7 & 4.9**). Inward-dips overall ranged from 17° near the surface to up to 35° just above the chamber. At the end of any axis, a greater accommodation of subsidence by inward tilting of strata seems balanced by a reduction of vertical displacements on faults (e.g. contrast the C- and D-ends of Cal Stat B5 – **Figure 4.5**). Like those formed above the circular reservoirs, the reverse faults on both long and short axes of elliptical collapses generally had upward-decreasing displacement. In contrast, the normal faults had downward decreasing displacement. As shown in the circular experiments (**Chapter 2**), the accommodation of central subsidence by a combination of sag, tilt and fault displacement reflects a geometric coherence between the structures in the system. The anisotropy in roof thickness/diameter ratio in the elliptical case means that sagging plays a more prominent role in accommodating central displacement along the long axis, whereas faulting is more prominent along the short axis (as, respectively, in the 'thin' and 'thick' roof examples in **Figure 2.9**). This effect is accentuated with increasing ellipticity. At the highest ellipticity (A/B=2.0), the majority of the central vertical displacement is taken up by sagging along the long axis, but conversely by faulting along the short axis (**Figure 4.9**).

4.3.3 Collapse of 'thin' elliptical roofs with non-centred conduit: kinematics

These experiments were designed to isolate any effects of conduit position on the initiation, development, and final geometry of 'thin-roof' elliptical collapse structures. The conduit was positioned at 2.2 – 2.7 cm (Cal Stat E1-E4) or 1.6 - 2.0 cm (Cal Stat F1-F8) from one end of the long axis of an intermediate ellipticity reservoir of (A/B = 1.5) (**Figure 4.13**). The patterns of initiation and overall development of faulting in the two sets, for which experiments Cal Stat E3 and F7 (**Figures 4.14, 4.15 & 4.16**) are representative, mirrored that in the Cal Stat C sets **(see Figures 4.6 & 4.11)**.

Collapses again usually commenced with centrally symmetric sagging and marginal tensional fracturing that developed best around the ends of the roof's short axis (**Figures 4.14a & 4.15a**). Slightly asymmetric sagging in some experiments (Cal Stat E2-E4 & F8) maximised near one end of the short axis, with tension fractures best developed near the other end **(Figure 4.14a**).

First localisation of reverse faults in all experiments again occurred on the long sides (i.e. above the ends of the short axis) of the reservoir (**Figures 4.13, 4.14a & 4.15b**). With asymmetric pre-failure sagging (**Figure 4.15b**), reverse faults first formed around the short axis end next to the point of maximum subsidence. As in the conduit-centred Cal Stat C series (**Section 4.3.1**), failure and unzipping patterns either comprised: *Pattern 2* (e.g. **Figure 4.14b-c**), or *Pattern 3* **(**e.g. **Figure 4.15a-c**) – see also **Figures 4.11 & 4.13**.

Immediately after the reverse fault(s) formed, subsidence became asymmetric in all experiments, and the roof tilted toward the conduit. Reverse faults consequently propagated most rapidly toward, and then went around or linked at, the long axis end adjacent the conduit (**Figure 4.14b & 4.15c**). The strong subsidence asymmetry again induced horizontal motion of the central zone toward the maximum point of subsidence at the long axis end nearest the conduit. An extensional hinge zone therefore formed at the opposite long axis end (**Figures 4.14c, 4.15c & 4.16**). The fully formed reverse ring-fault accordingly displayed the same circumferential variation in slip kinematics as described for asymmetric collapses in other sets (see **Chapter 2 & Section**

4.3.1). Slip was purely down-dip at the point of most subsidence, away from which an oblique-to-strike slip component progressively increased and maximised where the reverse fault linked into the extensional hinge zone (**Figures 4.14d & 4.15e**).

As previously, the main normal ring-fault system began to form once the reverse fault(s) had linked or propagated around the long axis end. In 10 out of 12 experiments, the normal fault system first formed around the short axis ends (e.g. **Figures 4.14b-c & 4.15c-d**), and sometimes also the hinge zone, and then rapidly propagated toward the long axis end with most subsidence (i.e. next to the conduit).

In the outer sub-zone of the peripheral zone (Zone 3 in **Chapter 2**), concentric to sub-concentric oblique-normal faults, defined by complex network of intersecting fracture sets, again formed concurrently with the normal ring fault system. Extensional faults and gräben were again best developed along the long sides (i.e. around the ends of the short axis) of the reservoir in nearly all experiments, despite the maximum point of subsidence occurring at the end of the long axis (**Figures 4.14c-d, 4.15c-e & 4.16**). In the inner sub-zone of the peripheral zone (Zone 2 in **Chapter 2**), concentric to sub-concentric strike-slip faults and oblique splays from the inner reverse ring-fault again formed to accommodate concentric shortening caused by inward movement of the peripheral zone material (e.g. **Figure 4.15d**). Oblique-reverse fault splays again formed near the point of maximum subsidence (controlled in these experiments by the conduit position), and in some cases dissipated along strike into sub-concentric strike-slip faults (e.g. **Figure 4.15d**). The pronounced focus of subsidence at one end of the long axis commonly imparted a predominantly dextral sense to oblique and strike-slip faulting along one side of the caldera and a predominantly sinistral sense along the other side (e.g. **Figure 4.15e**).

Second generation concentric reverse faults localised inside the earlier main reverse fault system toward the end of most Cal Stat F experiments. The pronounced subsidence asymmetry strongly affected this localisation, however. In Cal Stat F2, F5 and F6, an inner reverse fault nucleated between the short axis and the end of long axis with most subsidence, whilst in Cal Stat F1, F4 and F8, inner reverse faults nucleated around the long axis end with most subsidence (**Figure 4.13**).

4.3.4 Collapse of 'thin' elliptical roofs with non-centred conduit: geometric features

The overall geometric relationships between the plan-view ellipticities of the peripheral zone, the central zone and the reservoir were as in elliptical experiments with centred conduits (**Tables 2 & 4**). Again the outer limit of the peripheral zone was always less elliptical (average A/B = 1.28) than the reservoir, whereas the central zone was always more elliptical (average A/B = 2.0) than the reservoir (A/B = 1.5) (**Table 4.4**).

Cross-sections, e.g. through Cal Stat F7 (**Figure 4.16**), show that the main underlying reasons for these geometric differences were the same as in the Cal Stat B-D sets. Firstly, the outer limit of peripheral zone fracturing at the surface again extended slightly further outside the projected edge of the honey reservoir along the model short axis than along the model long axis. Secondly, the surface limit of the central zone (defined by the outermost reverse-fault scarp) usually occurred at a slightly greater distance inward from the projected reservoir edge along the short axis than along the long axis, or at a similar distance along both axes.

The further outward appearance of peripheral surface fracturing from the reservoir edge along the short axis vs. the long axis was again usually reflected in upward divergence of reverse and normal faults from just above vs. far above the magma chamber edge (contrast A- and C-ends of Cal Stat F7 – **Figure 4.16**). Normal faults near the point of maximum subsidence on the long axis were usually steeper and less deeply penetrating than on the short axis (Cal Stat F8 was an exception). Also, the normal faults on the long axis commonly formed as the upper part of a hybrid reverse-normal fault (e.g. at the A-end of Cal Stat F7 - **Figure 4.16**), rather than as a discrete fault or as a branch from the reverse fault (e.g. at the C- and D-ends of Cal Stat F7 - **Figure 4.16**). Normal faults in the extensional hinge zone located at the opposite end of the long axis were conversely very well developed and penetrated all they way to the chamber top (e.g. at the A-end of Cal Stat F7 - **Figure 4.16**), but still did not extend far beyond the reservoir margin. Thus, although some of the extensional fault development related to the highly asymmetric subsidence and the correspondingly strong component of horizontal motion toward one end of the long axis, the overall arrangement mimicked symmetric or slightly asymmetric collapses with centred conduits.

The appearance of the reverse fault trace further inward from the reservoir edge along the short axis is again mostly reflected in the generally shallower overall dips of reverse faults on the short axis compared with those on the long axis (**Figure 4.16 - see also Table 4.3**). In some cases, around the point of maximum subsidence, the dip of the reverse fault along the long axis often decreased dramatically very near surface (e.g. at the A-end of Cal Stat F7 - **Figure 4.17**). This caused the surface trace to sometimes appear at a similar distance inward from the reservoir edge to that of reverse faults on the short axis, despite the overall steeper dip of the reverse fault on the long axis.

The final width of the peripheral zone was therefore again greater on the short axis than on the long axis in 9 out of 12 experiments (Cal Stat E1, E3 – **Figure 4.14d**, E4, F2-F6, F8), even though most subsidence occurred around the latter. Horizontal inward motion of the peripheral zone was most commonly roughly equal on both axes, though it was in some cases slightly greater on the long axis adjacent the point of maximum subsidence - e.g. Cal Stat E3 (**Figure 4.14d)**. In all these cases, however, the initial distance from the outermost tension fracture to the point of reverse fault trace nucleation was 0.5 – 1.0 cm greater on the short axis than on the long axis. This difference exceeded any horizontal inward motion, and so was again the main factor in determining the circumferential variation in peripheral zone width.

The circumferential variation in deformation style seen on either axis in the Cal Stat B-D sets was thus replicated also. Some differences are not so pronounced, however, mainly because of the focussing of maximum subsidence at one long axis end. In particular, intensity of faulting on the short axis was in most cases similar to that on the long axis end with most subsidence (**Figures 4.14d, 4.15e & 4.16**). However, peripheral normal faults and associated marginal gräben again more numerous and better developed on the short axis. Vertical displacement at the long axis end next to maximum point of subsidence is taken up almost exclusively on steep reverse faults. As in other collapses, reverse faults usually show upward decreasing displacement, whereas normal faults show downward decreasing displacement (**Figure 4.16**). Overall, faulting again took up a slightly greater proportion of the net subsidence on the short axis, whereas sagging took up a slightly greater proportion of the net subsidence on the long axis.

In summary, the laterally-sited conduit did not seem to have any major effect on either development of early sagging, the position of initial roof failure (i.e. main reverse ring fault localisation), or overall reverse fault 'unzipping' patterns. In relation to the latter, it is worth noting that a more central conduit (Cal Stat E set) did not promote bidirectional reverse fault propagation from two nucleation sites (**Figure 4.13**). Likewise, a more off-centred conduit (Cal Stat F set) did not promote mainly unidirectional reverse fault propagation from one nucleation site (**Figure 4.13**). Outer normal ring-fault development was similarly unaffected.

Once the roof had failed, however, the off-centred conduit position strongly influenced subsidence symmetry and induced some second-order effects on the reverse fault propagation and the position of secondary reverse fault localisation. Every collapse became highly asymmetric, with the point of maximum subsidence rapidly shifting to the long axis end adjacent the conduit. This caused the first formed reverse faults to propagated more rapidly toward this long axis end, and either link or pass around it. The pronounced conduit-induced asymmetry also caused localisation of late stage, inner reverse faults near or around the long axis end adjacent the conduit. Thus an overall more compressive deformation and more intense faulting at the end of the long axis adjacent the conduit resulted in the later stages of deformation. The offset conduit position and associated subsidence asymmetry did not notably influence the geometric relationships between the ellipticities of the peripheral zone, central zone, and the reservoir margin, however (**Table 4.4**).

4.3.5 Collapse of 'thick' elliptical roofs: kinematics

Although some noteworthy geometric and developmental differences were also found, the structural evolutions and geometric attributes of 'thick-roof' collapse in Cal Stat G1-G2 and Cal Stat G3-G4 broadly approximated those of their equivalent 'thin roof' sets - Cal Stat F and Cal Stat C respectively. Models Cal Stat G2 (**Figures 4.17 & 4.18**) and Cal Stat G4 (**Figures 4.19 & 4.20**) illustrate many of the main points. Results of this set were less internally consistent, which may reflect the lower sample size (4 experiments) or a more inherent variability and complexity of 'thick roof' collapse.

As in 'thick-roof' circular collapse (**Chapter 2**), neither pre-failure sagging nor marginal tension fracturing was initially very pronounced in 'thick-roof' elliptical collapse (**Figures 4.17a & 4.19a**). In Cal Stat G2 and G3, two arcuate reverse faults localized in rapid succession around either of the reservoir's short axis ends, and rapidly propagated to one of the long axis ends of the reservoir, where they linked (**Figures 4.17a-c & 4.21**). Unusually for elliptical collapse, but like thick-roof circular collapse (Cal Stat H1-H2, **Figure 4.21**), the reverse ring-fault in Cal Stat G4 localised almost instantaneously all around the reservoir (**Figure 4.19a-b**). Even more unusually for an elliptical collapse, the reverse fault trace in Cal Stat G1 first appeared at one end of the *long* axis and from here propagated bi-directionally to the opposite end (**Figure 4.21**).

Once the reverse ring-fault had formed, subsidence of the central zone again became slightly asymmetric. Compared to that in conduit-centred Cal Stat G3-G4, subsidence asymmetry was more pronounced in Cal Stat G1-G2, where after failure the central caldera zone rapidly tilted and moved horizontally toward the off-centered conduit (as in the Cal Stat E and F sets). In Cal Stat G2 (**Figure 4.17c**), onset of asymmetry and horizontal motion led to deactivation of the first-formed reverse fault, around which the second-formed reverse fault propagated in a wider diameter arc toward the opposite side of the reservoir. As previously, the horizontal component to subsidence in the highly asymmetric Cal Stat G1 and G2 collapses also caused the outer normal fault system to first form opposite the maximum point of subsidence (**Figure 4.17c**). From here, the normal fault again propagated bi-directionally around the reservoir. Unusually, the normal fault system in both G3 and G4 nucleated at each end of the reservoir's long axis, and propagated bi-directionally from there toward the ends of the short axis (**Figure 4.19c-d**).

Second-generation reverse faults cut through the caldera floor *outside* the earlier reverse ring-fault (**Figure 4.21**) in most 'thick roof' elliptical collapses. As in other experiments (e.g. Cal Stat A5, H2 (**Chapter 2**) & Cal Stat F7 – **Figure 4.15**), these second-generation reverse faults usually first nucleated around the area of maximum subsidence and propagated laterally to link with the outer normal fault. At the surface, they comprised two types: 1) obliquely-trending splays from the first-formed reverse fault (most common – e.g. Cal Stat G2 – **Figure 4.17c**, G3, & G4 - **Figure 4.19c**), or 2) seemingly independent sub-concentric faults (e.g. Cal Stat G2 - **Figure 4.17d**). At depth, however, both types often linked to the first-formed reverse fault or the outer normal fault (e.g. Cal Stat G2 – **Figure 4.18**). Faults seen at the surface were thus often splays from a single sub-vertical shear zone at depth - (e.g. A-end of Cal Stat G2 – **Figure 4.18**). As in circular thick-roof equivalents (**Chapter 2**), formation of second-generation reverse fault splays usually caused partial deactivation of the first-formed reverse ring-fault (e.g. Cal Stat G4 - **Figure 4.19c**), as displacement accumulation transferred to the newly-formed faults. In 2 of the 4 experiments, second-generation reverse faults localized along or splayed from the 'long side' of the reservoir, (**Figures 4.17c-d & 4.19c**). Unlike in 'thin roof' elliptical experiments, no late-stage *inner* reverse faults developed in the 'thick roof' elliptical experiments.

Although slightly lower sand/gypsum cohesion limited their resolution here, complex extensional fracture systems and marginal gräben again formed in the outer part of the peripheral zone (Zone 3 in **Chapter 2**). As in equivalent 'thin-roof' experiments, these extensional fractures were best developed along the 'long sides' of reservoir in all the 'thick-roof' elliptical experiments (Marti et al. 1994; Roche et al. 2000) (**Figure 4.2)**, often in the hanging walls of the second-generation reverse faults (**Figures 4.17e & 4.19d –** cf. Cal Stat H1-H2 in **Chapter 2**). The width of the area of extensional faulting was also similar to that in other collapses, whether circular or elliptical, 'thin-roof' or 'thick-roof'. In the inner part of the peripheral zone (Zone 3 in **Chapter 2**), i.e. between the first-formed reverse ring fault and the area of extensional faults, oblique thrusting along the reverse fault splays accommodated concentric shortening (**Figures 4.17d & 4.19c**).

Towards the experiment end, over-steepened faults scarps - particularly those of the inner reverse fault and the outer normal fault, again decayed to form grain flows (**Figures 4.17e & 4.19e**).

4.3.6 Collapse of 'thick' elliptical roofs: geometric features

Geometric relationships between the peripheral zone, central zone and magma chamber were broadly similar to those in 'thin roof' elliptical collapses, but also showed a noteworthy difference. The surface limit of peripheral fracturing was again less elliptical, and the surface limit of the central zone more elliptical, than the reservoir margin than the reservoir margin (**Table 4.4**). The diameter of the central zone was smaller in Cal Stat G experiments than in equivalent 'thin-roof' experiments (**Table 4.4**). Central zone dimensions in 'thin-roof' A/B=1.5 collapses measured 7.5-9.1 cm x 3.7–5.4 cm, whereas central zone dimensions in 'thick-roof' A/B=1.5 collapses measured 5.8-7.9 cm x 3.3–4.0 cm (**Table 4.4**). Central zone ellipticity was nonetheless roughly the same in A/B=1.5 'thick-roof' and 'thin-roof' collapses (**Table 4.4**). The diameter of the peripheral zone in Cal Stat G experiments differed from equivalent 'thin-roof' experiments, however (**Table 4.4**). Peripheral zone dimensions in A/B=1.5 'thin-roof' collapses measured 11.9-13.1 cm x 9.4-10.6 cm, whereas 'thick-roof' experiments measured 11.3-12.1 cm x 9.6-11.3 cm (**Table 4.4**). The thick-roof peripheral zone was thus roughly the same or slightly narrower along the long axis and was wider along the short axis compared to equivalent 'thin-roof' experiments. As a consequence, peripheral zone ellipticity was on average near circular (1.09 - **Table 4.4**) in 'thick-roof' collapses (**Figure 4.19e**).

The decrease in central zone diameter with a thicker roof reflects the decreased diameter of the trace of the conical reverse ring fault as the distance from the magma chamber top (base of the cone) to the surface is increased. If the variation in reverse ring-fault dip from the long axis to short axis remains the same, then the reverse fault trace should maintain the same ellipticity, regardless of the distance from magma chamber top to the surface (i.e. regardless of roof thickness). Indeed in cross-sections through elliptical ‘thick-roofs’ (**Figures 4.18 & 4.20; Table 4.5**), reverse fault dips are in general slightly steeper along the long axis (73-84°) than along the short axis (70-76°) - as observed in elliptical ‘thin-roofs’ (**Sections 4.3.1 & 4.3.2 above**). Parity between the ellipticities of the ‘thick-roof’ and ‘thin-roof’ central zones care thus related to a similarly roughly conical shape of the outward-dipping reverse ring fault.

Conversely, the decreased ellipticity of the peripheral zone in ‘thick-roof’ elliptical collapse compared to that in ‘thin-roof’ elliptical collapse reflected cross-sectional changes in: 1) the circumferential shape of the outer limit of fracturing and 2) the circumferential dip of main normal fault. Firstly, whilst the limit of peripheral fracturing extended outward from the reservoir margin by a similar distance along ‘thick-roof’ and ‘thin roof’ long axes (0 - 0.8cm), it extended outward by a much greater distance along the ‘thick-roof’ short axes that along ‘thin-roof’ short axes (1 – 2.0 cm vs. 1 - 1.3cm) (**Figures 4.18 & 4.20**). Secondly, and perhaps reflecting the first factor, normal faults in ‘thick-roof’ experiments dipped more shallowly on average along the short axis (70-85°) than along the long axis (80-89°) (**Figures 4.18 & 4.20, Table 4.5**), whereas normal faults in ‘thin roof’ experiments had roughly similar dips on both axes (**Table 4.3**).

Like most ‘thin-roof’ elliptical collapses, the peripheral zone width in all ‘thick-roof’ elliptical experiments was consequently greatest along the short axis (**Figures 4.17e & 4.19d**). The distance from the outermost tension fracture to the nucleation point of the first-formed reverse fault trace was again far greater on the short axis than on the long axis. Horizontal inward motion of the peripheral zone was also greatest in the short axis, but of comparable magnitude to that in the experiments with ‘thin roofs’. The greater width of the peripheral zone along the short axis thus primarily related to greater inward localisation of reverse fault trace and outward localization of normal fault trace from the reservoir edge, as reflected in shallower fault dips and a deeper point of upward divergence of the normal and reverse faults (**Figures 4.18 & 4.20**).

In cross section (**Figures 4.18 & 4.20**), strata of the central zone are sagged just above the reservoir, but are typically much straighter near surface. This reflects the less pronounced surface sagging relative to the thin-roof experiments. In general, reverse faults are also in general steeper in the ‘thick roof’ experiment relative to ‘thin-roof’ experiments (cf. similar observations by Odonne et al. 1999 and Kennedy et al. 2004). As seen in other experiments, displacements on reverse faults typically decrease upward, whilst displacements on normal faults usually decrease downward. Peripheral zone faulting in thick roof experiments was not generally as intense as in the thin-roof experiments (though this may be partly a function of lower material cohesion in the Cal Stat G set). In Cal Stat G2 and G4, greater extensional deformation around the short axis ends of the reservoir is again seen in the much better (or even exclusive) development of the outer normal fault and peripheral fault systems there. Nonetheless, peripheral extension seems to have mainly localized on the outer normal fault system; unlike in thin-roof collapses, the complex fracturing and key stone gräben seen inside it on the surface do not penetrate any appreciable depth (**Figures 4.18 & 4.20**).

4.4 Discussion

Firstly, the kinematic evolution of the elliptical collapses is discussed. A mechanical rationale is given for the localisation and propagation ('unzipping') patterns of reverse and normal faulting in experiment. Secondly, the experimental evidence is then integrated with observations from numerical and field studies of subsidence above elliptical hydrocarbon reservoirs to show that the physical models' closely reproduce geometric and kinematic aspects of elliptical subsidence in nature. Thirdly, it is proposed that the structural evolution of elliptical collapse seen in experiment may explain important aspects of the eruptive histories and structural behaviour of several elliptical calderas in nature. Finally, the distinctive geometric relationship between central and peripheral zone ellipticities of elliptical calderas, as noted in experiment, is shown to also characterise the plan-view geometry of several elliptical calderas. This similarity may thus help constrain the 3D structure of these calderas.

4.4.1 Mechanical rationale for patterns of reverse ring fault localisation and lateral propagation ('unzipping') above elliptical reservoirs

In experimental circular collapses, reverse ring faults either localised synchronously right around the reservoir circumference, or with any slight asymmetry to sagging, as was common in 'thin-roof' experiments, localised along an arc nearest the area of most pre-failure subsidence. In elliptical collapses, pre-failure sagging almost always led to initial failure around the ends of the elliptical reservoir's short axis. If there was any asymmetry to sagging in 'thin-roof' experiments, reverse faults initially formed around the end of the short axis nearest the area of most pre-failure subsidence.

Localisation of initial failure in the reservoir roof is thus closely linked to the pre-failure strain induced in the roof by the depressurised reservoir. The reservoir roof initially undergoes roughly centrally-directed sagging, and ultimately fails along a shear fracture, which dips outward with a reverse sense of slip. This shear fracture is in Riedel orientation, and localises with sufficient vertical shear strain (γ) - or angular shear (ψ), since $\gamma = \tan \psi$ - between the down-going roof and its comparatively unaffected surrounds (cf. Roche et al. 2000 **- Figure 4.22**).

For a circular reservoir roof, net angular shear and shear strain from the roof centre to the unaffected surrounds should be equal on all cross sections. This is because the vertical displacement at the roof centre is accommodated over the same horizontal distance on any line of section. The locus of initial failure in circular roofs should thus ideally occur as a complete ring, but with subtle anisotropies in roof loading it may instead occur as an apparently randomly located arc (e.g. **Figure 4.10 Aii**).

In an elliptical roof, however, net angular shear and vertical shear strain are at a maximum along the roof's short axis, since here the vertical displacement at the roof centre is accommodated over the shortest horizontal distance. Conversely, they are at a minimum along the roof's long axis **(Figure 4.22 a,b)**. Angular shear along either axis peaks at the zone of maximum angular deflection of the roof from horizontal. This zone occurs just inside the reservoir margin, around the inflection points of the roof's deflection profile **(Figure 4.22e,f)**. As they are proportional to the net angular shear, peak angular shear and peak shear strain are also greatest along the short axis. Ultimate failure of a down-warped elliptical roof via a shear fracture therefore first occurs along, and near the end of, the roof's shorter principal axis **(Figure 4.22e,f)**, and proceeds from there toward the long axis.

Reservoir ellipticity not only controlled initial localisation of experimental reverse faulting, but also strongly influenced the pattern of subsequent lateral propagation ('unzipping') of the reverse ring-faults, as inferred from observation of the fault traces. At low to moderate ellipticities (A/B = 1.33-1.5), the reverse fault initially localised around one end of the roof's short axis only. From here, the ring-fault propagated bidirectionally around the reservoir to the opposite end of the short axis (Unzipping Pattern 1 - similar to the circular collapses – **Figures 4.10 & 4.11**), or propagated mainly unidirectionally (clockwise or anticlockwise) around the reservoir, past the opposite end of the short axis, and on to one end of the long axis (Unzipping Pattern 2 - **Figures 4.10 & 4.11**). At high ellipticities (A/B = 1.5-2.0), two discrete reverse faults localised, one at each short axis end, and then each fault typically propagated bidirectionally toward the long axis ends (Unzipping Pattern 3 - **Figures 4.10 & 4.11**). Previous experiments (Roche et al. 2000) only tested A/B ratio = 2.0 and so found only unzipping Pattern 3. The results of this study show more diverse reverse fault unzipping patterns that can be systematically related to increasing roof ellipticity.

As A/B ratio increases, shear strain is increasingly greater on a roof's short axis than on its long axis for a given central subsidence. At intermediate A/B ratios (1.33-1.5), this disparity may still be low enough such that as anisotropies in roof load shift subsidence toward the end of the short axis where initial failure occurred. This delays or inhibits reverse fault formation on the opposite end of the short axis until after failure has occurred at both ends of the long axis, thus yielding a bidirectional propagation (e.g. **Figure 4.10 Bi-iv**). Similarly, if initial shear strain disparity is low enough and anisotropies in roof load rapidly shift subsidence toward one end of the long axis, a unidirectional unzipping pattern may result (e.g. **Figure 4.10 Ci-iv**). At high A/B ratios (~2.0), however, the initial shear strain disparity is so great that, regardless of anisotropies in roof loading, two discrete reverse faults always rapidly nucleate along the roof's short axis, one at each end, before propagating laterally toward the long axis (e.g. **Figure 4.10 Di-iv**). This increasing shear strain disparity with increasing ellipticity may also explain the apparent greater instability of more elliptical reservoirs noted by Roche and Druitt (2001).

4.4.2 Effects of conduit position and increased roof thickness on elliptical reverse ring-fault development

With either centrally-sited or laterally-sited conduits, development of sagging, initial reverse fault position, and overall reverse fault 'unzipping' patterns were essentially the same (**see Figures 4.11 & 4.13**). This precludes a major influence from the conduit on the initial patterns of first-generation elliptical reverse fault development, and shows that this development is primarily governed by roof geometry.

Second-generation *inner* reverse faults occurred only in 'thin-roof' experiments (e.g. **Figures 4.4e & 4.8d**). Second-generation inner reverse faults were not noted in previous analogue studies of caldera collapse (e.g. Branney 1995; Roche et al., 2000; Walter and Troll 2001; Kennedy et al., 2004). Successive nucleation of reverse faults in the central zone only occurred in an outward direction in these works. The observation of successive inward nucleation of reverse faults noted in this work may thus largely relate to the experimental method. These second-generation inner reverse faults usually also localised first around the ends of the model roof's short axis, but where subsidence was highly asymmetric due to an offset conduit, localisation shifted toward the ends of the long axis.

Second-generation *outer* reverse faults, as seen in previous work, formed concentrically to the first-formed reverse fault as a consequence of radial shortening, but occurred only in 'thick-roof' experiments. Only one such concentric second-generation reverse fault was noted in an elliptical collapse (**Figure 4.17e**), it also formed first around the model caldera's short axis. Second-generation *outer* reverse faults that splayed obliquely from the first-formed reverse faults occurred in both 'thin-roof' and 'thick-roof' experiments of this study, as a consequence of concentric shortening. These oblique-reverse faults sometimes also localised around the ends of the short axis (e.g. **Figure 4.15d),** or else splayed from the long side of the model caldera (**e.g. Figure 4.19c**).

In general therefore, the above mechanical explanation for the first localisation of reverse faults in a subsiding elliptical roof therefore seems to hold for nucleation of second-generation reverse faults also, although asymmetric subsidence may also play an important deviating role.

The exact effect of increased roof thickness on the elliptical ring fault development is slightly uncertain from the evidence presented here, probably because of the low sample size. Two out of four thick-roof elliptical collapses in this study displayed unzipping patterns seen in the equivalent A/B=1.5 'thin-roof' elliptical experiments – i.e. Patterns 2 or 3 (**Figure 4.21**). Roche et al. (2000) reported one elliptical collapse experiment with a very high thickness/diameter ratio; this also showed Pattern 3, as their thin roof collapses (**Figure 4.2b**). Two out of four thick-roof elliptical collapses in this study did not display this failure pattern, however. The reverse fault localised instantaneously all around the reservoir circumference in Cal Stat G4 (as in thick-roof circular collapses - **Figure 4.21**), and first formed at the end of the long axis in Cal Stat G1.

The increased effects of stress arching in thick roofs may account for departures from the usual pattern of initial reverse fault localisation around the ends of the short axis. Thicker roofs behaved more rigidly than thin roofs, as evidenced by minimal pre-failure sagging at the surface (**Figures 4.18a & 4.19a**) and unbent strata in the upper parts of the roof in cross-section (**Figures 4.19 & 4.21**). Such rigidity is compatible with the increased effects of stress arching due to increased roof thickness/diameter ratio (cf. Jones et al. 1993; Roche et al. 2000), which also acts to reduce the magnitudes of differential stress within the roof for a given pressure drop in the reservoir (cf. Folch and Marti 2004). With a thicker elliptical roof, the thickness/diameter ratio is increased much more along the short axis than along the long axis. The strengthening effect of stress arching should thus also increase much more along the short axis than on the long axis. Consequently, the differential in shear stress between the long and short axes as a result of initial chamber depressurisation may thus be less pronounced with a thicker roof. Localisation of the reverse fault may thus be almost synchronous around the reservoir roof, or if significant anisotropies exist in roof loading, may even first occur on around the end of the long axis. Another possibility is that the failure pattern observed in 'thin roof' experiments occurs at depth in the 'thick roof' experiments, but that the inheritance of these early structures may then induce greater variability in the subsequent pattern of generation and propagation of newer, higher-level faults that cut the surface. Further data, particularly from numerical models, are required to test these hypotheses.

4.4.3 Localisation and lateral propagation ('unzipping') of normal ring faults above elliptical reservoirs

Two factors, often in combination, controlled the initiation and lateral propagation of normal faulting in elliptical collapse experiments: 1) collapse symmetry, and 2) ellipticity. As in circular collapse experiments (**Chapter 2**), asymmetric collapse induced a component of horizontal motion in the central zone directed toward the point of maximum subsidence. Extension resulted in the hinge zone opposite the point of maximum subsidence, commonly at one end of the long axis, and consequently normal faulting often first localised there. At low ellipticities, the normal ring fault thus sometimes first localised at the end of the long axis co-incident the asymmetry-induced hinge zone (e.g. Cal Stat B5 – **Figure 4.4c**). Thereafter, normal faults usually next initiated around the short axis ends. At higher ellipticities, however, the normal ring fault first localised around the ends of the short axis and simultaneously at the end of the long axis (if coincident with a hinge zone) (e.g. Cal Stat C5 and F7 – **Figures 4.6 & 4.15**), or just first localised around the ends of the short axis (e.g. Cal Stat E3– **Figure 4.14**).

With symmetric collapse (linked with increased ellipticity), the outer normal faults first localised around the ends of the elliptical roof's short axis only and propagated toward the long axis end (e.g. Cal Stat D5 - **Figure 4.8b-d**). Normal fault unzipping therefore often mimicked that of the reverse faults, particularly at higher ellipticities (A/B = 1.5-2.0).

Conduit position did not seem to greatly affect these localisation patterns of the normal ring faults. Whilst increased roof thickness caused some deviations (first localisation at both ends of the long axis even with fairly symmetric subsidence), further data are required to assess its significance.

4.4.4 Evidence from existing analytical solutions, numerical models, and subsidence at elliptical hydrocarbon reservoirs

Analytical solutions used by engineers to calculate deflection profiles and stresses arising in uniformly loaded, elliptical or rectangular, elastic plates - similar to elongate magma chamber roofs under gravity – lead to similar conclusions to those from the above experimental results (Timoshenko & Woinowsky-Krieger 1959, Sato 2006). With relatively restrained plate edges, such as would be expected for a magma chamber roof, these solutions predict down-flexure toward the plate's centre, with maximum angular deflections, shear strains, and shear stresses near the ends of the plate's short axis. Bending stresses and marginal tensile reactions to central down-flexure also peak along the elliptical plate's short axis (Timoshenko & Woinowsky-Krieger 1959, p.312). This may account for both the general initiation and the greater intensity of tensile fractures and normal faults at the ends of the elliptical roof's short axis in experiment (cf. **Figures 4.10 & 4.22c**).

Such analytical solutions apply most rigorously to relatively thin plates, but Boundary Element models of surface subsidence profiles above depressurised, elliptical, and 'thick-roofed' hydrocarbon reservoirs (Gambolati et al. 1987 - **Figure 4.23**) also broadly agree with the experimental deflections profiles. In the two models shown (**Figure 4.23a-b** - Gambolati et al. 1987), the steepest surface slopes (i.e. greatest angular deflections) occur along the short axis and just inside the edge of the reservoir, as seen in experiment (e.g. **Figure 4.10, Di**). Furthermore, the disparity in angular deflection of the surface (i.e. in vertical shear strain) between the long and short axes is much greater above the more elliptical reservoir (**Figure 4.23c-d)**, as suggested in the theoretical explanation of experimental unzipping patterns in **Section 4.1.1**. The ellipticities of the vertical displacement contours with respect to the ellipticity of the reservoir in the numerical models also strongly parallels the relative ellipticites of the peripheral zone, central zone, and reservoir in experiment. The zone of steepest gradient just inside the reservoir edge encloses an area that is slightly more elliptical than the reservoir (**Figure 4.23a-b**). Conversely, the contours outside the reservoir (e.g. the 0.05 contour) define a peripheral area of subsidence that is less elliptical than the reservoir and tends to circularity with at great distance (Gambolati et al. 1987).

Moreover, calculated surface subsidence values above the model reservoir centre decrease with increasing ellipticity (Gambolati et al. 1987 – **Figure 23c,d**). This is consistent with increased rigidity resulting from an increased stress-arching effect, as the roof's thickness/diameter ratio increases along the short axis. A consequence of this increased rigidity is that bending becomes less important, and faulting more important, in the accommodation of subsidence along the roof's short axis (as in experiment - see **Figure 22c vs. d**).

Observed ('real-time') surface subsidence profiles, related to *upward* fluid extraction several elliptical oil fields, also strongly mimic those in experiment, as do fracture patterns. At the Goose Creek oil field, Texas (3.5 x 2.2 km - Yerkes & Castle 1976) and the Wilmington oil field, California (16 x 6 km - Allen 1968), elliptical subsidence profiles again closely match those in experiment, with the steepest gradients along the reservoir's short axis (**Figure 4.24a-b**). Moreover, after about 1 m of surface subsidence at Goose Creek oil field, early high-angle normal faults first appeared around each of the oil field's short axis ends (**Figure 4.24a** - Yerkes and Castle 1976). This mirrors the early localization of surficial tensile fractures and normal faults around the short axis end of the sagged elliptical roofs in physical models. Surface subsidence of nearly 9 m at the Wilmington oil field also generated horizontal surface displacements that, as in experiment, were directed radially in toward the centre of the subsiding area and were at a maximum along the subsiding area's short axis (**Figure 4.24b**). Moreover, earthquakes at Wilmington coincide with the steepest gradient of the deflected surface (i.e. the zone of peak angular shear), where they are associated with contraction (Kovach 1974 in Odonne et al. 1999 - **Figure 4.25a**). This is very similar to the location and mode of reverse faulting in the models (see **Figure 4.25b,c** - Odonne et al. 1999). Indeed, subsidence of 2.3m at the highly elliptical Buena Vista oilfield, California (16.9 x 6.6 km) not only caused maximum horizontal displacements along the short axis of the field, but also generated a reverse fault with a surface trace sited on the short axis and parallel to the long axis of the reservoir (Yerkes and Castle 1970 – **Figure 4.25d**). These observations of subsidence at depressurized hydrocarbon reservoirs, which represent analogues to the early stages of caldera formation and have similar upward fluid extraction direction, further support the experimental results' transferability to nature.

4.4.5 Unzipping Long Valley: an explanation for vent migration patterns during an elliptical ring fracture eruption in nature

The catastrophic 760,000 B.P. eruption of the Bishop Tuff from Long Valley caldera, California (**Figure 4.26a**), was the third largest volcanic outburst in Pleistocene North America (Mason et al. 2004). In only a few days to weeks, some 750 km^3 of rhyolite erupted and a magma chamber roof subsided by 2-3 km (Hildreth & Mahood 1986; Wilson & Hildreth 1997). Over half of the erupted tuff consequently ponded within a highly-elliptical, 32 x 16 km caldera, but an area of >2200 km^2 around the caldera was buried under >200 km^3 of ignimbrite. Also, at least 50 km^3 of ash-fall blanketed an area of over 8,100,000 km^2 stretching from California to Kansas (Izett et al.

1982). Long Valley caldera is now resurgent and restless, and so is one of the world's most closely monitored volcanoes (see Newhall & Dzurisin 1988 and Sorey et al. 2003 for reviews).

Hildreth & Mahood (1986) and Wilson & Hildreth (1997) constrained the temporal and spatial evolution of Bishop Tuff vents through detailed petrologic, lithologic, and stratigraphic studies of successively erupted extra-caldera deposits. These authors also estimated the short duration of the Bishop Tuff eruption from model calculations of fall deposit accumulation and from the observations of compound cooling zonations and insignificant erosion or reworking between successive eruptive units. Several fall units and two major ignimbrites - an earlier pyroxene-free 'Ig1' and a later pyroxene-bearing 'Ig2' (Wilson & Hildreth 1997) – were erupted. The letters E, N, NW, etc. denote the extra-caldera sector in which an ignimbrite is found, and lower case letters a,b,c, etc. denote ignimbrite sub-packages up-section.

The eruption began on the caldera's southern side with a sustained Plinian outburst in the caldera's SSE sector, as constrained by the early fall deposits hosting lithics from Mt. Morrison Pendant metasediments and Wheeler Crest Monzonite only (Hildreth & Mahood 1986 – **Figure 4.26b**). Ig1 is coeval with early Plinian fall units, and similar lithic suites indicate a similar vent location. However, the overlying Ig2E displays marked up-section increases in the proportion of Glass Mountain rhyolite lithics from Ig2Ea to Ig2Ec (Wilson & Hildreth 1997). This is thought to reflect vent migration as a result of ring fracture propagation from the SSE caldera sector to the E sector **(**i.e. from near the end of the caldera's short axis toward the end of its long axis - **Figure 4.26c**). Granodiorite fragments (Hildreth & Mahood 1986) suggest some fracture propagation to the SW also. Significantly, Glass Mountain clasts in Ig2E are typically weathered and rounded; fresh angular rhyolite is rare. The southern ring fracture thus passed through Glass Mountain's volcaniclastic apron, but not into the Glass Mountain edifice (i.e. did not cross the caldera's long axis - Wilson & Hildreth 1997 - **Figure 4.26c**).

On the caldera's northern side, Ig2NW slightly predates Ig2N. Metamorphic and basalt fragments are abundant in Ig2NWa, granitoid and quartz-latite lithics are rare and Glass Mountain rhyolite lithics are absent (Wilson & Hildreth 1997). This constrains the earliest Ig2 vent site to the zone of basaltic and metamorphic rocks on the caldera's northern side - perhaps S or SW of Bald Mountain (**Figure 4.26b,c**). Glass Mountain rhyolite lithics dominate Ig2Na and Ig2Nb, however, and fresh angular Glass Mountain rhyolite is particularly abundant in upper Ig2Nb. This reflects propagation of the northern ring-fracture vents from the NNW caldera sector, to the NE sector, and through the Glass Mountain edifice (Wilson & Hildreth 1997 - **Figure 4.26**).

Wilson & Hildreth (1997) hence proposed that two separate ring-fractures formed simultaneously in the north and south of the collapsing Long Valley caldera, and propagated toward the east (**Figure 4.26**). These authors acknowledged that the exact reasons for this peculiar pattern of ring-fracture 'unzipping' were unclear, however. That a "deep-seated line of weakness" might have localised the points of initial ring fracturing was suggested, since the initial Plinian and ring fissure vent sites seems aligned along the main NW-SE regional fault trend (Wilson & Hildreth 1997). Later, Lavallee et al. (2004) speculated from experimental evidence that a topographic load exerted by Glass Mountain (**Figure 4.26a**) might have caused the ring fractures' propagation toward the east. Intriguingly, Roche et al. (2000) noted similar ring-fracture development to that at Long Valley caldera in a physical model of a subsiding reservoir roof that simply had an elliptical plan-view shape. Their model only tested one value of plan-view ellipticity, however, and the reason for this result was unexplained

The new physical modelling data of this study systematically illustrate how a range of magma chamber plan-view ellipticities may affect patterns of ring-fracture localisation and propagation during roof subsidence (**Figures 4.10 & 4.11**). The attributes of the pre-collapse Long Valley system are most closely replicated by the highly-elliptical 'thin-roof' experiment subset. The length ratio, $l^* = l_{Model}/l_{Nature}$, was 5×10^{-6}, 1 cm in the models scales to ~ 2 km in nature. If it is assumed that the diameter of Bishop Tuff reservoir was smaller than the present 32 x 16 km topographic outline of Long Valley caldera (as would be generally predicted from experimental evidence), the ideally 14 x 7 cm model reservoirs (actually 13 x 6.5 cm: A/B = 2.0) thus approximate the dimensions of the pre-collapse Bishop Tuff reservoir. In addition, and the model reservoir's 3 cm depth also scales closely to the ~5-6 km pre-eruptive depth of the Bishop Tuff reservoir (Anderson et al. 2000). With a temperature of 700-800°C, crystal content of 1-25 vol.%, and H2O content of 4-6 wt.% (Anderson et al 2000; Hildreth and Wilson 2007), erupted Bishop rhyolite viscosity was probably ~10^5 - 10^7 Pa.s (Wolff et al. 1990; Dingwell 1999). When its mushy to semi-solidified margins (Hildreth and Wilson 2007, p. 982) are also considered, however, the Bishop reservoir's bulk viscosity was likely much higher, and the median honey viscosity of 400 Pa.s, which scales to $\eta_{nature} = 3.6 \times 10^9$ Pa.s, may approximate this.

Collapse into the thin-roofed and highly-elliptical (A/B = 2.0) model reservoirs very closely and most consistently reproduced the ring fracture evolution inferred at Long Valley (**Figures 4.10 & 4.11**). Model collapses with lower ellipticities and thicker roofs either failed to reproduce the observed patterns, or else did so inconsistently. In nature, factors identified by previous workers such as regional faults and topographic loading (Wilson & Hildreth 1997; Lavallee et al. 2004) may have exerted complementary influences on the pattern of ring fault development. For instance, faults could have influenced the exact position of vents around the ends of the short axes. The NW-SE faults cannot have readily caused the ring fractures' W-E propagation, however. It is also possible that the proposed point load effect from Glass Mountain might have acted like the off-centred conduit position in experiments of this study - i.e. by effectively increasing loading at a certain point in the roof and so promoting ring fault propagation toward that point. Such factors may have exerted some complementary influences on the pattern of ring fault development, but on balance, the evidence presented here strongly suggests that these factors were secondary to highly elliptical roof geometry. Even without differential loading or mechanical anisotropy, Long Valley's thin and highly elliptical roof geometry (from caldera dimensions, $A/B \geq 2.0$) could by itself produce *both* the localisation *and* the migration of ring fractures inferred for the Bishop Tuff eruption.

The experimental and numerical evidence presented in this work thus leads to a simplified explanation for the pattern of vent migration and ring-fracture unzipping at Long Valley, and relates it to two interlinked factors: 1) the high ellipticity of the pre-collapse magma chamber roof; and 2) the occurrence, upon the onset of chamber depressurisation and roof sagging, of maximum pre-failure shear strain along the elliptical roof's short axis.

4.4.6 Location and migration of ring fracture vents at other elliptical calderas

Long Valley caldera is not alone in having initial vent position and migration patterns compatible with the evolution of elliptical subsidence and ring-fracturing in the experimental models. At the N-S elongated Campi Flegrei caldera (17 x 11.5 km), Italy, Rosi et al. (1996) inferred from a similar study of lithics that early vents during the caldera-forming eruption of the trachytic Campanian Ignimbrite were located in the east. Variability of lithic populations in higher eruptive units is also suggestive of vent migration in later phases of this eruption (Rosi et al. 1996). At Suswa caldera (11 x 8.6 km), Kenya, vents for syn-collapse trachytic lavas and ignimbrites occur along a set of concentric fractures ('Ring Feeder Zone' - **Figure 4.27a**) lying just outside the main caldera ring fault and best expressed where straddling the ends of the caldera's short axis (Johnson 1969; Skilling 1993). At the Laacher See depression, Germany (3.5 x 2.5 km), syn-collapse ignimbrite vents are thought to have migrated along the 'long side' of the collapsing volcano (**Figure 4.27b –** Van den Bogaard & Schmincke, 1984; Freundt et al., 2000) in a fashion similar to those at Long Valley. It thus seems possible that these patterns relate to the localization and propagation of ring fractures during subsidence of an elliptical magma chamber roof.

At some elliptical calderas, major vents are located at or near the short axes of ring fractures that were formed in *earlier* collapse events. The caldera of Volcan Alcedo, Galápagos Islands (8 x 5.5 km - Geist et al. 1994) is one such example and is the only active Galapagos volcano to have erupted rhyolite (~ 1 km^3), most of which blanketed the island with a distinctive Plinian tephra layer. The main vent for this ~ 120 ka eruption is preserved along the ring faults in the SW of the caldera, near the end of the caldera's short axis (**Figure 4.27c-d**). As at Long Valley, a second 'hidden' ring-fracture vent is suspected to have opened late in the eruption and on the opposite side of the caldera (Geist et al. 1994). The caldera probably formed prior to rhyolite eruption, however, as sub-rhyolite basalt flows show thicknesses (~20m) consistent with lava lake ponding (Geist et al. 1994). The main rhyolite vent is located on or just outside an inner 'moat-fringing fault', the last movement on which postdates the rhyolite and has left the central part of the caldera up-thrown with respect to the moat. The dip and nature of this fault are unclear. From comparison to the experiments, the fault could represent an inner normal fault bounding a marginal graben, or a reactivated (inverted) outward-dipping reverse fault. Alcedo's rhyolite eruption nonetheless seems to represent a case where eruptions are focused at the ends of the short axis of pre-existing elliptical ring fault systems, as might be predicted for renewed subsidence of an elliptical reservoir roof.

A noteworthy observation is that vents at Suswa, and possibly Alcedo, are not only located around the short axis end of the caldera, but also seem to have formed in the extensional peripheral zone of the caldera (**Figures 4.27a & c–** Johnson 1969; Skilling 1993; Geist et al. 1994). This suggests that syn-collapse magmas may ascend up the main outer normal fault system and its associated minor normal faults as easily as up along outward-dipping reverse ring fault, although the latter pathway is the more classical view (e.g. Richey and Thomas 1932; Kokelaar and Moore 2006). Preferential localisation of syn-subsidence vents along peripheral normal faults near the ends of an elliptical caldera's short axis may be the result of greater horizontal extension and deeper penetration of normal faulting here, as seen in experiment (e.g. **Figures 4.5, 4.7 & 4.9**).

It is thus worth considering whether the ring fractures plumbing the Bishop Tuff magmas, for example, could have been reverse faults or normal faults (or both). It is more difficult to judge, however, implications of experimental normal fault unzipping patterns (see **Section 4.4.3** above) than those of experimental reverse fault unzipping patterns for natural vent migration patterns. This is because it is uncertain if a normal fault observed at surface in experiment had penetrated all the way down to magma chamber at any particular time (see **Chapter 2**), and so could tap magma. Conversely, reverse faults observed at the surface were always connected directly or indirectly to the reservoir at depth and so were potentially available to tap magma throughout their trace's lifetime. Nonetheless, the unzipping pattern of experimental normal faults at horizontal aspect ratios equivalent to that at Long Valley (~2.0) generally mimics that of experimental reverse faults. One could therefore conclude that the overall initiation and migration patterns of syn-collapse ring fracture eruptions at highly elliptical calderas, such as Long Valley, should be similar regardless of which ring fault systems the magmas ascend through.

Finally, deflation-related circumferential variation in horizontal displacement at the Sierra Negra caldera (9.1 x 7.1 km), Galapagos Islands closely matched that observed during subsidence into elliptical experimental reservoirs and hydrocarbon reservoirs (e.g. **Figures 4.24 and 4.25**). Analysis of Global Positioning System (GPS) data shows that from 2001 to 2002 Sierra Negra's caldera floor subsided symmetrically by 10-12 cm (Geist et al. 2006) with greater horizontal motion near the caldera's short axis than near the long axis (**Figure 4.28a**). Indeed, the best-fit numerical model for Sierra Negra's displacement field was a highly elongate deflating sill at ~2 km depth (Geist et al. 2006) (**Figure 4.28b**).

4.4.7 Implications for uplift-related faulting and eruption above horizontally elongate magma bodies

In theory, the concentration of stresses and strain at the ends of a an elliptical reservoir roof's short axis should also occur if the deformation occurs in the opposite sense – i.e. if the magma chamber expands rather than contracts and if the roof uplifts rather than subsides. Thus pre-collapse tumescence of an elliptical magma reservoir might cause initial location of uplift-related faulting and vents around the ends of the caldera's short axis. Faulting and vents associated with post-collapse uplift or resurgent doming might also be initially focussed on the short axis ends of the elliptical magma body, where either new volcano-tectonic faults may form or earlier collapse-related faults may undergo inversion.

At Sierra Negra caldera (**Figure 4.29a**), Galapagos Islands, analysis of interferometric synthetic aperture radar (InSAR) data showed inflation (1992-2001) prior to the deflation phase of 2001-2002 (Amelung et al. 2000, Jonsson et al. 2005, Geist et al. 2006). Inflation generated uplift of around 3 m and was mainly symmetric (**Figure 4.29b**), except from 1997 to 1998, when highly asymmetric or 'trapdoor' uplift was noted (**Figure 4.29c** - Amelung et al. 2000, Jonsson et al. 2005). The interferogram for 1997-1998 shows the point of maximum uplift in the S of the caldera, with an interferometric phase discontinuity across the inner part of the intra-caldera fault system (**Figure 4.29c**). The point of maximum uplift corresponds with maximum displacement on the inner ring fault system, as detected in the field by Jonsson et al. (2005) (**Figure 4.29 d-f**). Prolonged uplift at Sierra Negra thus ultimately led to faulting and trapdoor uplift (Jonsson et al. 2005 - **Figure 4.29b-c**), with initial failure focused at near the ends of the caldera's short axis – exactly the inverse of what happened in the elliptical experimental models of subsidence.

At the rhyolitic Rabaul caldera complex, Papua New Guinea, (14 x 8 km - Nairn et al. 1995), there are two major vents, Tavurvur and Vulcan (**Figure 4.30a**), on opposite sides of the caldera. Although there is no obvious tectonic or other lineament connecting them (Nairn et al. 1995), these vents erupted simultaneously in 1878, 1938-43, and 1994 (Newhall and Dzurisin 1988, Saunders 2001). Rabaul caldera complex comprises at least three nested subsidence structures, the latest of which probably formed during the 1400 BP eruption of the 11 km^3 Rabaul Ignimbrite (Nairn et al. 1995 - **Figure 4.30a**). Within the topographic margin of the 1400 BP caldera, recent and ongoing seismicity at Rabaul has uniquely allowed the definition of a steep, mainly outward-dipping elliptical ring fault (**Figure 4.30a**- Mori and McKee 1987; Nairn et al. 1995: Jones and Stewart 1997).

Two facts render difficult a direct comparison between Rabaul and the experiment results. First, the seismically-active ring structure is geometrically complex; the data are compatible with two partially linked elliptical ring structures, a smaller shallow ring and a larger deep ring (Jones & Stewart 1997; Saunders 2001 - **Figure 4.30b**). Second, the tomographically-imaged magmatic system beneath the ring fault also has a very complex 3D geometry (Finlayson et al. 2003).

Nevertheless, it seems noteworthy that Vulcan is located along the short axis of both the 1400 BP caldera and the deeper ring structure (**Figure 4.30b-c**). Tavurvur is not located on the short axis of the 1400 BP caldera, but does lie along the short axis of the shallower part of the seismically active ring structure.

In 1994, these two vents erupted at the end of a phase of elliptical tumescence (Saunders 2001), heralded by two major (M5.1) earthquakes at 1.2 km depth in the east part of the seimic zone, near Tavurvur (McKee et al. 1994). Seismic activity then abruptly switched to the west part of the seismic zone, near Vulcan, where a remarkable pre-eruption uplift of ~ 6 m was recorded. Vulcan and Tavurvur then started to erupt almost simultaneously on September 19th (McKee et al. 1994). Eruption was much more powerful at Vulcan, but longer-lived at Tavurvur. During the eruption, the ground subsided at a slowly declining rate, with several strong earthquakes on the caldera ring fault (possibly in the SE part) on September 23rd, as the system adjusted to the withdrawal of magma (McKee et al. 1994). These earthquakes seemed to herald a decline in the vigour of the eruptions at both vents, but especially Vulcan, which stopped erupting on October 2nd (McKee et al. 1994). Tavurvur persisted erupting in association with further surface subsidence, but activity eventually petered out on December 23rd (McKee et al. 1995).

A curious feature of Rabaul caldera is that Volcan and Tavurvur do not lie on the trace of the seismically active ring fault, but are located about 0.5-1 km outside it (Mori and McKee 1987; Saunders 2001). By comparison with the experimental models, this would position both vents in the extensional peripheral zone formed during the initial collapse, perhaps even on the trace of the main outer normal fault. It seems plausible that inversion of this main outer normal fault as a reverse fault could occur during elliptical tumescence (cf. Acocella et al. 2000, 2001, Walter and Troll 2001). Tumescence-related reverse faults in experiment display a substantial component of dilation across them (cf. Walter and Troll 2001), and so are potentially good magma conductors. A similar explanation for Volcan and Tavurvur's outward locations from the seismically active ring fault was proposed by Saunders (2001), who noted that in cross section the earthquake epicenters spread at shallow levels and may define inward-dipping faults or extensional fractures (**Figure 4.31c**). From the experimental results here, and by analogy with tumescence-related reactivation of the elliptical ring fault system at Sierra Negra caldera, it seems possible that the vent positions at Rabaul might be related to elliptical doming and reactivation of the collapse-generated peripheral normal fault systems by focusing of strain at the ends of the caldera's short axis.

4.4.8 3D geometry of experimental elliptical calderas and associated ring faults

This study provides the most comprehensive three-dimensional models of the structures accommodating caldera subsidence into an elliptical magma reservoir to date. Both in plan view and in cross-section, striking circumferential variations in deformation style and ring fault geometry were observed in model elliptical collapses.

In plan view, model calderas formed by collapse into elliptical reservoirs consistently showed a distinctive geometry, whereby the limits of the peripheral zone, reservoir, and central zone were respectively of greater ellipticity (**Figure 4.12**; **Tables 4.2 & 4.4**). On the whole, this geometric characteristic was demonstrably independent of roof thickness and of subsidence symmetry, and therefore seems to be an inherent property of elliptical collapse. Consequently, the peripheral zone was consistently widest along the caldera's short axis and narrowest along its long axis. This circumferential variation in peripheral zone width resulted because 1) horizontal motion of the peripheral zone toward the caldera centre, and 2) the distance between the outermost extensional fracture and the nucleation point of the reverse fault trace, were nearly always greatest on the short axis. Of there two factors, the second was the more important.

Cross-sections through the 'thin-roof' models reveal that the circumferential difference in peripheral zone width in plan reflected two features at depth. Firstly, the outward dips of reverse faults were usually gentler (ave. 66°) on the caldera's short axis and steeper on the long axis (ave. 77° - **Tables 4.3**). Consequently, the reverse fault trace appeared further inward from the reservoir edge along the short axis than along the long axis (e.g. Figures **4.5, 4.7 & 4.9**). Secondly, extensional deformation was much deeper rooted, and spread out further into the sand away from the reservoir edge along the short axis than along the long axis. In 'thin-roof' experiments, the further outward appearance of the main normal fault(s) along the short axis did not on average reflect shallower dip there, however. The main normal fault(s) instead localised further outward from the reservoir, and so propagated further downward, along the short axis (hence the deeper-seated upward divergence of reverse and normal faults along the short axis cross-section (e.g. Figures **4.5, 4.7 & 4.8**). These circumferential variations in reverse fault dip and intensity of peripheral extension at depth are thus the macroscopic structural basis for why the limits central zone and peripheral zone at the surface were respectively more elliptical and less elliptical than the edge of reservoir.

In 'thick-roof' elliptical collapses, central zone ellipticities were broadly similar regardless of roof thickness, but average peripheral zone ellipticities were lower (i.e. caldera outline was closer to circular) than 'thin-roof' equivalents (**Tables 4.2 & 4.4**). This difference between 'thin-roof' and 'thick-roof' elliptical model calderas is thus related to the localisation of extensional faulting yet further outward along the short axis than along the long axis. In cross-section, this is reflected not only by further outward localisation, but also by shallower dip, of the normal fault along the short axis.

The circumferential variation in dip of reverse ring-faults is demonstrably unrelated to any circumferential variation in inward rotation – i.e. faults do not form at the same initial angle of dip then get rotated to shallower dips along short axis. At the end of many experiments, the steepest reverse faults (on the long axis) ran through strata with the highest inward dips (e.g. A-B sections of Cal Stat C5 and D5 – **Figures 4.7 & 4.9**). The circumferential variation in reverse fault dip must instead be established upon the fault's localisation. As discussed in **Section 4.4.1**, the reverse ring fault in experiment can be viewed as a Riedel shear that forms in a near-vertical shear zone between the down-going roof and the unaffected surrounds (Roche et al. 2000). The orientations at which faults and other structures localise in a shear zone strongly depend on the relative proportions of incremental shear strain parallel to the shear zone and shortening/extension perpendicular to the shear zone (cf. Ramsay and Huber 1983; Sanderson and Marchini 1984; Krantz 1995 – **Figure 4.31a**).

In simple shear, there is neither contraction nor extension perpendicular to the shear zone (**Figure 4.31a, centre**). The minor axis (Z-axis) of the incremental strain ellipse represents the direction of maximum incremental shortening in the shear zone, and lies in the same orientation as the maximum compressive stress ($\sigma 1$) at an angle of 45° to the shear zone (Sanderson & Marchini, 1984). Fold axes and thrust fault traces form perpendicular to the Z-axis, whilst veins, dykes and normal fault traces form parallel to the Z-axis. These structures are thus also initially orientated at 45° to the shear zone (**Figure 4.31a** - see also Woodcock & Schubert 1994). Riedel (R) shears and Anti-Riedel (R') shears are conjugate faults, the acute angle between which is bisected by the Z-axis **(Figure 4.31a**). Riedel shears form at an angle of 45°- $\phi/2$ to the Z-axis and so an angle of $\phi/2$ to the shear zone (Woodcock & Schubert 1994), where ϕ is the angle of internal friction of the deforming material (ϕ ~38°). Riedel shears thus initially form at ~19° to the shear zone in simple shear. If the central shear zone in **Figure 4.31a** is viewed as a cross-section through a vertical shear zone, rather than as a map, then the Riedel shears initially dip at ~ 71° (see also Roche et al. 2000).

In transtension, i.e. with a component of extension perpendicular to the shear zone, the Z-axis is rotated to lie at an angle of < 45° to the shear zone (Sanderson and Marchini 1984). Riedel shears consequently form at a lower angle to the shear zone than in the case of simple shear (**Figure 4.31a**), and if the shear zone is viewed as a cross section, they dip more steeply. In transpression, i.e. with a component of shortening perpendicular to the shear zone, the Z-axis is rotated to lie at an angle of > 45° to the shear zone (Sanderson and Marchini 1984). Riedel shears thus form at a higher angle to the shear zone than in the case of simple shear (**Figure 4.31a**), and if the shear zone is viewed as a cross section, they dip less steeply.

Sand-box experiments by Horsfield (1977) illustrate the effect of a component of horizontal extension within a zone of vertical shear on reverse fault orientations **(Figure 4.31b)**. These experiments simulated deformation of a sedimentary cover sequence as a result of the reactivation of a pre-existing basement fault. The orientation of the basement fault controls the relative proportions of incremental vertical shear and horizontal extension (**Figure 4.31b**). In the upper experiment, the vertical fault imparts little or no horizontal extension in addition to the vertical shear. Reverse faults form in Riedel orientation with dips of 63-72°, which is close to the orientation predicted in simple shear. In contrast, the experiment with an inclined fault imparts a component of horizontal extension in addition to vertical shear. In this case, reverse faults form with steeper dips of 78-83°, as would be predicted in transtension.

Numerical models of basement fault reactivation (Patton and Fletcher 1995) provide complementary insights into the geometric variations seen along the long and short axes of an elliptical caldera in experiment. In **Figure 4.32a**, reactivation of a high-angle reverse fault induces a strong component of horizontal shortening in addition to vertical shear in the overlying cover sequence. In **Figure 4.32c,** the basement fault is vertical so any component of horizontal shortening or extension is minimal. In **Figure 4.32a**, trajectories of conjugate faults are consequently rotated and should produce a very shallowly dipping Riedel shear, whereas in **Figure 4.32c**, a more steeply-dipping Riedel shear should result. In addition, the geometry of the zone of deformation (probably extensional – cf. Friedman et al. 1976) in the hanging walls of the potential reverse faults is different. In the case where there is a strong component of horizontal shortening with vertical shear (**Figure 4.32a)**, the zone of potential extensional deformation is wider and deeper than in the case where a component of horizontal shortening is minimal (**Figure 4.32c)**. Moreover, the conjugate fault trajectories suggest that peripheral normal faults may dip more shallowly with the stronger component of horizontal shortening than with minimal horizontal shortening. These numerically-predicted relationships in **Figures 4.32a & c** accord closely with those observed in experiment above the reservoir edge along the short axis and long axis respectively (**Figure 4.32b & d).**

In summary, the circumferential geometric variation of structures formed during elliptical caldera collapse can therefore, at least to a first approximation, be related to circumferentially varying components of horizontal contraction or extension above the reservoir edge as the roof subsides. The exact means by which these varying components arise is presently unclear; by analogy with the models of basement faulting and forced folding of a cover sequence, it most likely relates to the imposed geometry of downwarping of the roof upon initial reservoir decompression. Along the short axis of the down-going elliptical roof, vertical shear is inferred to occur with a greater component of horizontal contraction than along the long axis. This produces more shallowly-dipping reverse faults and a wider, deeper zone of extensional deformation along the short axis than along the long axis. In addition, the stronger horizontal contraction may cause peripheral normal faults to dip more shallowly along the short axis, as seen in some thick-roof elliptical collapse experiments. These geometric variations at depth are reflected in the characteristic plan-view pattern of a peripheral zone limit that is less elliptical than the underlying reservoir and a central zone limit that is more elliptical than the underlying reservoir.

4.4.9 3D structure of natural elliptical calderas: Rabaul, Sierra Negra, and Miyakejima

At Rabaul caldera (**Figure 4.33a**), seismic (Mori and McKee 1987; Jones and Stewart 1997) and tomographic evidence (Finlayson et al. 2003) indicate that the magma chamber top presently lies at 3-4 km depth. Assuming this depth value was same prior to formation of the 14 km x 8 km 1400 BP caldera, the range of thickness/diameter ratios for Rabaul's roof coincides within that in most 'thin-roof' experiments (**Table 4.1**). Indeed, the geometric relationship between the inner seismogenic ring and the outer topographic margin of Rabaul's 1400 BP caldera is very similar to the relationship between the main normal and reverse ring-faults in 'thin-roof' elliptical collapse experiments (**Figure 4.33b)**. The less elliptical 1400 BP topographic margin is aligned parallel to the more elliptical inner seismogenic ring structure, and the distance between the ring structures is at a maximum along the short axis ends of the caldera and at a minimum at the long axis ends. The ellipticities of the peripheral topographic margin (~ 1.34) and the central seismogenic ring (~2.57) seem intermediate between those for experimental collapses into reservoirs of A/B = 1.5 and 2.0 (**Table 4.2**). Indeed, inferring the position of the pre-1400 BP magma reservoir edge by comparison to the experimental structures (**Figure 4.33b**) gives a pre-caldera reservoir ellipticity of A/B = ~1.7 (**Figure 4.33a**).

Although the seismogenic ring fault is centred within the elliptical topographic margin of the 1400 BP caldera (Nairn et al. 1995), some uncertainty exists about whether the active ring fault was formed during the 1400 BP eruption or relates to a later, or even an incipient, collapse event (Saunders 2001). Given the close geometric similarity of the 1400BP topographic margin and the seismogenic ring to experimental elliptical calderas, however, the experimental evidence strongly suggests that the outer 1400 BP margin is indeed genetically related to the outward-dipping seismogenic ring fault system.

Sierra Negra's caldera in the Galapagos Islands displays a peripheral zone of complex, but predominantly normal faulting (**Figure 4.33c** - Reynolds et al. 1995). This extensional peripheral zone is widest at the short axis ends of the elliptical caldera and narrowest at the long axis ends – as in model elliptical calderas (**Figure 4.33d**). The peripheral zone lies between an outer, possibly inward-dipping normal fault and a prominent sinuous ridge of uplifted and down dropped blocks, many of which are steeply inward tilted. The area inside the sinuous ridge is presently uplifted with respect to the peripheral zone (Jonsson et al. 1995 - **see Figure 4.29**). From comparison with the asymmetrically-subsided thin-roof experimental models (**Figure 4.33d**), the sinuous ridge seems most likely to mark the course of an outward-dipping normal fault that defined the inner edge of a complexly faulted marginal graben formed during caldera collapse (see also Figure 10 of Reynolds et al. 1995). This marginal fault was subsequently reactivated during later and ongoing uplift (Jonsson et al. 1995 - **see Figure 4.29**). The inner side of the sinuous ridge, along which lavas dip steeply toward the caldera centre (**Figure 4.33c** - Reynolds et al. 1995) seems to correspond to the hanging wall of an inner, and presently buried, reverse fault (**Figure 4.33d** - see also Figure 4.10 of Reynolds et al. 1995). The eastern end of the caldera seems to be a hinge zone formed during asymmetric caldera subsidence (**Figure 4.33c-d**).

The outer structural boundary of Sierra Negra's caldera is also of lower ellipticity (~1.34) than the probable inner structural boundary (~1.8 - **Figure 4.33c**). These ellipticities are compatible with experimental data for thin-roof subsidence into reservoir of A/B = 1.5 (**Table 4.2**). Estimation of the pre-caldera reservoir margins by comparison to the experimental structures (**Figure 4.33c-d**) thus gives a pre-caldera reservoir ellipticity at Sierra Negra of A/B ~1.52.

In terms of diameter (just over 1km) and roof thickness/diameter ratio (~ 3.0 - Geshi et al. 2002), Miyakejima caldera, Japan (**Figure 4.33e**), can be considered to represent the opposite end of the spectrum of natural elliptical calderas to that represented by Rabaul and Sierra Negra. The roof thickness/diameter ratio of Miyakejima caldera was more extreme than simulated in this study, but the surface geometric relationship between inner reverse ring fault system and outer normal ring fault system is nonetheless again very similar to that in 'thick-roof' elliptical caldera experiments (**Figure 4.33f**). Not only is the distance between the ring structures (i.e. width of the peripheral zone) again greatest along the short axis of the caldera (**Figure 4.33e**) and the ellipticity of the central zone high (~ 1.46), but the ellipticity of the outer normal ring fault is very low (~1.01 - near circular).

The plan-view geometric relationships between the ellipticities of the peripheral zone, central zone and reservoir in the model elliptical calderas, and the variation of these relationships with increased roof thickness, thus seem closely replicated at natural calderas. By comparison with the experimental data, it thus seems possible to approximate the lateral dimensions of an elliptical pre-caldera reservoir in nature. The geometric similarities with experimental calderas is strong evidence that Miyakejima caldera's pre-collapse reservoir was elliptical, perhaps with an A/B = 1.33 (**Figure 4.33e**). Progressive subsidence led to mass wasting from the more circular outer normal ring fault scarp, however, and as a result the diagnostic elliptical inner reverse ring fault was subsequently completely buried. The final 'funnel-like' caldera measured 1.7 x 1.7 km. Inferring that a pre-collapse reservoir was circular from a caldera's circular topographic outlines may thus be erroneous when roof thickness/diameter ratios are high.

The three-dimensional architecture of elliptical collapse, as constrained in this study, therefore also seems generally applicable to natural calderas and other elliptical subsidence structures. For elliptical calderas like Sierra Negra and Rabaul, reverse ring faults should be more shallowly dipping along the short axis than along the long axis. In addition, the outer normal ring faults may have a shallower inclination along the short axis than along the long axis end, particularly with high roof thickness/diameter ratios (e.g. at Miyakejima caldera). Also, and although asymmetric subsidence toward the long axis (e.g. as inferred at Sierra Negra) may tend to equalise any disparity, structures accommodating peripheral extension should be better developed in lateral and vertical extent around the ends of the caldera's short axis.

4.4.10 Effect of vent position on subsidence

Non-centred vents exerted a strong control on symmetry of roof subsidence, once the roof had failed. The principal result was a preferential propagation of reverse faults toward the vent end of the chamber roof. The vent control may be related to creation of a pressure gradient across the magma chamber, with lowest magma pressure and hence reduced roof support in the vicinity of the vent. Since the vent's diameter of 0.8 cm scales to 1.6 km in nature, the vent's effect on collapse development may be greater models than might be expected in natural systems, perhaps in particular where natural magmas are of low viscosity (such that pressure differentials can be equalised more rapidly).

It is nonetheless worth noting that a link between the point of maximum subsidence and vent positions has been noted or postulated for some calderas - e.g. Snowdon caldera, Wales (Howells et al. 1986) and Bonanza caldera, Colorado (Varga and Smith 1984). In the former case, maximum point of subsidence is coincident with main vent position (Howells et al. 1986; Roche et al. 2000), as in experiment. In the latter case, however, the vent positions are not coincident with point of maximum subsidence, and preferential withdrawal of magma from one side of the caldera is suggested to have contributed to maximum subsidence on the other side. These apparently contrasting field relations in terms of vent position and maximum subsidence at Snowdon and Bonanza calderas, both asymmetrically subsided, highlight the uncertainty over the impact of vent position on caldera subsidence.

Numerical studies of caldera collapse evolution, where considering the presence also of a conduit (e.g. Roche et al 2001; Marti et al. 2000), assume pressure gradients with in the magma chamber due to the vent to be negligible. Whilst assumption of negligible influence of pressure gradients may be a reasonable approximation when the vent position is central (due to the symmetry of those gradients), the experiments in this study indicate that effects of pressure gradients due to an off-centred vent *may* be substantial. Future numerical work is suggested to more rigorously test the effects of the vent system and its position on the initiation and development of caldera collapse.

4.5 Conclusions

1) Combined with existing field and numerical evidence, new experimental evidence presented here confirms that the location of initial roof failure during subsidence into an elliptical reservoir is systematic and hence predictable. Indeed a similar pattern of fault initiation is observed or inferred at several elliptical oil reservoirs and calderas in nature. Failure in experiment occurs along reverse faults that consistently first localise near the ends of an elliptical roof's short axis. This is ascribed to the occurrence of maximum shear strain along the short axis at the onset of reservoir depressurisation and down-warping of the reservoir roof.

2) In simulating collapse into magma reservoirs of systematically varying plan-view ellipticity, a continuum of potential reverse fault unzipping patterns during elliptical caldera collapse was this identified. This continuum is bound by those end-member patterns characteristic of circular (A/B = 1.0) and highly elliptical (A/B = 2.0) plan-view geometries. Unzipping patterns at these geometries were more consistent, whereas unzipping patterns for intermediate ellipticities (A/B = 1.33 – 1.5) were more variable. Although it may also be sensitive to roof thickness/diameter ratio, the systematic variation of unzipping patterns with increasing roof ellipticity is related to the increasing disparity in shear strain around the down-warped elliptical roof as roof ellipticity increases.

3) Ring fracture unzipping patterns at the highly elliptical Long Valley caldera, as deduced from inferred vent migration patterns during the 760 ka Bishop Tuff eruption, match those observed in experimental collapse of roofs with A/B = 2.0. The long enigmatic evolution of ring fractures during collapse at Long Valley caldera is thus interpreted as a direct consequence of the highly elliptical plan-view shape of the pre-collapse magma chamber roof.

4) Vent positions, vent migration patterns, and reactivations of ring faults at several other elliptical calderas of various dimensions are also consistent with a control from elliptical reservoir geometry. In some of these examples, eruptions and faulting is demonstrably related to inflation of an elliptical reservoir rather than deflation. However, it is noted that the same mechanical principals governing strain distribution during elliptical subsidence should also apply during elliptical tumescence. The plan-view ellipticity of a magma chamber roof may thus decisively influence the dynamics of caldera-related faulting and eruption at all scales, and in any volcano-tectonic regime (tumescence, collapse or resurgence)

5) The experimental results here also indicate that vent position, which has not previously been tested as an influencing factor in experimental or numerical studies, may be important in caldera collapse. *Once the roof has failed*, the conduit position strongly influences the eventual point of maximum subsidence in the models. Field evidence for a similar control in nature is ambiguous, however. There may therefore be a complex interplay in nature between initial conduit position, initial roof loading conditions (e.g. vertical anisotropies in roof thickness from pre-collapse topography), ellipticity of the reservoir roof, ring fault propagation, and the opening of new conduits. Further numerical and analogue study of such complex interactions may be a fruitful path for further research.

6) The geometries of fault systems resulting from model caldera collapse into elliptical reservoirs have been documented in detail and in 3D. Subsidence-controlling reverse faults in experiment generally have shallower (~60-70°) outward dips along the short axis of the magma chamber roof, than along the long axis (~70-80°). In addition, the zone of peripheral extension adjacent the reverse faults penetrates further outward from the reservoir margin

and to a deeper level from the surface along the short axis of an elliptical model caldera than along the long axis. This is manifested as greater intensity and better development of crevasse, normal faults, and gräben around the ends of the model caldera's short axis.

7) This circumferential variation in the 3D geometry of elliptical model caldera faulting is tentatively related to a circumferential variation in the components of horizontal contraction and vertical shear along the edge of an elliptical reservoir during subsidence, with greater horizontal contraction occurring along the roof' short axis. As seen in existing numerical models of cover sequences deformed by reactivated basement faults, a stronger component of horizontal contraction with vertical shear causes reverse faults to form with shallower dips and induces deeper and laterally more extensive deformation in the reverse fault's hanging wall.

8) A consequence of this 3D fault architecture is that calderas formed by collapse into an elliptical magma reservoir display a characteristic geometric relationship between the limits of the zones of peripheral extension and central contraction at the surface and the reservoir at depth. The limit of peripheral extension is typically less elliptical than the underlying reservoir, whereas the limit of the central zone is typically more elliptical than the reservoir. Again these relationships are sensitive to roof thickness/diameter ratio, with 'thick' roof producing a less elliptical peripheral zone than an equivalently elliptical 'thin' roof. These model characteristics are closely matched by the geometric attributes of several calderas in nature. The surface relationships between the peripheral zone and central zone geometries may allow both approximation of the limits of pre-collapse magma reservoirs, and estimation of caldera fault geometries at depth.

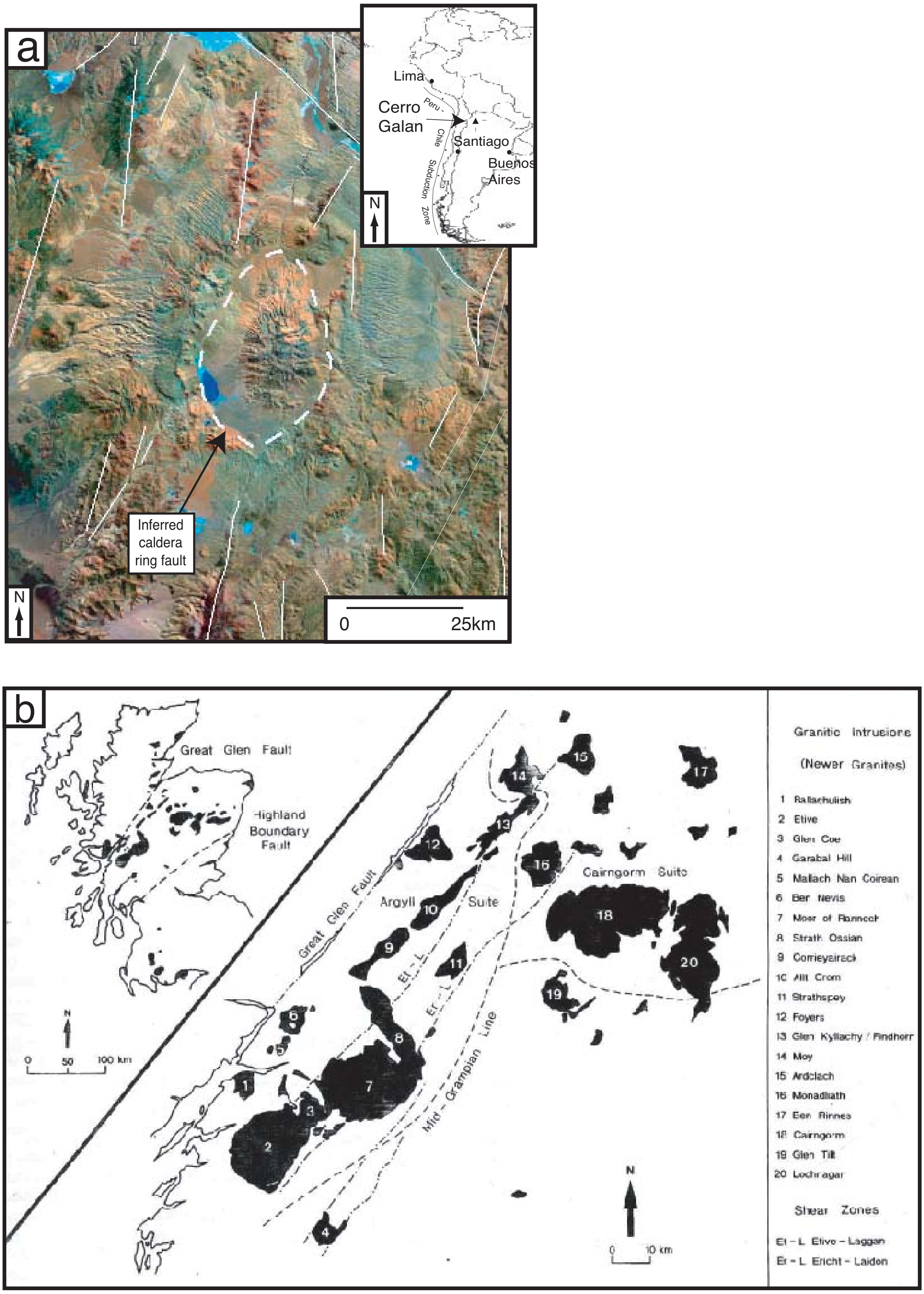

Figure 4.1:
a) Landsat false colour image of the highly elliptical and presently resurgent Cerro Galan caldera, Argentina. Thin white lines are inferred normal or strike slip faults: dashed white line is caldera ring fault (from Francis et al. 1978).
b) Map of Caledonian granitoid plutons in the Grampian Highlands of Scotland (from Jacques and Reavy 1994). Note that, despite effects on the exact outcrop pattern from exposure level and topography, most plutons are horizontally elongated, and many are significantly so.

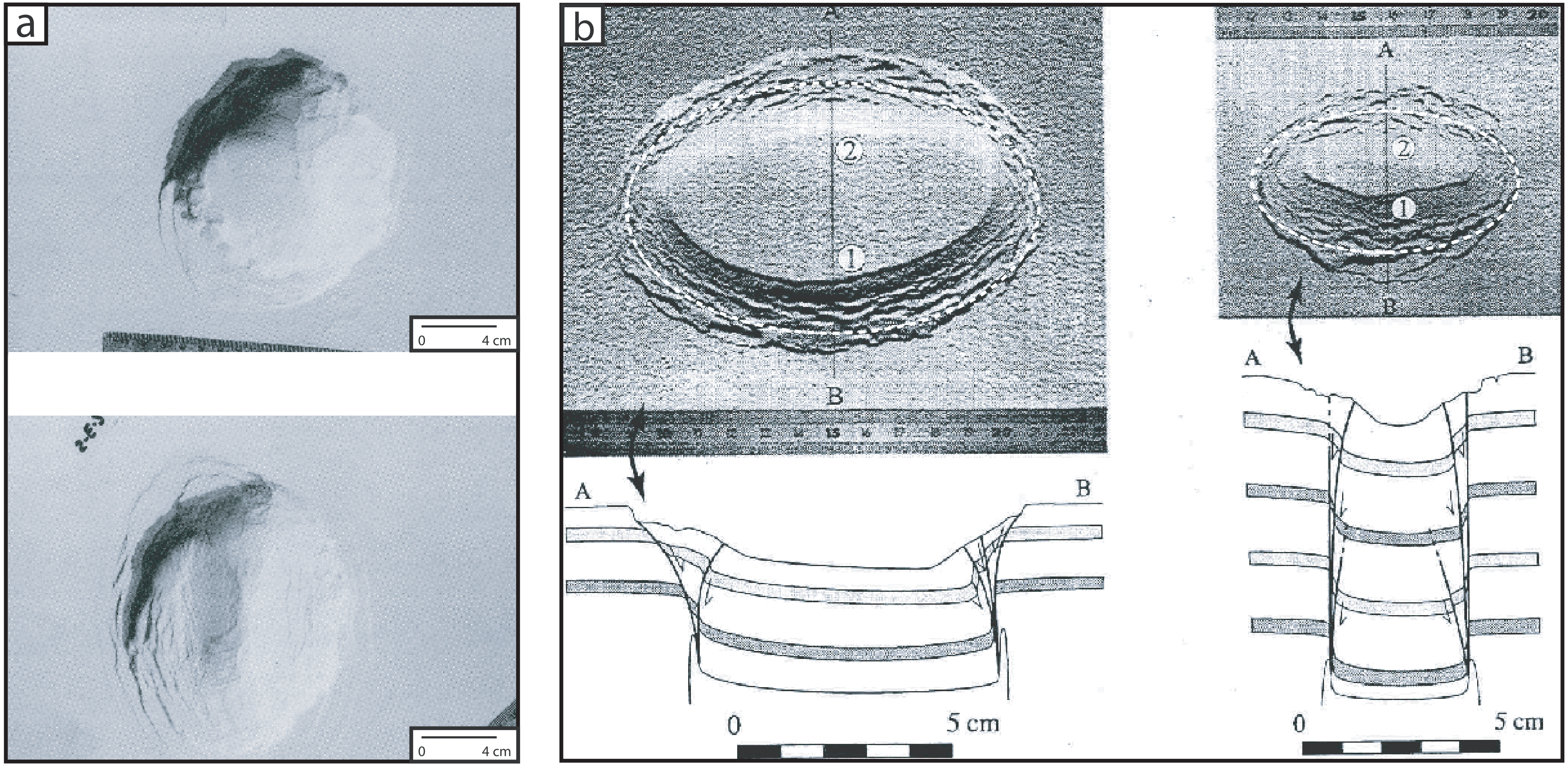

Figure 4.2: Previous experimental simulations of caldera collapse into reservoir that is elliptical in plan view.
(a) Plan-view photos of collapse depressions formed by deflating spherical (above) and ellipsoidal (below) balloons. No cross sections are available. From Marti et al. (1994)
(b) Depressions formed by collapse into sill-like silicone reservoirs that are elliptical in plan view and have thin (left) and thick (right) roofs. Note rulers for scale. Limit of reservoir is indicated by dashed white line and numbers refer to order of reverse fault formation. Cross sections are available only along the short axis of the models. From Roche et al. (2000).

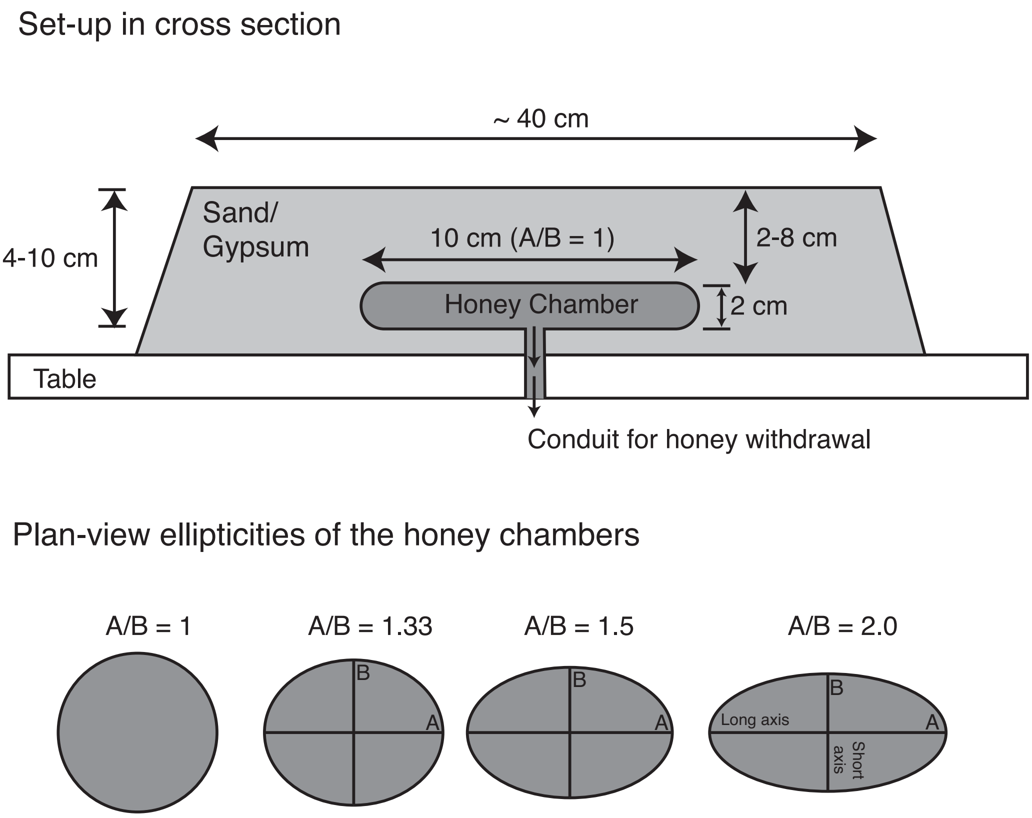

Figure 4.3: Cross-section of experimental set up (above) and plan-view outlines of variously elliptical honey reservoirs employed in this study (below).

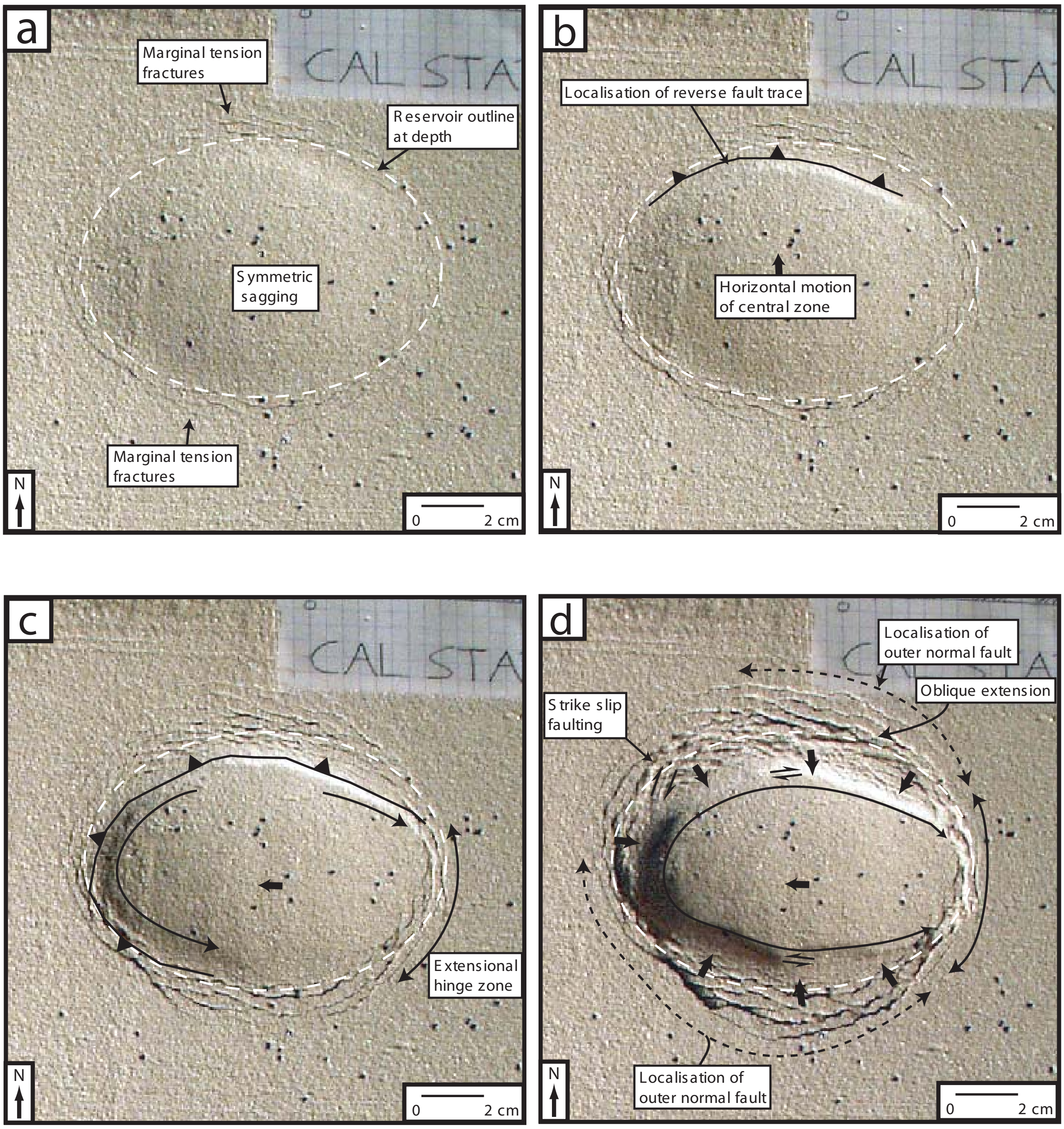

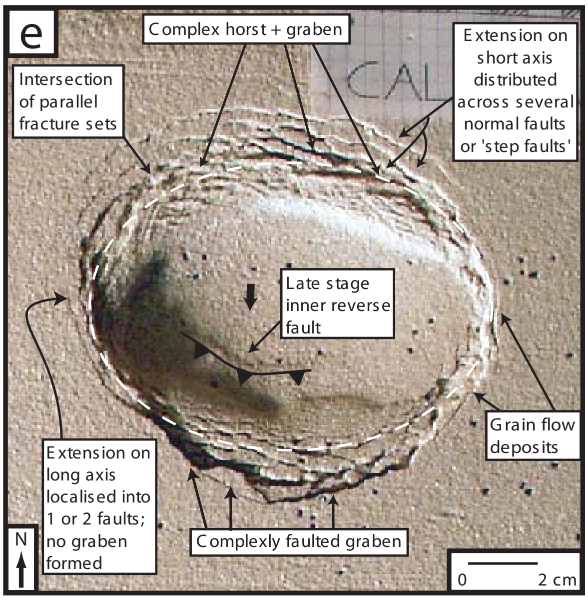

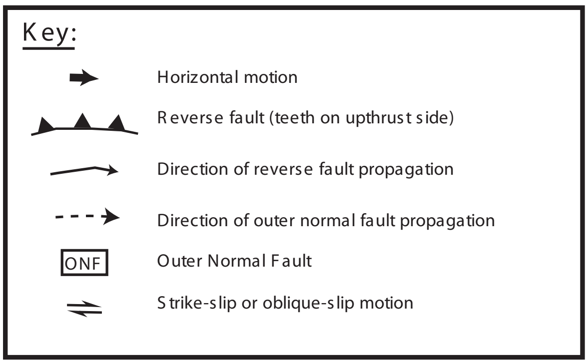

Figure 4.4: Developmental sequence of A/B = 1.33 elliptical collapse (Cal Stat B5). Light is from SW.

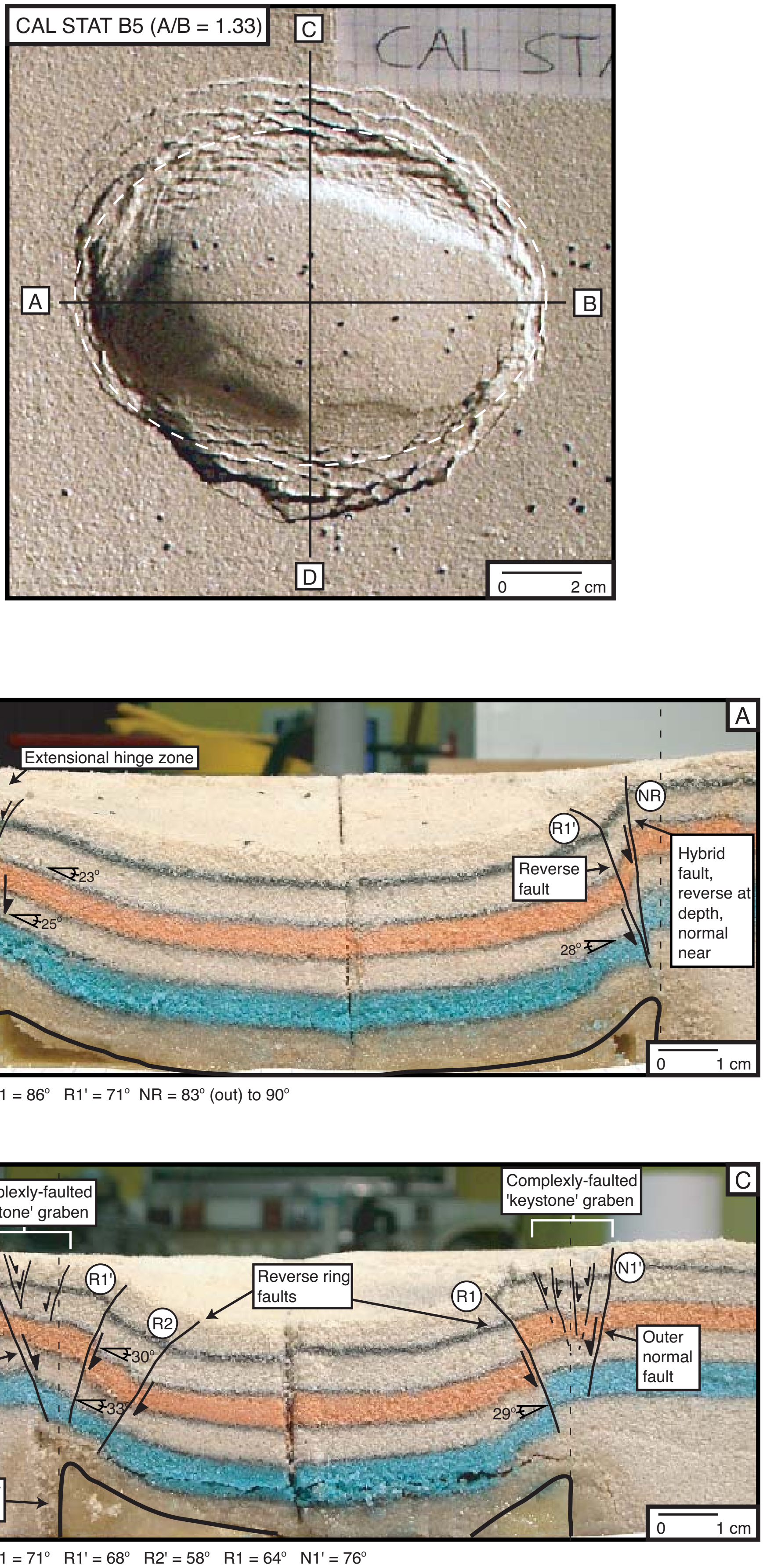

Figure 4.5: Cross-sections through the long (A-B) and the short (D-C) axes of a model caldera formed above a reservoir of A/B = 1.33 (Cal Stat B5). Top picture represents the final collapse stage in plan-view (Figure 4.4e). Dashed black vertical lines on the cross-sections mark the upward projections of the reservoir edge.

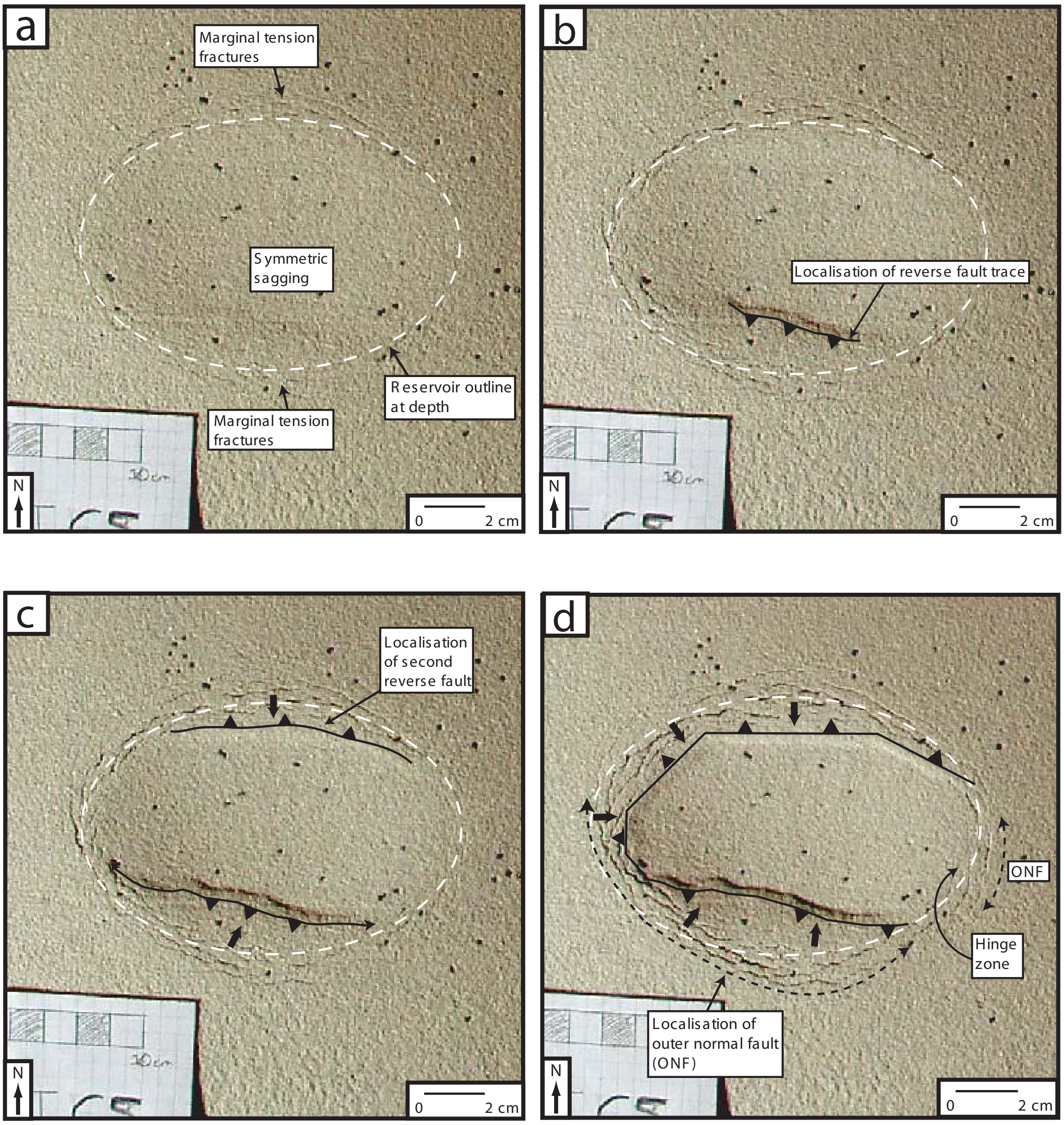

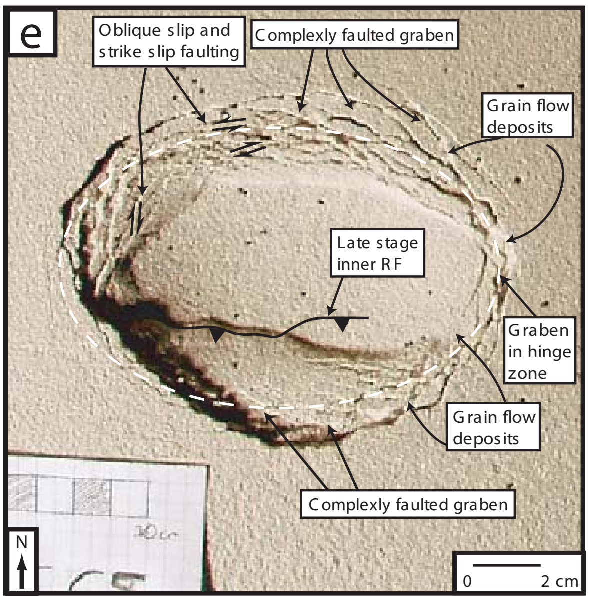

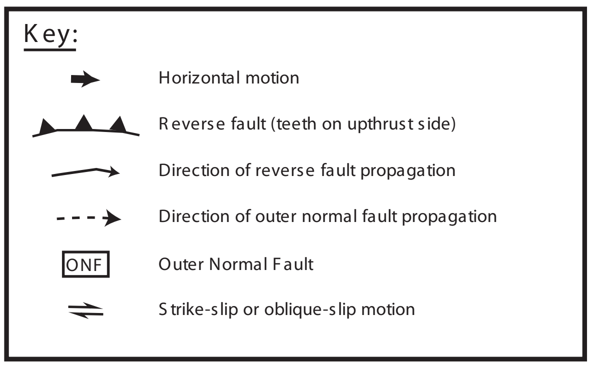

Figure 4.6: Developmental sequence of A/B = 1.5 elliptical collapse (Cal Stat C5). Light is from SW.

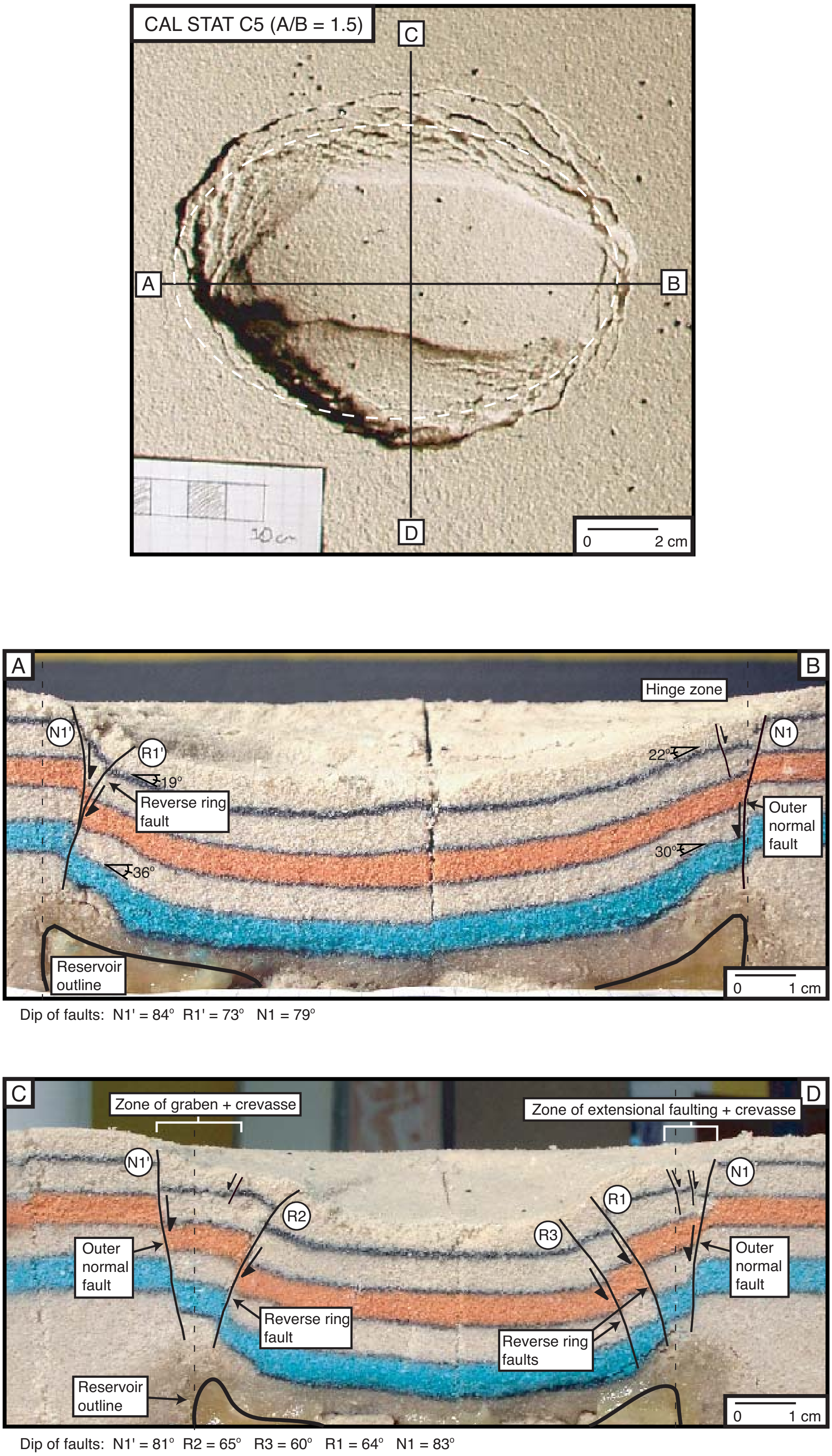

Figure 4.7: Cross-sections through the long (A-B) and the short (C-D) axes of a model caldera formed above a reservoir of A/B = 1.5 (Cal Stat C5). Top picture represents the final collapse stage in plan-view (Figure 4.6e). Dashed black vertical lines on the cross-sections mark the upward projections of the reservoir edge.

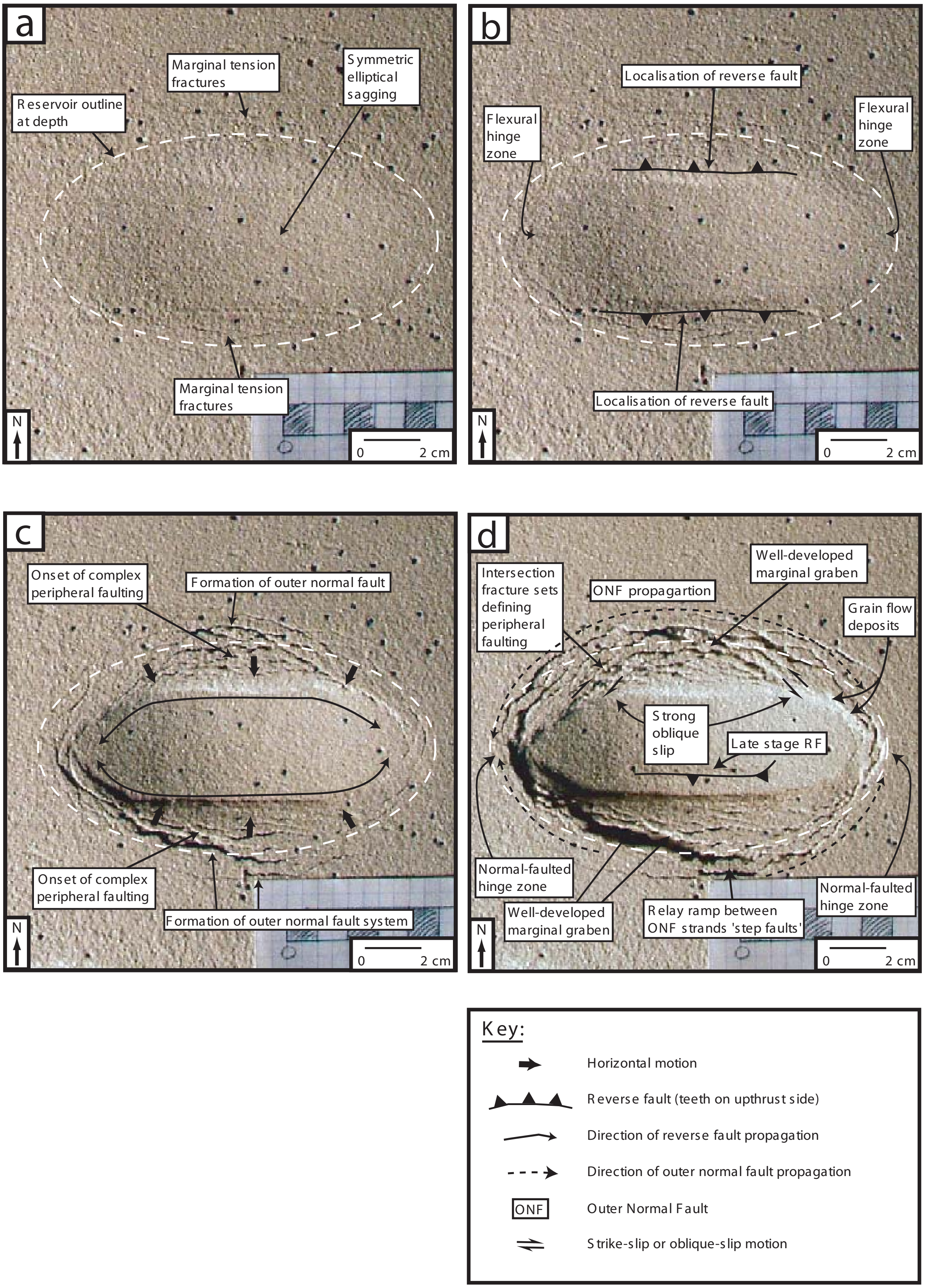

Figure 4.8: Developmental sequence of A/B = 2.0 elliptical collapse (Cal Stat D5). Light is from SW. RF = reverse fault.

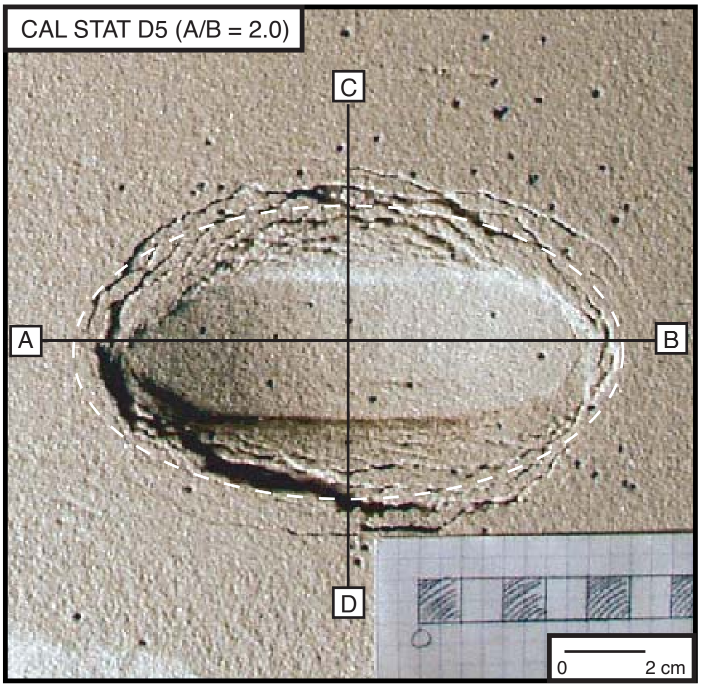

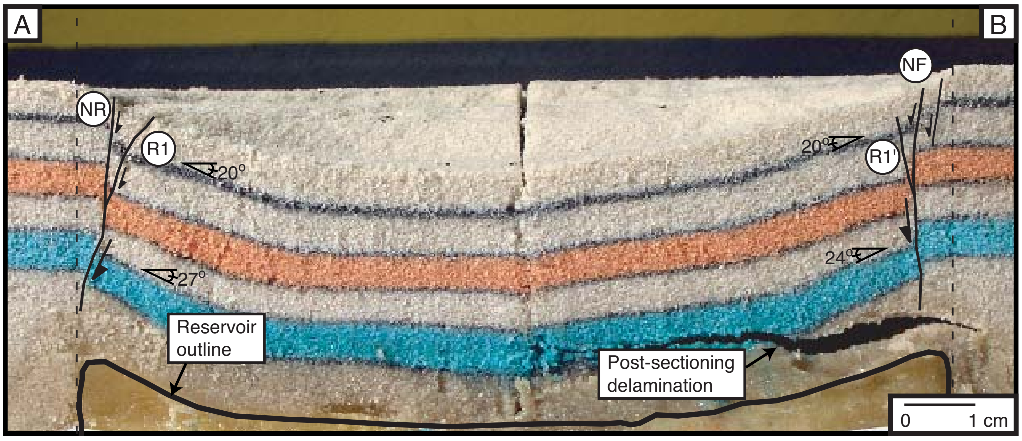

Dip of faults: NR = 90° R1 = 75° R1' = 80° NF = 77°

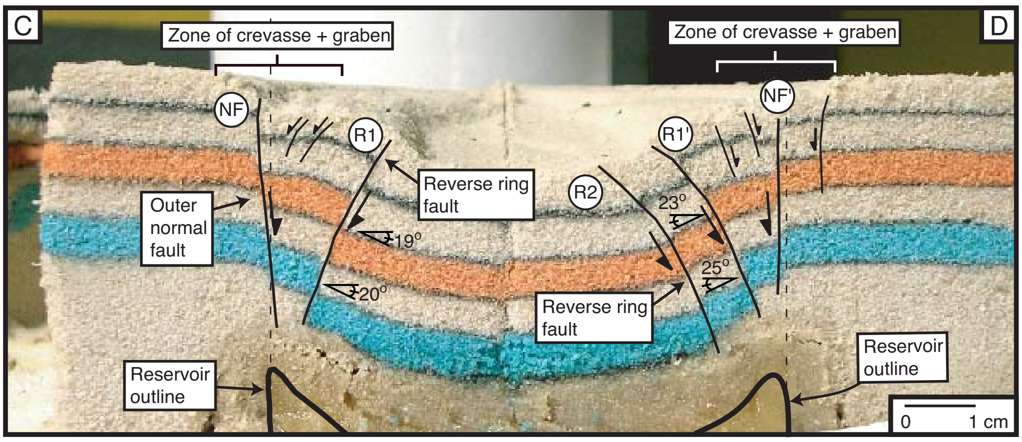

Dip of faults: NF = 84° R1 = 66° R2 = 62° R1' = 60° NF' = 89°

Figure 4.9: Cross-sections through the long (A-B) and the short (C-D) axes of a model caldera formed above a reservoir of A/B = 2.0 (Cal Stat D5). Top picture represents the final collapse stage in plan-view (Figure 4.8e). Dashed black vertical lines on the cross-sections mark the upward projections of the reservoir edge.

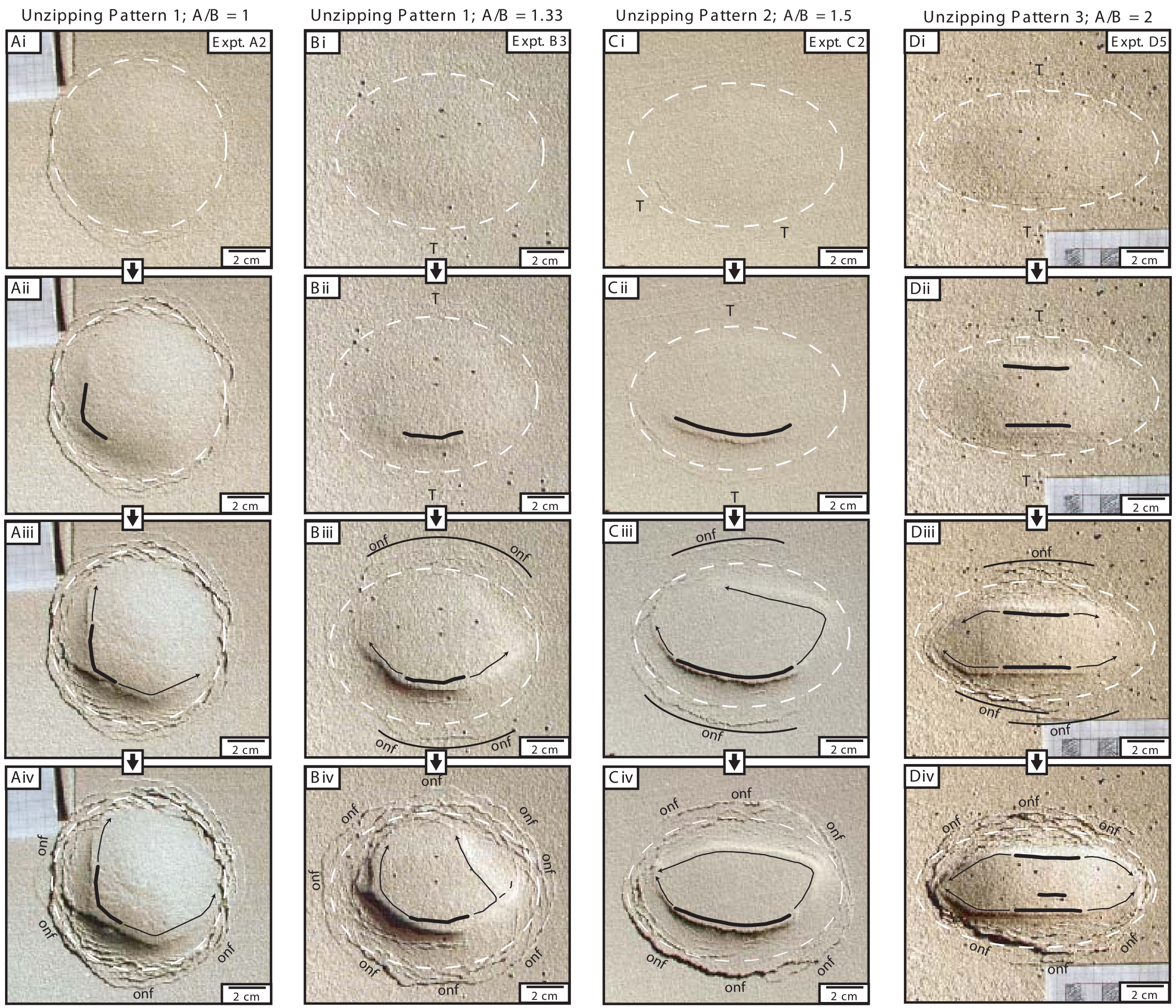

Figure 4.10: Time-lapse photos of experimental caldera collapses. These represent the main unzipping patterns observed, but note that A/B = 1.33 produced both Patterns 1 and 2, whilst A/B = 1.5 both produced Patterns 2 and 3. See Figure 4.11 for full data set.

Ai-Di: pre-failure sagging and surface tension cracks (T). Dashed white line is approximate chamber outline at depth;

Aii-Dii: Localization of inner reverse fault(s) (trace indicated by thick black line);

Aiii-Diii: Lateral propagation of reverse fault trace(s), tracked by thin black line and arrows. Also see onset of outer normal faulting (onf – medium black lines).

Aiv-Div: Completion of ring-fault propagation.

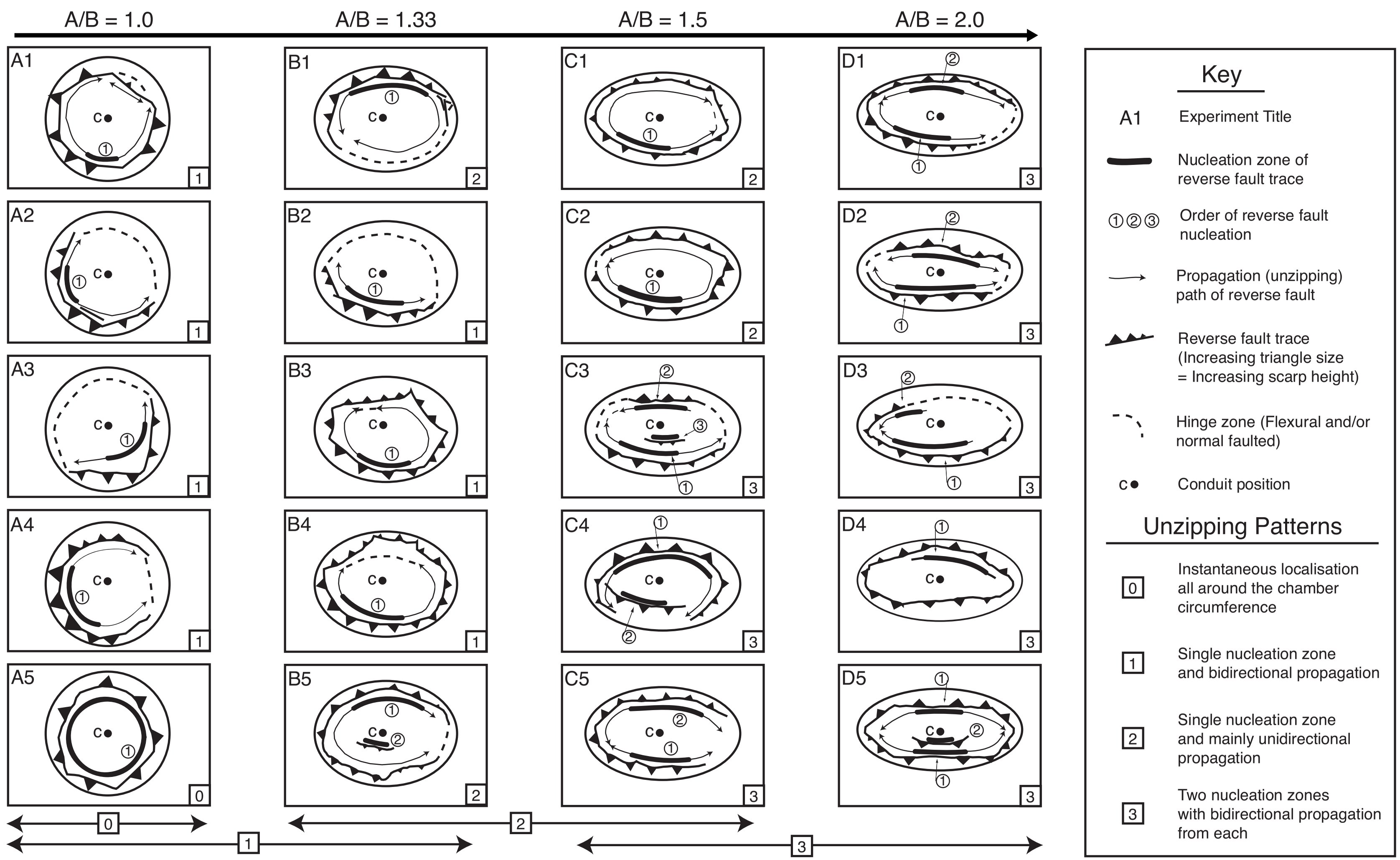

Figure 4.11: Sketches of all unzipping patterns observed in experiments with a centred conduit. Plan-view ellipticity was varied for each experiment set: A1-A5 (A/B = 1.0), B1-B5 (A/B = 1.33), C1-C5 (A/B = 1.5), and D1-D5 (A/B = 2.0). Unzipping patterns comprise a continuum in which the patterns gradually but systematically change with increasing A/B ratio.

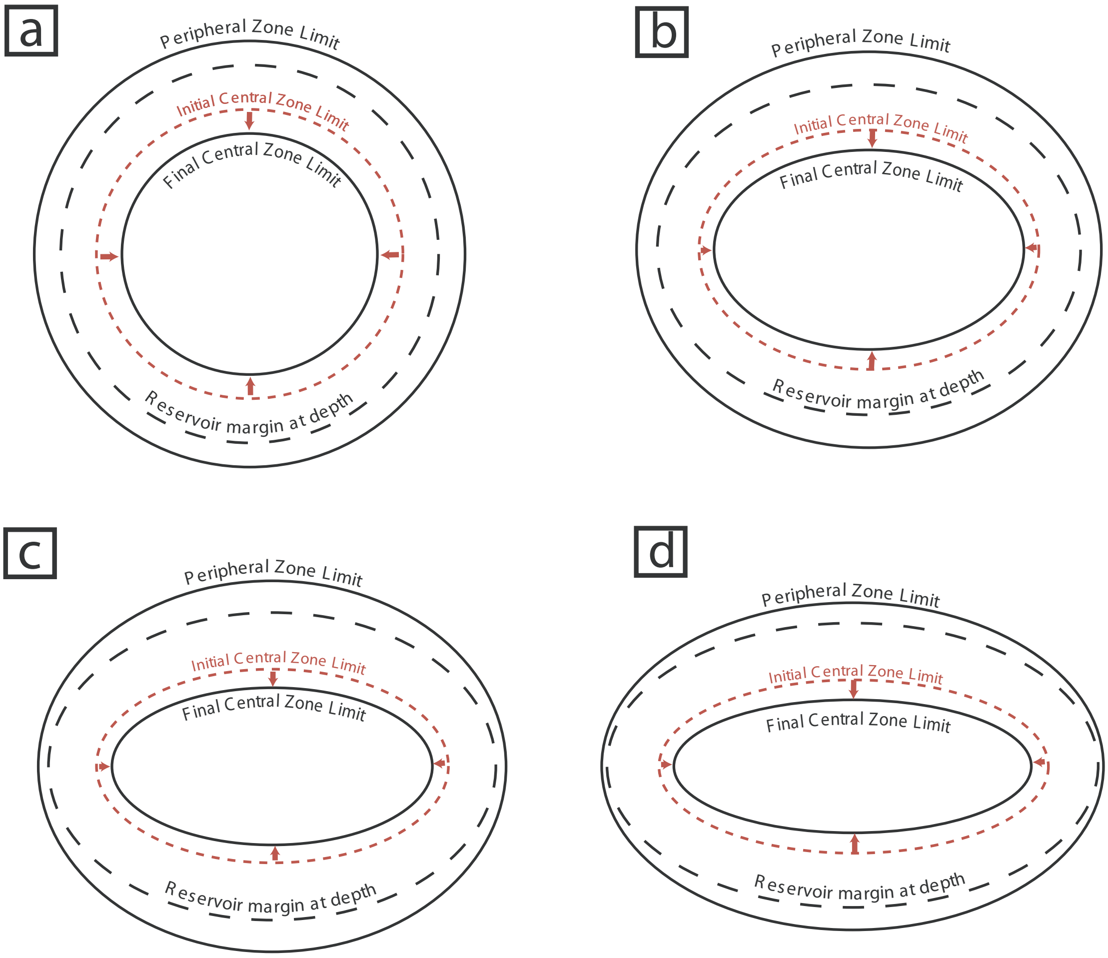

Figure 4.12: Plan-view sketches (to scale) of average dimensions of the limits of the peripheral zone, central zone and reservoir for each of the experient sets **a)** Cal Stat A1-A5, **b)** Cal Stat B1-B5, **c)** Cal Stat C1-C5, **d)** Cal Stat D1-D5. Also shown (schematically) in each case is the initial limit of the central zone, as defined by the point of initial reverse fault localisation.

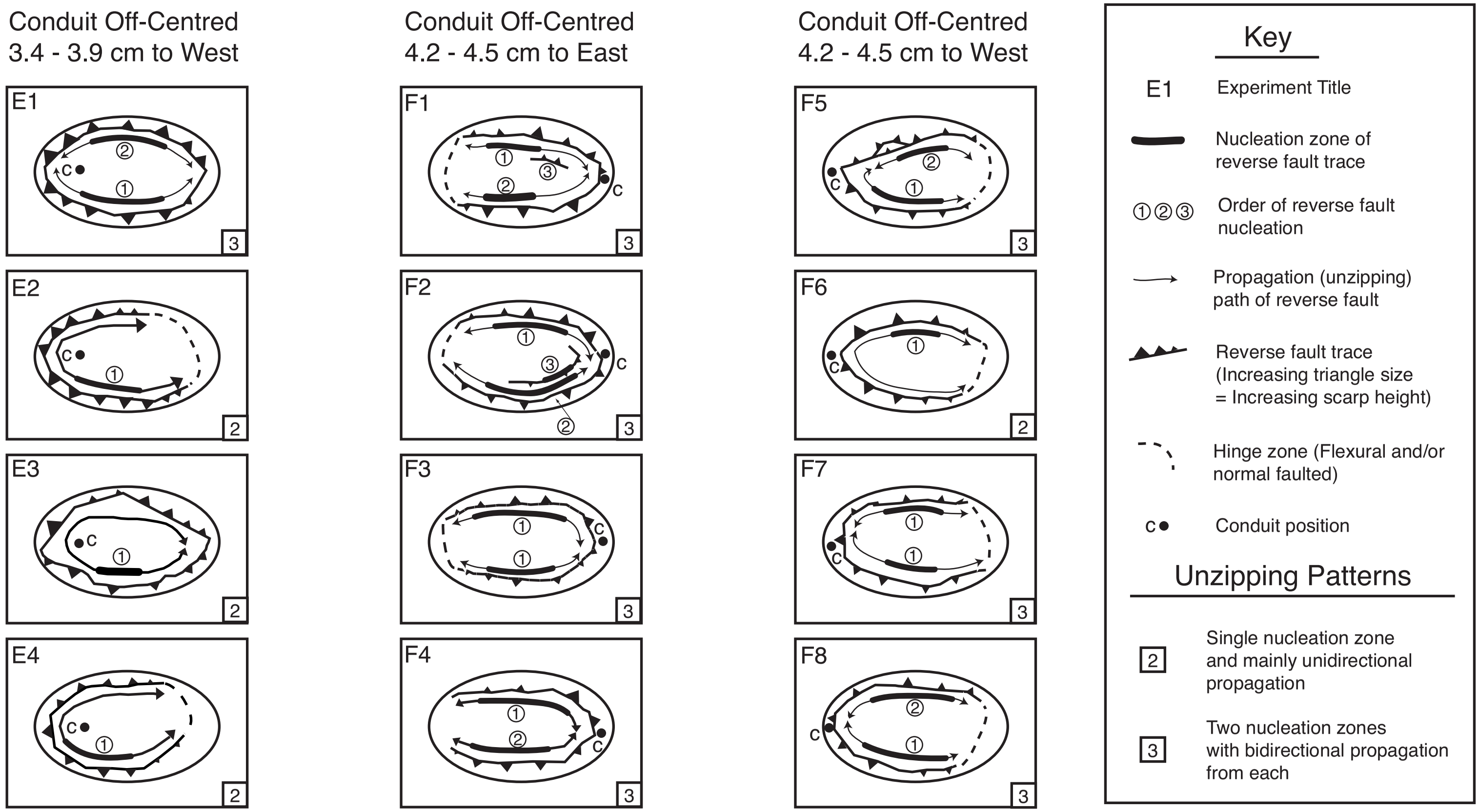

Figure 4.13: Sketches of unzipping patterns observed in experiments with an off-centred conduit. Plan view ellipticity was the same for each case at A/B = 1.5, and the conduit was positioned along the long axis at: 3.4 - 3.9 cm west from the centre for experiments E1-E4, 4.2 - 4.5cm east from the centre for experiments F1-F4, 4.2 - 4.5cm west from the centre for experiments F5-F8. Note that regardless of conduit position, the patterns of reverse fault localisation and propagation are essentially the same as for A/B = 1.5 with a centred conduit (i.e. first nucleation near the roof's short axis ends, followed by unzipping pattern 2 or 3).

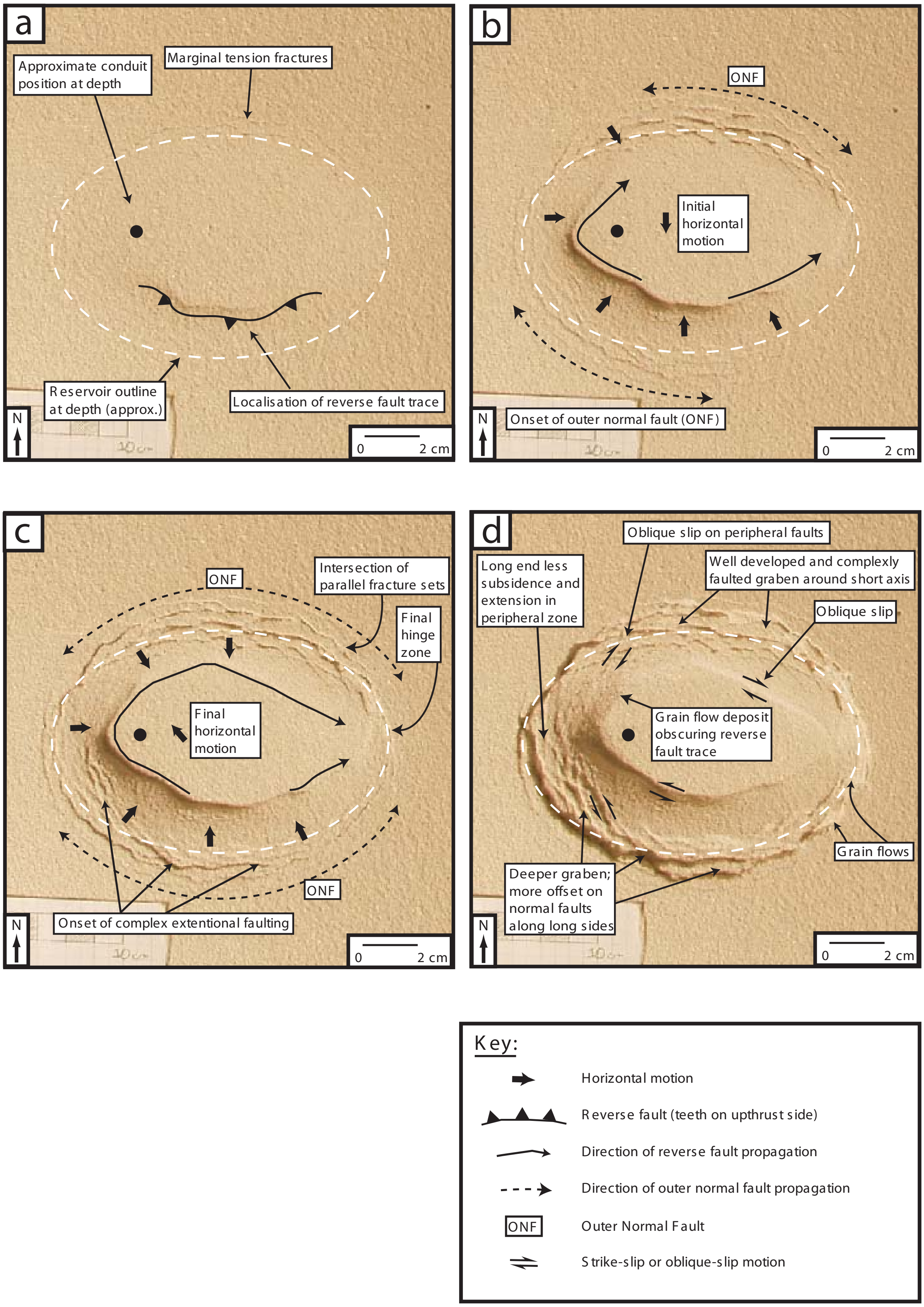

Figure 4.14: Developmental sequence of A/B = 1.5 elliptical collapse to test effect of slightly off-centred conduit (Cal Stat E3). Light is from SW. Unzipping Pattern 2 is observed, as in experiment of equivalent ellipticity and centred conduit. Point of maximum subsidence changes through course of collapse, but final point of maximum subsidence is coincident with conduit position.

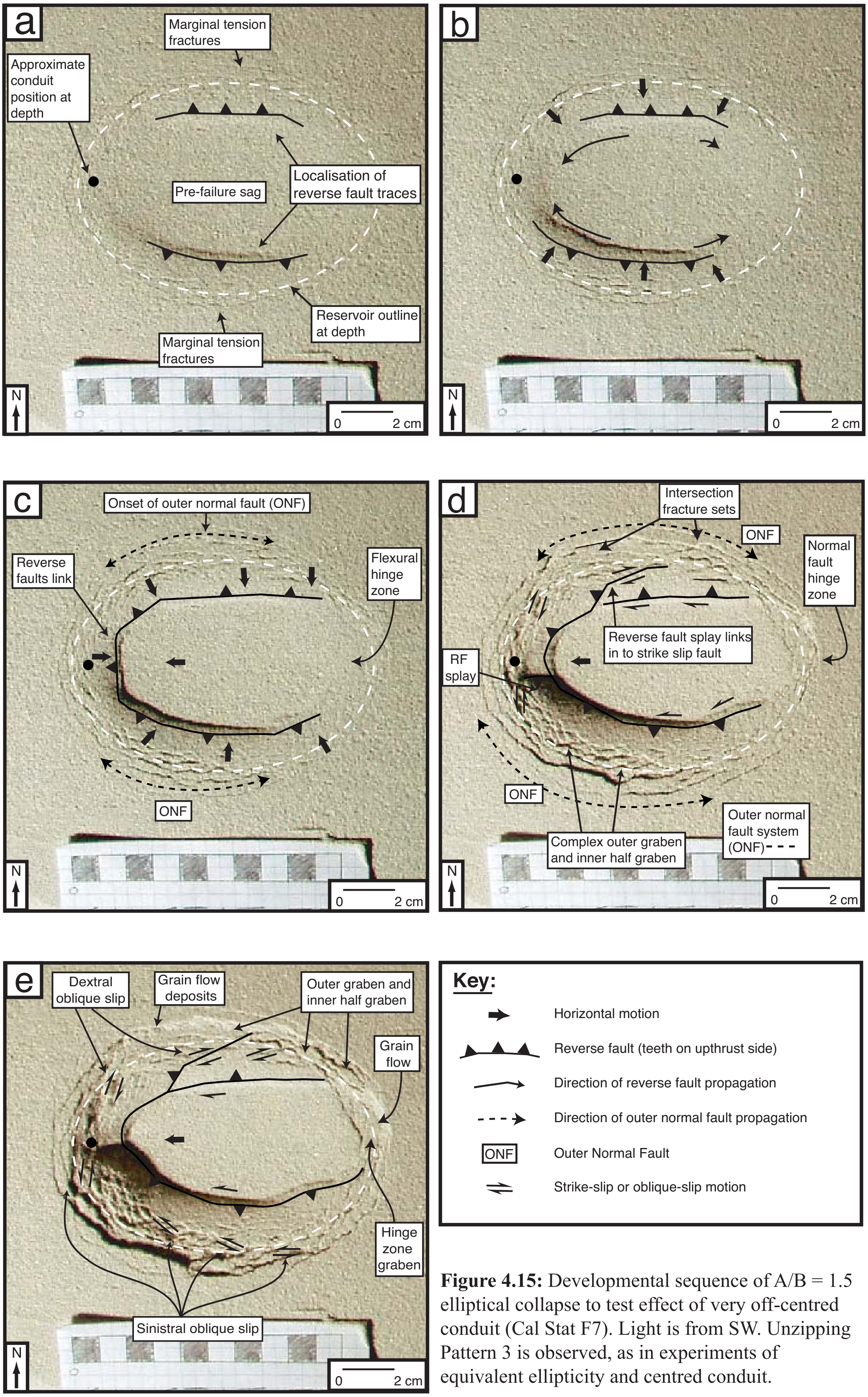

Figure 4.15: Developmental sequence of A/B = 1.5 elliptical collapse to test effect of very off-centred conduit (Cal Stat F7). Light is from SW. Unzipping Pattern 3 is observed, as in experiments of equivalent ellipticity and centred conduit.

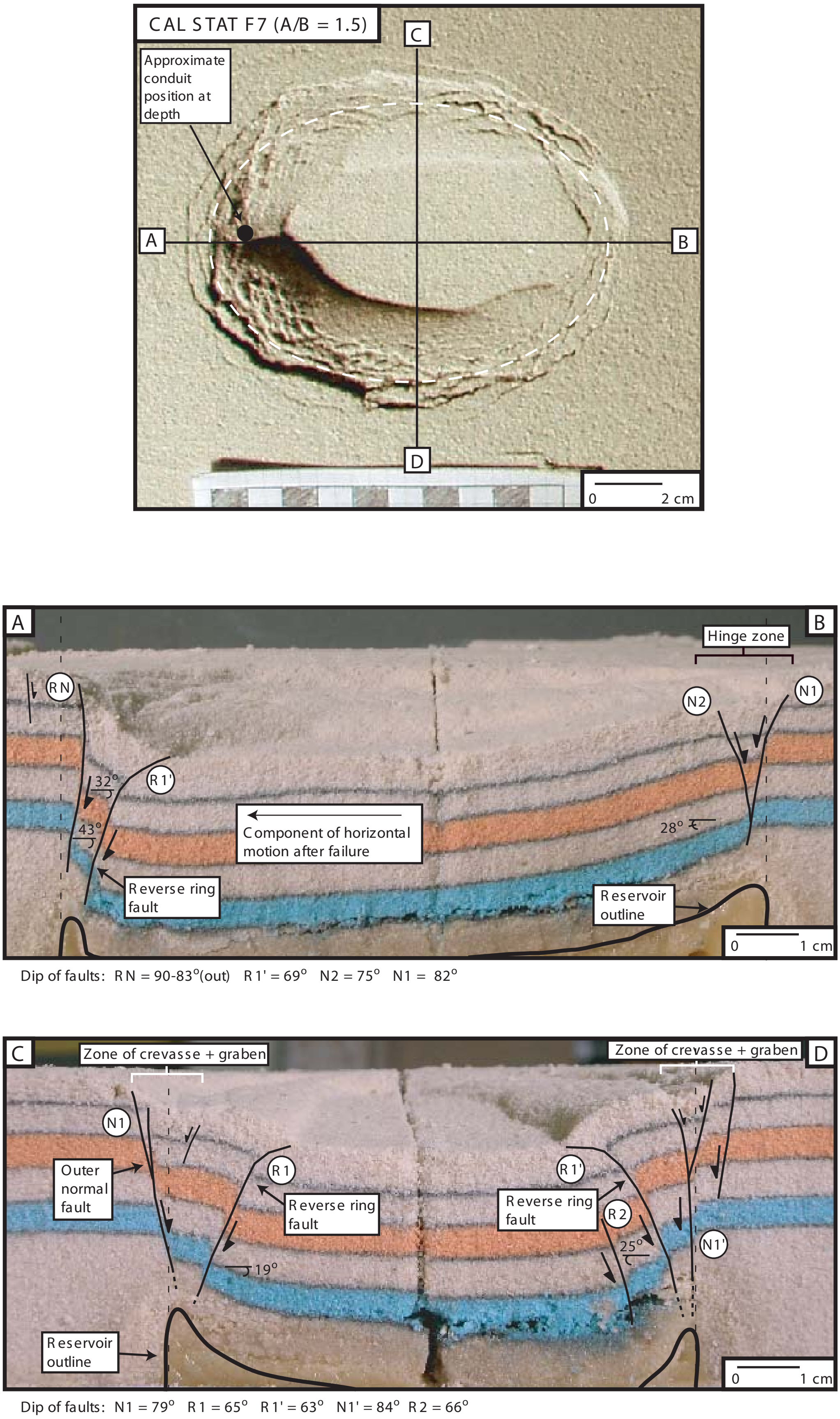

Figure 4.16: Cross-section through the long (A-B) and the short (D-C) axes of a model caldera formed above a reservoir of A/B = 1.5 with a very off-centred conduit (Cal Stat F7). Top picture represents the final collapse stage in plan-view (Figure 4.15e). Dashed black vertical lines on the cross-sections mark the upward projections of the reservoir edge.

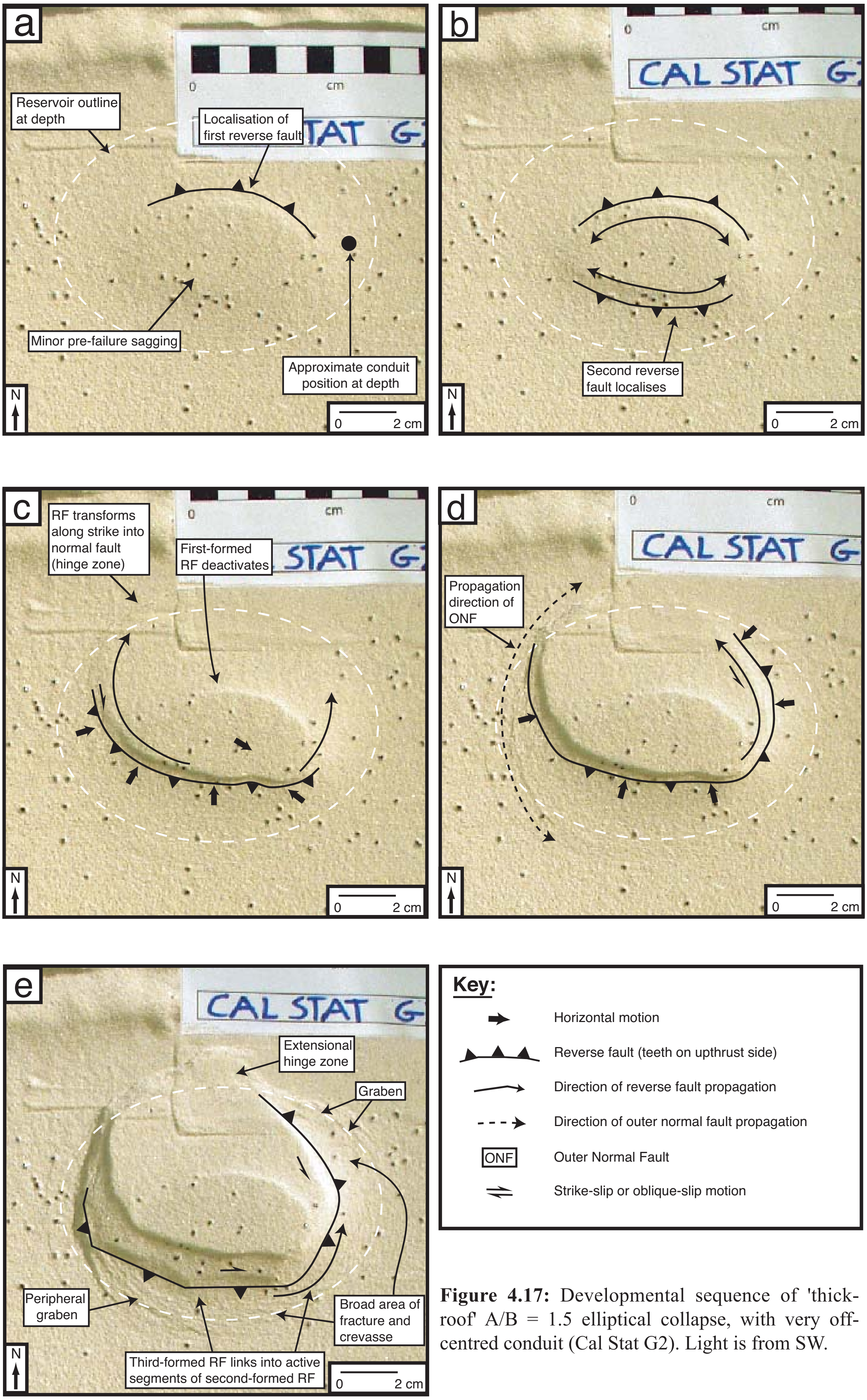

Figure 4.17: Developmental sequence of 'thick-roof' A/B = 1.5 elliptical collapse, with very off-centred conduit (Cal Stat G2). Light is from SW.

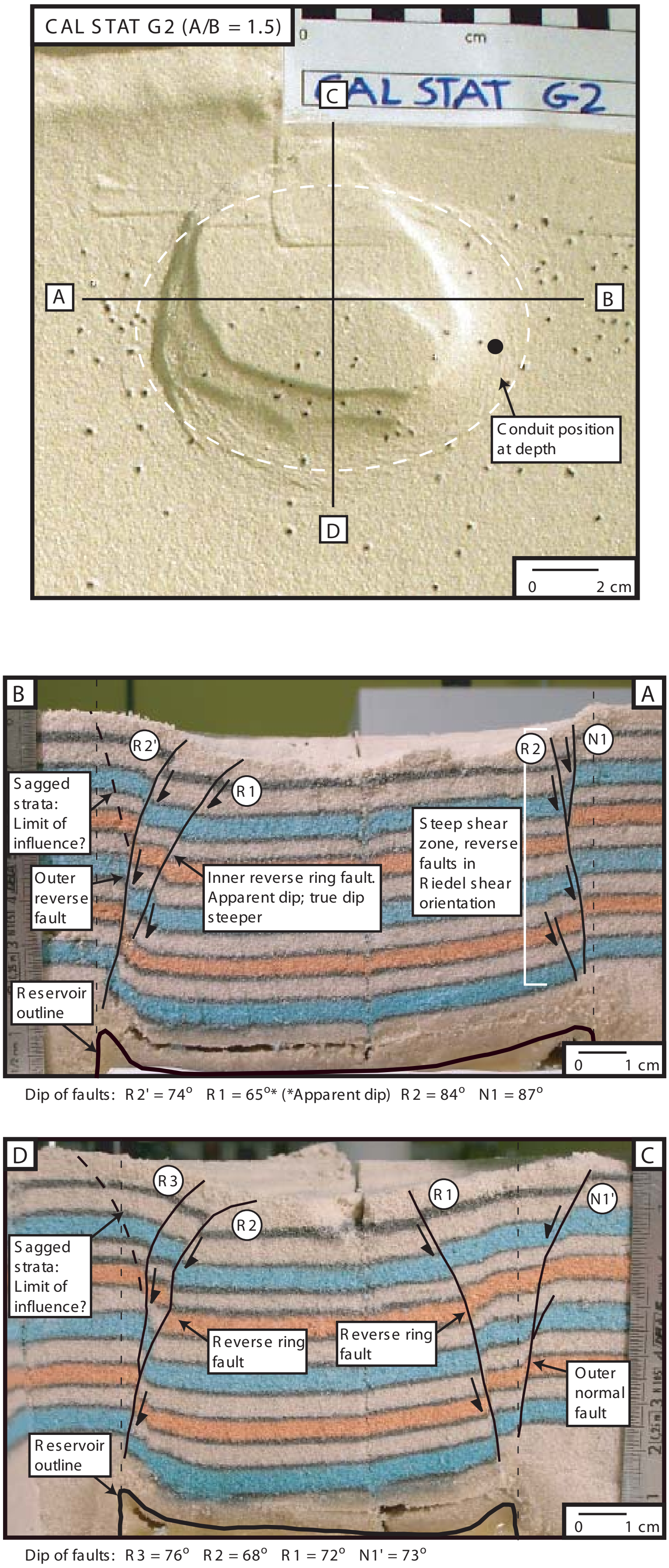

Figure 4.18: Cross-sections through the long (B-A) and short (D-C) axes of collapsed 'thick' elliptical roof (A/B = 1.5) with a very off-centred conduit (Cal Stat G2). Top picture represents the final collapse stage in plan-view (Figure 4.17e). Dashed black vertical lines on the cross-sections mark the upward projections of the reservoir edge.

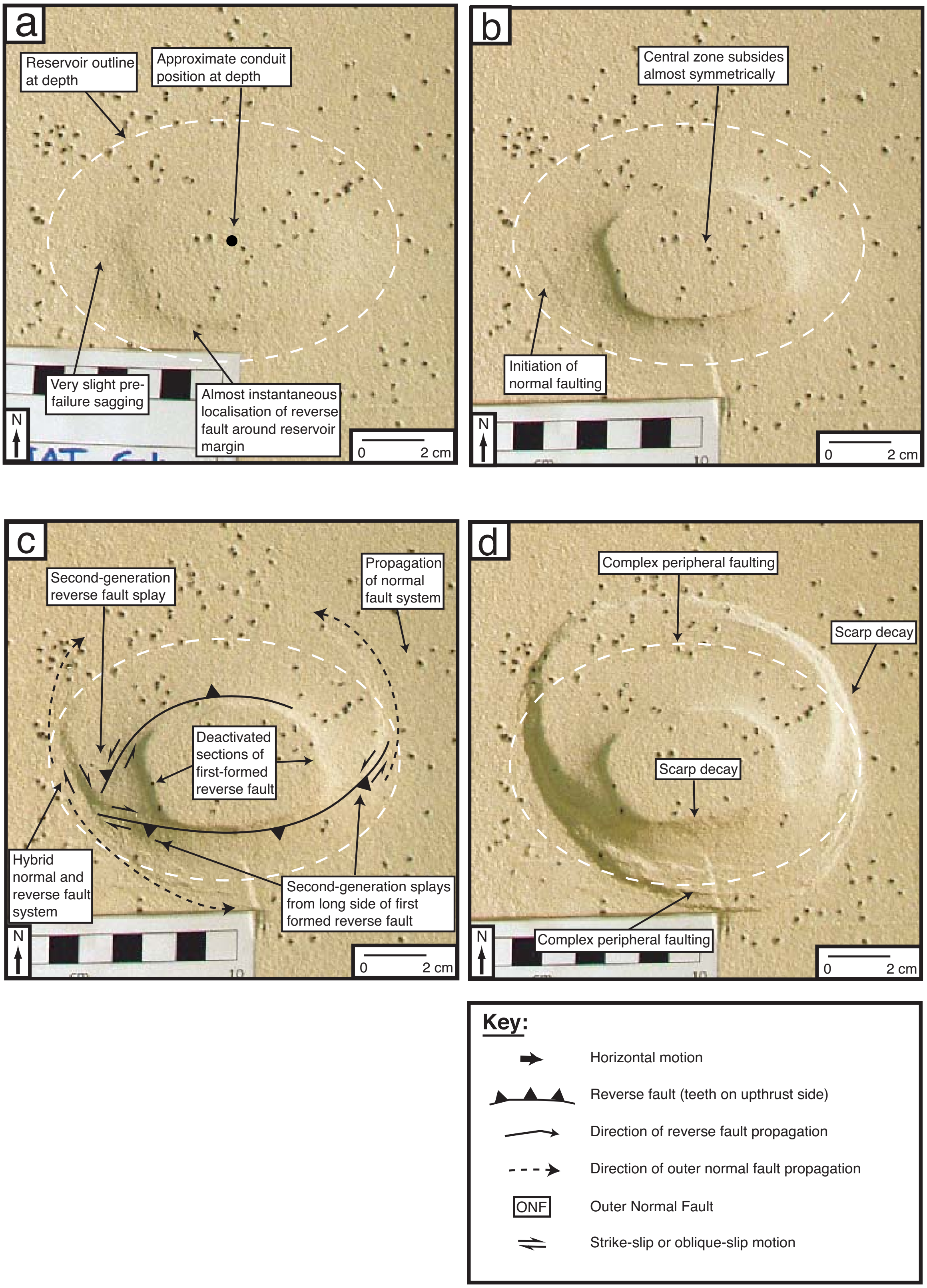

Figure 4.19: Developmental sequence of 'thick-roof' A/B = 1.5 elliptical collapse with very off-centred conduit (Cal Stat G4). Light is from SW.

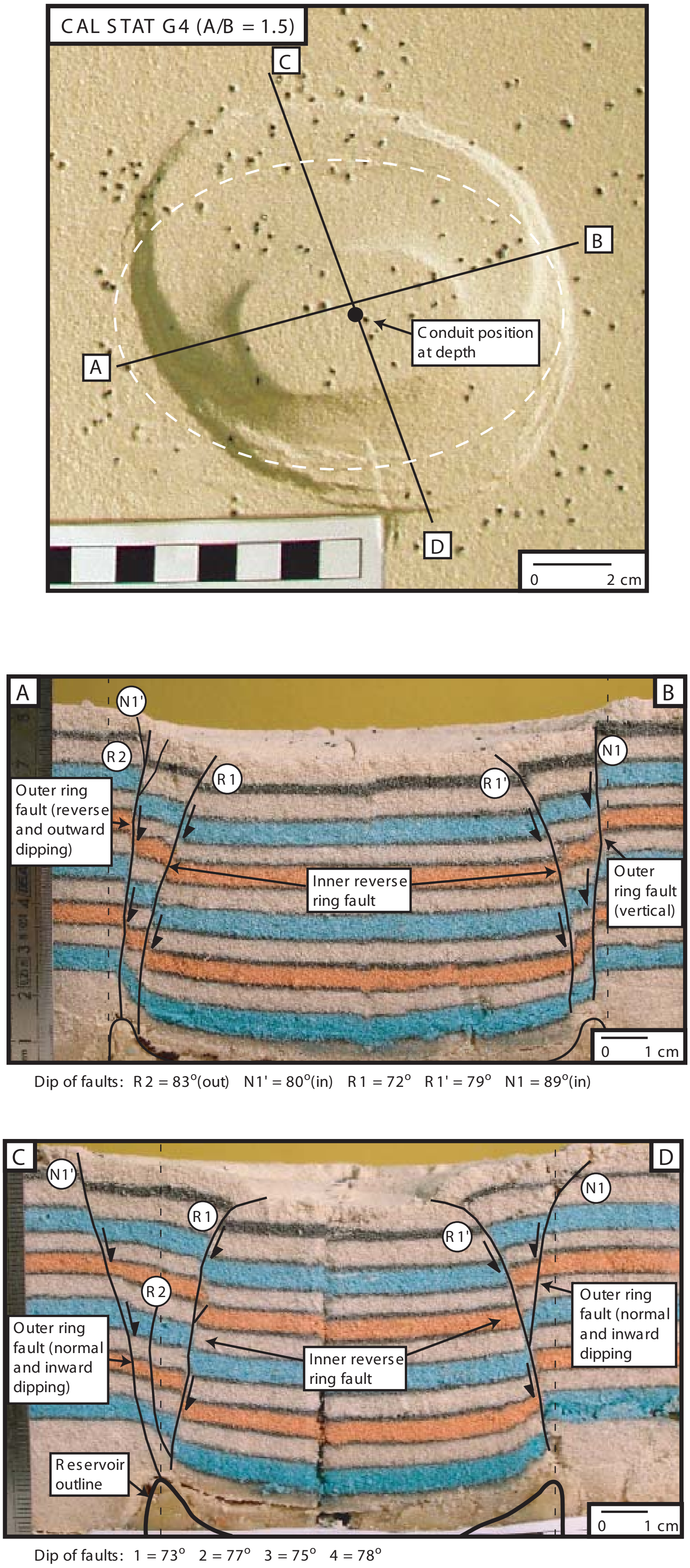

Figure 4.20: Cross-sections through the long (A-B) and the short (D-C) axes of a collapsed 'thick' elliptical resevoir roof with a centred conduit (Cal Stat G4). Top picture represents the final collapse stage in plan-view (Figure 4.19d). Dashed black vertical lines mark the upward projections of the reservoir edge.

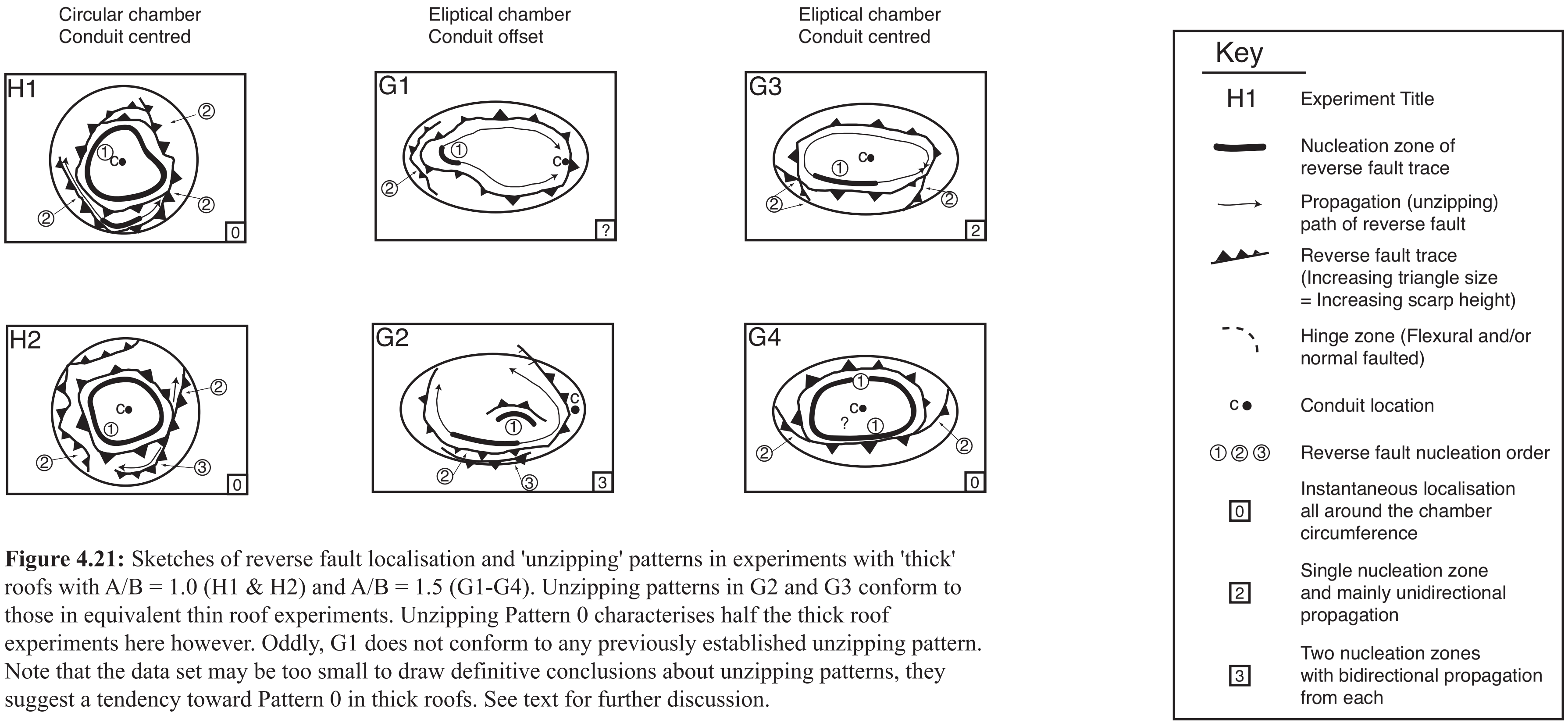

Figure 4.21: Sketches of reverse fault localisation and 'unzipping' patterns in experiments with 'thick' roofs with A/B = 1.0 (H1 & H2) and A/B = 1.5 (G1-G4). Unzipping patterns in G2 and G3 conform to those in equivalent thin roof experiments. Unzipping Pattern 0 characterises half the thick roof experiments here however. Oddly, G1 does not conform to any previously established unzipping pattern. Note that the data set may be too small to draw definitive conclusions about unzipping patterns, they suggest a tendency toward Pattern 0 in thick roofs. See text for further discussion.

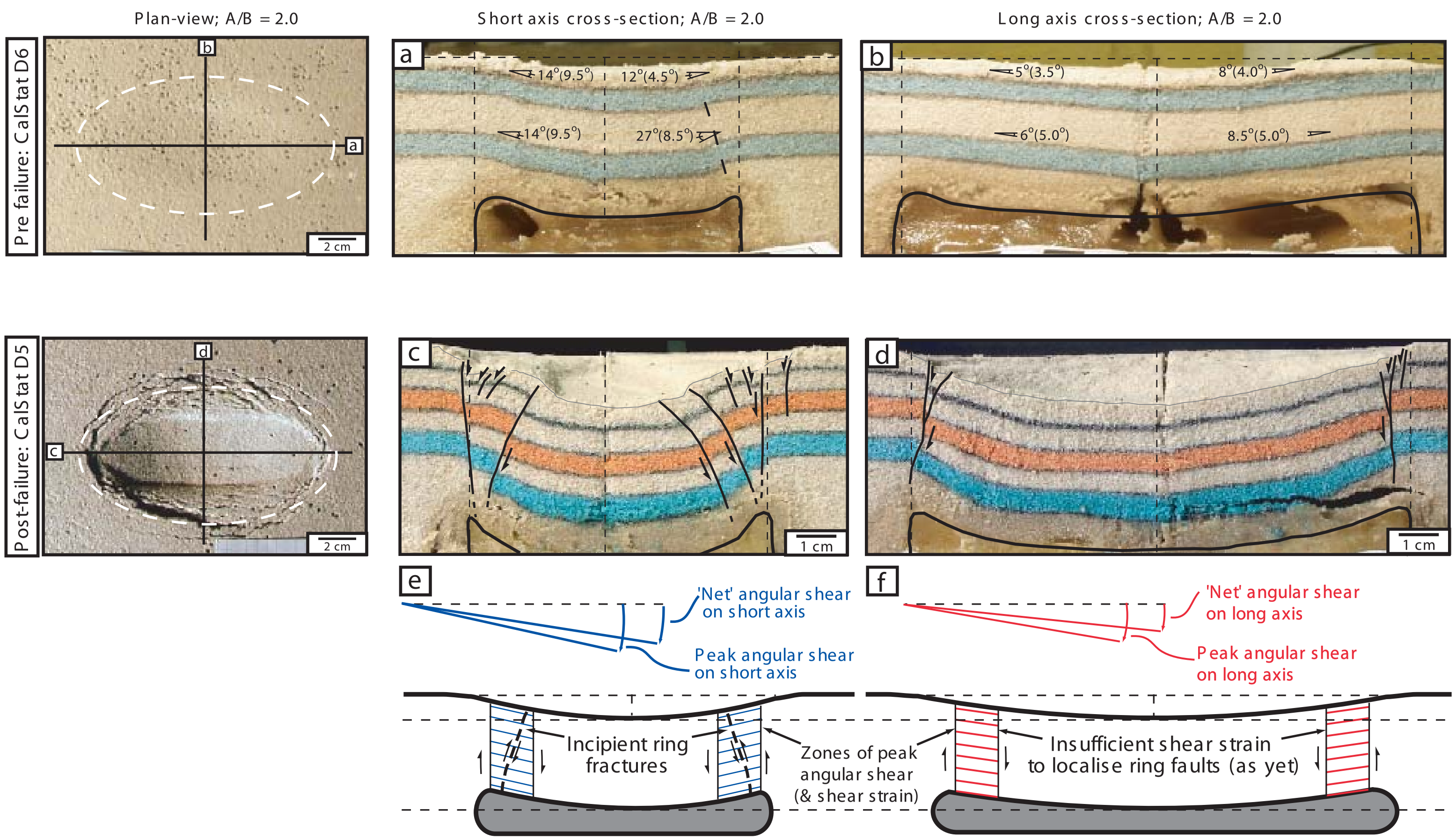

Figure 4.22:
(a & b) Cross-sections through the A/B = 2.0 elliptical collapse model prior to failure and formation of reverse faults. Angles outside parentheses are measured peak angular shear values for tops of blue layers. Angles inside parentheses are 'net' angular shear values, as calculated from reservoir margins to centre line of the cross section (vertical black dashed lines). Peak and net angular shear values are greatest along the short axis. An incipient reverse fault is noted with dashed line at zone of peak angular shear in (a).
(c & d) Cross-sections through the A/B = 2.0 elliptical collapse model at final stage of deformation after formation of reverse faults.Note the greater accommodation of central vertical displacement by shear fractures along the short axis.
(e & f) Sketch cross-sections of idealised pre-failure deflection profiles along the short and long axes of an elliptical magma chamber roof. Profiles are based on *pre-failure* surface deflections in experiment - cf. Figure 4.10; Di and upper plan-view photo above. Deflection angles are shown over same horizontal length to ease visual comparison. Greatest angular shear, and hence shear strain, along the short axis leads to earliest shear failure here.

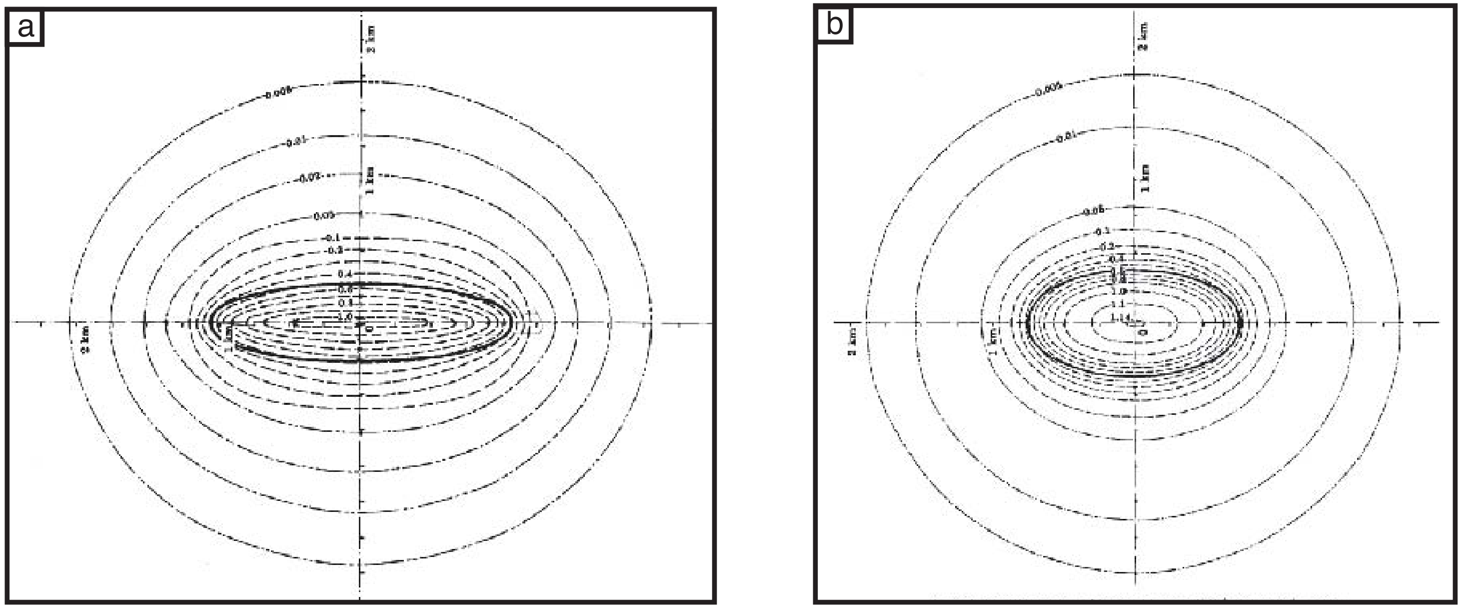

Figure 4.23: a) & b) show calculated contours of surface subsidence formed above hydrocarbon reservoirs by numerically-simulated compaction. Reservoirs are of equivalent area and of A/B = 4 and A/B = 2, respectively. Note that contours inside the reservoir edge (solid black line) are more elliptical that the reservoir and those outside are less elliptical; the contours furthest away from the reservoir tend toward circularity. From Gambolati et al. (1987).

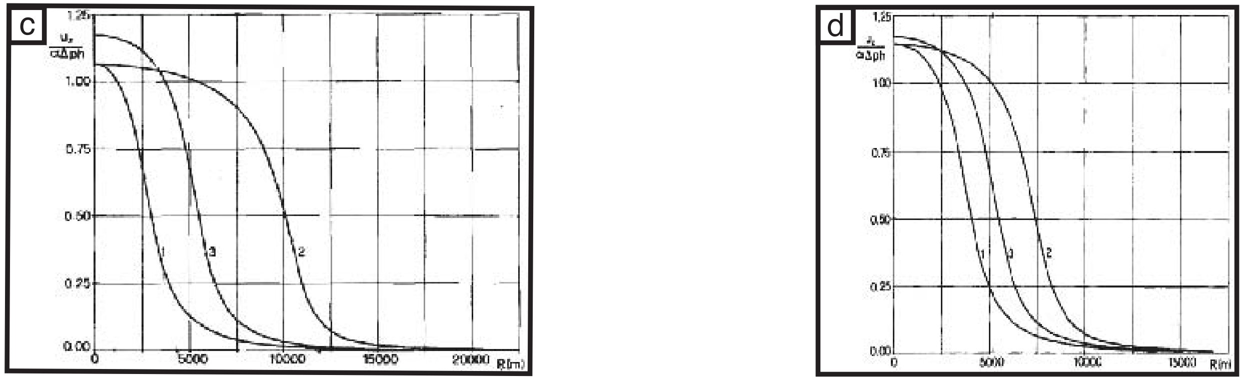

Figure 4.23: c) & **d**) respectively show surface subsidence profiles (normalised to soil compressibility, α, reservoir pore pressure reduction, Δp, and reservoir thickness, h) along long axes (**1**) and short axes (**2**) of each reservoir. Also shown is the subsidence profile (**3**) on an areally equivalent circular reservoir. From Gambolati et al. (1987). Profiles along the short axes are steepest, reflecting greater angular shear here. Also, the disparity in angular shear between long and short axes subtly increases from A/B = 2 to A/B = 4. Note also that subsidence at the model centre decreases with increasing reservoir ellipticity. This may reflect stiffening of the reservoir roof as thickness/diameter ratio along the short axis increases (see also Jones et al. 1990).

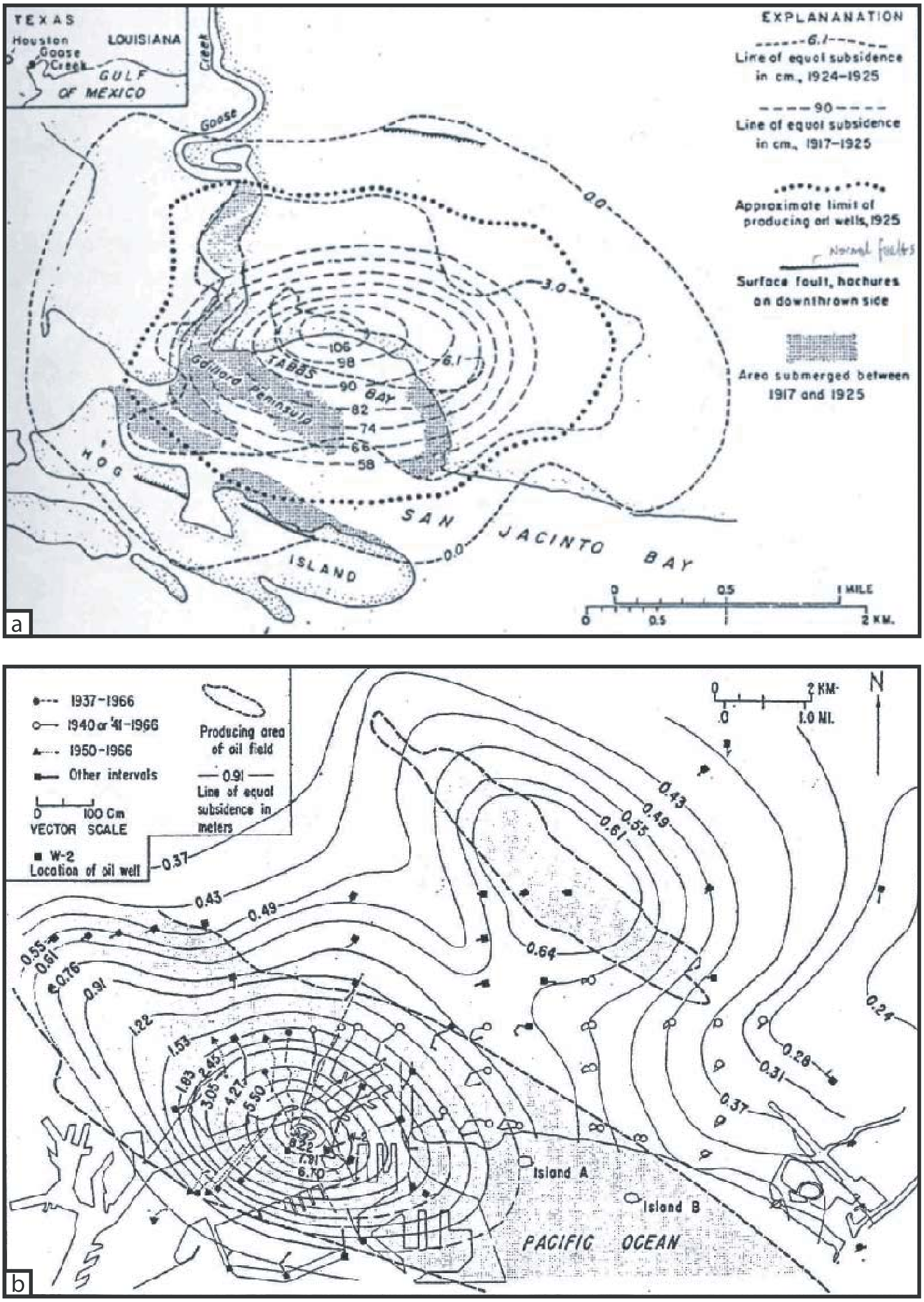

Figure 4.24: Maps of surface subsidence contours above the elongate oil fields of **a)** Goose Creek, Texas, **b)** Wilmington, California. From Yerkes and Castle (1976) and Allen (1968) respectively. Compaction of the oil reservoirs after oil withdrawal has led to the development of elliptical subsidence profiles, with steepest gradients along the short axes of the oil fields, as in experimental collapses. At Goose Creek, marginal extensional fracturing occurs outboard of the reservoir's short axis; this closely matches the pattern of early marginal tensile fracturing and normal faulting in experiments. At Wilmington, horizontal displacements are at a maximum along the short axis, as observed in experiment. The localtion of seismicity at Wilmington is also in agreement with experimental predictions (see Figure 4.25a).

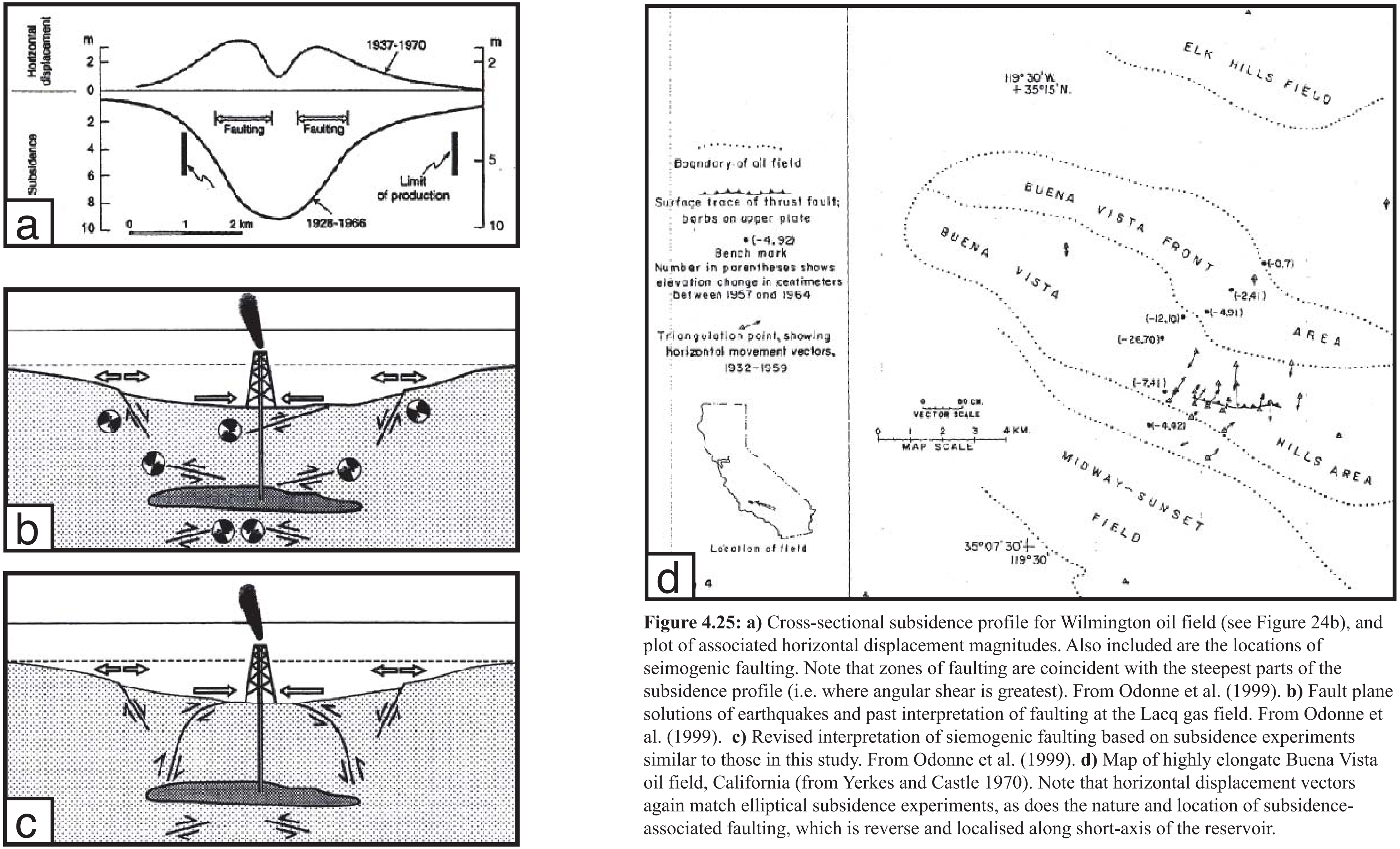

Figure 4.25: a) Cross-sectional subsidence profile for Wilmington oil field (see Figure 24b), and plot of associated horizontal displacement magnitudes. Also included are the locations of seimogenic faulting. Note that zones of faulting are coincident with the steepest parts of the subsidence profile (i.e. where angular shear is greatest). From Odonne et al. (1999). **b)** Fault plane solutions of earthquakes and past interpretation of faulting at the Lacq gas field. From Odonne et al. (1999). **c)** Revised interpretation of siemogenic faulting based on subsidence experiments similar to those in this study. From Odonne et al. (1999). **d)** Map of highly elongate Buena Vista oil field, California (from Yerkes and Castle 1970). Note that horizontal displacement vectors again match elliptical subsidence experiments, as does the nature and location of subsidence-associated faulting, which is reverse and localised along short-axis of the reservoir.

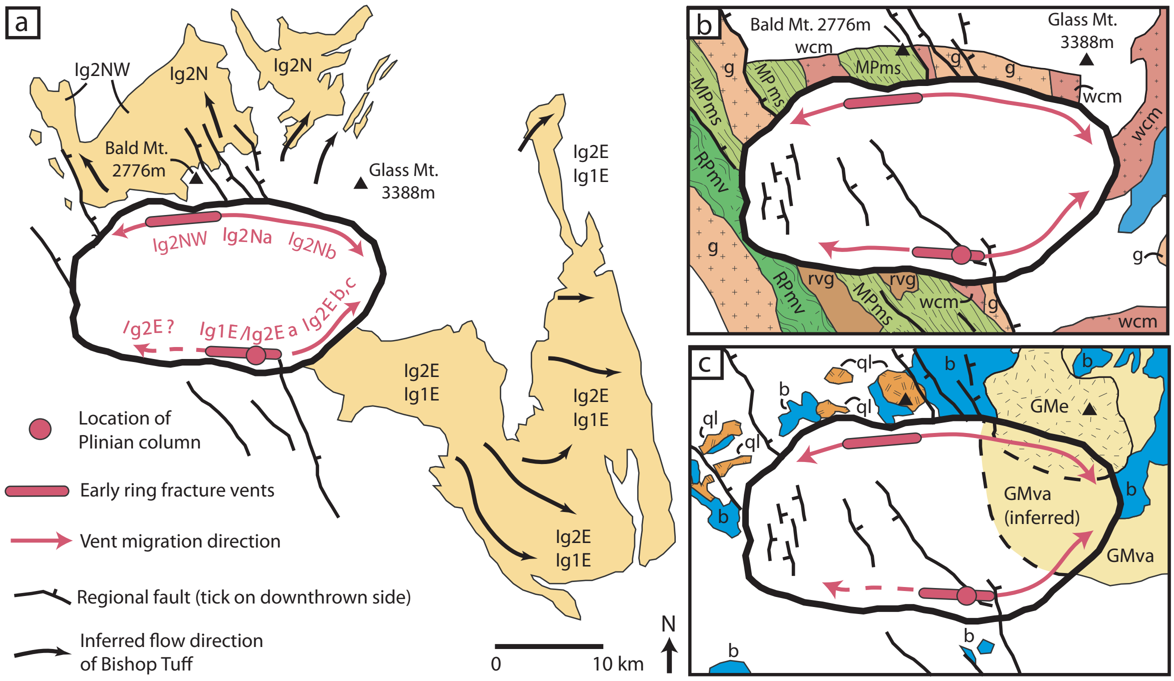

Figure 4.26: Maps of **(a)** Long Valley caldera (thick black line) and Bishop Tuff outcrop (yellow), with inferred migration pattern of ring-fracture vents for successive ignimbrite packages; Two main ignimbrites, an earlier 'Ig1' and a later 'Ig2', were erupted. Letters E, N, NW denote the extra-caldera sector in which an ignimbrite is found; letters a,b,c, etc. denote ignimbrite sub-packages up-section (see main text for further details). **(b)** pre-caldera basement rocks; **(c)** pre-caldera volcanic rocks (modified from Hildreth & Mahood, 1986 and Wilson & Hildreth, 1997). MPms = Mt. Morrison Pendant metasediments; RPmv = Ritter Pendant metavolcanics; wcm = Wheeler Crest Monzonite; rvp = Round Valley Peak granodiorite; g = other granitoids; b = basalt; ql = quartz-latite; GMva = Glass Mountain volcaniclastic apron; GMe = Glass Mountain edifice

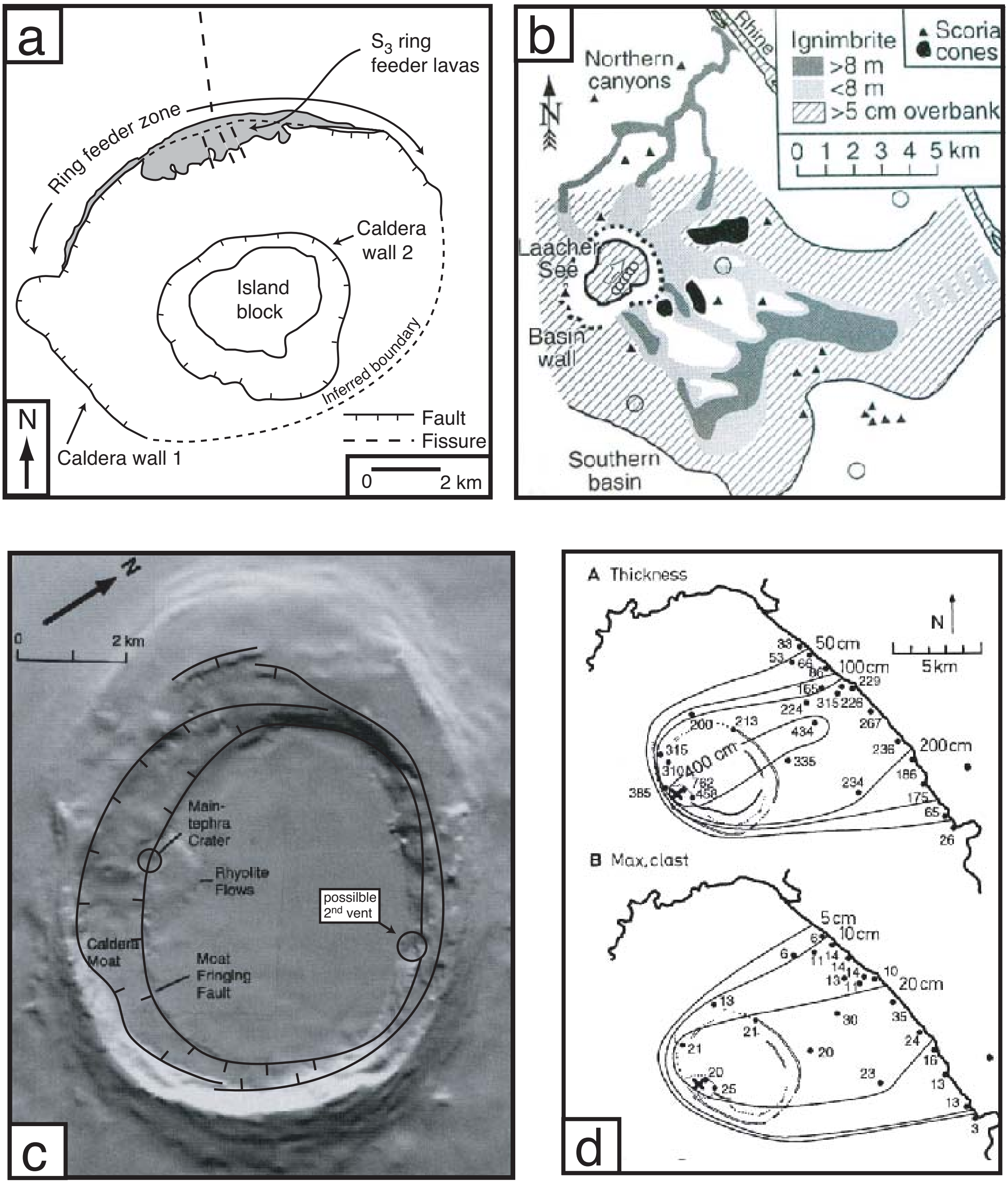

Figure 4.27: Calderas with possible influence on vent positions from reservoir ellipticity
a) Simplified structural map of Suswa caldera, Kenya, showing position of vent system or 'ring feeder zone' for probable syn-collapse lavas (S3 formation). Modified from Skilling (1993).
b) Map of Laacher See volcano, Germany, showing early migration of syn-collpse ignimbrite vents (white circles and white arrow), as inferred by van den Bogaard & Schmincke (1984). From Freundt et al. (2000).
c) Digital shaded relief model of Volcan Alcedo's caldera, with main ring-fault structures and locations of major Plinian rhyolite vent. Modified from Geist et al. (1994). Also included is the location of a suspected second vent for rhyolite eruption (see Geist et al., 1994)..
d) Isopach (thickness) and isopleth (max-clast) plots indicating the position of the main Plinian vent at Alcedo. From Geist et al. (1994).

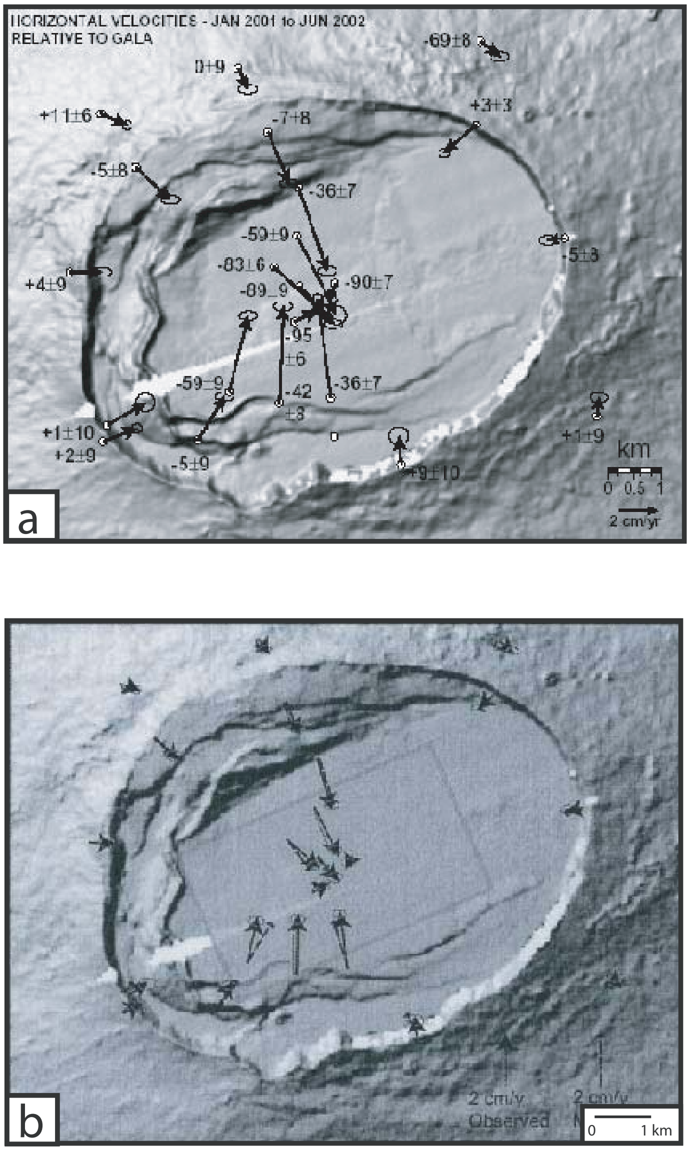

Figure 4.28: a) Digital shaded relief model off Sierra Negra's caldera, showing horizontal displacements measured by GPS during subsidence from January 2001 - June 2002. (From Geist et al. 2006).
b) Same as (**a**) but with limits of an elongate sill at 2km depth. Deflation of this sill provided the best fit to the observed horizontal displacements. (From Geist et al. 2006).

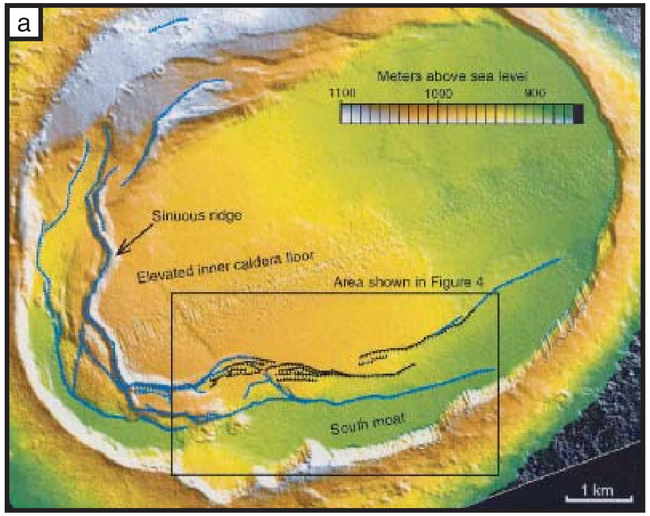

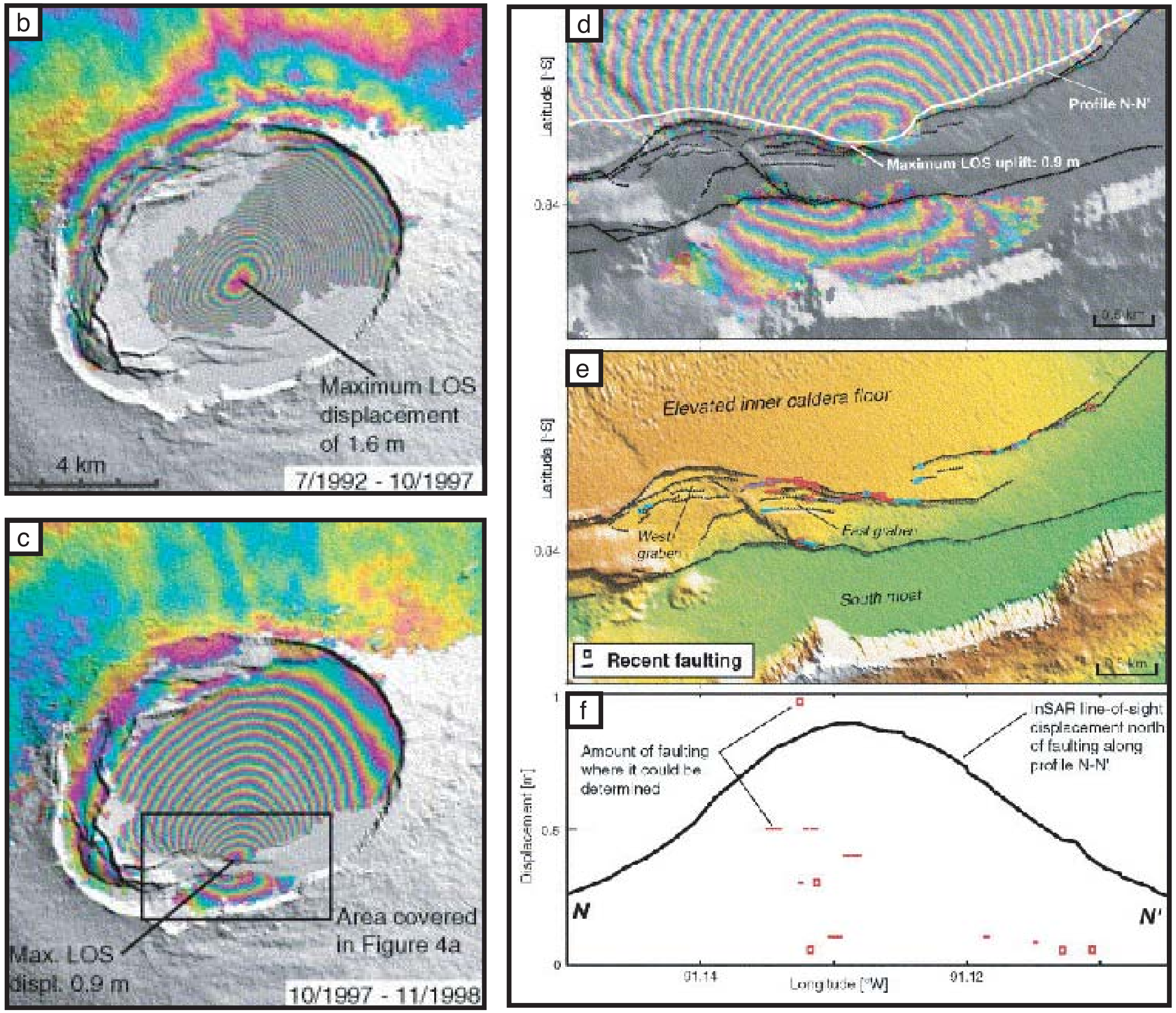

Figure 4.29: (from Jonsson et al. 2005)
a) Coloured relief map of Sierra Negra's caldera.
b) Intergerogram of symmetric inflation and uplift at Sierra Negra from July 1992 to October 1997.
c) Interferogram showing asymmetric (trapdoor) uplift from October 1997 to November 1998. Note centre of uplift and discontinuity in interferogram occur along fault systems in south of caldera, along its short axis.
d) Close-up of uplifted area along the south side of the caldera, as delimited by black rectangle in parts (a) and (c).
e) Map of recent faulting along the south of the caldera.
f) Plot of calculated and measured displacements along the length of the faults in the south of the caldera. Faulting and maximum fault displacement thus occurred along the caldera's short axis, as predicted as an inverse corrollary of the observations and analysis of ellipitcal subsidence.

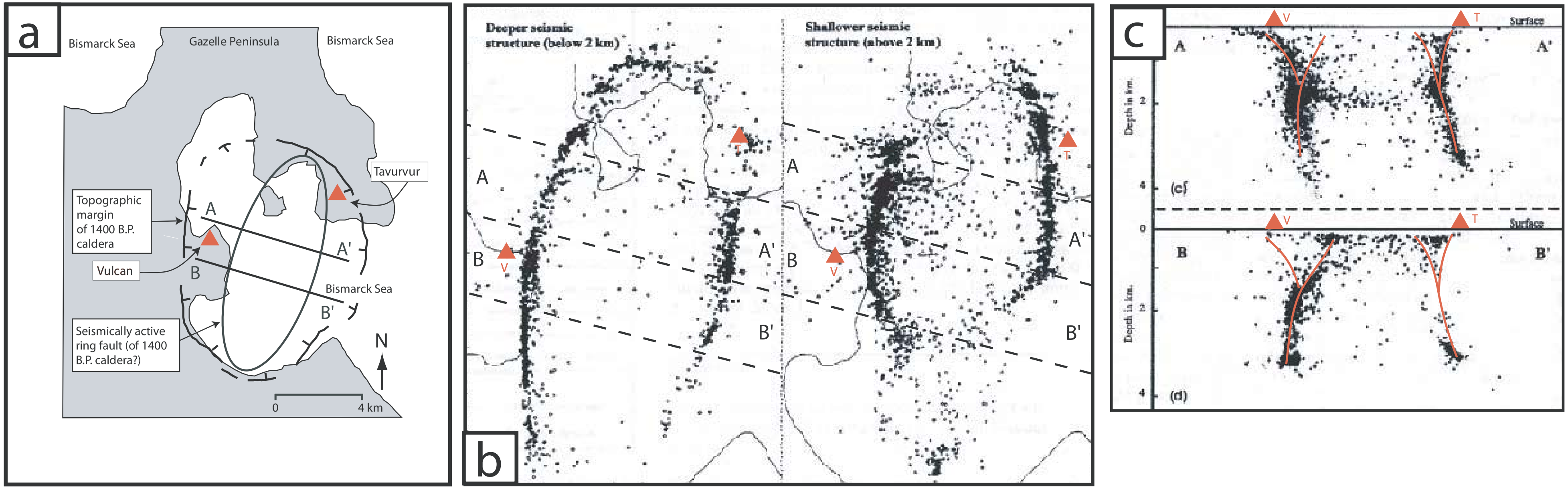

Figure 4.30:

a) Sketch map of the 1400 BP caldera in the nested Rabaul caldera complex, Papua New Guinea (adapted from Nairn et al. 1995) Two active vents, Tavurvur and Vulcan, lie on either side of the lie on either side of the caldera, but not on the trace of the seismically active ring fault. By comparison with experiments, they seem to lie in the peripheral zone of the caldera.

b) Close-up maps of earthquake epicenters that define the seismically active ring fault system. These maps plot epicentres below and above 2 km depth respectively. The structure of the ring fault is revealed to be much more complex than a simple outward-dipping ring. There is a suggestion of two partially intersecting/overlapping ring structures. From Saunders (2001).

c) Cross section plots of earthquake epicentres with red lines approximating fault geometries seen in experimental collapse (adapted from Jones and Stewart, 1997). The earthquake epicentre distribution seems compatible with a central steeply outward dipping reverse ring fault, from which normal faults branch at higher levels. The vents Tavurvur and Vulcan thus seem to be sited on the caldera's peripheral normal faults.

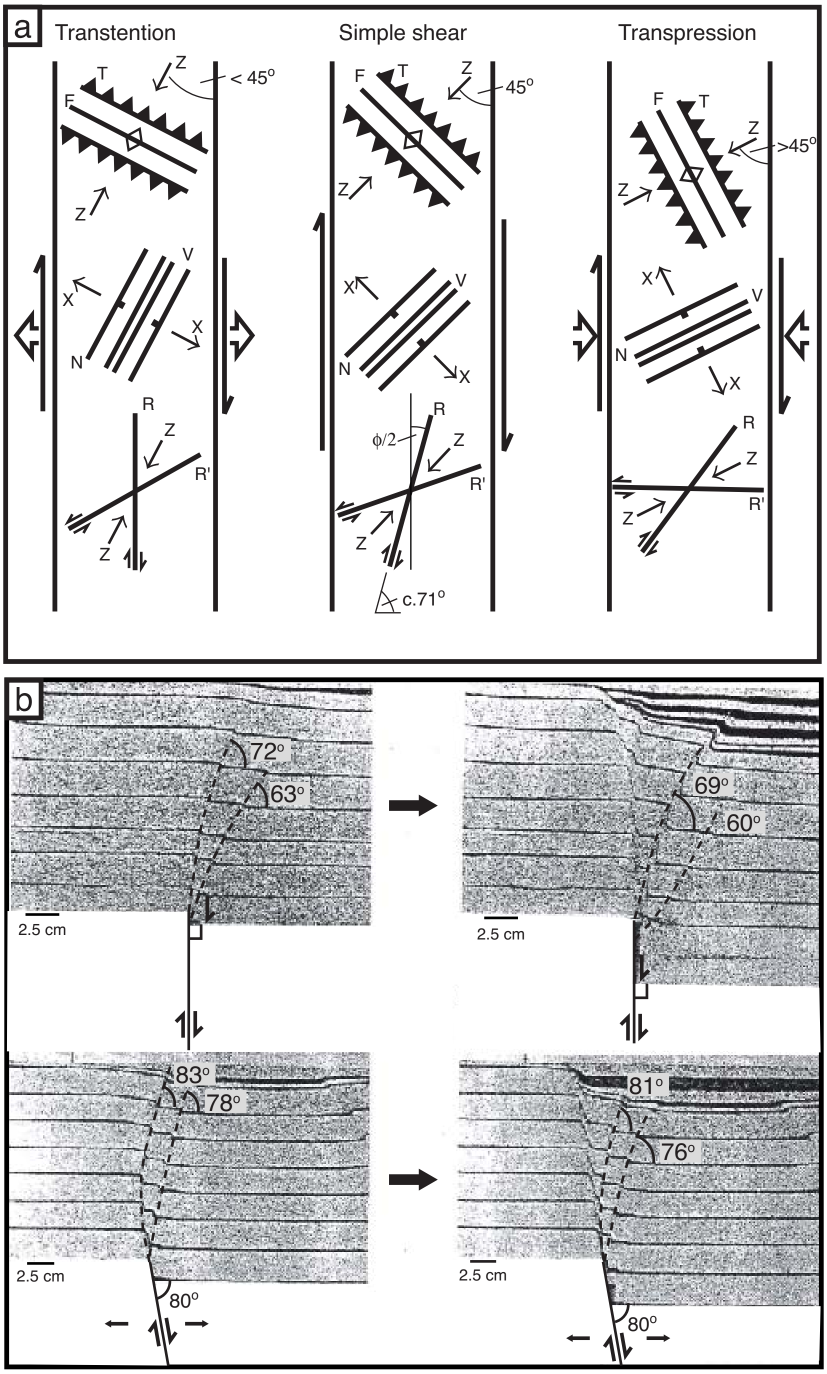

Figure 4.31:
a) Map-view sketches of zones with shear plus extension (transtension), shear only (simple shear), or shear plus contraction (transpression). Adapted from Sanderson and Marchini (1984). Note that the orientation of the z-axis (direction of maximum incremental shortening and maximum compressive stress) changes with respect to the shear zone depending on magnitude of shortening or extension across the shear zone. As a result, the orientations at which structures first form with respect to the shear zone also changes. T= Thrust faults, F = Fold axes, N = Normal faults, V = Veins/Dykes, R = Rieldel shear, R'= Anti-riedal shear.

b) Cross-sections through sand-box simulations of faulting induced in a sedimentary cover sequence by reactivation of a pre-existing basement fault. Thin black sand layers are 25 mm apart. Adapted from Horsfield (1977). Top two images show sequence of faulting where basement fault is vertical. Deformation thus approximates simple shear and precursory reverse faults (R-shears) form in an orientation close to that predicted for the simple shear case in part (a). Bottom two images show sequence of faulting where basement fault is steeply inclined and normal. Deformation in this case entails shear plus a component of horizontal extension (i.e. transtension). This causes the precursory reverse faults (R-shears) to form at a lower angle to the shear zone, and so dip more steeply, as predicted for the transtension case in part (a). Faults in both models are then bodily rotated to slightly lower dips during subsequent deformation.

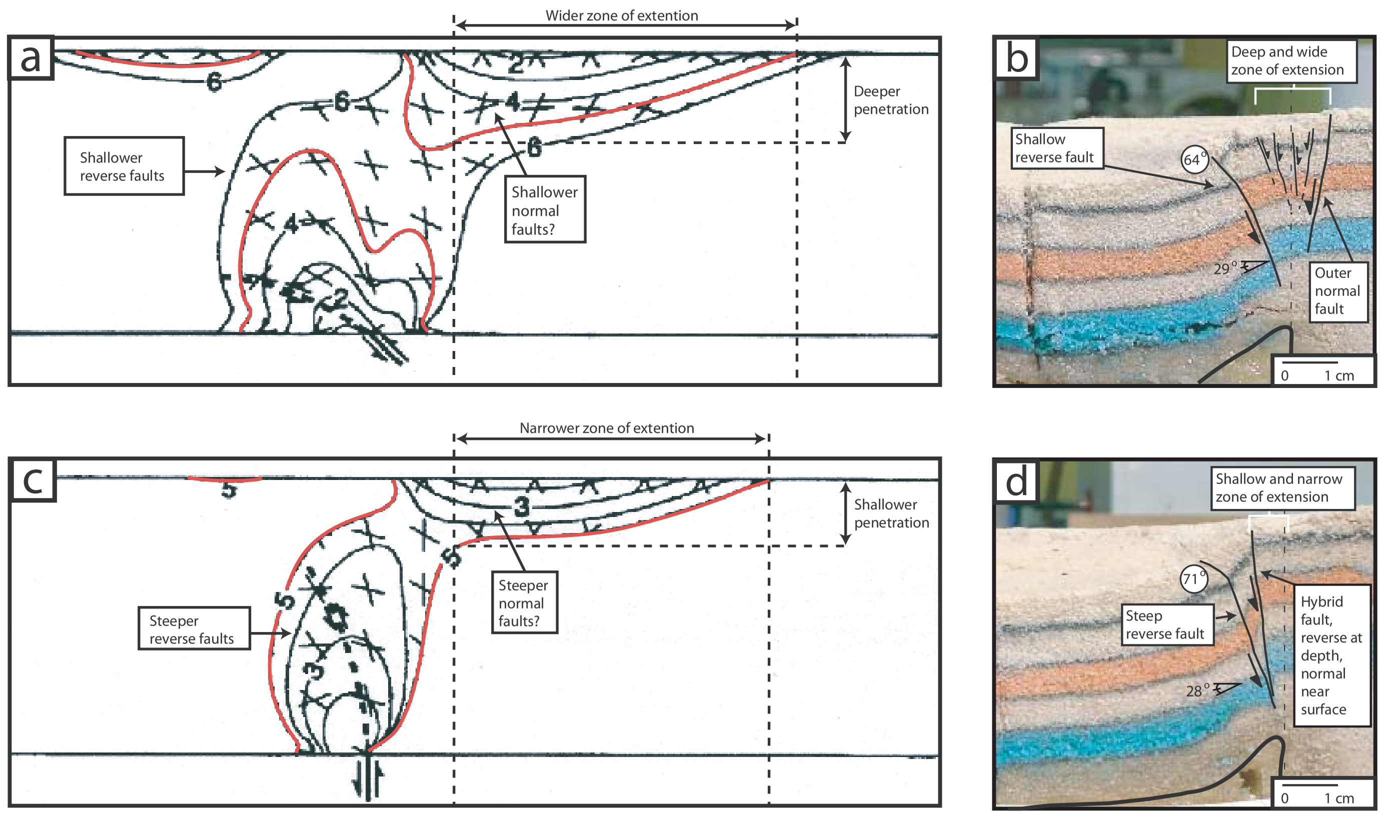

Figure 4.32: a) Numerical model of regions of potential failure in a cover sequence above a reactivated basement fault of moderate dip and reverse sense of slip (adapted from Patton and Fletcher 1995). Contours connect loci of probable failure for a given basement fault displacement (in m); the red contours = 5m. Conjugate fault (~Riedel shear) trajectories are indicated by 'X'. Thick dashed line indicates a possible reverse fault orientation. The inclination and sense of slip on the basement fault induces vertical shear plus a strong component of horizontal contraction in the cover.
b) Half-section along the short axis of Cal Stat B5. The structural relationships above the reservoir edge along model caldera short axes (less steep reverse faults and shallow/narrow zones of peripeheral extension) strongly resemble those produced when vertical shear is accompanied by a large component of horizontal contraction in the numerical model (**a**).
c) Second numerical model of potential failure regions above a reactivated basement fault that is this time vertically orientated (adapted from Patton and Fletcher 1995). The component of horizontal contraction induced by the vertical basement fault is thus greatly reduced compared to (**a**). Consequently, predicted reverse fault trajectories are steeper.
d) Half-section along the long axis of Cal Stat B5. Structural relationships above the reservoir edge along the long axes of model calderas (steep reverse faults and shallow/narrow zones of peripeheral extension) strongly resemble those produced when vertical shear is accompanied by a small component of horizontal of contraction in the numerical model (**c**).

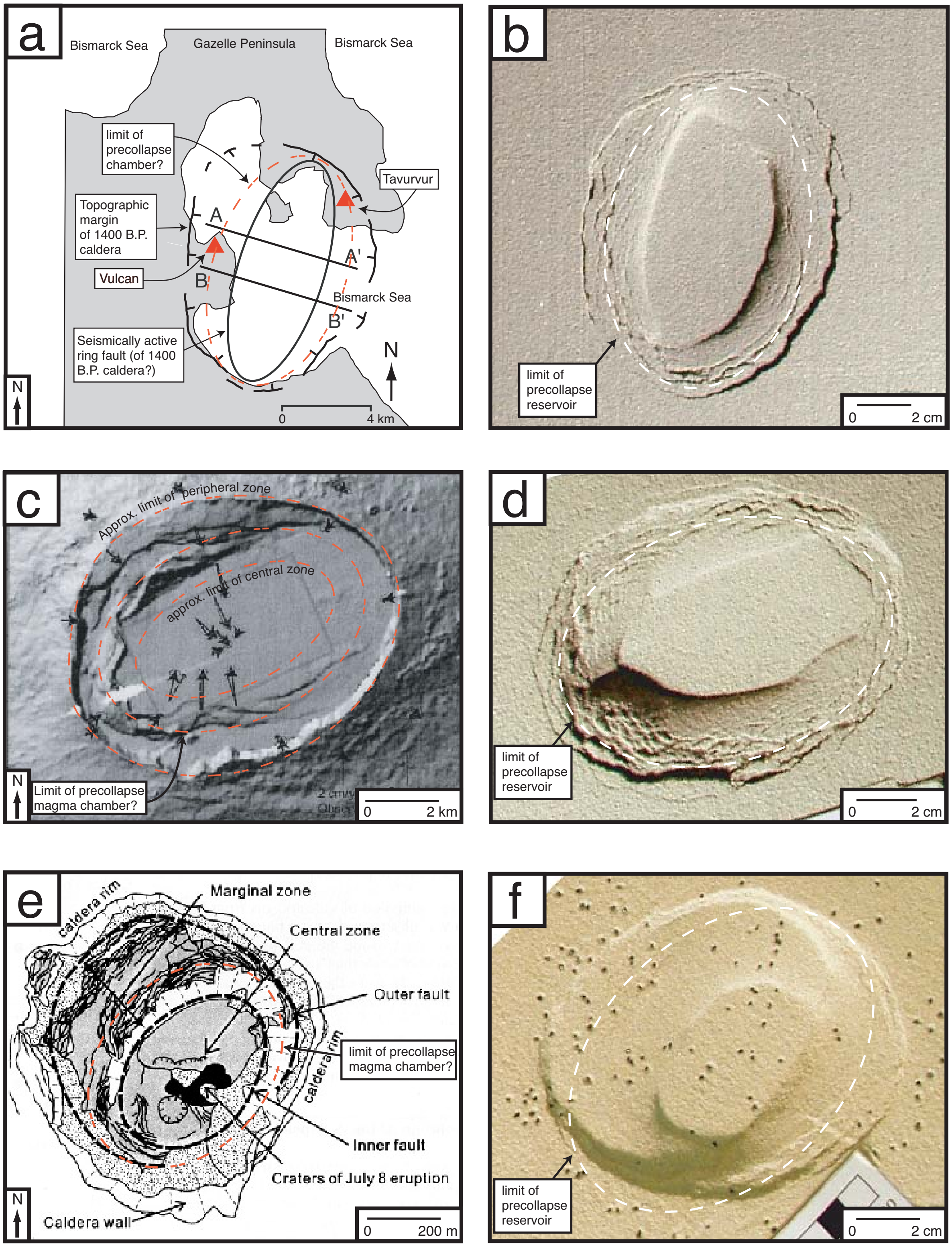

Figure 4.33:
(a) Sketch of map of the 1400BP Rabaul caldera, with inferred limit of precollapse reservoir. Adapted from Nairn et al. (1995). The geometric relationship between the reverse ring fault and topographic margin at Rabaul strongly that in seen in slightly asymmetric, 'thin-roof', collapse structure (Cal Stat C2) in (**b**).
(c) Digital shaded relief model of Sierra Negra caldera with inferred limits of peripheral zone, central zone and reservoir margin. Adapted from Geist et al. (2006). The geometric relationship between the reverse ring fault and topographic margin at Rabaul strongly that in seen in highly asymmetric, 'thin-roof' collapse structure (Cal Stat F7) in (**d**). Both Rabaul and Sierra Negra have low roof thickness/diameter ratios.
(e) Sketch map of structures produced during the 2000 collapse of Miyakejima, Japan. From Geshi et al. (2000). Mijakejima has a high roof thickness/diameter ratio, and strongly resembles the 'thick-roof' elliptical collapse model (Cal Stat G4) **(f),** in displaying the enhanced tendency of the peripheral limit to circularity.

Experiment	Chamber Short Axis (B) (cm)	Chamber Long Axis (A) (cm)	Horizontal Aspect Ratio (A/B)	Ideal A/B	Roof thickness (T) (cm)	Vertical Aspect ratio max (T/B)	Vertical aspect ratio min (T/A)	Conduit Position
Cal Stat A1	9.50	9.50	1.00	1.00	3.00	0.32	0.32	Centred
Cal Stat A2	10.20	10.50	1.03	1.00	3.00	0.29	0.29	Centred
Cal Stat A3	9.70	9.90	1.02	1.00	2.00	0.21	0.20	Centred
Cal Stat A4	10.20	10.20	1.00	1.00	3.00	0.29	0.29	Centred
Cal Stat A5	10.30	10.40	1.01	1.00	3.00	0.29	0.29	Centred
Cal Stat B1	8.70	11.50	1.32	1.33	3.00	0.34	0.26	Centred
Cal Stat B2	9.10	11.50	1.26	1.33	3.00	0.33	0.26	Centred
Cal Stat B3	8.10	10.60	1.31	1.33	2.00	0.25	0.19	Centred
Cal Stat B4	9.10	10.90	1.20	1.33	3.00	0.33	0.28	Centred
Cal Stat B5	8.70	11.50	1.32	1.33	3.00	0.34	0.26	Centred
Cal Stat C1	7.70	12.00	1.56	1.50	3.00	0.39	0.25	Centred
Cal Stat C2	8.70	11.90	1.37	1.50	3.00	0.34	0.25	Centred
Cal Stat C3	7.80	11.80	1.51	1.50	2.00	0.26	0.17	Centred
Cal Stat C4	8.50	12.00	1.41	1.50	3.00	0.35	0.25	Centred
Cal Stat C5	8.00	11.50	1.44	1.50	3.00	0.38	0.26	Centred
Cal Stat D1	6.60	13.40	2.03	2.00	3.00	0.45	0.22	Centred
Cal Stat D2	7.40	13.20	1.78	2.00	3.00	0.41	0.23	Centred
Cal Stat D3	6.80	12.90	1.90	2.00	2.00	0.29	0.16	Centred
Cal Stat D4	6.80	12.60	1.85	2.00	3.00	0.44	0.24	Centred
Cal Stat D5	7.10	12.6	1.77	2.00	3.00	0.42	0.24	Centred
Experiment	**Chamber Short Axis (B) (cm)**	**Chamber Long Axis (A) (cm)**	**Horizontal Aspect Ratio (A/B)**	**Ideal A/B**	**Roof thickness (T) (cm)**	**Vertical Aspect ratio max (T/B)**	**Vertical aspect ratio min (T/A)**	**Conduit Position**
Cal Stat E1	7.90	11.50	1.46	1.50	3.00	0.38	0.26	Non-centred
Cal Stat E2	8.10	11.50	1.42	1.50	3.00	0.37	0.26	Non-centred
Cal Stat E3	7.90	11.70	1.48	1.50	3.00	0.38	0.26	Non-centred
Cal Stat E4	7.80	11.40	1.46	1.50	3.00	0.38	0.26	Non-centred
Cal Stat F1	8.10	11.30	1.40	1.50	3.00	0.37	0.27	Non-centred
Cal Stat F2	8.20	11.30	1.38	1.50	3.00	0.37	0.27	Non-centred
Cal Stat F3	8.70	11.70	1.34	1.50	3.00	0.34	0.26	Non-centred
Cal Stat F4	8.30	11.70	1.41	1.50	3.00	0.36	0.26	Non-centred
Cal Stat F5	7.70	11.30	1.47	1.50	3.00	0.39	0.27	Non-centred
Cal Stat F6	7.90	11.30	1.43	1.50	3.00	0.38	0.27	Non-centred
Cal Stat F7	8.10	11.60	1.43	1.50	3.00	0.37	0.26	Non-centred
Cal Stat F8	8.00	11.50	1.44	1.50	3.00	0.38	0.26	Non-centred
Experiment	**Chamber Short Axis (B) (cm)**	**Chamber Long Axis (A) (cm)**	**Horizontal Aspect Ratio (A/B)**	**Ideal A/B**	**Roof thickness (T) (cm)**	**Vertical Aspect ratio max (T/B)**	**Vertical aspect ratio min (T/A)**	**Conduit Position**
Cal Stat G1	7.70	11.50	1.49	1.50	6.00	0.78	0.52	Non-centred
Cal Stat G2	8.30	11.70	1.41	1.50	6.00	0.72	0.51	Non-centred
Cal Stat G3	8.30	11.70	1.41	1.50	6.00	0.72	0.51	Centred
Cal Stat G4	7.70	11.50	1.49	1.50	6.00	0.78	0.52	Centred
Cal Stat H1	10.00	10.00	1.00	1.00	8.00	0.80	0.80	Centred
Cal Stat H2	10.00	10.00	1.00	1.00	8.00	0.80	0.80	Centred

Table 4.1: Main geometric variables in experiments testing effects of magma chamber elongation on caldera collapse structures. Vertical roof aspect ratio for experiments with an elliptical reservoir is a range, with the minimum and maximum ratios attained along the long and short horizontal axes respectively.

Initial Plan-view Reservoir Dimensions					*Final Plan-view Caldera Dimensions*							
Experiment	**Chamber Short Axis (B) (cm)**	**Chamber Long Axis (A) (cm)**	**Horizontal Aspect Ratio (A/B)**	**Ideal A/B**	**PZ Long Axis (PL) (cm)**	**PZ Short Axis (PS) (cm)**	**PZ Ratio (PL/PS)**	**CZ Long Axis (CL) (cm)**	**CZ Short Axis (CS) (cm)**	**CZ Ratio (CL/CS)**	**Max. Subsidence (cm)**	**Vol. Honey Extracted (cm3)**
Cal Stat A1	9.50	9.50	1.00	1.00	11.20	11.20	1.00	7.20	7.20	1.00	1.60	80.00
Cal Stat A2	10.20	10.50	1.03	1.00	11.60	11.20	1.04	8.00	7.00	1.14	1.30	
Cal Stat A3	9.70	9.90	1.02	1.00	11.70	11.70	1.00	6.50	6.50	1.00	1.30	40.00
Cal Stat A4	10.20	10.20	1.00	1.00	11.30	11.30	1.00	6.20	5.50	1.13	1.50	70.00
Cal Stat A5	10.30	10.40	1.01	1.00	11.20	11.00	1.02	5.90	5.70	1.04	1.30	50.00
		Ave. =	**1.01**			**Ave. =**	**1.01**		**Ave. =**	**1.06**		
Cal Stat B1	8.70	11.50	1.32	1.33	12.20	10.70	1.14	9.50	6.50	1.46	1.00	30.00
Cal Stat B2	9.10	11.50	1.26	1.33	11.70	10.10	1.16	9.00	5.20	1.73	0.90	
Cal Stat B3	8.10	10.60	1.31	1.33	12.70	10.50	1.21	7.30	4.30	1.70	1.20	50.00
Cal Stat B4	9.10	10.90	1.20	1.33	12.20	10.40	1.17	7.70	5.30	1.45	1.60	80.00
Cal Stat B5	8.70	11.50	1.32	1.33	12.70	10.70	1.19	7.50	5.10	1.47	1.20	50.00
		Ave. =	**1.28**			**Ave. =**	**1.17**			**1.56**		
Cal Stat C1	7.70	12.00	1.56	1.50	12.70	9.50	1.34	9.00	5.10	1.76	1.50	75.00
Cal Stat C2	8.70	11.90	1.37	1.50	11.90	9.30	1.28	8.00	4.30	1.86	1.50	
Cal Stat C3	7.80	11.80	1.51	1.50	12.70	10.00	1.27	8.80	3.90	2.26	1.40	60.00
Cal Stat C4	8.50	12.00	1.41	1.50	12.00	10.10	1.19	7.50	3.70	2.03	1.70	85.00
Cal Stat C5	8.00	11.50	1.44	1.50	12.60	10.20	1.24	9.10	3.80	2.39	1.30	50.00
		Ave. =	**1.46**			**Ave. =**	**1.26**		**Ave. =**	**2.06**		
Cal Stat D1	6.60	13.40	2.03	2.00	13.20	8.10	1.63	10.30	3.70	2.78	1.20	40.00
Cal Stat D2	7.40	13.20	1.78	2.00	13.30	9.20	1.45	9.80	3.70	2.65	?	?
Cal Stat D3	6.80	12.90	1.90	2.00	13.60	8.50	1.60	7.70	4.00	1.93	1.30	50.00
Cal Stat D4	6.80	12.60	1.85	2.00	13.10	8.30	1.58	9.80	3.10	3.16	1.50	50.00
Cal Stat D5	7.10	12.6	1.77	2.00	13.20	9.20	1.43	9.70	3.10	3.13	1.25	50.00
		Ave. =	**1.87**			**Ave. =**	**1.54**		**Ave. =**	**2.73**		

Table 4.2: Initial reservoir dimensions and final plan-view geometric data from thin-roof elliptical collapse exeriments with centered conduits. Data from circular collapse experiments are included for comparison. PZ = Peripheral Zone; CZ = Central Zone. Note that the for B,C and D sets, the ellipticities of the central zone and peripheral zone are respectively greater and smaller than the resevoir ellipticity

Experiment	NF Long 1	RF Long 1	RF Long 2	RF Long 3	RF Long 4	NF Long 2	NF Short 1	RF Short 1	RF Short 2	RF Short 3	NF Short 2
Cal Stat A4	83	62					80	71	66		
Cal Stat A5	75	66	64			88	80	63	67		83
Cal Stat B4	84	85	85			84	78	72	82		82
Cal Stat B5	86	83	71			90	76	68	64	58	78
Cal Stat C4	83	78				89	84	71	71		78
Cal Stat C5	84	73				79	81	65	62	60	83
Cal Stat D4	83		77			86	81	68	66		84
Cal Stat D5	86	75	80			82	84	66	60	62	89
Cal Stat F5	86	72				84	86	60	66		80
Cal Stat F6	82	80	71	62	66	81	77	67	63	68	79
Cal Stat F7	83	70	81			77	79	65	63		84
Cal Stat F8	76	68		68		82	82	55	63		81

	Circular case		Elliptical case - Long Axis		Elliptical case - Short Axis	
	Normal Faults	Reverse faults	Normal Faults	Reverse Faults	Normal Faults	Reverse Faults
	75	64	84	85	78	72
	88	63	86	83	76	68
	83	66	83	78	84	71
	80	67	84	73	81	65
	83	62	83	75	81	68
	80	71	86	72	84	66
		66	86	80	86	60
			82	70	77	67
			83	68	79	65
			76	85	82	55
			84	71	82	82
			90	77	78	64
			89	80	78	71
			79	71	83	62
			86	81	84	66
			82		89	60
			84		80	66
			81		79	63
			77		84	63
			82		81	63
Average Dip:	**82**	**66**	**83**	**77**	**81**	**66**

Table 4.3: Dips of main faults (in degrees) in cross-sections of thin-roof elliptical collapse experiments (above) and the average dip values on long and short axes (below). Data from thin-roof circular collapse experiment are included for comparison. NF = Normal Fault, RF = Reverse Fault. RF1 & RF2 are first generation reverse faults; RF3 & RF4 are second generation inner reverse faults.

Initial Plan-view Reservoir Dimensions					*Final Plan-view Caldera Dimensions*							
Experiment	**Chamber Short Axis (B) (cm)**	**Chamber Long Axis (A) (cm)**	**Horizontal Aspect Ratio (A/B)**	**Ideal A/B**	**PZ Long Axis (PL) (cm)**	**PZ Short Axis (PS) (cm)**	**PZ Ratio (PL/PS)**	**CZ Long Axis (CL) (cm)**	**CZ Short Axis (CS) (cm)**	**CZ Ratio (CL/CS)**	**Max. Subsidence (cm)**	**Vol. Honey Extracted (cm3)**
Cal Stat E1	7.90	11.50	1.46	1.50	13.00	10.00	1.30	9.00	4.50	2.00	1.20	60.00
Cal Stat E2	8.10	11.50	1.42	1.50	12.70	9.90	1.28	8.20	5.40	1.52	1.60	60.00
Cal Stat E3	7.90	11.70	1.48	1.50	12.50	9.80	1.28	8.20	4.50	1.82	1.50	70.00
Cal Stat E4	7.80	11.40	1.46	1.50	12.80	9.80	1.31	7.80	4.60	1.70	1.50	70.00
		Ave. =	**1.45**			**Ave. =**	**1.29**		**Ave. =**	**1.76**		
Cal Stat F1	8.10	11.30	1.40	1.50	12.60	9.70	1.30	8.20	4.40	1.86	1.40	70.00
Cal Stat F2	8.20	11.30	1.38	1.50	12.20	9.60	1.27	9.00	4.60	1.96	1.50	60.00
Cal Stat F3	8.70	11.70	1.34	1.50	12.40	9.40	1.32	7.90	4.30	1.84	1.60	60.00
Cal Stat F4	8.30	11.70	1.41	1.50	12.40	9.70	1.28	8.00	3.90	2.05	1.40	55.00
Cal Stat F5	7.70	11.30	1.47	1.50	12.90	9.70	1.33	8.30	3.70	2.24	1.30	50.00
Cal Stat F6	7.90	11.30	1.43	1.50	13.10	10.60	1.24	8.40	4.50	1.87	1.40	50.00
Cal Stat F7	8.10	11.60	1.43	1.50	12.70	9.90	1.28	8.50	4.00	2.13	1.40	55.00
Cal Stat F8	8.00	11.50	1.44	1.50	12.60	10.30	1.22	8.00	3.90	2.05	1.40	50.00
		Ave. =	**1.41**			**Ave. =**	**1.28**		**Ave. =**	**2.00**		
Cal Stat G1	7.70	11.50	1.49	1.50	11.60	9.60	1.21	6.90	3.70	1.86	0.80	50.00
Cal Stat G2	8.30	11.70	1.41	1.50	12.10	10.60	1.14	7.90	4.00	1.98	1.00	60.00
Cal Stat G3	8.30	11.70	1.41	1.50	11.30	11.30	1.00	7.60	3.30	2.30	1.30	60.00
Cal Stat G4	7.70	11.50	1.49	1.50	11.33	11.16	1.02	*5.80*	*3.50*	1.66	1.20	60.00
		Ave. =	**1.45**			**Ave. =**	**1.09**		**Ave. =**	**1.95**		
Cal Stat H1	10.00	10.00	1.00	1.00	12.50	12.30	1.02	6.00	5.50	1.09	1.50	?
Cal Stat H2	10.00	10.00	1.00	1.00	12.50	12.00	1.04	5.80	5.20	1.12	1.50	?
		Ave. =	**1.00**			**Ave. =**	**1.03**		**Ave. =**	**1.10**		

Table 4.4: Initial reservoir dimensions and final plan-view geometric data from (E1-F8) thin-roof elliptical collapse exeriments with non-centered conduits and from (G1-H2) thick-roof collapse experiments with centred or non-centred conduits. Data from circular collapse experiments are included for comparison. PZ = Peripheral Zone; CZ = Central Zone. Note that the general relationships between ellipticities of the PZ, CZ, and reservoir, as seen in Table 4.2, are present here also despite the offset conduits and increased roof thickness. Note also that average PZ ellipticity of the thick-roof collapses tends toward circularity.

Experiment	NF Long 1	RF Long 1	RF Long 2	RF Long 3	RF Long 4	RF Long 5	NF Long 2	NF Short 1	RF Short 1	RF Short 2	RF Long 3	RF Long 4	RF Sho 5	NF Short 2
CalStat G1	88	78	72	82	75	85	86	87	73	78	86	70	67	81
CalStat G2		74	84	79			87		76	68	72			73
CalStat G3	85	80	75	80			87	73	73	70				70
CalStat G4	90	83	72	79			89	73	74	70				78
CalStat H1	85	87	78	74	75	85	85	83	80	75	76	77		87
CalStat H2	86	75	79	85			75	85	78	78	86	83	83	78

	Circular case		Elliptical case - Long Axis		Elliptical case - Short Axis	
	Normal Faults	Reverse faults	Normal Faults	Reverse Faults	Normal Faults	Reverse Faults
	85	87	88	78	87	73
	86	75	85	74	73	76
	85	78	90	80	73	73
	75	79	86	83	81	74
	83	74	87	72	73	78
	85	85	87	84	70	68
	87	75	89	75	78	70
	78	85		72		70
		80		82		86
		78		79		72
		75		80		70
		78		79		67
		76		75		
		86		85		
		77				
		83				
		83				
Average Dip	**83**	**80**	**87**	**78**	**76**	**73**

Table 4.5: Dips of main faults (in degrees) in cross-sections of thick-roof elliptical collapse experiments (above) and the average dip values on long and short axes (below). Data from thin roof circular collapse experiment are included for comparison. NF = Normal Fault, RF = Reverse Fault. Fault numbers are arbitrarily assigned here and do not signify anything about order of formation.

5 Elliptical Calderas in Active Tectonic Regimes: An Experimental Approach

5.1 Introduction

Previous experimental studies of caldera formation have focused on examining the structural effects of local volcano-tectonic stresses generated by doming (or resurgence), due to a rising or expanding magma body, and/or collapse, from magma chamber evacuation and deflation (e.g. Komuro et al., 1984; Komuro, 1987; Marti et al., 1994; Acocella et al., 2000; Roche et al., 2000; Roche and Druitt, 2001; Walter and Troll, 2001; Troll et al., 2002). These analogue studies, as well as analytical and numerical approaches (e.g. Gudmundsson, 1988, Gudmundsson et al., 1997), demonstrate that magma chambers that are circular in plan view and do not experience far-field stresses produce calderas and domes that are also of circular surface expression. In nature however, many calderas lie in extensional and compressive regional tectonic settings (**Table 5.1**), where they have an elliptical shape with a long axis parallel to the direction of least horizontal compressive stress (see also Lipman 1997). These calderas include Valles (New Mexico, USA), Long Valley (California, USA), Yellowstone (Wyoming, USA), and Cerro Galan (Puna, Argentina). In addition, regional tectonic faults are thought to strongly influence the structure many of these calderas are (e.g. Taupo caldera, New Zealand).

The aim of this study was to investigate the effects of far-field (i.e. regional tectonic) stresses and related structures on caldera development and its associated near-field structural patterns. Scaled analogue experiments were conducted in order to examine the possible influences of interacting of volcanic and regional stress fields during caldera formation. These experiments concentrated on structures formed during evacuation and deflation of a magma reservoir under orthogonal (i.e. no strike slip) extensional and compressive tectonic regimes. These experiments highlight the possible contribution of a 'distortion' of caldera faults due to interaction of volcanic and regional stress fields during caldera formation. This interaction may help explain why many calderas are elongated parallel to the regional least compressive horizontal stress. In addition, the experiments provide insights into the interaction of regional tectonic and volcano-tectonic faults during caldera collapse.

The account of the results of this work below is an abridged version of a similarly titled peer-reviewed article by Holohan et al. (2005).

5.2 Experimental Set-up and Procedure

5.2.1 Experimental Apparatus and Materials

Since different apparatus and materials were employed in these experiments, for reasons outlined in Chapter 1, their properties and scaling are described separately here. The experimental apparatus (**Figure 5.1**) consisted of a sand-filled box with two free walls (end walls), similar to that used by Mandl (1987) and Cailleau et al. (2003). Inward and outward motions of the end walls respectively exerted horizontal compressive stress and horizontal extensional stress on the sand medium. A rubber sheet beneath the sand pile was securely fixed to the bottom of the end walls only. When the end walls moved apart, the basal rubber sheet was stretched and, apart from a slight necking at the unrestrained edges, distributed the regional stresses uniformly across the deforming medium (as evidenced by an even distribution of consistently spaced faults). Sill-like rubber balloons buried in the sand were used to simulate magma chambers in the brittle crust. These balloons were circular in plan-view and had rigid rims that preserved their plan-view shape when under regional stress, the influences of which during collapse could thus be discerned from any pre-collapse regional deformation of the reservoir (as simulated in experiments in **Chapter 6**). The balloons were inflated and deflated via a narrow tube connected to an air inlet valve outside the sandbox.

Two end-member analogue materials, sand and wheat flour, were used in the experiments to simulate brittle deformation of the crust (see Walter and Troll, 2001 for more detailed description). We used sieved (mean grain diameter 300 μ~ m) dry, aeolian quartz sand, with a bulk density (ρ_S) of 1300-1500 kgm^{-3} and dry flour (mean grain diameter 100-200 μm) with a bulk density (ρ_F) of 570 kgm^{-3}. Combinations of sand and flour (mixed respectively in ratios of 3:1 and 12:1 by weight) with corresponding bulk densities (ρ_{SF}) of 1400 and 1200 kgm^{-3}, were also used as intermediates between the two end-member materials (see Walter and Troll, 2001, and Belousov et al., 2004, for more detailed description).

Material properties and forces in the experiments should obey the principle of geometric and dynamic similarity (Hubbert, 1951) and operate according to a consistent scaling ratio (X^*), determined by $X^* = X_{Model}/X_{Nat}$ure (see also Roche et al., 2000). The geometric scaling factor (length ratio, $l^* = l_{Model}/l_{Nature}$) was approximately 10^{-5}, so that 1 cm in the model corresponds to ~1 km in nature. The dynamic scaling factor (stress ratio, $\sigma^* = \sigma_{Model}/\sigma_{Nature}$) is calculated from the equation $\sigma^* = \rho^* g^* l^*$. The density range for natural rocks is approximately 2000 – 3300 kgm^{-3}, with most rocks (granites, basalts, hard limestones etc.) lying between 2600 - 3000 kgm^{-3} (Goodman, 1989). As the densities of the analogue materials are less than natural rocks by a factor of approximately 2 (i.e. $\rho^* = 0.5$) and gravitational acceleration is the same in both model and nature (i.e. $g^* = 1$), the required stress ratio for a geometric scaling factor of 10^{-5} was $\sigma^* = 5 \times 10^{-6}$.

Dry, medium-grained sand obeys a straight-line Mohr-Coulomb failure criterion, which was also assumed to apply to rocks in the brittle crust (Hubbert, 1951). Cohesion of natural rocks lies in the range of 10^5-10^7 Pa, which when scaled down by 5 x 10^{-6}, gives a required cohesion of 0.5 – 50 Pa for the analogue materials. Both analogue materials were subjected to direct shear tests to find their angles of internal friction (ϕ) and coefficients of internal friction (C). The cohesion for sand used was C_S = 30-40 Pa, while that of the flour was C_F = 35 Pa. Angles of internal friction of the sand (ϕ_S = 33°) and the flour (ϕ_F = 43°) closely resemble those in natural rocks (ϕ = 30-45° - Goodman, 1989). Time was not scaled in the experiments, as the brittle behaviour of sand and other Mohr-Coulomb materials is generally believed to be independent of strain-rate. Scaling of regional-tectonic deformation follows the principles described in **Chapter 1**.

5.2.2 Experimental Procedures

A series of control experiments was first conducted in the absence of regional stress to compare with experiments that incorporated regional extension or compression. The experimental procedure for collapse experiments free of regional stress began with inflation of the balloon via the air inlet pipe and its subsequent burial in the sand box. The surface of the analogue material was then planed down until the balloon was located at the required depth, providing an even surface on which to observe fracture formation. The balloon was then deflated, by opening the valve on the air inlet pipe, to simulate reservoir evacuation and consequent subsidence of the overlying roof. Subsidence of 3-4 cm was almost instantaneous, lasting 2-4 seconds in all experiments conducted. This may be regarded as equivalent to the subsidence rates inferred for major caldera forming eruptions in nature, in which down-faulting of one or two kilometres may occur over a period of days to weeks (i.e. geologically instantaneous – see Wilson and Hildreth 1997).

The experimental procedure for collapse experiments under regional stresses followed that of the control experiments up to burial of the inflated balloon and smoothing of the analogue material's surface. Compressive or extensional stresses were then applied to the sand medium by movement of the end walls until the desired amount of regional strain was achieved. The rate of strain applied during the pre-caldera regional compression/extension phase was regarded as unimportant based on the aforementioned assumption strain rate independence for sand/flour deformation. Towards the end of the extension/compression phase, the balloon was deflated to simulate reservoir evacuation and accompanying caldera collapse. Balloon deflation was conducted syntectonically, with a half revolution of the driveshafts (equaling two millimeters displacement) over the course of caldera collapse so as to maintain regional stresses in the system. Measurements of model caldera dimensions were taken along axes orientated perpendicular to and parallel to the end walls, respectively termed the A-axis and B-axis (**Figure 5.2**).

5.2.3 Limitations of the set-up

Many limitations of this materials and set-up here are similar to those discussed in Chapter 1 for the honey and sand/gypsum models. 'Edge effects', such as frictional forces operating around the surfaces of the deformation rig, can potentially disrupt scaling in analogue models. These effects were minimized in these experiments by the large size of the deformation rig (70-100cm x 80cm x 40cm – **Figure 5.1**), which permitted the studied deformation area (30cm x 25cm) in the centre of the model to be sufficiently far away from the walls. The use of rubber balloons to simulate a magma chamber causes a separation of the chamber from its surroundings by an impenetrable membrane. This ignores possible effects on collapse dynamics and pressure variations in a chamber due to subsidence of roof blocks. The crust immediately around the magma chamber is subjected to very high temperatures in nature, which could locally induce ductile behaviour. In the experiments here, this section of the crust was assumed to behave in a brittle manner, the basis for which is that local strain rates involved in magma chamber inflation and deflation are typically very high and would favour brittle deformation.

A further assumption was that brittle behaviour in the crust extended regionally down to depths of 12 km or more. In nature, the brittle to ductile transition typically occurs between depths of 4-12km. In areas of thickened crust, the transition may extend deeper than this range. Beneath the Southern Puna of the Central Volcanic Zone of the Andes for instance, the brittle-ductile transition is thought to be located at a depth of around 15 km (Seggiaro, 1999). However, the transition is likely to be at the shallower end of this range in areas of high heat flow and thin crust. A follow-on to the assumption of brittle behaviour in the model is that time was assumed to exert little control in the style of deformation. In nature however, rheology of crustal materials may deviate from Mohr-Coulomb behaviour, particularly on longer time scales, and so the models cannot account for variation due to such effects. Strain in the model was assumed to be homogeneous, whereas concentrations of strain are likely in nature. Transtensional or transpressional tectonic regimes, with associated strike-slip faulting, were not simulated using the above set-up and the impacts of pre-tectonic crustal inhomogeneties and pre-caldera topography (e.g. a conical volcanic edifice load) were not studied.

5.3 Experimental results

5.3.1 Caldera formation in a regional stress field

In the absence of far-field stress, calderas were predictably circular in plan (**Figure 5.2a**). As in previous simulations (see **Chapters 2-4**), caldera subsidence initially occurred as a central zone of downsag accompanied by an outer concentric zone of tensional fractures. Downsag subsequently progressed into collapse along outward-dipping reverse faults in the central zone, accompanied by normal faulting in the peripheral zone.

In experiments simulating extensional tectonic regimes, an evenly spaced series of fractures formed across the analogue medium, orientated parallel to the moving end walls. At higher regional strain levels, these fractures developed into normal faults that defined a horst and graben pattern. In compressive regimes, a similarly equally-spaced series of reverse fractures (albeit fewer in number) formed parallel to the end-walls. Calderas produced from circular magma chambers in both the compression and extension experiments were elliptical in shape and typically elongate parallel to the direction of the regional least horizontal compressive stress (ShMin). For experiments with regional extension, ShMin is parallel to the regional extension direction, while for experiments with regional compression, ShMin is perpendicular to the regional compression direction (**Figure 5.2b and 5.2c**).

Data sets representative of the experimental series are given in **Tables 5.2 and 5.3**. The tables show that the average central zone area formed under extension and compression increases with decreasing depth. This can be related to the level at which the outward dipping (bell-shaped) reverse ring fault(s) that bound the central zone intersect the sand surface (cf. Walter and Troll, 2001). In contrast, the average area of the normal fault bound peripheral zone decreases with decreasing depth. Another feature of the data is that the average area encompassed by central zones formed in compression is slightly lower relative to those formed in extension. This may well be due to a slight thickening of the sand pile during the pre-collapse regional compression phase. A corresponding increase in the peripheral areas in compression relative to those in extension is also shown in **Table 5.3**, while its absence in **Table 5.2** may simply be a function of minor variability in that particular dataset.

Thus the area of calderas formed in stressed and non-stressed experiments was controlled by depth and initial plan-view area of the underlying magma chamber (**Figure 5.3a**). The areas encompassed by the central zone and the peripheral fault zones in stressed experiments remained approximately constant with (and therefore independent of) increasing pre-collapse regional strain (**Figure 5.3b**). However, calderas formed in experiments with regional stress appeared increasingly elliptical in plan with increasing pre-collapse regional strain. A positive linear relationship between the total regional strain and ellipticity of the model calderas was observed (**Figure 5.3c**). The ellipticity of the central caldera zone tended to be more pronounced than that of the corresponding peripheral zone for a given value of regional strain. This discrepancy became larger with increasing regional strain.

5.3.2 Interaction of caldera-related and regional fault patterns

A significant influence on the development of caldera structures encountered during some experiments was the presence of pre-existing regional faults. Especially in experiments simulating extensional tectonic regimes, several key observations were made where normal faults intersected the area affected by the developing caldera. Firstly, pre-existing normal faults intersecting the edge of the developing caldera were frequently re-used (sometimes with motion reversed) to accommodate the subsidence of the collapsing chamber roof. This was especially the case in experiments with lower sand/flour ratios where such normal faults dipped in the preferred orientation of reverse ring faults (**Figure 5.4**). Where such regional faults became caldera-bounding faults, some truncation of the preferred elliptical-subcircular surface expression of the central zone was observed, with displacement along ring fractures taken up by regional faults instead (**Figure 5.4**). Secondly, concentric extensional fractures in the caldera periphery were consistently 'captured' or re-orientated during their propagation in the proximity of pre-existing normal faults (**Figure 5.4**). The regional normal faults also accommodated some peripheral extension during collapse of the central zone, particularly at the ends of the caldera's A-axis. Thirdly, the floor of the caldera *sometimes* subsided as discrete blocks along regional fractures ("piecemeal subsidence") rather than as a fully coherent block. The locally compressive stress regime in the subsiding central zone basin resulted in differential down faulting of these blocks (some appearing as fault-bound 'pop-ups' within the caldera floor), forming irregular and stepped caldera floor topographies.

Continued regional extension or compression after collapse led to progressive distortion of the newly formed caldera structure, causing it to be even further elongated. This process affected the caldera area however, progressively increasing the A-axis length in extensional experiments and decreasing the A-axis length in compressive experiments.

5.4 Discussion

Analogue experiments were conducted to examine possible mechanisms for the formation of elongate calderas under regional stress and to evaluate the effect of regional tectonic faults on caldera structures. In the absence of regional forces, the local stress field due to a deflating (or inflating) oblate or spherical magma chamber will produce a circular caldera, consistent with earlier theoretical studies (e.g. Gudmundsson et al., 1997) and physical modelling experiments (e.g. Roche et al., 2000; Acocella et al., 2000, Walter and Troll, 2001). The experiments here investigated the effects of regional stresses and associated structures on the local fault pattern produced during evacuation collapse of a magma chamber of known dimensions. The key observation of these pure collapse experiments was that elliptical calderas formed above circular magma chambers when subjected to regional stress during formation. This suggests that a distortion of the local stress field associated with the collapsing balloon occurred due to interaction with a far-field stress regime. In addition, regional tectonic faults were almost always locally reactivated during caldera collapse, with reactivation occurring most commonly near the edges of the balloon.

5.4.1 Influence of far-field stress on local caldera structures - 'fault distortion' and possible implications

Two or more stress fields can interact to produce a combined or composite stress field (Park, 1997). Analogue studies conducted by van Wyk de Vries and Merle (1996, 1998) examined the effects of volcanic loads on regional fault patterns associated with orthogonal and pull-apart (strike-slip) rifting. These studies show interplay between the local volcanic and regional stress regimes, the result of which is the distortion of regional and local fault trajectories in the vicinity of the superimposed stress fields. A similar distortion effect may account for the structures produced in the above simulations of caldera collapse under regional stress.

In experiment, the stress fields to consider are: 1) a local stress field associated with the deflating magma chamber and 2) a regional stress field, due to either regional extension or far-field shortening. A qualitative two-dimensional mechanical analysis of the observed reverse ring fault patterns along the A- and B-axes of the experimental set-up is schematically presented in **Figure 5.5**. This analysis is based on the experiments with regional extension only, but, as the results from regional compression experiments are essentially the reverse of the regional extension experiments, the analysis can be reversed to account for ring fault patterns produced in regional compression. Following the convention of van Wyk de Vries and Merle (1996, 1998), the principal axes of stresses induced by the collapsing chamber are denoted σ_V, those for regional stresses are symbolised by σ_R and the combined stresses are represented by σ_C.

The deflation of the balloon is characterised by a greater rate of contraction over its centre with respect to its margins (**Figure 5.5a**). This disparity results in shearing of the down-going roof, and creation of a main local compressive stress, $\sigma 1_V$, at 45° to the applied shear. According to the Coulomb criterion, shear fractures will develop at an angle of 30-35° to $\sigma 1_V$, and thus dip steeply outward (~75°) with a reverse motion.

The stress field resulting from orthogonal regional extension is characterised by a vertical main compressive stress, $\sigma 1_R$, and a horizontal least compressive stress, $\sigma 3_R$ (**Figure 5.5b**). Interaction of the regional and local stress fields produces resultant (combined) principal stress axes, $\sigma 1_C$ and $\sigma 3_C$, which are rotated outward relative to $\sigma 1_V$ and $\sigma 3_V$. The degree of rotation will depend on the relative magnitudes of the local and regional stresses. As a consequence, the reverse fault orientation is also rotated outward and its dip steepened. If the caldera-bounding reverse fault is steeper, it will intersect the surface at a greater distance from the caldera centre, resulting in an elongation of the caldera radius in the A-direction (**Figure 5.2a**).

The extension of the deformation rig causes the rubber base to contract or 'neck' in the B-direction. This contraction exerts a regional stress on the sand defined by a horizontal main compressive stress, $\sigma 2_R$, and vertical least compressive stress, $\sigma 3_R$ (**Figure 5.5c**). Therefore, the opposite occurs to what happens along the A-axis, with $\sigma 1_C$ and $\sigma 3_C$ rotated inward along the B-axis relative to $\sigma1_V$ and $\sigma3_V$. This results in a shallowing of the ring fault, which, when the fault reaches the surface, causes shortening of the caldera radius in the B-direction. For chamber collapse under regional compression, the situation along the A- and B-axes is reversed and so the caldera is elongated along the A-axis and shortened along the B-axis. Mandl (1988) simulated the deformation of 'pre-stressed' sand cover sequences, in which the sand was initially stretched or contracted via a rubber sheet prior to its deformation by subsiding basement fault-blocks. A very similar re-orientation or 'distortion' of reverse faults to that in the caldera experiments was observed (Mandl 1988).

The discrepancy between the ellipticities of the central zone area and the surrounding peripheral fault zone (**Figure 5.3b**) may be related to the horizontal displacement or heave along the reverse ring faults. The steeper a reverse ring fault, the less its heave and, correspondingly, the less extension is exerted in its periphery. For the case of regional extension, reverse ring faults are steepest along the A-axis. As this is where the horizontal displacement along the ring fault is least, the outward extent of the peripheral fault zone will be shortest. The opposite occurs along the B-axis, where the heave on the ring fault is greatest and so the outward extent of the peripheral fault zone will be greatest. The result is a peripheral fault zone that has an aspect ratio less than that of the central zone it encloses. With increasing regional strain, the disparity in aspect ratios increases (**Figure 5.3b**). This can be related to a consequent increased steepening of the reverse fault sections facing the least regional horizontal compressive stress (ShMin) and the increased shallowing of those sections facing the main regional horizontal compressive stress (ShMax).

The circumferential variation in ring fault dip due to 'fault distortion' – or perhaps more accurately, 'local stress field distortion' - may have significant implications for syn- and post-caldera ring-fault eruptions. Magma may be injected along fractures if the magma pressure exceeds the compressive stress across the fracture plane (Park, 1997). Moreover, injection along a fracture is more likely if the angle between fracture and a intruding magma body is small. The experiments imply that the angle made by ring faults with magma pushing upward from top of the magma chamber would be smallest along the ring fault sections striking perpendicular to the regional ShMin. Furthermore, the compressive stress across the reverse ring-fault will be lowest along the fault sections striking perpendicular to the ShMin. It seems possible therefore that injection of magma along an elliptical ring fault under regional stress will preferentially occur along the fault sections facing the regional ShMin.

Once formed, natural calderas remain subject to the regional stresses that acted during collapse. The experiments showed that continuing regional strain increases the ellipticity of the newly formed caldera structure by further elongating it. Therefore, post-caldera regional deformation is likely to add to the 'distortion' of caldera structures. This effect in altering the ellipticity of a caldera is likely to be more pronounced with increasing age of the caldera structure, increased duration of regional strain and increasing regional strain rate.

Finding field evidence for the occurrence of such a 'fault distortion' effect at calderas in nature is likely to be difficult. Mapping the ring faults at calderas to see if dips change as predicted in these models is commonly hindered by limited exposure. Alternatively, comparison of a caldera's structural dimensions with the dimensions of the magma chamber that lies beneath would be required. It may be possible to image the chamber remnants beneath a caldera, either with seismic or gravity studies and compare its geometry with that of the caldera. However, a major uncertainty of this approach is whether the original chamber into which collapse occurred is being imaged and has not been already modified or even destroyed during or after caldera formation (Wolff and Gardner, 1995).

While the 'fault distortion' effect is likely to apply to reservoirs of any geometry, the initial magma chamber dimensions will nonetheless still exert a fundamental control on caldera geometry. Assuming Newtonian behaviour, a viscous material like magma will deform under the slightest differential stress (Twiss and Moores, 1992), while even a more realistic non-Newtonian fluid character will also permit flow and deformation, once yield strength is exceeded. Newhall and Dzurisin (1988) quote natural examples of caldera floor uplift and subsidence that have been related to 'squeezing' or stretching of magma chambers resulting from regional strain. It is therefore likely that chambers that are non-circular in plan view underlie natural calderas in tectonically active regions. One aspect of future work must be to more fully understand what controls initial geometry of an underlying chamber in tectonically active settings.

5.4.2 Role of pre-existing structures in caldera collapse

In the above experiments, reactivation and exploitation of pre-existing regional structures also played a role in the formation of model calderas. In general, their influence related to the frequent development of three features of the model calderas: 1) the occasional formation of a segmented, 'piecemeal' caldera floor with variable down-faulting of neighbouring blocks, 2) the truncation of caldera ring faults and 3) the creation of a distinctly polygonal caldera outline. Ramberg's (1981) centrifuge experiments previously demonstrated the capacity for pre-existing fractures to accommodate caldera-like subsidence without the generation of new fractures. The development of many natural calderas is clearly influenced by faults parallel to regional trends (see **section 5.4.3** below). The experiments here thus further underline the potential importance of regional fault in controlling the geometry of collapse calderas.

Where piecemeal caldera collapse was observed (**Figure 5.2c**), individual blocks in the caldera floor were bounded by a combination of local caldera faults and pre-existing regional fractures. This type of 'random' piecemeal caldera subsidence differs from the more regular pattern observed in experiments simulating cyclic doming and collapse (Walter and Troll, 2001; Troll et al., 2002), where radial and concentric segmentation of the caldera floor occurs due to faulting resulting from phases of doming. In experiments here, truncation of caldera ring faults occurred when regional faults accommodated collapse, preventing the generation of a complete ring fracture. However, in some experiments, displacement transfer from ring fractures to regional structures was also observed (**Figure 5.4**). In this case, a complete ring fracture was generated, but the major displacement was nonetheless accommodated along the regional faults. A similar reactivation and utilisation of regional faults by caldera faults was observed in analogue experiments that simulated caldera formation and resurgence in sand deformed by pre-existing extensional faults (Acocella et al., 2004). Such reactivations, as in this study, occurred preferentially at the edge of the analogue magma reservoir.

A subordinate feature of the experiments of this work was the 'capture' or propagation of peripheral caldera faults toward pre-existing regional faults, which can perhaps be explained in terms of the tendency of fractures to propagate toward free surfaces or discontinuities. Alternatively, this phenomenon could be related to the switchover from a composite stress regime dominated by the deflating magma chamber to one where the regional stresses again become more dominant.

Based on his experiments, Komuro (1987) discussed the formation of polygonal calderas purely due to doming. In his model, perpendicularly intersecting radial and concentric faults, generated by the near field stresses of magma chamber inflation, result in the formation of a polygonal caldera at the apex of the domed region. However, the formation of radial faults is unlikely to occur in caldera formation due to magma chamber deflation only (Walter and Troll 2001). Although the formation of many calderas has indeed been associated with regional tumescence, many other natural calderas apparently show little evidence of pre-collapse doming (Lipman 1984, Branney 1995). In these cases, which approximate a pure collapse scenario in nature, formation of calderas with polygonal surface expressions may be more strongly controlled by the intersection of regional faults with caldera faults. Note also, however, that experimental calderas forming without any regional tectonic structures are also polygonal any way (**Chapters 2, 4, & 6**). Regional tectonic faults, if reactivated during volcano-tectonic collapse, may thus act as an additional factor to enhance an inherent tendency for calderas to attain a polygonal shape.

5.4.3 Comparison of experimental results with natural examples

Calderas that are elongate parallel or sub-parallel to the regional minimum horizontal compressive stress can be found in extensional as well as in compressive settings. Examples of such calderas in extensional settings include Valles caldera, New Mexico (Goff and Gardner, 1994; Aldritch et al., 1996), Furnas caldera, Sao Miguel Island Azores (Guest et al., 1998), Suswa caldera, Kenyan Rift Valley (Skilling, 1993; Bosworth et al., 2000), and Taupo caldera, New Zealand (Wilson et al., 1995). Of these examples, the Taupo caldera most closely matches the calderas produced in the experiments here (**Figure 5.6a)**. Field and remote sensing data gathered by Acocella et al. (2003) show that Taupo caldera lies in a segment of the Taupo Volcanic Zone rift, along which extension is purely orthogonal to the rift axis (i.e. no strike-slip component - as in our experiments).

Examples of calderas located in compressive regimes appear to be far less common. One example is Katmai caldera, Alaska (**Figure 5.6b**). Katmai is also elongate parallel to the regional minimum horizontal compressive stress, as inferred from the orientation of regional joints, dykes and eruptive fissures (Wallmann et al., 1990). Caldera collapse at Katmai occurred due to lateral withdrawal of magma from beneath the volcano and its distal eruption through the Novarupta vent in 1912 (Hildreth and Fierstein, 2000). The structural data collected by Wallmann et al. (1990) indicate that the compression direction around Katmai is more or less orthogonal to the volcanic axis of the Aleutian Arc. Thus the eruption scenario at Katmai and the resultant caldera surface expression are quite similar to that simulated in our experiments. It is also notable that the surface expression of the Novarupta vent, which is a collapse feature perhaps representative of the transition between calderas, vents and diatremes (see Lipman 1997 and **Chapter 3**), is also elliptical and elongate in the same orientation as Katmai caldera, as would be predicted from the above experimental results.

Many calderas are not located in areas of orthogonal or pure extension as is the case in the models. Some, for instance Gariboldi and Gedemsa calderas in the Ethiopian rift (Acocella et al., 2002), lie in regions undergoing extension oblique to the rift axis and are themselves elongated at an oblique angle to the rift and the extension direction. The caldera orientations in this scenario may be explained by magma chamber elongation along deep-rooted strike-slip faults accommodating the oblique extension direction. Others, like Kapenga caldera, New Zealand (Acocella et al., 2003) are clearly elongated parallel to the major extensional/strike slip faults of the rift axis and are sub-perpendicular to the regional extension direction. This implies pre-existing fault orientation as the major control on caldera elongation for such examples. Conversely, the massive Cerro Galan caldera, NW Argentina (Francis et al., 1978, Marrett et al., 1994 - **Figure 5.6c**), which formed under an initially transpressive tectonic regime, is also elongate parallel to regional fault and crustal lineament trends, but parallel to the regional ShMin at the time of its formation, in agreement with the model results. The tectonic history of the regional around Cerro Galan has been quite complex, and perhaps serves as a note of caution that one must carefully distinguish between current stress regimes and those at the time of caldera formation.

Some calderas in transtensional tectonic settings, while not elongate parallel to the regional minimum compressive stress, may be elongated parallel to a more localised minimum compressive stress resulting from second order tectonic movements. An example is the Somma-Vesuvius caldera complex, where the earliest collapse structure has a long axis trending obliquely (ESE-WNW) to the regional minimum compressive stress (NNE-SSW) of the surrounding Campanian Plain (Bianco et al., 1998; Cioni et al., 1999). In this case, regional extension is accommodated by two sets of perpendicularly intersecting oblique-normal faults. Sense of shear on these fault trends is opposite (conjugate), which generates a zone of localised ESE-WNW extension around the Somma-Vesuvius complex.

The influence of pre-existing regional fault patterns on caldera surface expression can be seen in many natural calderas. Regional faults may impact on the geometry of a caldera by defining the boundaries of the underlying magma chamber, which may then exert the main control on caldera geometry (see above), or by providing lines of weakness that can be exploited by a forming ring fault. For example, the first major collapse at the Campi Flegrei Caldera, Italy may have been accommodated to a very significant degree along pre-existing, regional oblique-slip normal faults (Orsi et al., 1996). The 1883 collapse at Krakatau, Indonesia, may have been also (Deplus et al., 1995). Regional extensional/strike slip faults are also regarded as the primary control on the subsidence of the massive Toba caldera, Indonesia (Aldiss and Ghazali, 1984) and hence its direction of elongation.

A variation on this theme is seen in **Figure 5.4**, where the main ring fault is observed to splay out eastward to join up with two regional normal faults, resulting in the down faulting of a radial graben extending into the periphery. The Taupo caldera, New Zealand is characterised by a similar down-faulted half-graben extending southeast from the area bound by the main ring fault (Cole et al., 1998 – **Figure 5.6a**). Campi Flegrei caldera also exhibits this splaying-out of caldera faults toward regional faults with resultant volcano-tectonic graben subsidence in the periphery. Ring faults have been inferred to play a role in all of the above examples, but the extent to which they accommodate subsidence in calderas under regional stress is very variable.

A further product of the intersection of regional faults with the caldera structures in the experiments was the dissection of the caldera floor by regional faults. This sometimes resulted in a piecemeal-like caldera floor structure similar to that inferred by Branney and Kokelaar (1994) at Scafell caldera in the English Lake District and by Moore and Kokelaar (1998) at Glencoe caldera, Scotland. These combined experimental and field observations thus underline the importance of pre-existing and syn-tectonic regional structures in volcano-tectonic processes.

5.5 Conclusions

From the experimental observations above, the interaction of regional and local stress fields may be of significance for caldera formation in active tectonic regimes. This interaction results in elongation of the caldera's concentric inner and peripheral fault systems in the direction of least horizontal compressive stress (ShMin). As a consequence of the stress-related 'distortion', ring fault orientation may be slightly more steeply dipping when facing the ShMin, and slightly more shallowly dipping when facing the ShMax. This variation of caldera fault dip may play a role in the localization of eruptions or intrusions.

The experiments also show that reactivation of the pre-existing fault systems associated with the regional stress field is a major factor in caldera formation in active tectonic regimes. Although occasionally taking place within the central zone, these reactivations occurred mostly at the edges of the magma reservoir, and affected both central zone reverse faults and peripheral zone normal faults. Truncation and 'capture' of peripheral faults by regional faults can lead to enhancement of the caldera's polygonal morphological expression.

Distinction between the precise roles played by caldera fault distortion and elliptical magma chamber growth at a particular caldera in nature may be difficult. This is due to the potentially complementary effects of these mechanisms on the caldera structure produced. Only detailed analysis of further field and experimental data will resolve the relative importance of either mechanism in nature.

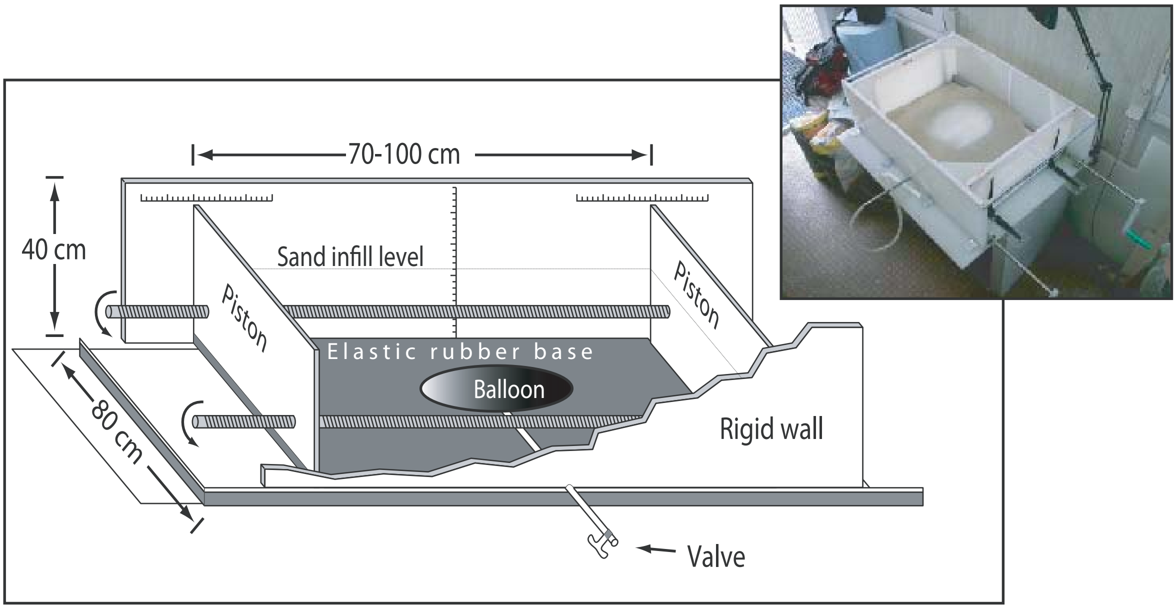

Figure 5.1: Photograph and technical sketch of the experimental set-up. Turning the handles moved the end walls inward/outward, simulating regional compression/extension respectively. The rubber balloons were sill-like with rigid rims to preserve plan-view circular shape. A basal rubber sheet maintained an approximately uniform strain distribution across the deforming medium.

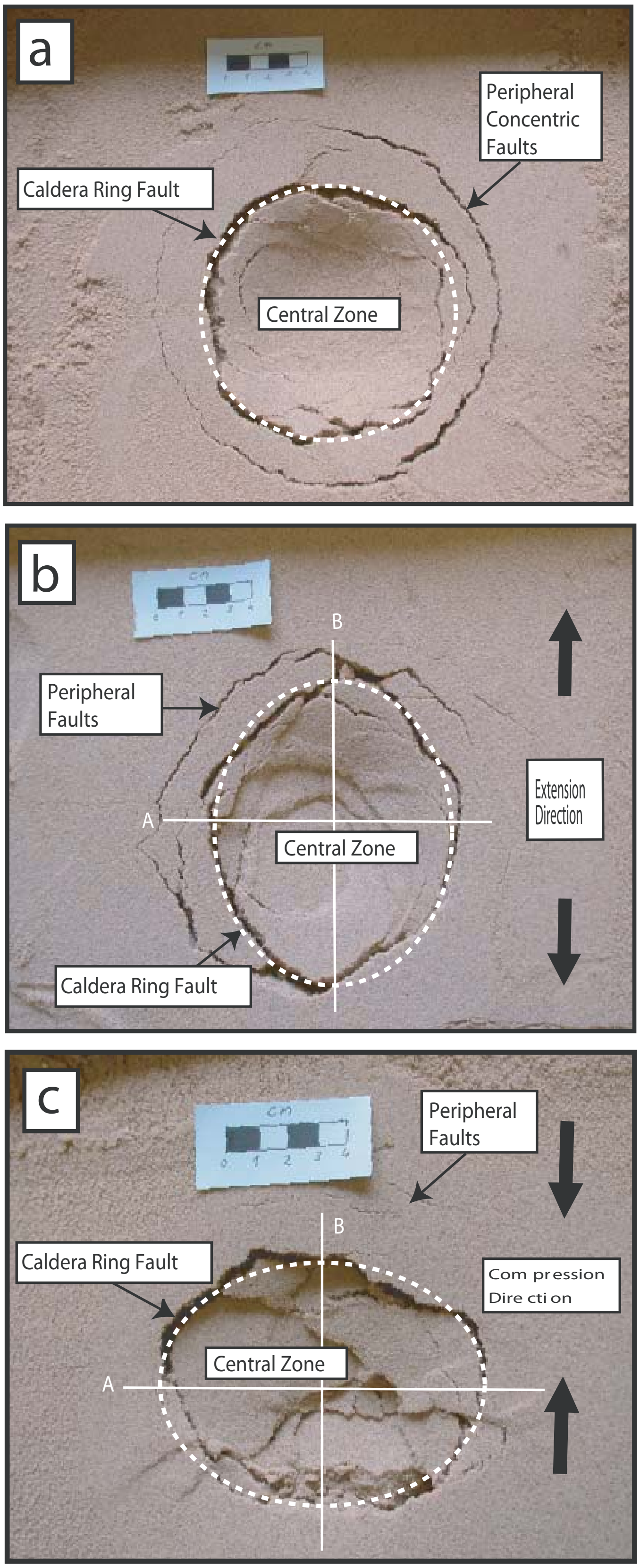

Figure 5.2: Plan view photographs of model calderas made in sand under a) stress-free conditions, b) regional extension and c) regional compression. The major axes of calderas in compression/extension experiments were denoted the A- and B- axes. The A-axis was taken as perpendicular to the end walls and the B-axis parallel to the end walls. Illumination is from the top of the photographs.

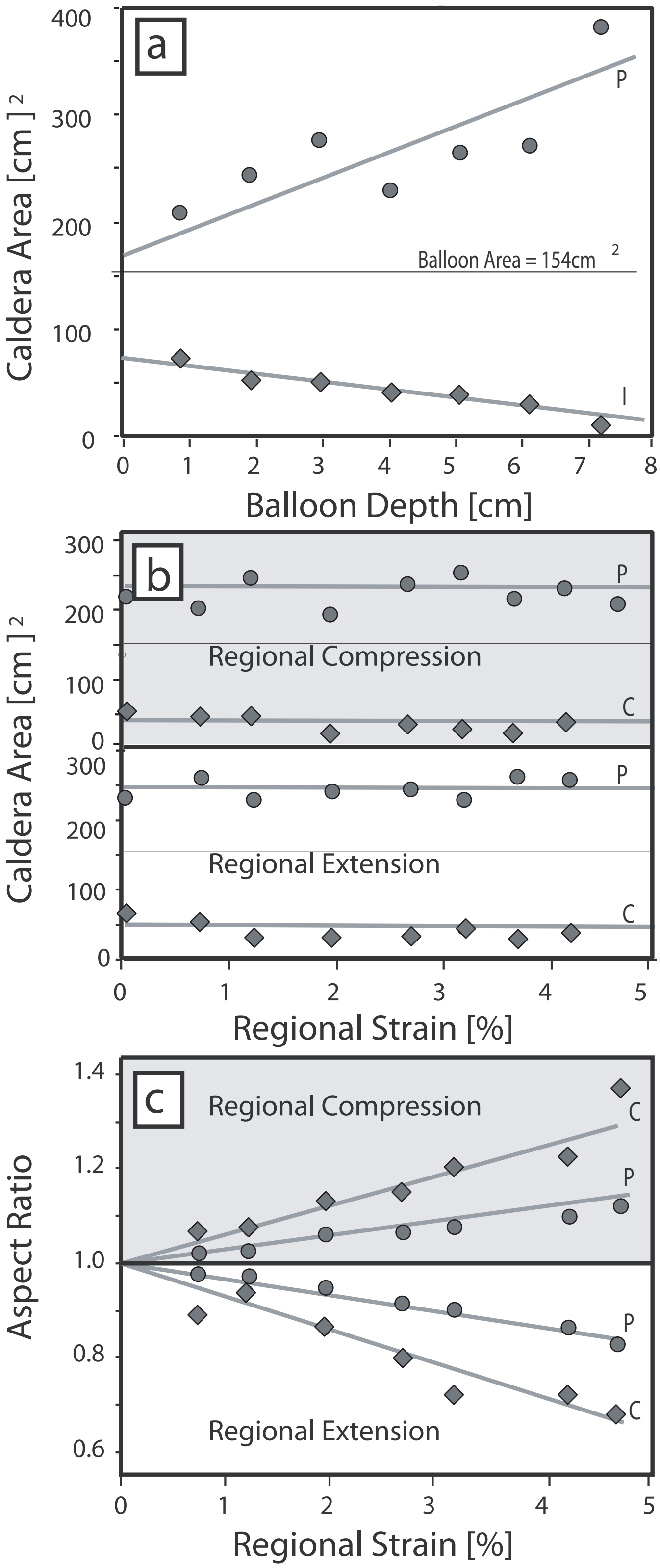

Figure 5.3: a) Plot of change in caldera areas with reservoir burial depth. The area of the caldera central zone (C) decreases with depth (as it is bound by reverse faults), whereas the overall morphological expression (T) increases with depth.
b) Plots showing model caldera areas are independent of regional strain. Regional strain (eR) perpendicular to the end walls was measured as a percentage, given by the initial length (lo) of the sand-box subtracted from the final length (lf) and then divided by the initial length [i.e. eR = (lf - lo)/lo].
c) Plot showing change in aspect ratios (A-axis/B-axis) of the central zone (C) and total morphological expressions (T) of the calderas with increasing regional strain. {Data in b) and c) from experiments run with a magma chamber of 14 cm diameter (plan view area, A=155 cm2) at depth of 4 cm in a 12:1 sand/flour mix - see Table 5.2}.

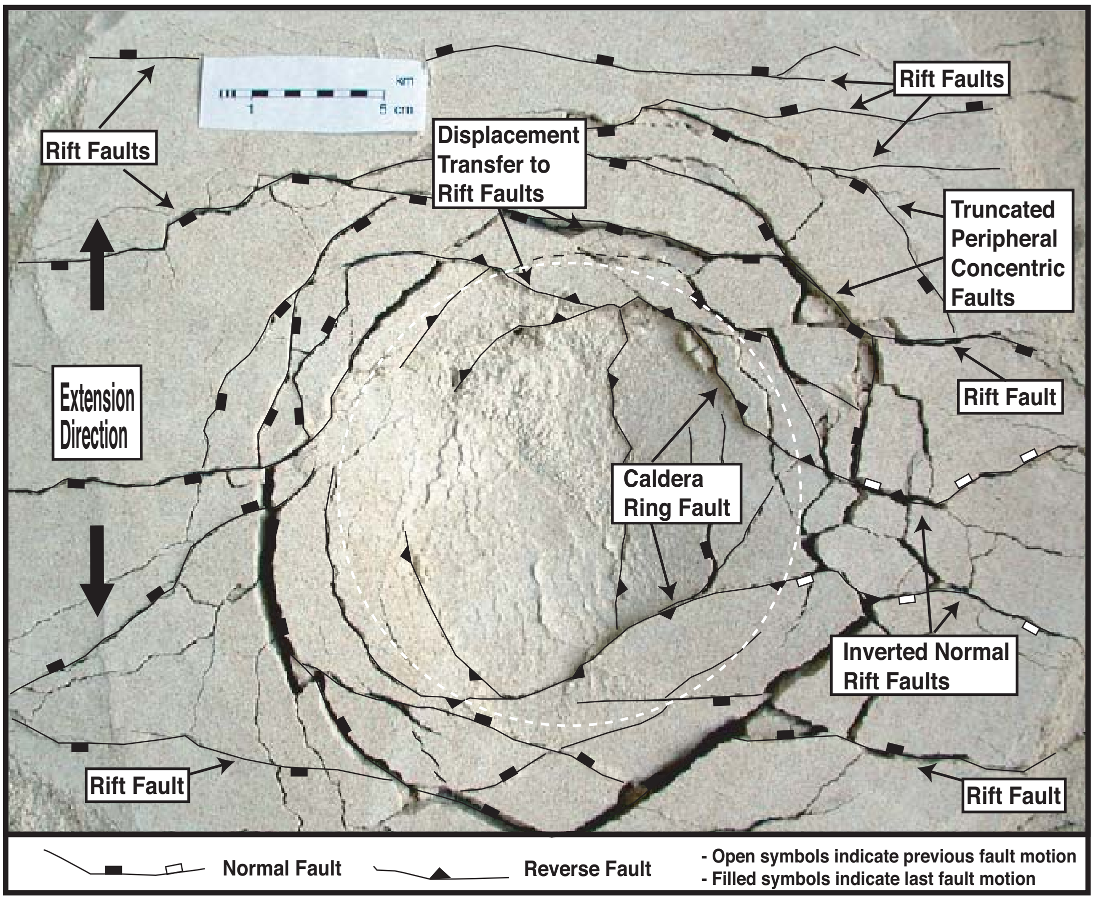

Figure 5.4: Plan view photograph of collapse model (3:1 sand/flour ratio) showing interaction of pre-collapse regional structures with syn-collapse structures resulting from caldera formation under regional extension. Illumination is from the right of the photograph. Dashed white line is approximate outline of balloon at depth. Note the truncation of peripheral zone and central zone faults by the regional structural grain. Note also the westward projection of the caldera depression via the formation of a graben along inverted regional normal faults.

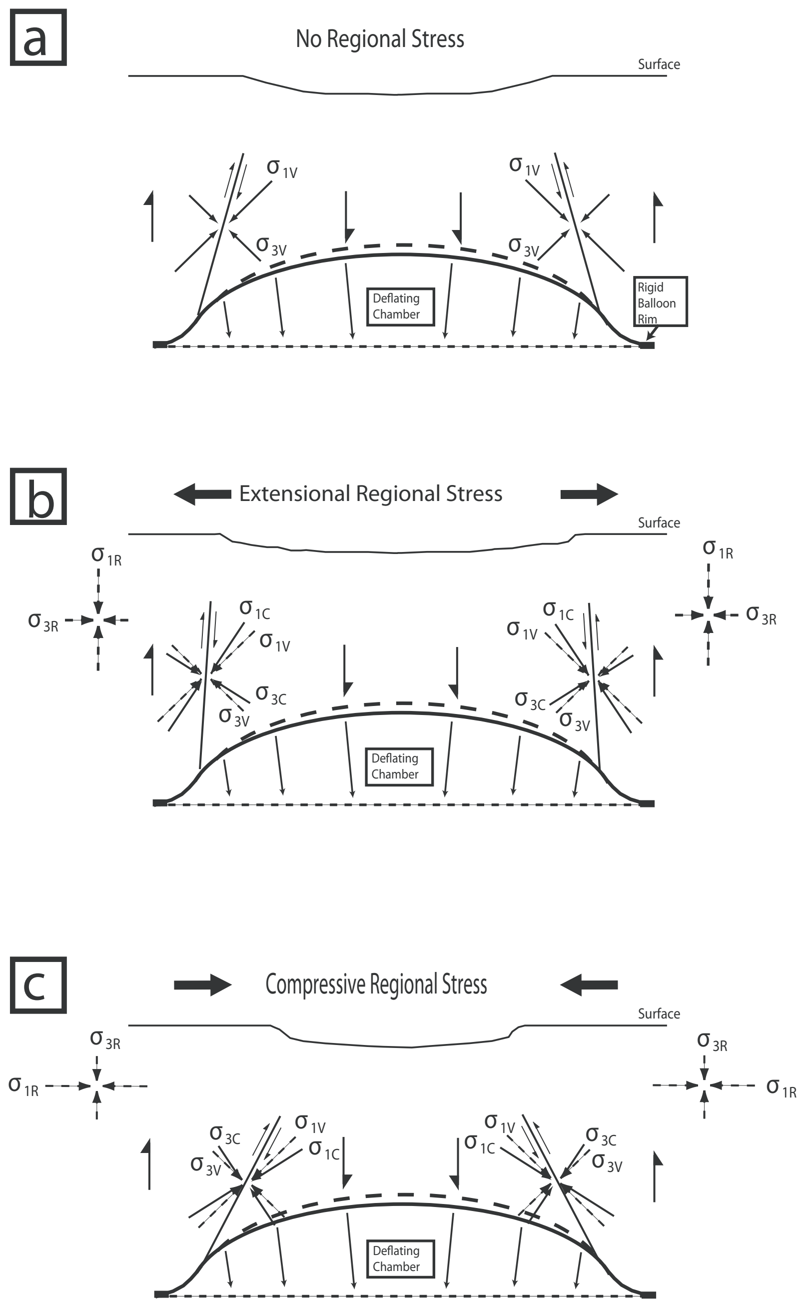

Figure 5.5: A 2D analysis of the interaction of regional and caldera stress fields to produce 'fault distortion':
a) Chamber deflation without tectonic stress. The black arrows in the chamber schematically represent contraction velocities. Faster deflation of the balloon over its centre sets up two shear zones at the margins of the down-going roof. Outward-dipping reverse ring fractures (Riedel shears) propagate at ~30º to the main local compressive stress $\sigma 1V$ to accommodate collapse (Roche et al. 2000).
b) Chamber deflation under extensional tectonic stress in section view parallel to the regional extension direction. Superposition of a regional stress with a vertical main compressive stress axis, $\sigma 1R$ results in a composite main compressive stress axis $\sigma 1C$, which has been rotated outward relative to the main local compressive stress axis $\sigma 1V$. The steeper $\sigma 1C$ produces steeper reverse faults, which elongate the caldera structure in the direction of regional extension.
c) Chamber deflation under compressive tectonic stress in section view parallel to the regional compression direction. Superposition of a vertical main regional compressive stress axis, $\sigma 1R$ on the local stress field results a composite main compressive stress axis $\sigma 1C$, which has been rotated inward relative to the main local compressive stress axis $\sigma 1V$. The shallower $\sigma 1C$ produces correspondingly shallower reverse faults, which shorten the caldera structure in the direction of regional compression.

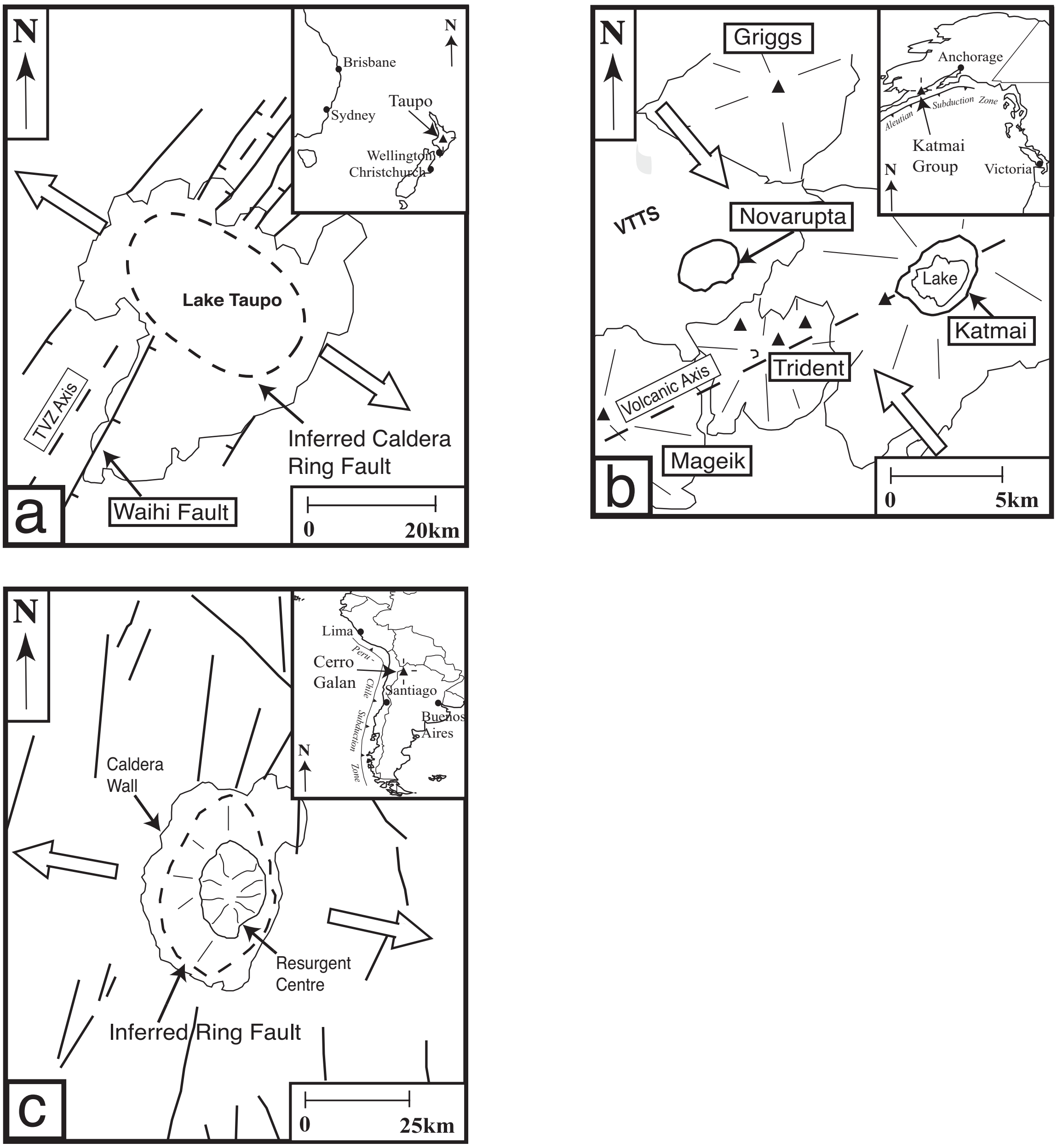

Figure 5.6: a) Sketch map of Taupo caldera, New Zealand (redrawn from Cole et al., 1998 and Acocella et al., 2003). Taupo, like the calderas produced in experiment, was formed under orthogonal extension and is elongated parallel to the regional least compressive stress (white arrows). The volcano-tectonic half-graben, which extends southwest from the caldera and is bounded by the pre-existing regional Waihi fault, closely resembles a similar feature observed in some of our model calderas (Figure 5.4). TVZ = Taupo volcanic zone.
b) Sketch map of the Katmai Volcanic Cluster (redrawn from Hildreth and Fierstein, 2000). Situated in an area of orthogonal compression (Wallmann et al. 1990), the Katmai caldera and the collapsed area around the associated Novarupta vent are both elongate perpendicular to the regional main compressive stress (white arrows), as was the case for model calderas in our experiments. ASZ = Aleutian Subduction Zone.
c) Sketch map of Cerro Galan caldera, NW Argentina. Cerro Galan was most likely located in an area of transpressional tectonics at the time of its initial formation. Like Katmai caldera and in our experiments, it is elongated parallel to the least compressive stress (white arrows). Cerro Galan is also orientated parallel to the major crustal lineaments in the area, however suggesting that these could have played role in controlling its subsidence geometry. Magma chamber elongation either along basement faults or through the borehole break out mechanism (Bosworth et al. 2003), could also be responsible for this particular caldera's surface geometry. PCSZ = Peru-Chile Subduction Zone.

Caldera	Location	Tectonic Setting	Long Axis (km)	Short Axis (km)	Ω	ß	Data Source(s)
Katmai	Aleutian Arc, Alaska	Compressional	4	2.5	0	90	Wallmann et al. 1990; Hildreth & Fierstein, 2000
Suswa	Kenyan Rift Valley	Extensional	11.3	8.6	0	90	Skilling, 1993; Bosworth et al., 2000
Taupo (Oruanu	TPZ, New Zealand	Extensional	27.6	14.5	0	90	Wilson et al., 1995; Acocella et al., 2003
Cerro Galan	Central Andes (NW Argentina)	Transpressional (?)	34	20	0	0	Francis et al., 1978; Marrett et al., 1994
Valles	Rio Grande Rift, New Mexico	Transtensional	17.2	12.5	0	70	J. Wolff, 2003 (pers. comm.); Aldrich et al., 1986
Long Valley	Basin and Range, California	Transtensional	20.4	8	0	65	Moos & Zoback, 1993; Bosworth et al. 2003
Campi Flegrei	Campanian Plain, Italy	Transtensional	17.1	11.5	5	30	Orsi et al., 1996; Bianco et al., 1998
Gariboldi	Ethiopian Rift valley	Transtensional	7.5	5	34±20	16±20	Acocella et al., 2002
Gedemsa	Ethiopian Rift Valley	Transtensional	9	7	34±9	18±9	Acocella et al., 2002
Kapenga	TPZ, New Zealand	Transtensional	27.4	14.8	85	0	Wilson et al., 1995; Acocella et al., 2003

Table 5.1: Examples of elliptical calderas and their tectonic setting. Tectonic regime quoted is that at time of formation as can best be reconstructed. Ω is the acute angle between the caldera's long axis and the regional least horizontal compressive stress. ß is the acute angle between the caldera's long axis and the main regional fault trend. TVZ = Taupo Volcanic Zone.

				Central Zone (C)				Total Morphological Expression (P)			
Balloon Depth [cm]	Driveshaft Revs.	Strain [cm]	Strain [%]	A-axis [cm]	B-axis [cm]	Aspect Ratio (B/A)	Area of C	A-axis [cm]	B-axis [cm]	Aspect Ratio	Area of P
No tectonics											
4	0	0.000	0.000	8.75	8.75	1.000	60.132	22.75	22.75	1.000	406.493
4	0	0.000	0.000	8.50	8.50	1.000	56.745	21.00	21.00	1.000	346.361
4	0	0.000	0.000	8.50	8.50	1.000	56.745	21.50	21.50	1.000	363.050
4	0	0.000	0.000	8.20	8.20	1.000	52.810	16.60	16.60	1.000	216.424
4	0	0.000	0.000	8.20	8.20	1.000	52.810	16.60	16.60	1.000	216.424
					Average:	1.000	55.848		Average:	1.000	309.750
Extension											
4	3	0.540	0.740	8.40	7.40	0.881	48.820	18.50	18.00	0.973	261.538
4	5	0.900	1.233	6.40	6.00	0.938	30.159	17.40	16.80	0.966	229.588
4	8	1.440	1.973	9.00	7.70	0.856	54.428	18.00	17.00	0.944	240.332
4	8	1.440	1.973	7.10	5.70	0.803	31.785	18.50	17.50	0.946	254.273
4	11	1.980	2.712	8.60	6.80	0.791	45.930	18.50	17.00	0.919	247.008
4	11	1.980	2.712	9.00	6.20	0.689	43.825	19.40	16.80	0.866	255.977
4	13	2.340	3.205	10.00	8.00	0.800	62.832	17.00	15.50	0.912	206.952
4	13	2.340	3.205	9.8	7	0.714	53.878	15	13.50	0.900	159.043
4	15	2.700	3.699	6.60	6.00	0.909	31.102	19.50	17.70	0.908	271.080
4	17	3.060	4.192	9.00	6.50	0.722	45.946	17.50	15.00	0.857	206.167
					Average:	0.810	44.871		Average:	0.919	233.196
Compression											
4	3	0.540	0.740	7.10	7.50	1.056	41.822	15.50	16.50	1.065	200.866
4	5	0.900	1.233	7.5	8	1.067	47.124	17.4	17.8	1.023	243.254
4	8	1.440	1.973	5.5	6.6	1.200	28.510	15.5	16.5	1.065	200.866
4	11	1.980	2.712	7	7.5	1.071	41.233	16.5	18.7	1.133	242.335
4	13	2.340	3.205	6.5	7	1.077	35.736	17.9	18.5	1.034	260.085
4	15	2.700	3.699	5.70	7.00	1.228	31.337	16.00	17.80	1.113	223.681
4	17	3.060	4.192	7.20	8.40	1.167	47.501	17.00	18.00	1.059	240.332
4	19	3.420	4.685	5.4	7.40	1.370	31.385	15.70	17.5	1.115	215.788
					Average:	1.155	38.081		Average:	1.076	228.401

Table 5.2: Results of experiments simulating caldera formation under regional compression/extension with balloon of radius 14cm and at 4cm depth. Sand:Flour Ratio = 12:1

				Central Zone (C)				Total Morphological Expression (P)			
Balloon Depth [cm]	Revolutions	Strain [cm]	Strain [%]	A-axis [cm]	B-axis [cm]	Aspect Ratio (B/A)	Area of C	A-axis [cm]	B-axis [cm]	Aspect Ratio (B/A)	Area of P
No tectonics											
2.5	0	0.000	0.000	7.30	7.20	0.986	41.281	18.00	18.00	1.000	254.469
2.5	0	0.000	0.000	7.20	7.30	1.014	41.281	18.00	18.00	1.000	254.469
					Average:	1.000	41.281		Average:	1.000	254.469
Extension											
2.5	3	0.540	0.740	8.30	7.40	0.892	48.239	17.00	16.50	0.971	220.304
2.5	5	0.900	1.233	7.50	7.00	0.933	41.233	16.80	16.00	0.952	211.115
2.5	8	1.440	1.973	8.20	6.10	0.744	39.286	17.80	16.50	0.927	230.671
2.5	11	1.980	2.712	7.60	6.50	0.855	38.799	17.70	16.20	0.915	225.205
2.5	13	2.340	3.205	9.5	8.7	0.916	64.913	18.5	17.00	0.919	247.008
2.5	15	2.700	3.699	8.00	6.70	0.838	42.097	17.50	15.20	0.869	208.916
2.5	17	3.060	4.192	8.75	7.25	0.829	49.824	16.50	14.00	0.848	181.427
					Average:	0.858	46.342		Average:	0.914	217.807
Compression											
2.5	3	0.540	0.740	6.80	7.10	1.044	37.919	16.50	17.40	1.055	225.488
2.5	5	0.900	1.233	7.70	7.90	1.026	47.776	17.40	18.40	1.057	251.453
2.5	8	1.440	1.973	6.50	6.80	1.046	34.715	16.25	17.25	1.062	220.157
2.5	11	1.980	2.712	5.90	6.75	1.144	31.278	16.20	17.50	1.080	222.660
2.5	13	2.340	3.205	5.50	7.20	1.309	31.102	16.70	17.75	1.063	232.812
2.5	15	2.700	3.699	7.40	8.50	1.149	49.402	16.50	17.80	1.079	230.671
2.5	17	3.060	4.192	7.20	8.50	1.181	48.066	16.50	18.50	1.121	239.743
2.5	19	3.420	4.685	7.75	10.50	1.355	63.912	15.50	17.25	1.113	209.996
					Average:	1.157	43.021		Average:	1.079	229.122

Table 5.3: Results of experiments simulating caldera formation under regional compression/extension with balloon of radius 14cm and at 2.5cm depth. Sand:Flour Ratio = 12:1

6 Analogue Models of Caldera Collapse in Strike-Slip Tectonic Regimes

6.1 Introduction

Building on recent work by Acocella et al. (2004) and Holohan et al. (2005), this chapter reports results of scaled analogue models constructed to study of the potential effect of regional-tectonic faults on caldera formation, with a focus on the case of regional strike-slip systems. Regional-tectonic settings with active strike-slip deformation and young or 'restless' calderas include:

1) *Oblique rifts* of varied transtensive components, e.g. Taupo Volcanic Zone – Rotorua and Kapenga calderas (Spinks et al. 2005); Ethiopian Rift - Fantale and Gedemsa calderas (Acocella et al. 2003);

2) *Transfer zones* between segments of orthogonal or oblique rifts, e.g. Rio Grande Rift - Valles caldera (Goff and Gardner 1994); Phlegrean Volcanic District - Campi Flegrei caldera (Acocella et al. 1999); East African Rift - Suswa and Longonot calderas (Skilling 1993); and

3) *Major shear zones,* along which calderas may form either in zones of diffuse lateral shear, e.g. Olacapato – El Toro fault zone - Negra Muerta caldera (Riller et al. 2001) or in pull-apart gräben at releasing bends or relay zones, e.g. Great Sumatran Fault Zone - Toba and Ranau calderas (Bellier and Sébrier 1994), Nicaraguan depression - Masaya caldera (Girard and van Wyk de Vries 2005).

Volcano-tectonic reactivation of regional-tectonic strike-slip faults is thought to have profoundly influenced the development and geometry of many of these calderas, which include some of the world's largest and most active - e.g. Toba caldera (Aldiss and Ghazali 1984; Bellier and Sébrier 1994) and Campi Flegrei caldera (Orsi et al. 1996). One possible influence of strike-slip faults on the formation of such calderas is to provide a structural grain to be exploited during subsidence, as inferred at the ancient and deeply eroded Glencoe caldera (Moore and Kokelaar 1998). Another possible influence of strike-slip faults is to define the pre-collapse magma chamber (granitic pluton) boundaries. Field (e.g. Hutton and Reavy 1992), theoretical (e.g. Bosworth et al. 2003) and experimental (e.g. Roman-Berdiel 1999) studies conclude that regional-tectonic structures and stress fields strongly affect pluton geometry during and after emplacement. Resultant pre-caldera plutons are predominantly elongate in plan-view, and commonly have some fault-controlled boundaries (e.g. Cruden 1998). Although the strong control of magma chamber geometry on subsequent caldera geometry is experimentally well-established (e.g. Roche et al. 2000), most previous analogue and numerical caldera studies assumed a perfectly circular plan view chamber shape. Considering therefore the case of elongate magma chamber deflation in strike-slip to transtensional regimes, evidence is presented in this chapter that regional-tectonic structures can indeed influence caldera development through a combination of structural grain exploitation and magma chamber boundary control.

6.2 Experiment Design & Model construction

For rock at shallow crustal levels, fine-grained (0.09-0.25 mm diameter), well-sorted sand mixed at 4:1 by volume with gypsum powder was used (cf. Donnadieu and Merle 1998; Girard and van Wyk de Vries 2005). Creamed honey, which has a surface tension and viscosity high enough to retard significant permeation into the sand, was used to simulate granitic magma. Balloons were avoided for these experiments, mainly in order to examine the effect of regionally induced deformation of the analogue magma reservoir on the development of caldera structures. Scaling considerations for these materials in simulating regional-tectonic deformation (phase 1) and volcano-tectonic collapse (phase 2), are discussed in **Chapter 1**. As this analysis focuses on high-level deformation above the brittle-ductile transition in the Earth's upper crust, a ductile lower crust component was excluded from the models.

Four experiment series were conducted to establish: 1) structures due to regional strike-slip deformation; 2) how a passive (i.e. neither inflating nor deflating) magma chamber might affect these regional strike-slip structures *prior* to caldera collapse; 3) structures due to caldera collapse into circular and elliptical magma chambers; and 4) how caldera collapse structures develop after regional strike-slip faulting of the magma chamber roof and environs.

6.2.1 Regional Strike-slip Control Experiments (Con 1-8, Con B1-B2)

On a fixed table, lay a 5.5 cm thick sand-gypsum pack, beneath one half of which was a thin, rigid basal plate (**Figure 6.1a,b**). Computer-controlled motion of the basal plate generated a velocity discontinuity (V.D.), and consequently a shear zone, within the sand pack. Dextral strike-slip motion was arbitrarily imposed in all experiments with regional shear. The 'opening angle' between the base plate's long edge and its horizontal motion vector determined the component of dilation accompanying shear along the velocity discontinuity (cf. Girard and van Wyk de Vries 2005), and was varied between experiments (**Tables 6.1 and 6.2**). Parallel marker lines on the sand surface (e.g. **Figure 6.2**) helped track lateral offsets.

6.2.2 Regional Strike-slip with Passive Magma Chamber Experiments (Mag 1-22, Mag B1-B8)

The set-up here (**Figure 6.1c**) matched that described above, but with the inclusion in the sand pile of a honey chamber of laccolithic or tabular geometry (thought to be the most common form for natural granitic plutons - Cruden 1998). The sand pile was initially levelled off at the desired depth of the honey chamber base. A cylindrical mould was placed on the sand surface and filled with honey to the scaled chamber thickness (1 - 2.5 cm). The sand pile was then built up around the mould to the honey level, and the mould was slowly extracted. After sufficient time elapsed to ensure a flat honey surface (no wrinkles or ridges), sand was carefully and evenly placed over the chamber to make the roof. The sand-pile was then levelled off at a total height of 5.5 cm. If any roof subsidence occurred during this procedure, the experiment was aborted. Chambers were initially circular and 7 cm in plan view diameter, except for three slightly elliptical chambers (7 x 6 cm) with long axes parallel to the velocity discontinuity. The thickness of the honey lozenge, the distance from its centre to the velocity discontinuity, and its depth in the sand pile were varied (**Table 6.1b**).

6.2.3 Caldera Collapse Control Experiments (Cal Stat 1-7)

To construct a conduit for honey evacuation (**Figure 6.1d**), a vertical hole of 1 cm diameter was first drilled through the table and lined with a pipe of 1 mm wall thickness. The pipe was plugged at its lower end and a honey-filled syringe was fixed upright in its upper end. The sand pile was then levelled off around the syringe at a height corresponding to the desired depth of the chamber base. To fill the pipe and link it to the chamber base, the syringe was withdrawn upward to the levelled sand surface, while simultaneously squeezing out more honey. The honey chamber was then emplaced into the sand-pack as described above. Unplugging the lower end of the pipe caused evacuation of the honey chamber via the conduit, destabilization of the roof, and onset of caldera collapse. Although collapse was thus in response to fluid outflow, rather than vice versa (see Roche et al. 2000), resultant structures closely matched those of past analogue studies (e.g. Roche et al. 2000; Kennedy et al. 2004), and so any deformation imposed by fluid flow was negligible.

6.2.4 Syn- to Post-tectonic Caldera Collapse Experiments (Cal Mag 1 – 19)

Construction of all components in this set-up (**Figure 6.1e**) is described above. All chambers were initially circular, 7 cm in diameter, and centered on the conduit. Chamber depth, thickness, and distance from the velocity discontinuity to the chamber centre were varied (**Table 6.2b**). Transtensive regional motion was imposed on the sand pile at the same velocity as for the passive chamber experiments. After around 1.7 cm of regional strike-slip displacement, the conduit was unplugged to initiate caldera collapse and basal plate motion was reduced to the slowest speed possible (0.03 cm h^{-1}), or stopped (most cases). This caused 0-2 mm of regional-tectonic fault movement (0-400 m in nature according to the scaling below) during collapse. Experiments run with and without syn-collapse regional-tectonic displacement showed essentially the same outcomes, however.

6.3 Experimental results

To aid description of results from experiments with tectonic deformation, a compass-like directional convention is used, whereby the moving base plate occupies the 'southern' half of the model and the screw-jack lies to the 'east' (**Figure 6.1a**). Here, structures generated by regional-tectonic deformation (phase 1) are first described, followed by structures related to volcano-tectonic collapse (phase 2).

6.3.1 Strike-slip Tectonic Controls

With low opening angles (< ~5°), Riedel shears (R-shears) with limited dip-slip displacement formed at ~17° to the velocity discontinuity. These locally delineated small transpressive pop-ups and/or narrow transtensive pull-aparts (**Figure 6.2a; Table 6.1a**). Synthetic faults at lower angle R-shear and at P-shear orientations subsequently cut the earlier R-shears to form an anastomosing fault pattern encompassing rhombic gräben, half-gräben, and/or pop-ups. With moderate opening angles (> ~5°), initial R-shears had greater dip-slip displacement (oblique-normal), and delineated rhombic gräben and/or half-gräben in an evenly-spaced, en-echelon array. With high opening angles (> ~ 7°), an 'axial' graben system formed all along the velocity discontinuity, with R-shears mostly restricted to the graben margins (**Figure 6.2b; Table 6.1a**). Where formed in the graben centre, R-shears defined relay ramps between sections of the axial graben system.

Regardless of opening angle, an almost vertical, gently sinuous or straight fault (Y-shear or 'Principal Displacement Zone') later localised along the velocity discontinuity and cut all the above structures. Most strike-slip displacement in the model then transferred to this fault. In several experiments, particularly those with lower opening angles, the Y-shear developed by linkage of some lower-angle Riedel-like shears. Fractures in anti-Riedel (R') orientation (~75° to the shear zone) formed early in all the deformation sequences, but were generally ill developed and mostly confined to the floors of gräben or tops of pop-ups.

6.3.2 Strike-slip Tectonics with a Passive Magma Chamber

Overall kinematic development in this series resembled that in the strike-slip controls. With low opening angles, the honey chamber had little effect on regional-tectonic structures - apart from slightly widening the shear zone above it in one or two cases (**Figure 6.3a,b; Table 6.1b**). With higher opening angles (> 3-4° - **Figure 6.4**), however, normal faults localised around, and linked at depth to, the NE and/or SW chamber margins (**Figure 6.3d,e**). These faults trended 30-45° to the velocity discontinuity - almost perpendicular to the long axis of the theoretical incremental strain ellipse (Woodcock and Schubert 1994) – and delimited pull-apart-like gräben or half-gräben marginal to the shear zone axis. Gräben floors typically sloped toward the axis of the shear zone (**Figure 6.3e**). Chambers centered on the velocity discontinuity tended to localise two normal faults (NE and SW); offset chambers usually localised one normal fault (NE or SW). With very shallow chambers (0.5-1 cm depth) zero subsidence or even rare upward bulging occurred directly above the velocity discontinuity. Bulges trended NE-SW at around 45º to the shear zone - perpendicular to the short axis of the theoretical incremental strain ellipse - and overlaid similarly orientated, slightly sigmoidal ridges or folds in the chamber top surface. Development of chamber-localised pull-apart gräben diminished or ceased once the Y-shear cut through all structures. Upon excavation, most honey chambers were slightly sigmoidal and stretched roughly parallel to the regional NE-SW extension direction. Some also displayed a deformed basal ridge or a marginal 'apophysis', where honey was sucked down into or dragged along the shear zone (**Figure 6.3c,f**).

6.3.3 Caldera Collapse Control Experiments (Cal Stat 1-7)

Evacuation of circular honey chambers typically resulted in asymmetric, trapdoor-like collapses (**Figure 6.5a-c; Table 6.2a**). Following a brief downsag phase, a reverse fault trace with a characteristic scarp morphology nucleated at an apparently random site on the chamber circumference (**Figure 6.5a**). This reverse fault then propagated in both directions around the chamber edge from the most subsided roof section toward the least subsided section ('trapdoor hinge') sited opposite. The final reverse fault trace was not a smooth curve, but comprised several straight segments. Typically, a concentric peripheral zone of extensional cracking and faulting then formed (**Figure 6.5b**). Material in the peripheral zone moved bodily inward toward and over the subsiding central caldera zone; this movement can only be accommodated along outward-dipping reverse faults around the central zone.

Evacuation of elliptical chambers (**Figure 6.5d-f**; **Table 6.2a**) also caused sequential downsag, reverse fault formation, and asymmetric trapdoor-like subsidence. However, reverse faults consistently nucleated at or near the ends of the elliptical chamber's short axis, and then propagated toward the ends of the chamber's long axis (**Figure 6.5d**). In Cal Stat 5 & 7, two reverse faults nucleated above or near both of the chamber's short axis ends, but at different times during the course of subsidence. Consequently, the site of maximum subsidence shifted from one caldera side to the other. Both faults linked at the long axis ends to produce a single elliptical, but subtly polygonal, ring-fracture (**Figure 6.5d,e**). Inward movement of the peripheral fault zone over the subsiding central caldera zone culminated in slumping of peripheral zone material from the over-steepened reverse fault scarp into the caldera centre (**Figure 6.5e**).

The arcuate reverse faults were always closely associated with marginal ridges on the remnant honey chamber's top surface (**Figure 6.5c,f**). The more pronounced ridges frequently had vertical to steeply outward-dipping (70-85°) inner walls, just inside and parallel to which were outward-inclined furrows. The inner ridge walls and furrows thus represent traces of the reverse ring-faults that cut down into the chamber's top-surface. The ridges themselves perhaps represent chamber-remnant 'ring-dykes', as envisaged by Smith and Bailey (1968).

6.3.4 Strike-slip Tectonics with Passive Magma Chamber, followed by Caldera Collapse

Because of regional-tectonic elongation of the initially circular honey chambers, close similarities existed between collapse development in this set and that in elliptical chamber controls

(**Figures 6.5 and 6.6**; **Table 6.2b**). After early downsag, reverse faults again nucleated at the short axis ends of the underlying elliptical chamber's circumference and propagated toward the long axis ends (**Figure 6.6a-c**). Reverse faults typically formed on one side of the chamber first, which again led to an asymmetric trapdoor-like subsidence style. Again, subsidence asymmetry often decreased after a second reverse fault formed above the opposite side of the chamber (**Figure 6.6d**).

Important differences related to pre-collapse regional faulting existed between experiment sets, however (**Table 6.3**), mainly because of volcano-tectonic reactivations of regional-tectonic faults. Even with very high rates of scaled syn-collapse regional fault movement, such reactivations were clearly discernable, as scarp growth on regional faults within the limit of collapse influence far exceeded that elsewhere in the model. As noted above, collapse development in experiments with or without syn-collapse regional displacement (the latter is geologically more realistic) was essentially the same (**Figures 6.6**, **6.7 and 6.8**).

Pre-collapse regional faulting had two main effects on caldera development. Firstly, parts of the pre-collapse structural grain, usually Riedel shears and/or chamber-localised faults close to the chamber margins, were reactivated to accommodate caldera floor subsidence (**Figures 6.5, 6.6, 6.7, 6.8**; **Table 6.3**). Generally, such reactivated regional faults also had tangential orientations to the collapse centre, whereas un-reactivated faults had non-tangential orientations. Faults located outside the chamber margin, but within the influence of collapse, reactivated as peripheral normal faults (**Figures 6.6a,b and 6.7a**). Regional faults located inside, but close to, the chamber margin, linked with adjacent volcano-tectonic reverse faults and reactivated as bounding faults to the central zone (**Figures 6.6d,e and 6.7a,b**). A rare exception to this pattern is seen in **Figure 6.7e**, where a Riedel shear lying inside the chamber margin reactivates as a peripheral normal fault. In this case, however, the reactivated Riedel shear also lies in the typically extensional hinge zone of an asymmetrically subsiding roof.

Secondly, volcano-tectonic reverse faults were arrested at sharp corners defined in the magma chamber margins by regional-tectonic faults, typically Y-shears (**Table 6.3**; **Figures 6.6d,e and 6.7e,f**). In contrast, reverse-fault propagation was unaffected where chamber margins lacked such sharp regional-fault defined corners (**Figure 6.7b,c**). Reverse fault arrest was commonly associated with a sharp bend of the marginal ridge into the regional fault (typically Y-shear) trend, with little or no change in ridge height. This may be evidence for local deep-level transfer of volcano-tectonic displacement from arrested reverse fault onto the regional fault (**Figure 6.6f**). Similar deep-level displacement transfer is inferred along a blind reverse fault in **Figure 6.7f**. The typical upwards-decreasing displacement on such reverse faults (cf. Roche et al. 2000; Kennedy et al. 2004) means that such reactivation could occur at depth and not noticeably show at the surface.

In contrast to the smooth floor surfaces of central caldera zones in non-tectonised control experiments, central zone floor morphology in caldera experiments following regional deformation was irregular (**Figures 6.6d,e; 6.7a,b,d,e; 6.8a,b**). Dissection of the central zone by regional structures formed a pre-collapse topography comprising regional fault-controlled segments of varying structural level. During subsequent caldera subsidence, this fault-controlled topography subsided coherently, however (**Figures 6.6a,d; 6.8a,b**). No significant syn-collapse motion (scarp growth) was noted on the segment-bounding regional faults.

Cross-sections (**Figure 6.8c,d**), demonstrate the connection of the reactivated chamber-localised normal faults to the honey chamber margin. Similarly, the outward dips and reverse sense of the faults bounding the central caldera zone are also visible; these also connect at depth to the chamber margin. Note also the upward decreasing displacement on the volcano-tectonic reverse faults and downward decreasing displacement on the volcano-tectonically reactivated normal faults. Gently sagged pre-collapse strata in the central caldera zone also display offsets along regional-tectonic faults; these offsets predate caldera collapse, however.

6.4 Discussion

Firstly, a discussion of the generation of structures during experimental regional-tectonic transtensive shear (deformation phase 1) is presented. The discussion then focuses on the impact of such structures upon the development of experimental volcano-tectonic caldera collapse (deformation phase 2) and the implications for the influence of regional strike-slip structures in natural calderas is deduced.

6.4.1 Regional-tectonic structures related to strike-slip and transtensive shear

Development of strike-slip structures in a homogeneous medium

Fault geometries and their sequential development during strike-slip deformation of homogeneous sand/gypsum piles matched those produced in previous experimental investigations of strike-slip and transtensive faulting (e.g. Schöpfer and Steyrer 2001 and references therein). These studies, report similar formation of en-echelon Riedel shears at an angle of $\phi/2$ (where $\phi \sim 37°$ = angle of internal friction of sand) to the maximum regional stress direction, σ_1, (~ Z-direction of incremental strain ellipse – **Figure 6.2**) followed by generation of Y- and P-shears, which link as a through-going ‘principle displacement zone’. With low components of dilation, both compressive and extensional structures form locally at restraining and releasing bends along the principle displacement zone. With higher components of dilation, compressive structures are absent, and a broader zone of deformation forms as an axial graben system with segment-linking relay ramps in Riedel orientation, as seen in these experiments.

Development of pull-apart-like structures and elongation of pre-collapse magma chambers

The geometries and sequential development of structures localised around the passive honey chambers during strike-slip deformation are akin to structures formed in analogue studies of pull-apart basin formation (e.g. Dooley and McClay 1997; Basile and Brun 1999). Previous model pull-aparts differed from this study's pull-apart-like structures, in that the former developed above a pre-defined releasing bend or step-over between two master fault strands (Y-shears), whereas the latter formed above a fluid body. Nonetheless, these studies also report early formation of oblique-normal faults at 30-65° to a basal velocity discontinuity (sub-perpendicular to the incremental strain ellipse long axis). These oblique-normal faults are termed 'sidewall faults' to the pull-apart basins (Dooley and McClay 1997), which also display late-stage development of a through-going 'principal displacement zone' (Y-shear in the models) - Dooley and McClay 1997; Basile and Brun 1999).

Field studies demonstrate that molten to semi-solidified granite plutons can undergo substantial rotation and elongation due to regional strike-slip tectonism during and after their emplacement. The Caledonian Rannoch Moor granite, Scotland, was emplaced at mid-crustal levels into a diffuse sinistral strike-slip regional tectonic regime (**Figure 6.9a** - Jacques and Reavy 1994). A sigmoidal swing in steeply-dipping pre-full crystallisation (PFC) magmatic foliations in Rannoch Moor is interpreted as evidence for synchronous inflation and regional-tectonic rotation and elongation of the pluton (Jacques and Reavy 1994). The PFC magmatic fabric is weakly overprinted by crystal plastic strain fabrics, which indicate further, late-stage, solid-state stretching of the pluton parallel to the maximum extension direction of regional strain ellipse (Jacques and Reavy 1994). A similar emplacement history is inferred for the nearby, contemporaneous, similarly elongate, but shallower level (3-6 km) Etive pluton (Jacques and Reavy 1994). The Caledonian Ardara granitic pluton, Ireland, also shows steeply dipping PFC magmatic foliations concentric to its margins (Molyneux and Hutton 2000 - **Figure 6.9c**). Distribution of flattening strain within the Ardara pluton indicates that it inflated from a near-central 'injection point' sited laterally to a major (later?) sinistral shear zone (Molyneux and Hutton 2000). Like the model honey chambers sited laterally to the velocity discontinuity (**Figure 6.9b**), the pronounced 'tail' of the Ardara pluton is considered to have formed by deformation in the intersecting major shear zone (Molyneux and Hutton 2000 – **Figure 6.10b,c**). This deformation is seen as a late-stage high-temperature solid-state strain fabric that is concentrated along the southern and north-eastern margin of the pluton. Like Rannoch Moor and Etive plutons, the Ardara pluton is elongate parallel to the direction of horizontal extension in the regional sinistral shear. The long axes of plutons forcefully emplaced into shear zones in past analogue experiments also tend to track the direction of maximum extension in the regional finite strain ellipse (Roman-Berdiel 1999; Corti et al. 2005). The overall geometry and elongation of magma chambers prior to caldera collapse in these experiments may thus closely reflect that of many magma chambers in natural strike-slip systems.

Can long-lived, shallow-level magmatic centres localise faults and pull-apart-like gräben?

The pull-apart-like gräben in the models formed through localisation of regional-tectonic strain (elongation and rotation) at the rheological discontinuity represented by the honey chamber's edge. Whilst the regional tectonic framework (strike-slip faults, shear zones, releasing bends and/or step-overs) likely provides the initial pathways for siting and emplacing magmatic centres (Hutton and Reavy 1992), the experiments presented here indicate the possibility that the rheological discontinuity represented by a semi-solidified and long-lived magmatic system may exert a localised post-emplacement influence on the subsequent development of the regional fault system around it. From similar experimental results, Girard and van Wyk de Vries (2005) explained the structural relationship between the Managua graben and the adjacent Masaya volcanic system in this way. Both structures are currently active and located in the Nicaraguan depression, and are proposed to reflect the localisation of a pull-apart graben by a deep-level basic intrusive complex. The results presented in this chapter support Girard and van Wyk de Vries's (2005) proposals that: a) such pull-apart localisation may occur if the transtensive component in the strike-slip regime is sufficiently high (opening angle of > 3-4° - **Figure 6.4**), and b) a similar effect might be possible above shallower-level magmatic centres.

An example of the latter may be the Pleistocene Mt. Guardia-Fossa 'volcano-tectonic depression', Italy (**Figure 6.10a**). This structure lies within the active dextral Tindari-Letojanni shear zone, and apparently formed during a long period of volcanic quiescence. Ventura et al. (1999) therefore proposed that the depression's arcuate bounding faults resulted from "re-orientation of tectonic stress around a shallow reservoir and/or inside the pull-apart" – i.e. perhaps by regional-tectonic strain localisation around a magma chamber. The 1.4 Ma Hopong Caldera (**Figure 6.10b**), Indonesia, lies beside the active Tor Sibohi strand of the dextral Great Sumatran Fault Zone, and the geothermally-productive Sarulla Graben (Hickman et al. 2004). Unlike other volcanoes along this strand, e.g. Sibualbuali volcano (**Figure 6.10b**), it is not clear if a step-over or bend in the strike-slip system played any role in siting the Hopong caldera. The structural setting, relationships, and morphology of the Hopong-Sarulla system are remarkably similar to those produced in the passive chamber with strike-slip models (**Figure 6.10c**) in this study, however. In addition to later volcano-tectonic caldera collapse, it is here hypothesised that localisation of regional-tectonic faults around this magmatic centre may have played a role in its evolution, but more detailed appraisal of this issue is beyond the scope of the present work.

6.4.2 Volcano-tectonic structures and displacements related to catastrophic caldera collapse

Caldera collapse without regional-tectonic influence

The structural evolution of 'simple' (single reservoir, single subsidence event) collapse due to honey chamber deflation mirrored that in previous experimental caldera studies, but displayed some noteworthy extra details. Firstly, reverse faulting above circular chambers initiated at an apparently random point around the chamber circumference, though subtle lateral variations in roof loading possibly influenced the exact location in each case (cf. Roche et al. 2000). In contrast, reverse faulting above elliptical chambers consistently initiated above the short axis ends of the chamber circumference, and propagated around to the long axis ends. This fault evolution reflects that at Long Valley caldera, California (Hildreth and Mahood 1986) and may thus be characteristic of subsidence into elliptical chambers (Roche et al. 2000). Secondly, this study is the first to report reversals of subsidence symmetry in experiment, though only above an elliptical honey chamber. This is tentatively attributed to the faulting pattern particular to elliptical subsidence and perhaps to the sensitivity of the low-viscosity honey to subtle variations in roof loading. Carr and Quinlivan (1968) inferred a similar symmetry reversal at Timber Mountain caldera, Nevada. Thirdly, arcuate reverse faults were subtly polygonal, rather than perfectly smooth curves (see also Kennedy et al. 2004). Past explanations for polygonal caldera ring faults have included: 1) the intersection of fractures related to doming and collapse (Komuro 1987) and 2) the reactivation of regional-tectonic faults (Nappi et al.1991; Orsi et al. 1996). However, the evidence supports Kennedy et al.'s (2004) proposition that the generation of polygonal ring faults may simply be more inherent on all scales to the caldera collapse process than hitherto recognised. If other mechanisms are invoked to account for a linear ring-fault segment, they require clear demonstration - e.g. regional-tectonic fault reactivation deduced from alignment and/or continuation of a segment with a regional fault.

Reactivation of pre-collapse regional-tectonic faults during collapse

Model collapse with regional-tectonic influence generally resembled that without regional-tectonic influence. This result supports inferences, from the generally sub-circular to elliptical caldera shapes in nature, of a magma chamber dominated syn-collapse stress/strain field (Lipman 1997; Roche et al. 2000). Pre-collapse regional-tectonic faults nonetheless substantially affected the experimental volcano-tectonic caldera structures in two ways. Firstly, regional-tectonic faults orientated tangentially to the chamber centre and located just inside the chamber margin linked with arcuate volcano-tectonic reverse faults and re-activated to become bounding faults to the central caldera zone (**Figures 6.6d,e and 6.7b** – see also Acocella et al. 2004; Holohan et al. 2005). Tangentially orientated regional-tectonic faults located beyond the chamber margin usually reactivated as bounding faults to the peripheral caldera zone (**Figures 6.6b; 6.7a,b; and 6.8a,b**). Secondly, where orientated non-tangentially, but defining corners in the chamber margins, regional faults often abruptly halted reverse fault propagation (**Figures 6.6d,e and 6.7e** - cf. Roche et al. 2000) and locally reactivated to accommodate some of the volcano-tectonic displacement. Regional-tectonic faults in non-tangential orientations and those located above the centre of the chamber did not otherwise noticeably reactivate during collapse.

In nature, the often highly elongated calderas in strike-slip zones (e.g. Toba, Ranau) very likely formed from non-circular reservoirs with variable regional fault control (e.g. Ardara pluton). Consequently, and as seen in experiment, elongate magma chamber geometry may primarily control the spatial and temporal development of subsidence-controlling faults (and associated vents) at these calderas. The influence of regional-tectonic faults on this volcano-tectonic development should depend largely on the extent to which they: a) are tangential to the collapse centre, and/or b) define or coincide with the magma chamber margins. Such regional faults can be viewed as optimally orientated and positioned for reactivation, as collapse-related strain (radially-directed extension and contraction, and vertical shear) mainly localises around the chamber margins (see also Roche et al. 2000; Kennedy et al 2004; Acocella et al. 2004; Holohan et al 2005).

Effects of pre-collapse regional-tectonic faults on collapse style (mode)

Branney and Kokelaar (1994) define piecemeal as "composed of many pieces; bit by bit" and suggest this definition "is useful to describe both the *morphology* of calderas with highly fragmented floors and the *mode of collapse* in which different parts subside at different times or rates" [Italics added]. Using the term 'piecemeal' to describe the floor morphology is potentially confusing, however, because it blurs the relationships between floor complexity and the different structural processes that can generate such complexity - e.g. regional-tectonic subsidence, volcano-tectonic collapse, landsliding, etc. Moreover, piecemeal subsidence as demonstrated at Scafell caldera (Branney and Kokelaar 1994) implicitly carries with it a genetic link between the complexly block-faulted floor morphology and differential, *syn-eruptive, volcano-tectonic* subsidence along the block-defining faults. The term 'piecemeal' is therefore here applied to <u>mode of collapse</u> only, whereby the caldera floor (= pre-collapse palaeo-surface) subsides as multiple, differentially-sinking fault blocks during volcano-tectonic deformation.

This distinction is important because, in experiments, the peripheral caldera zone floor usually broke up along a complex array of volcano-tectonic extensional faults – i.e. could be interpreted as subsiding in piecemeal style. Conversely, whilst the central zone caldera floor commonly comprised several regional-fault-bound, differentially-subsided segments, this differential subsidence seems to have occurred solely during pre-collapse regional-tectonic deformation. During volcano-tectonic collapse, the central zone floor apparently subsided coherently; no movement (scarp growth) was observed on the segment-bounding R- and Y-shears (**Figures 6.6a-d; 6.7a,b,d,e; and 6.8a,b**). The experiments presented here thus show that a fragmented <u>central</u> caldera zone floor can arise predominantly through *pre-collapse* regional-tectonic faulting, the effects of which may be subsequently preserved by essentially coherent caldera subsidence.

In nature, a coherently-subsided, fault-controlled palaeo-topography will produce abrupt, fault-scarp-defined lateral changes in accommodation space and hence in caldera infill thickness - especially with topography-blanketing ignimbrites. Such thickness changes might be misinterpreted as evidence of syn-eruptive growth faulting. This problem may be most acute where thickness changes are relatively small (a few 10's – 100 m) and where floor and infill structure is very poorly-exposed and mainly inferred – e.g. from borehole data and/or gravity anomalies. Alternatively, because pre-collapse (and post-collapse) regional-tectonics can generate significant differential movement between caldera floor blocks (as inferred at Glencoe caldera – Moore and Kokelaar 1998), the magnitude of any purely volcano-tectonic subsidence on a regional structure may be overestimated. In the absence of unequivocal evidence for reactivation of pre-collapse faults as syn-collapse growth-faults (cf. Branney and Kokelaar 1994), as seen in places at Glencoe caldera (Moore and Kokelaar 1998 - see below), caution is advised when estimating the extent to which regional-fault-defined changes in caldera fill thickness, and/or offsets of the caldera floor, reflect volcano-tectonic motion (cf. Ramelow et al. 2006).

Moore and Kokelaar's (1998) landmark study of the Caledonian Glencoe volcano, Scotland is to date the most detailed analysis of the influence of regional-tectonic faulting in caldera development (**Figure 6.11a**). Within a probably sinistral strike-slip regime, extension and/or transtension at Glencoe occurred along several orthogonally-intersecting regional-tectonic faults (Moore and Kokelaar 1998 – **Figure 6.11a**). The regional-fault-dissected caldera floor and a tightly-constrained caldera infill succession (**Figure 6.11b**) are preserved inside a large-displacement (>700m) ring fault system that is locally steeply outward-dipping (Kokelaar and Moore 2006 - **Figure 6.11a**). From thickness changes in ignimbrites across the regional faults, ponding of ignimbrites against regional fault scarps, and local intercalation of fault-scarp-derived breccias in ignimbrites, Moore and Kokelaar (1998) inferred a complex history of differential and incremental volcano-tectonic subsidence (i.e. piecemeal collapse) of caldera floor blocks along the regional-tectonic faults.

The area inside the ring fault system at Glencoe may be comparable to the central caldera zone in the experiments presented here, and hence volcano-tectonic reactivations along regional faults would seem to be possible there in nature – in contrast to the experimental results. Direct comparison between the experiments and Glencoe caldera, though pertinent, is difficult, however. Unlike in the single-collapse experiments, volcano-tectonic subsidence at Glencoe is thought to have occurred during several major eruptive/collapse events, which punctuated a protracted period (maybe 0.5 Myr - Moore and Kokelaar 1998) of pre- and post-collapse regional-tectonic faulting and differential graben subsidence. Moreover, the role played by ring faulting in accommodation of volcano-tectonic subsidence, important in experiment, is rather uncertain at Glencoe (Moore and Kokelaar 1998). Nonetheless, three possible explanations of disparities between the observations in experiment and at Glencoe are here considered.

Firstly, the apparent absence of regional fault reactivation above the experimental chamber's centre may largely relate to the boundary conditions imposed. Previous experimental studies (cf. Roche et al. 2000; Kennedy et al. 2004) consistently related low thickness/diameter ratios of the roof to more coherent collapse style in the central zone. In contrast, higher thickness/diameter ratios result in less coherent central collapse. Furthermore, a flat upper surface of the magma chamber tends to restrict reverse faulting to the chamber margins, whereas a curved convex-upward upper magma chamber surface promotes additional reverse faults in the central caldera zone (cf. Roche et al. 2000; Walter and Troll 2001; Kennedy et al. 2004). The coherent central caldera zones in the experiments may thus relate to an overriding control from the low roof thickness/diameter ratios and the flat tops of the honey chambers. More incoherent (piecemeal) central zone collapse, with reactivation of the regional faults, might have developed with higher roof thickness/diameter ratios and/or a curved chamber top-surface.

Secondly, disparity may be a function of model resolution, and single collapse events at Glencoe may to some extent be consistent with the single magma chamber experimental model. The inferred collapse-related reactivations of regional faults in the central zone of Glencoe caldera range from a few 10's of m to just over 100 m (Moore and Kokelaar 1998), which scales to less than 0.5 mm in experiments. Regional fault reactivations in the model central zone may thus have been comparable to those in nature, but too small to be resolved here. If this is the case, then one might expect that volcano-tectonic reactivation of pre-collapse regional structures in a down-sag dominated central caldera zone in nature may be of small displacement (< 100 m) relative to displacements on main ring faults and/or chamber-bounding regional faults (100's of m to >1 km). Such a scenario seems compatible with, for instance, the inferred collapse history during emplacement of the >200 m thick Upper Three Sisters Ignimbrite (**Figure 6.11b** - cf. Moore and Kokelaar 1998). Differential subsidence along regional faults is inferred to have accommodated ~ 40-50 m of the total 200 m of subsidence, with the majority accommodated by coherent sagging and probable ring faulting (Moore and Kokelaar 1998).

Thirdly, the pattern of differential volcano-tectonic subsidence of regional-fault-bound blocks at Glencoe may relate to several spatially and temporally discrete sub-caldera magma chambers. Indeed, Moore and Kokelaar (1998) suggested this possibility to account for differential subsidence at Glencoe. If regional faults delimited each magma chamber, their reactivation during eruption would be compatible with the focusing of regional fault reactivation at the experimental chamber margins.

Reactivation of regional tectonic structures has also been suggested to promote an asymmetric 'trapdoor' subsidence style (Lipman 1997; Riller et al. 2001; Ramelow et al. 2006). As this style characterised experiments with and without regional faults, the trapdoor-like subsidence in the experiments is ascribed to the influence of low roof thickness/diameter ratio (cf. Kennedy et al. 2004). Although regional-tectonic faults did not promote asymmetric collapse in experiment, it is noted that they occasionally facilitated it (e.g. **Figures 6.7b and 6.8b**).

Influence of regional strike-slip structures on caldera development in pull-apart-like settings

The general evolutions and geometries of calderas proposed to have formed in pull-apart structures show close similarities to the experiments presented in this chapter. From patterns of active and inactive (recent) faulting, Bellier and Sébrier (1994) inferred that the 0.074 Ma Toba and

0.55 Ma Ranau calderas, Indonesia, formed in contemporaneous, but presently inactive, pull-apart gräben. Firstly, a step-over or relay in the dextral Great Sumatran Fault Zone gave rise to a regional-tectonic pull-apart graben. Early volcanic activity at Toba and Ranau occurred around the pull-apart's 'sidewall' normal faults (**Figure 6.12a**). Secondly, the sidewall faults of the pull-apart graben reactivated to partly delimit volcano-tectonic caldera collapse (**Figure 6.12b).** Thirdly, a new regional-tectonic strike-slip fault (Y-shear or PDZ) cut through and deactivated the pull-apart structure (**Figure 6.12c**). A further evaluation of the role pull-apart structures may play in the caldera collapse phase at centres like Toba and Ranau is thus possible based on the experimental results generated for this study.

Firstly, Bellier and Sébrier (1994) proposed that the pull-apart faults might entirely substitute for ring-faults during caldera collapse. The experiments suggest that this might occur only if the pull-apart faults entirely delimit or coincide with the magma chamber margins. Here, the pull-apart side-wall faults seem most likely to accommodate extension in the caldera periphery (**Figures 6.6b-d, 6.7a and 6.12c**). Though they are likely to be buried in nature, subsidence controlling inner reverse ring-faults of purely volcano-tectonic origin may also form inside the side-wall faults (**Figures 6.6c,d, 6.7a,b and 6.12c**). Secondly, though the exact timing between stages 2 and 3 is unclear in these natural examples (**Figure 6.12**), the models show that where the Y-shear (or PDZ) cuts through the pull-apart and chamber prior to collapse, it can influence caldera development in the pull-apart by halting the propagation of subsidence controlling volcano-tectonic reverse faults (**Figures 6.6e,f, 6.7e,f and 6.12c**).

Finally, regional strike-slip faults hosting rhyolite intrusions dissect the central floors of the Negra Muerta (NW Argentina - Riller et al. 2001; Ramelow et al. 2006) and Hopong calderas in a pattern very similar to the roof-dissecting Riedel shears and Y-shears in the models (**Figure 6.10b,c**). These fault systems are therefore likely to be preferential pathways in nature for ascent of magma and other fluids before, during, or after caldera formation.

6.5 Summary and Conclusions

This study represents a first step in experimentally evaluating the role of strike-slip tectonics in caldera development that more detailed modelling and field analysis should complement. The main findings are as follows:

1) Magma chamber geometry will exert the primary control on the geometry and development of subsidence-controlling faults. At calderas forming above elliptical or elongate magma chambers, commonly found in strike-slip zones, reverse ring-faults should propagate from the short axis end of the chamber toward the long axis end. Since such 'ring' faults comprised several linear segments, even in experiments without regional faults, a regional-tectonic control on linear ring-fault segments at natural calderas cannot be assumed.

2) Regional fault reactivation during collapse can occur by structural grain exploitation and through fault-defined magma chamber margins. Where lying just inside and tangential to the magma chamber margins, regional strike-slip faults tend to reactivate to delimit the central caldera zone. Where lying just outside and tangential to the magma chamber margins, regional strike-slip faults tend to reactivate to delimit the peripheral caldera zone. Where defining 'corners' or sharp bends in the chamber margin, regional-tectonic faults can also arrest the propagation of central zone reverse faults, and locally take up the volcano-tectonic displacement. The extent to which regional faults control caldera collapse may thus primarily depend on the extent to which they define or are coincident with the chamber margins.

3) Long-lived, passive magma bodies or magmatic centres may localise marginal faults when subjected to regional transtension. These faults may result from rheological contrasts between the magmatic centre and the surrounding brittle crust, and are analogous to 'side-wall' faults of pull-apart gräben.

4) Regardless of how a pull-apart basin localises, it is inferred that calderas formed in such structural settings will be strongly influenced by 'side-wall' faults. If linked with and tangential to the magma chamber margins, these faults will accommodate collapse-related extension in the peripheral caldera zone and act as peripheral zone bounding faults. They may also serve as sites for eruption. Note, however, that purely volcano-tectonic reverse faults may also occur within such pull-apart settings.

5) Dissection of the magma chamber roof by pre-collapse regional faults did not noticeably result in piecemeal collapse style in the central caldera zone, unlike as inferred at e.g. Glencoe caldera, Scotland. Direct comparison of single-collapse experiments to field studies of such multi-collapse calderas is difficult, however, and disparity may have three possible explanations. First, the low roof aspect ratios and flat magma chamber tops in the experiments in this study may have promoted coherent central zone collapse. Second, the 10m to 100m volcano-tectonic displacements along regional faults inferred at Glencoe would scale to < 0.5 mm in the model, and thus may have been below the experimental 'detection limit'. Third, the differential volcano-tectonic collapse of regional-fault-bound blocks at Glencoe may relate to spatially and temporally discrete, perhaps regional-fault-delimited, magma reservoirs.

6) The experimental results highlight *pre-collapse* regional-tectonism as an important mechanism for generating a fragmented and differentially subsided caldera floor. Indeed, much of the differential displacement on regional faults at Glencoe caldera relates to background regional-tectonics rather than catastrophic volcano-tectonics. The experiments indicate that such differential pre-collapse floor displacements may be preserved by coherent to semi-coherent volcano-tectonic subsidence. This in turn highlights the need for demonstrable syn-collapse offset on a regional fault to accurately establish the extent to which an offset, or an ignimbrite thickness change, across the fault represents volcano-tectonic displacement.

7) The roof-dissecting strike-slip faults (R-shears and Y-shears) that cut the central zone in experiments may serve as pathways for magma ascent and eruption, as evidenced at several calderas in nature.

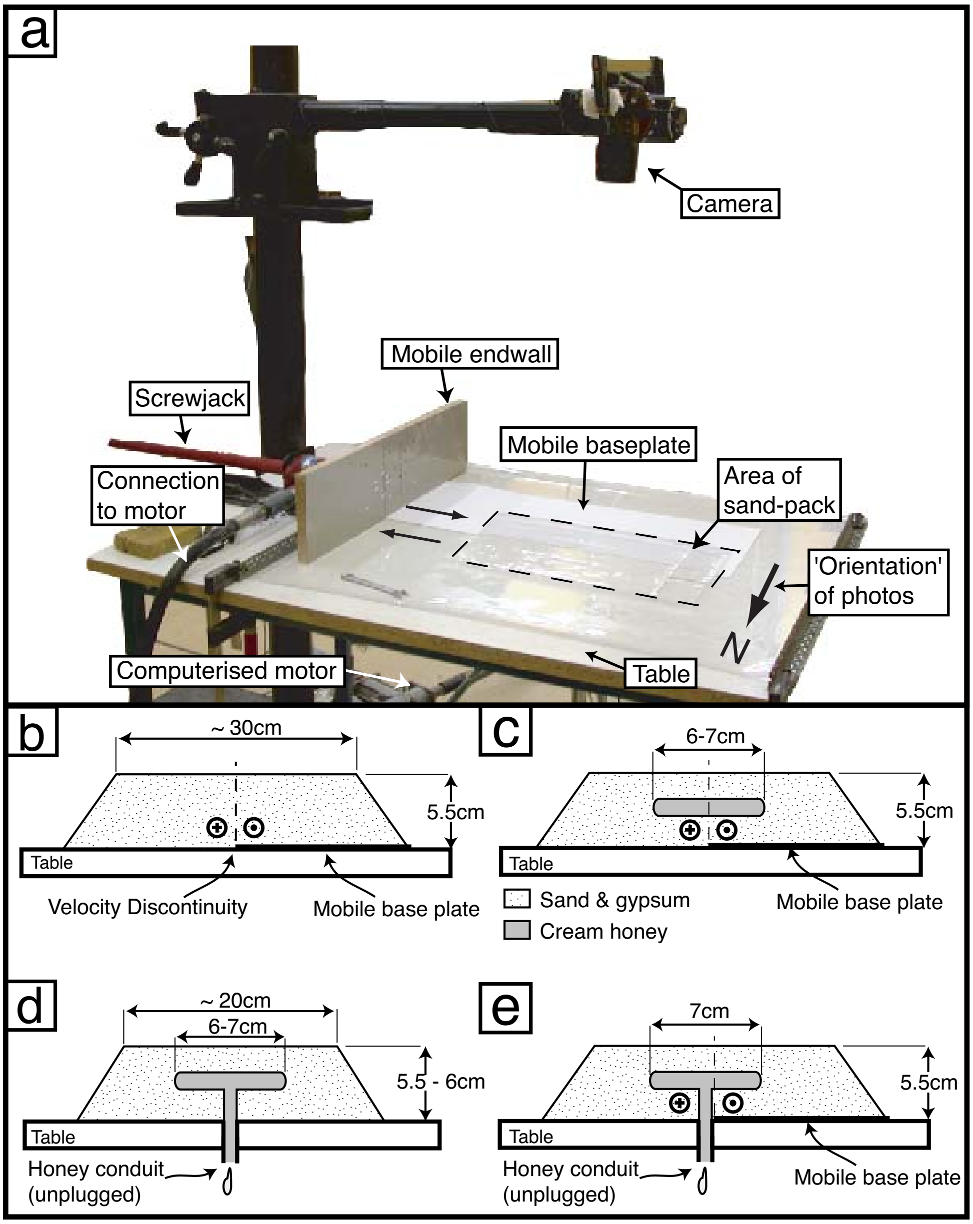

Figure 6.1: **(a)** Photo of experimental apparatus for strike-slip deformation. Cross-section sketches of experimental configurations for: **(b)** strike-slip deformation in purely brittle crust; **(c)** strike-slip deformation of brittle crust containing a passive magma chamber **(d)**; caldera collapse without regional faulting and **(e)** caldera collapse following regional strike-slip faulting.

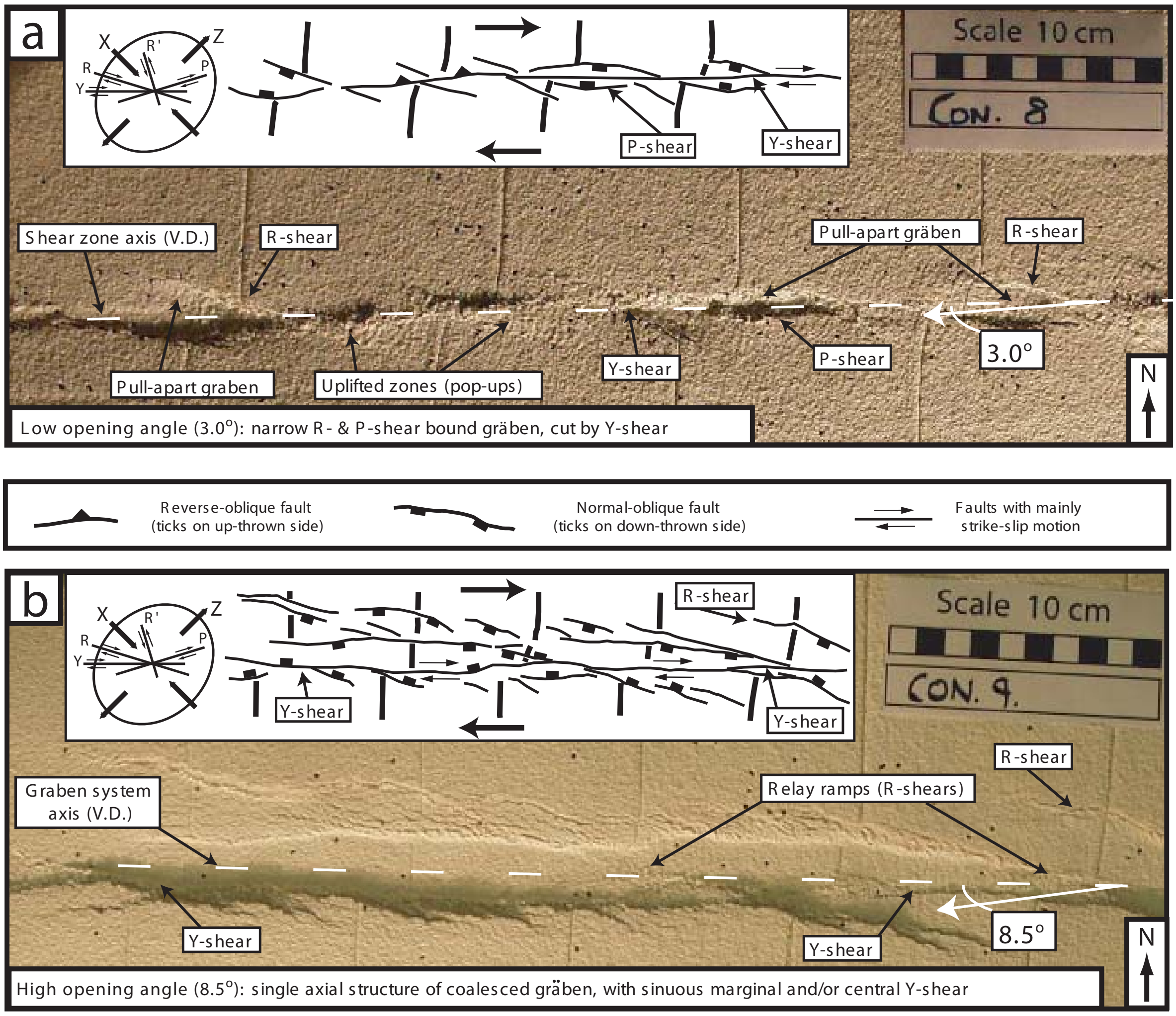

Figure 6.2: Simulation of strike-slip deformation in brittle crust (light from S). **(a)** At low opening angles (3), a narrow shear zone forms with small, Riedel shear bound, pull-apart-type gr‰ben and occasional pop-ups. **(b)** At higher opening angles (8.5), a series of rhombic pull-apart-type gr‰ben forms along a broader shear zone. These gr‰ben rapidly coalesce to form a single graben system. Insets show sketches of structures and their theoretical orientation with respect to the incremental strain ellipse (Woodcock and Schubert 1994).

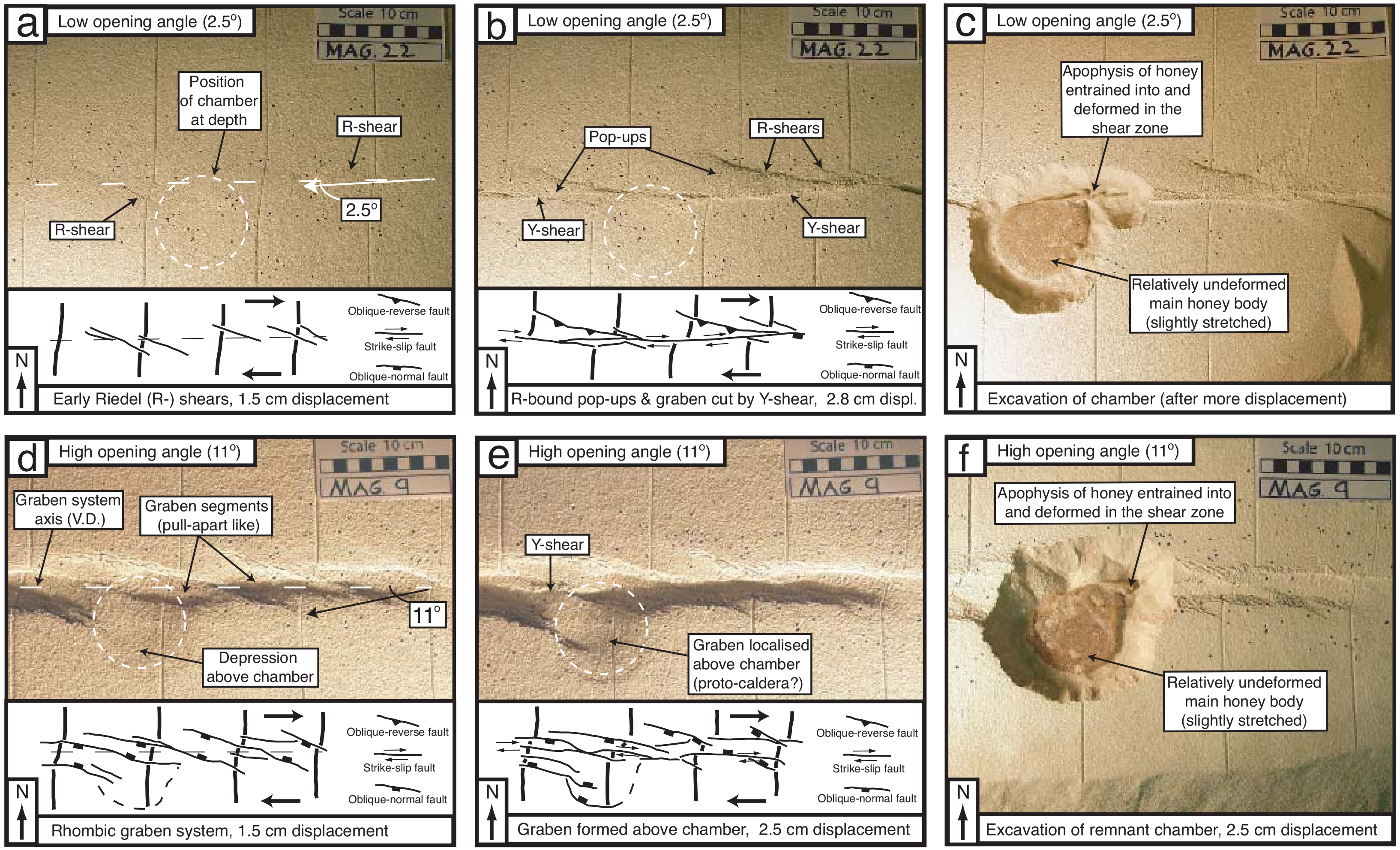

Figure 6.3: Simulation of strike-slip deformation of brittle crust containing a passive magma chamber (light from SW). **(a, b)** At low opening angles, little effect was seen. **(d, e)** At higher opening angles (> ~ 3-4°), pull-apart like graben formed marginal to and above the magma chamber. **(c, f)** Honey chambers are slightly elongated parallel to regional stretching direction (cf. **Figure 6.2**) and locally more intensely deformed along the Y-shear. Extension across the chamber localises as graben/normal faults at the rheological change along the chamber edge.

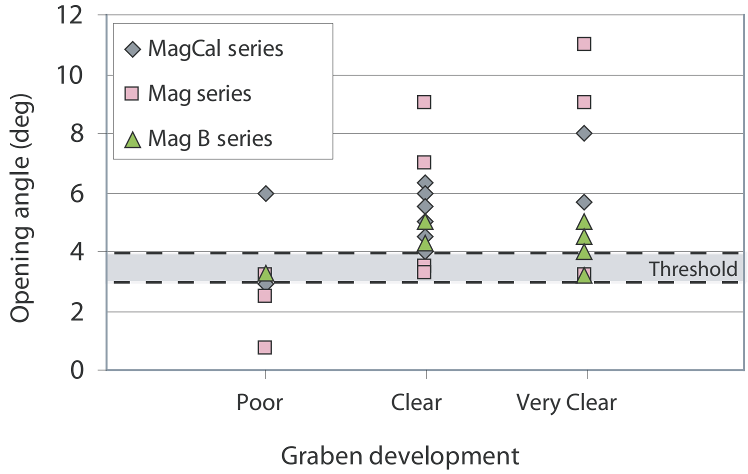

Figure 6.4: Plot of opening angles in passive magma chamber experiments vs. the development of chamber localised graben (categorised into poor, clear and very clear). A threshold, above which graben tended to localise, was reached at opening angles of 3-4°. At 95% confidence, mean opening angles for the 'clear' and 'very clear' categories are indistinct from each other, but both are distinct from the 'poor' category.

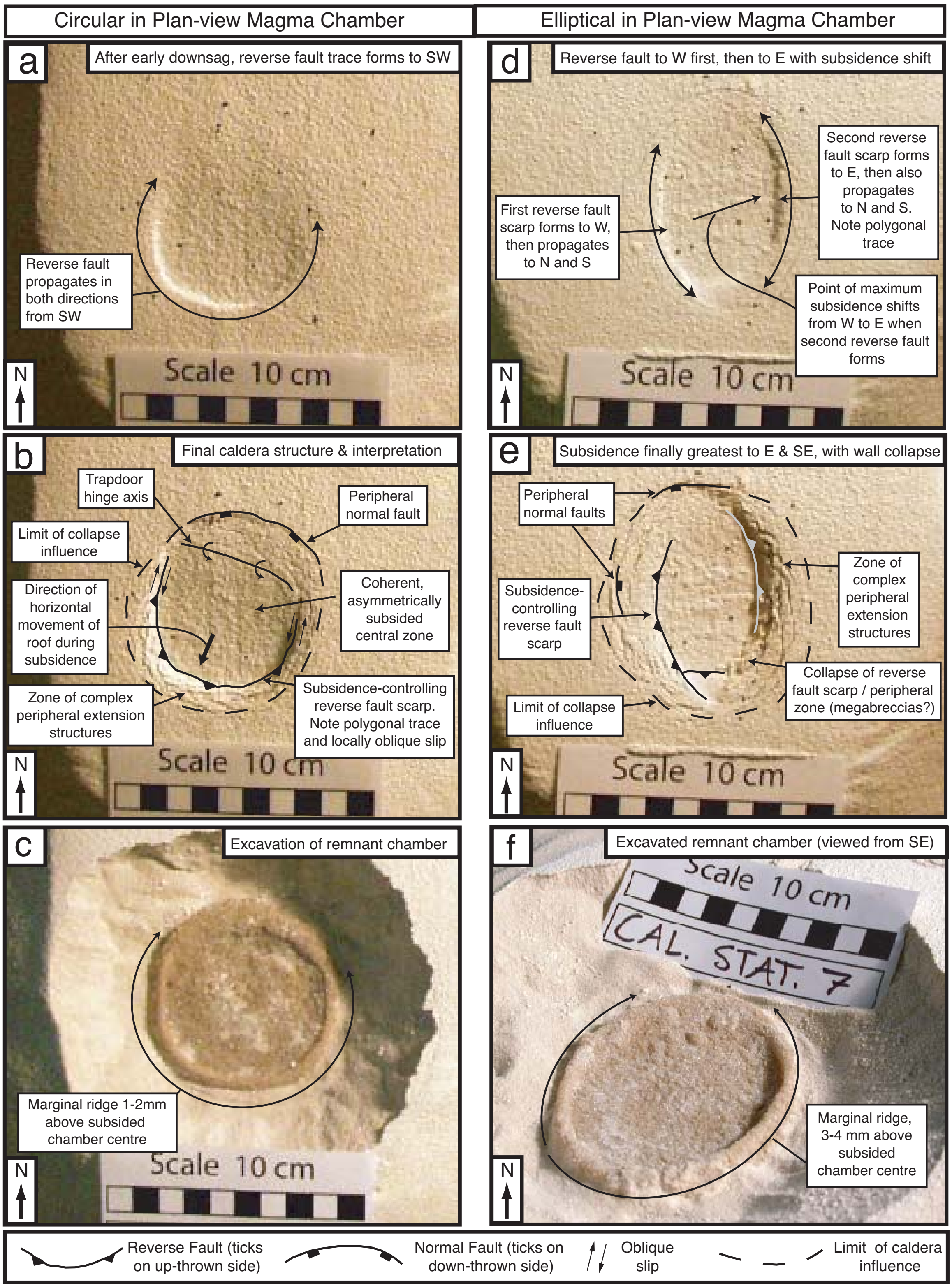

Figure 6.5: Evolution of caldera collapse into circular and elliptical magma chambers (light from E). Circular: **(a)** Following early sagging and peripheral cracking, a reverse fault trace appears at a random point above the circular chamber's circumference, and propagates bi-directionally toward the opposite side. **(b)** The final structure is an asymmetric (trapdoor-like) caldera with a hinge zone opposite the point of reverse fault initiation. **(c)** A ridge related to the reverse fault borders the underlying magma chamber remnant. Elliptical: **(d)** After sagging, reverse fault traces appear consecutively above either short axis ends of the elliptical chamber circumference. **(e)** Both faults propagate toward the chamber's long axis ends, where they link. Again, the final caldera is asymmetric (trapdoor-like) with a hinge located around the chamber long axis end. **(f)** Vertical to slightly outward-dipping ridges related to the reverse faults again mark the underlying magma chamber remnant.

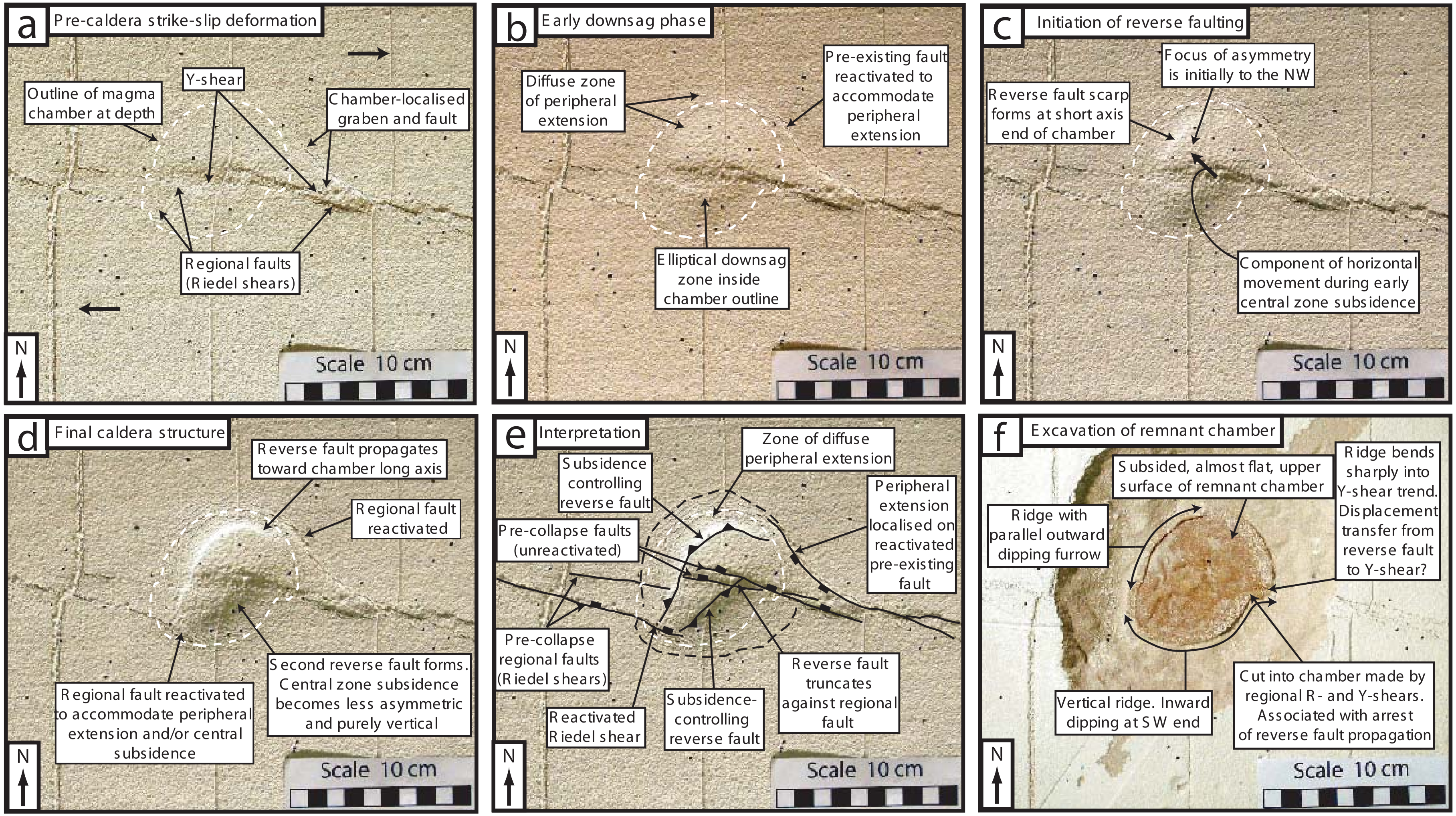

Figure 6.6: Caldera collapse evolution following regional strike-slip deformation (MagCal 2 - light from SE). **(a)** Pre-collapse regional structures include Riedel shears, a chamber-localised graben fault, and a partial Y-shear. **(b)** Collapse begins with down-sag and peripheral extension, the latter taken up along new fractures and/or the pre-collapse chamber-localised fault just beyond the chamber margin. **(c)** A reverse fault appears above the short axis end of the chamber, and **(d)** propagates to the long axis end, where a pre-collapse Riedel-shear reactivates. **(e)** A second reverse fault appears on the opposite side of the chamber, but its NE-ward propagation halts upon intersection with Riedel- and Y-shears. **(f)** Excavation of the chamber remnants reveals that the arresting regional faults define a sharp bend in the chamber margin at this point. Syn-collapse regional displacement was < 1mm.

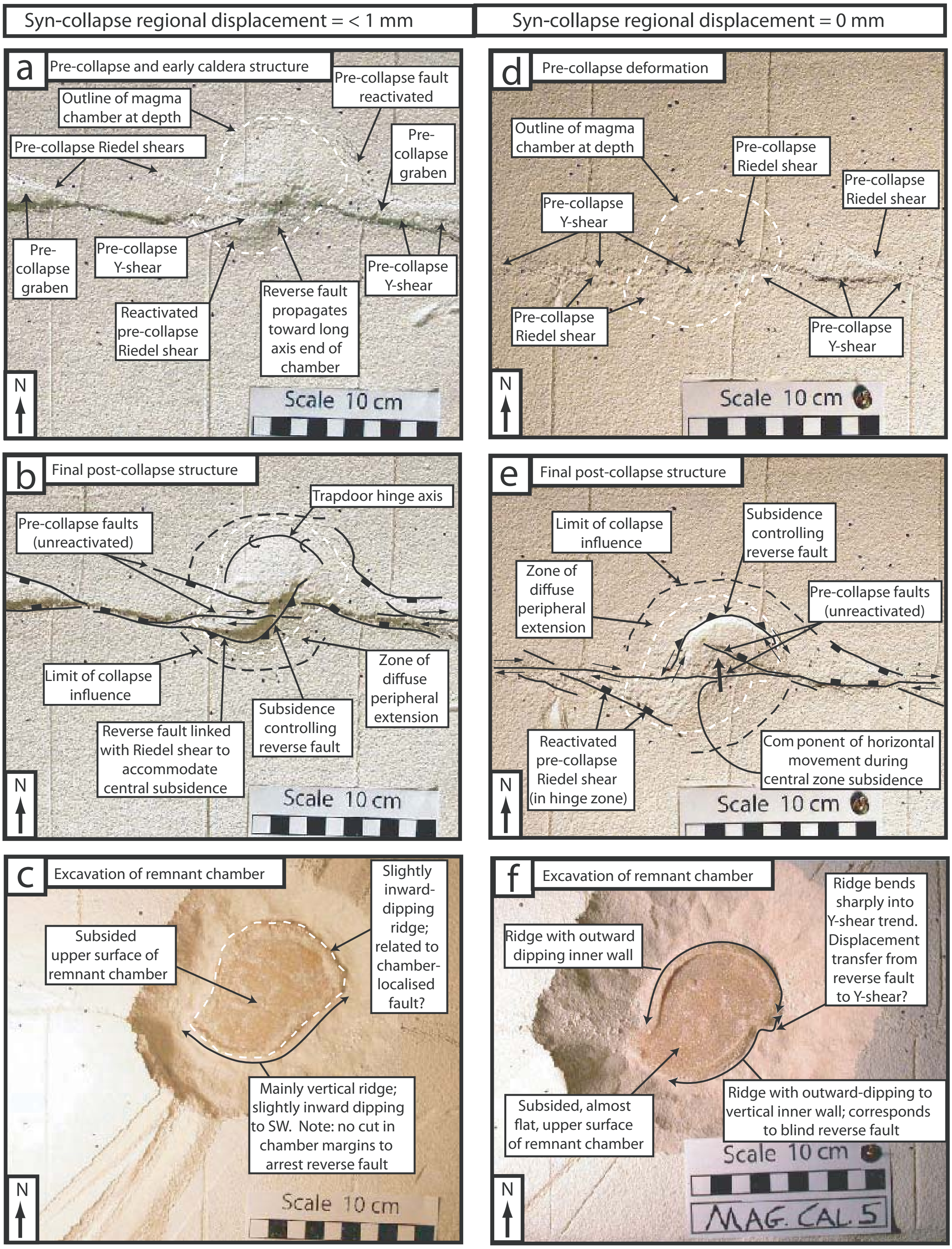

Figure 6.7: Further examples of caldera collapse after regional strike-slip deformation (Light from the SE in **(a)**, **(b)**, **(d)**, **(e)** and from SW in **(c)** and **(d)**. In MagCal 3, **(a)** peripheral extension again partly localised on a pre-collapse graben fault to the NE, **(b)** the reverse fault here propagates unimpeded toward both long axis ends and links with a pre-collapse Riedel-shear in the SW. **(c)** Excavation reveals no corners in the chamber margin. In MagCal 5 **(d-e)**, the reverse fault is arrested at a Y-shear defined corner in the W **(f)**, and a Riedel shear located just inside the chamber margin reactivates in the SW. Note the ridge to the E bends sharply into Y-shear orientation. Syn-collapse regional displacement: MagCal 3 < 1mm; MagCal 5 = 0 mm.

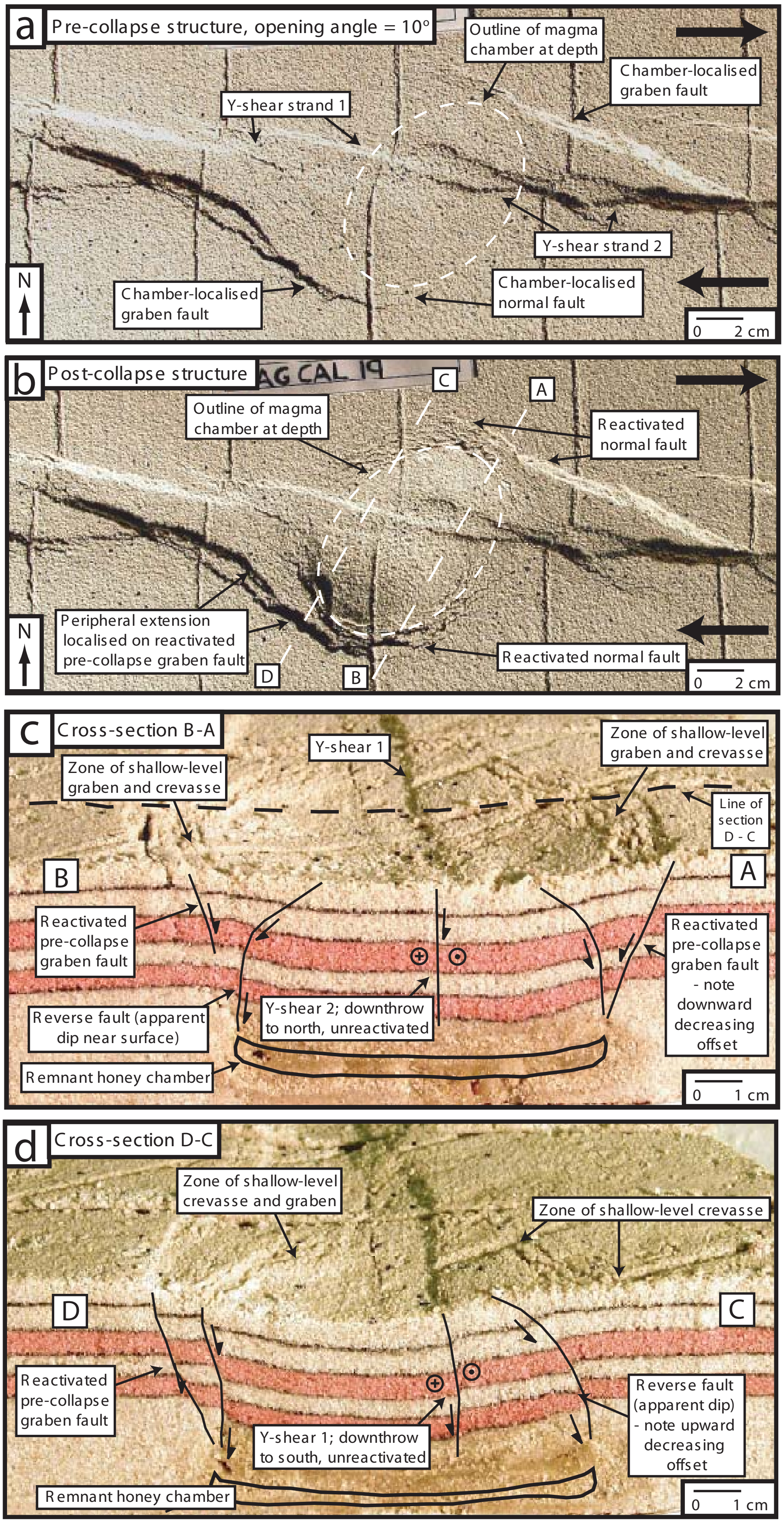

Figure 6.8: Cross-sections of a model caldera formed after regional strike-slip tectonism (Mag Cal 19). **(a)** Pre-collapse structure (light from SW). **(b)** Post-collapse structure - note reactivation of regional normal fault to SW and NE. Regional faults in caldera central zone were again unreactivated. **(c)** and **(d)** Cross sections along lines B-A and D-C, viewed from oblique angle to show relationship with surface deformation. Reverse faults are not well expressed at surface due to upward-decreasing displacement. Note that all structures with volcano-tectonic displacement converge on the honey chamber margin.

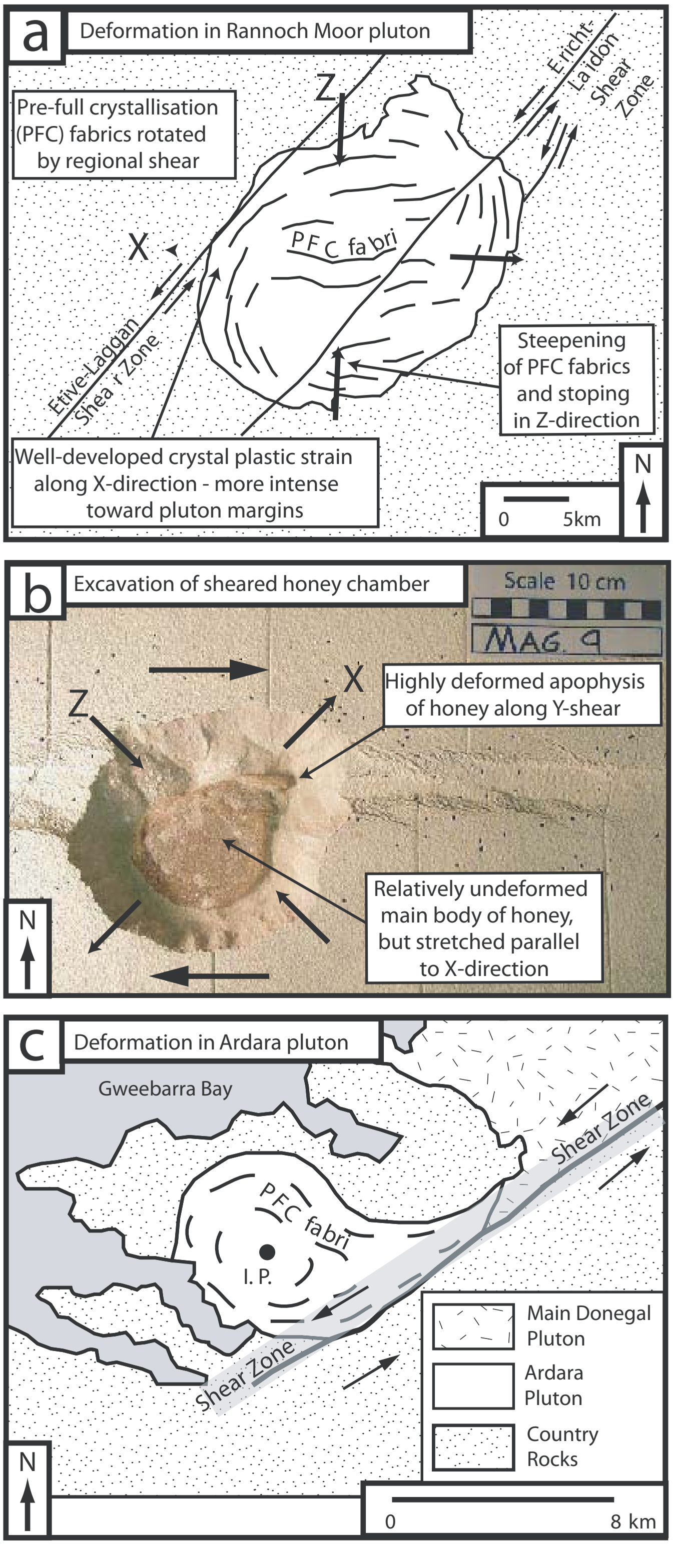

Figure 6.9: (a) Sited and partly shaped by regional faults, the Rannoch Moor granite, Scotland, was deformed and elongated prior to full crystallisation by transtensive regional-tectonics (adapted from Jacques and Reavy 1994). **(b)** In the models, honey chambers are similarly elongated and with respect to the regional shear, and extensional structures consequently localise along their margins. **(c)** The Ardara pluton, Ireland, is similarly elongated with respect to the regional shear sense. During and/or shortly after its emplacement at a low strain injection point (I.P.), Ardara pluton developed a strongly deformed 'tail' where intersecting the Donegal Shear Zone (adapted from Molyneux and Hutton 2000).

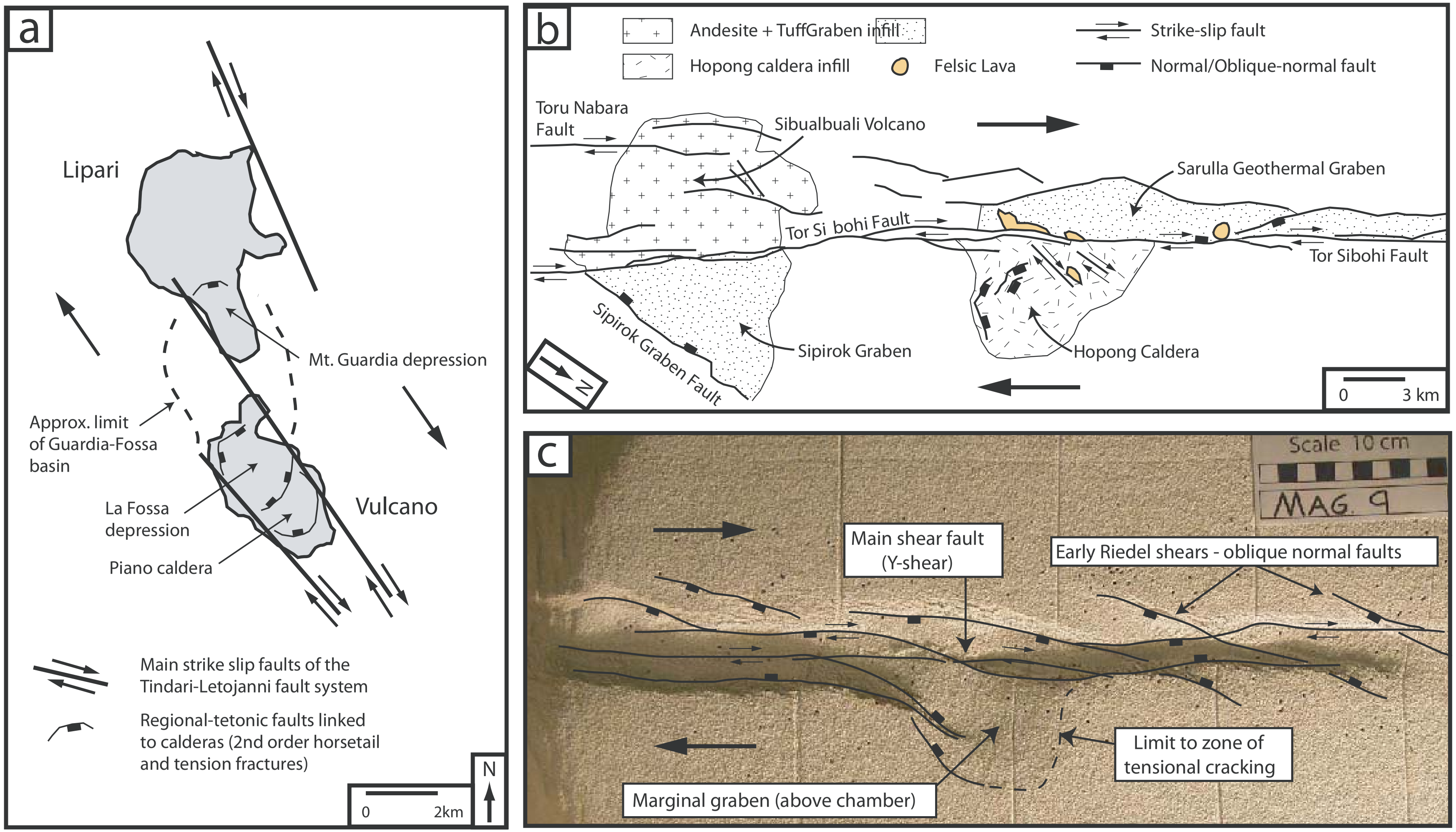

Figure 6.10: (a) The islands of Lipari and Vulcano are sited at a step-over in the Tindari-Letojanni strike-slip system (adapted from Ventura et al. 1999). The Guardia-Fossa depression is a caldera-like structure interpreted to have formed mainly from regional-tectonic subsidence, rather than catastrophic collapse. The depression's arcuate bounding faults are believed to be from regional stress/strain localisation on the Guardia-Fossa magmatic system's margins. **(b)** Arcuate normal fault structures preserved at the Hopong caldera, which lies beside the Tor Sibohi strike-slip fault, Indonesia (adapted from Hickman et al. 2004), are similar to those localised above passive honey chambers positioned laterally to a shear zone **(c)**.

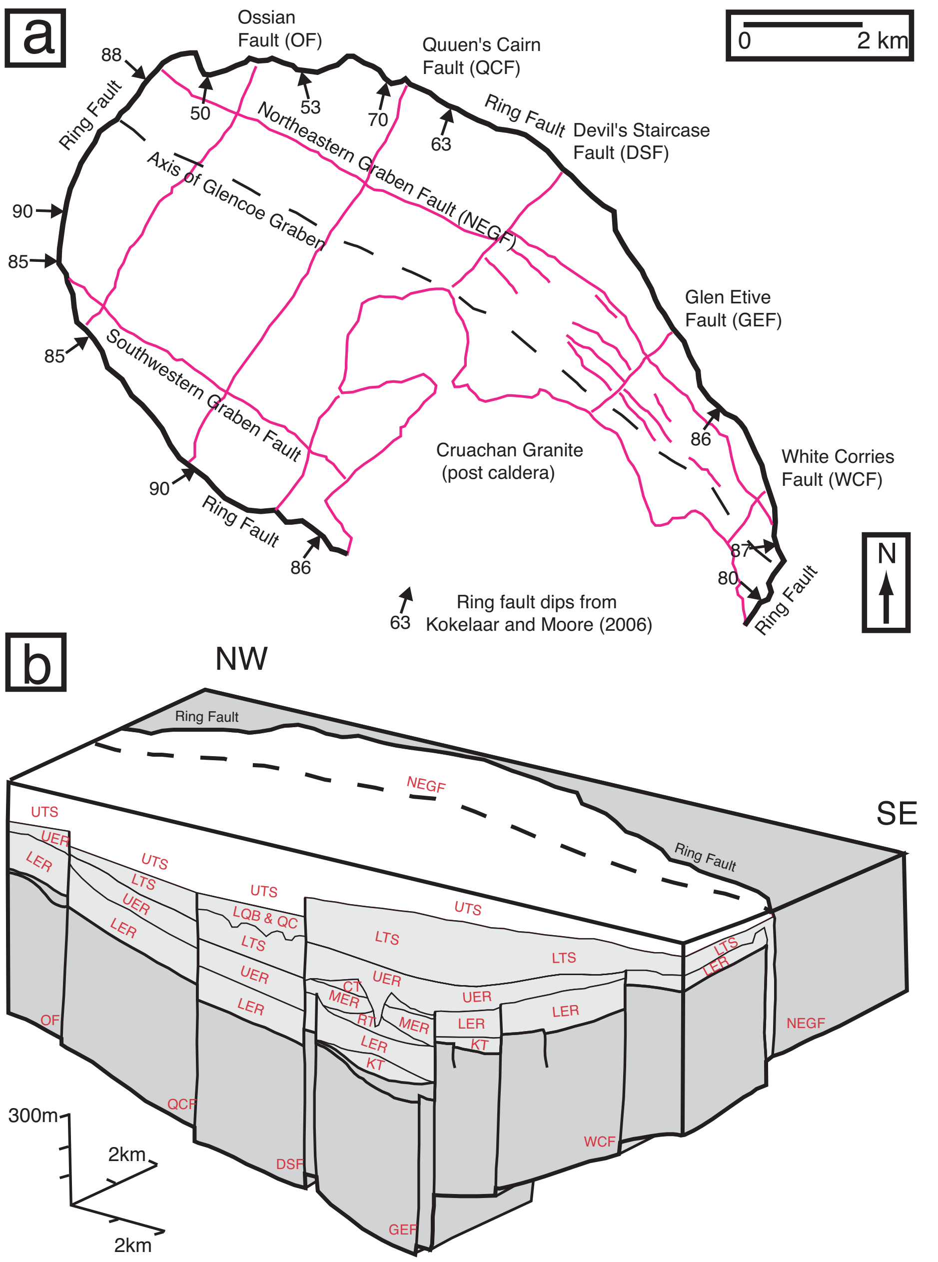

UTS	Upper Three Sisters Ignimbrite	CT	Crowberry Ridge Tuffs (Phreato-magmatic)
LQB	Lower Queen's Cairn Breccias	MER	Middle Etive Rhyolite
QC	Queen's Cairn Conglomerates	RT	Raven's Gully Tuffs (Phreato-magmatic)
LTS	Lower Three Sisters Ignimbrite	LER	Lower Etive Rhyolite
UER	Upper Etive Rhyolite	KT	Kingshouse Tuffs (Phreato-magmatic)

Figure 6.11: (a) Outline map of intersecting regional structures within the faceted ring fault of Glencoe caldera (adapted from Moore and Kokelaar 1998). The main NW-SE trending Glencoe graben is cross-cut by several NE-SW trending regional tectonic faults, some of which bound subsidiary orthogonal graben. Most faults now down-throw centrally. **(b)** Block diagram showing structure of floor and infill of Glencoe caldera, as restored to a plane horizontal surface presumed to have formed by eruption of the Upper Three Sisters (UTS) ignimbrite (adapted from Moore and Kokelaar 1998). The NW-SE line of section roughly coincides with the Glencoe Graben axis. The UTS possibly ponded against, but also extends beyond, the Northeast Graben Fault. UTS eruption is also inferred to have been associated with subsidence along the ring fault.

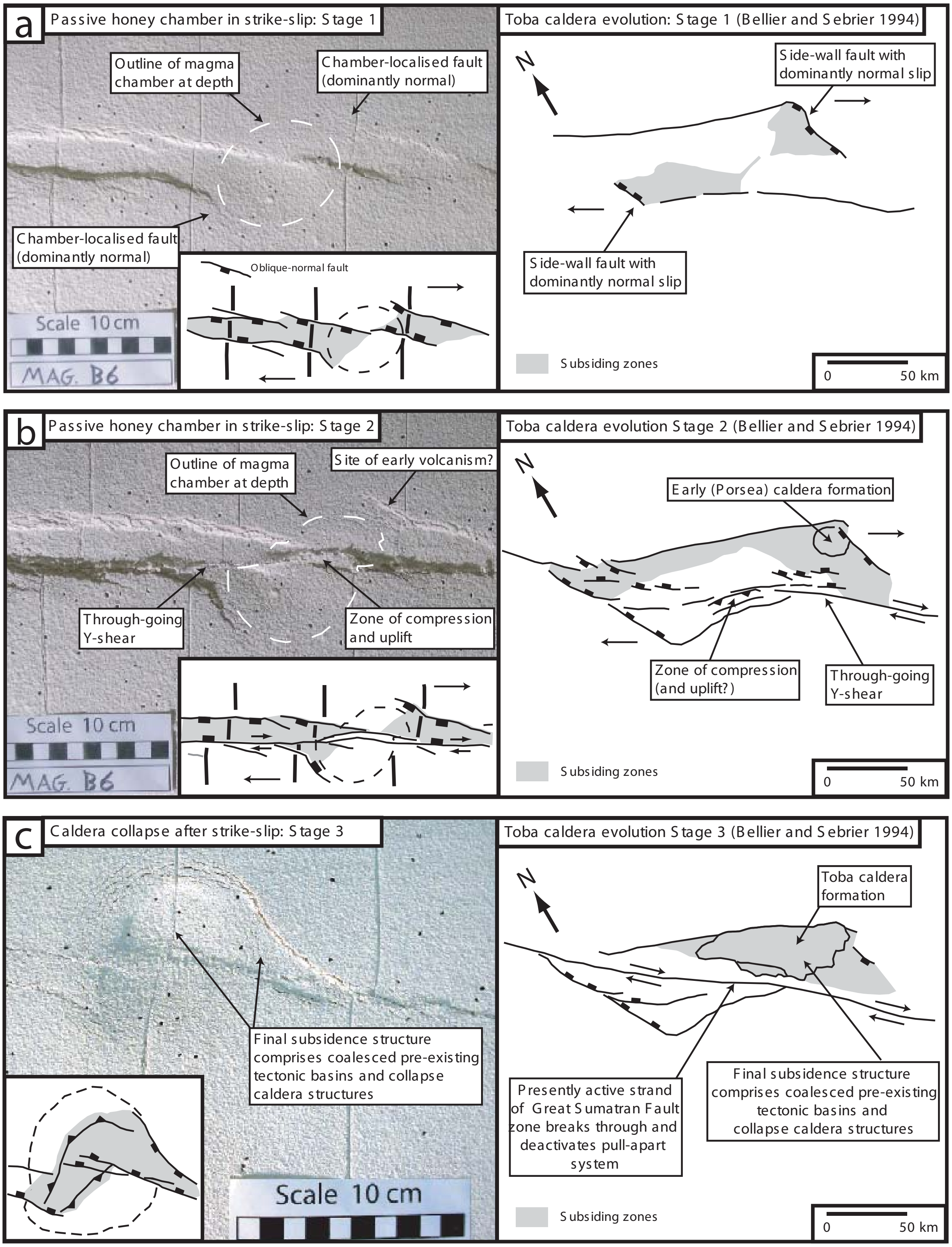

Figure 6.12: Tectonic evolutions of analogue models and of Toba caldera, Indonesia (Toba sketches redrawn from Bellier and Sebrier 1994). **(a)** Both begin with pull-apart-like graben formation and subsidence, localised by the chamber in the model and by a releasing step-over in nature. **(b)** Initial extension is followed by localised compression and formation of a through-going strike-slip fault, upon which all or most displacement is transferred. **(c)** Caldera subsidence and/or related peripheral extension are partly accommodated by reactivation of pre-existing structures. The relative timing of caldera formation and Y-shear breakthrough is unconstrained at Toba and Ranau. In the model, Y-shear breakthrough occurred just prior to collapse and arrests propagating caldera reverse faults (**Figures 6.6 and 6.7**).

a) Tectonic Controls

Expt. No.	Title	Opening Angle (deg.)	Piston displace-ment (cm)	Observations/Remarks
1	Con B2	2.4	6	Riedel-shears form along shear zone and bound poorly defined en-echelon gräben to E and W, with uplift or no subsidence in the central section.
2	Con 8	3	5	Evenly spaced Riedel-shears form above length of V.D. Lower angle Riedel-like & P-shears then form & bound small gräben and pop-ups, and later merge as a throughgoing Y-shear.
3	Con B1	3.1	4	Riedel-shears form along length of V.D. & bound pull apart gräben. Fairly straight Y-shear cuts through all these early structures toward experiment end.
4	Con 3	4.5	2.5	Evenly spaced Riedel-shears form along length of V.D. & bound pull apart gräben. Lower angle Riedel-like shears form & merge as a Y-shear. P-shears form late in evolution.
5	Con 6	5.5	2.8	Riedel-shears form along length of V.D. & bound rhombic pull apart gräben. Lower angle Riedel-like shears form next, followed by P-shears. Y-shear trace partly fomed in East.
6	Con 9	8.5	3.7	Almost straight-margined axial graben formed along length of V.D. from start. Riedel-shears initially weakly developed. Y-shear cuts through entire structure toward experiment end.
7	Con 4	11	2.5	Axial graben forms from start, but comprises several rhombic graben segments, each delimited by relay ramps in Riedel shear orientation.
8	Con 1	14	2.5	More or less straight-margined axial graben formed along length of V.D. from start. R-shears present, but weakly developed.

b) Chamber & Tectonic Interaction controls

Expt. No.	Title	Opening Angle (deg.)	Piston displace-ment (cm)	Chamber long axis (cm)	Chamber short axis (cm)	Chamber thickness (cm)	Chamber depth (cm)	Position of chamber centre*	Observations/Remarks	Chamber localised graben/faults?	Code
1	Mag 21	0.7	3	7	7	1.5	1	3.0 N	Pop-ups along shear zone. Subtle depression above chamber, otherwise as controls with low opening angle	No	1
2	Mag 1	2.5	2.3	7	6	1	2.5	1.5 N	Small gräben in shear zone. Intrusion or dragging of honey down the main shear zone (Y-shear), otherwise as controls with low opening angle	No	1
3	Mag 2	2.5	2.8	6	6	1	2.5	1.0 S	Sinistral regional shear imposed, not dextral. Small gräben along shear zone, except above chamber.	No	1
4	Mag 22	2.5	3	7	7	1.5	1	3.0 S	No gräben along shear zone, only pop-ups, as controls with low opening angle.	No	1
5	Mag Cal 6	2.9	1.5	7	7	1.5	1.5	2.0 N	Pop-ups and narrow pull-apart graben along shear zone, as controls with low opening angle.	No	1
6	Mag 17	3.2	2.8	6.5	6.5	1	1	0.75 N	Gräben in shear zone to W, pop-ups to E. Intrusion of honey down the main Y-shear. At chamber have sigmoidal bulge & shear zone widens.	Yes (sigmoidal & weak)	2
7	Mag 19	3.2	2.8	7	6.5	1	1	2.5 S	Narrow gräben along shear zone to E and W of chamber. Above chamber along shear zone , have pop-ups.	Yes (to S, weak)	2
8	Mag 20	3.3	3	7	7	1	1	3.0 N	Graben to W, gräben to E. Pop-ups where chamber intersects shear zone. V. subtle depression above chamber & curved fault along NE rim.	Yes (to N, v. weak)	2
9	Mag B2	3.3	4	7	7	1	1	0	Segmented axial graben system forms. Big bulge above chamber toward experiment end.	No	1
10	Mag 7	3.5	2.5	6.5	6.5	1.3	1.7	0	Initially pop-ups in E of shear zone, then narrow gräben all along shear zone.	Yes (to S, subtle)	2
11	Mag 18	3.5	2.8	7	7	1	1	0	Gräben in W of shear zone, but narrow. None to E. Sigmoidal bulge above chamber & shear zone widens to 7.5 cm here.	Yes (to N and S, weak)	2
12	Mag B1	4	7	7	7	1.5	1.5	0	Ran to & measurements at 7.5 cm reg. displ. Minimal subsidence above chamber centre.	Yes (v. good to S, subtle N)	3
13	Mag B5	4	3.5	7	7	1	3	0	Restricted subsidence over chamber. Narrow gräben to E and W along shear zone. Honey intrusion down Y-shear.	Maybe (to S)	2
14	Mag B8	4	6	7	7	1	2	3.0 S	Narrow graben system and Riedels formed. Deformation of chamber limited to edge next to shear zone (V.D.).	Yes (to S, v. good)	3
15	Mag B7	4.3	2.8	7	7	1	2	1.0 N	Restricted subsidence and even bulging over chamber. Narrow gräben to E and W. Anti-Riedel shears preserved as cracks in gräben floors.	Yes (subtle to N)	2
16	Mag B4	4.5	5	7	7	1	2	0	En-echelon gräben delimited by Riedel shears merge to form axial graben system. Restricted subsidence over chamber centre.	Yes (to N & S, v. good)	3
17	Mag Cal 5	4.5	1.7	7	7	1.5	2.5	1.0 N	Narrow gräben along shear zone E and W of chamber. Restricted subsidence above chamber.	Yes (to N, weak)	2
18	Mag B3	5	3.8	7	7	1	1.5	0	Axial graben system along shear zone E & W of chamber. Restricted subsidence over chamber centre. Anti-Riedel fractures preserved in gräben.	Yes (to N & S, v. good)	3
19	Mag Cal 12	5	1.7	7	7	1	3	2.0 N	En-echelon gräben delimited by Riedel shears along shear zone to E and W of chamber. Restricted subsidence over chamber centre.	Yes (to N, weak)	2
20	Mag Cal 11	5.7	1.5	7	7	1.5	1.5	2.0 N	En-echelon gräben delimited by Riedel shears along shear zone to E and W of chamber. Restricted subsidence over chamber centre.	Yes (to N, v. good, & S)	3
21	Mag Cal 1	6	1	7	7	2	1	1.0 N	Riedel shear bound graben to W. Otherwise limited subsidence along shear zone.	Yes (to N, weak)	2
22	Mag Cal 3	6	1.7	7	7	1.5	1.5	1.5 N	Narrow graben systems bound by Riedel shears and P-shears all along shear zone. Slightly less subsidence above chamber.	Yes (to N, weak)	2
23	Mag Cal 4	6	1.6	7	7	1	3	0.7 N	En-echelon gräben delimited by Riedel shears along shear zone to E and W of chamber. Restricted subsidence over chamber centre.	No	1
24	Mag Cal 2	6.3	1.5	7	7	1	2	1.0 N	En-echelon Riedel shears along shear zone to W. Riedel-bound graben to E of chamber. Restricted subsidence generally though.	Yes (to N, weak)	2
25	Mag B6	7.5	3.2	7	7	1	2	1.0 S	Axial graben system, partially segmented with Riedel-shear relay ramps. Restricted subsidence over chamber. Honey intrusion down Y-shear.	Yes (to S, v. good, subtle N)	3
26	Mag 11	7	2.7	7	7	1	2	2.5 S	Riedel and Y-shear bound gräben along shear zone, but narrower and shallower to E. Very little subsidence where chamber edge meets shear zone.	Yes (to S, v. subtle)	2
27	Mag 3	~ 8	2.6	6	6	1	2	0.5 S	Axial graben system, partially segmented, Riedel-shear relay ramps. Subsidence over chamber same as shear zone. Chamber cut by two Y-shears.	Yes (to N & S, v. good)	3
28	Mag Cal 7	8	4	7	7	1.5	1.5	2.0 N	Narrow axial graben forms. Unusual structure. Better developed along E and W of shear zone, less so in centre near chamber.	Yes (to N, v. good, & S)	3
29	Mag 5	9	2.7	6	6	1	2	0	Axial graben system, segmented with Riedel-shear relay ramps in E. Subsidence over chamber slightly less than elsewhere along shear zone.	Yes (to S, v. good, subtle N)	3
30	Mag 13	9	2.7	7	7	1.2	1.8	3.5 S	Axial graben system, segmented with Riedel-shear relay ramps in E. Shear zone widens across chamber.	Yes (to S, later overprinted)	2
31	Mag 9	11	2.5	7	6.5	1.5	1.5	2.5 S	Axial graben system, segmented with Riedel-shear relay ramps in E. Shear zone widens across chamber. Subsidence over chamber less.	Yes (to S, v. good)	3

* in cm south or north of the velocity discontinuity between baseplate and table

E = East; W = West; N = North; S = South; V.D. = velocity discontinuity between baseplate and table; Code for graben development: 1 = Poor, 2 = Clear, 3 = Very Clear

Table 6.1 Experimental data from control experiments simulating **(a)** strike-slip deformation in purely britlle crust, and **(b)** strike-sip deformation of brittle crust containing a passive magma chamber. Note the change in style of structural developement as opening angle increases.

a) Caldera collapse controls

Expt. No.	Title	Initial conditions: Initial plan-view chamber shape	Chamber long axis (cm)	Chamber short axis (cm)	Horizontal roof aspect ratio	Chamber thickness (cm)	Chamber depth (cm)	Vertical roof aspect ratio*	Final conditions: Collapse duration (mins)	Central zone long axis (cm)	Central zone short axis (cm)	Central zone aspect ratio	Perpipheral zone long axis (cm)	Peripheral zone short axis (cm)	Peripheral zone aspect ratio	Observations/Remarks
1	Cal Stat 1	Circle	6	6	1	1	0.5	0.08	120	5.2	5.2	1.00	7.6	7.2	0.95	Symmetric downsag collapse. No reverse fault traces at surface
2	Cal Stat 2	Circle	7	7	1	1.5	1.7	0.24	120	5.5	5.2	0.95	9.2	8.3	0.90	Asymmetric collapse to W. Reverse fault trace first to NW then SE.
3	Cal Stat 3	Circle	7	7	1	1.5	1.5	0.21	360	5.2	4.5	0.87	8.6	8	0.93	Asymmetric collapse to NE. Reverse fault trace first to NE.
4	Cal Stat 4	Circle	7	7	1	1.2	2.3	0.33	200	5.5	4.8	0.87	8	7.8	0.98	Asymmetric collapse to SE. Reverse fault trace first to SE.
5	Cal Stat 5	Ellipse	8	7	0.88	1.2	2.3	0.29	200	6	4	0.67	9.8	9	0.92	Asymmetric collapse to SE. Reverse fault trace to W first, propagating unidirectionally to E.
6	Cal Stat 6	Ellipse	8.1	6.5	0.80	1.2	2.3	0.28	200	6	2.4	0.40	9.5	8.1	0.85	Asymmetric collapse to W. Reverse fault trace to W only, propagating bidirectionally to N & S.
7	Cal Stat 7	Ellipse	8.5	7	0.82	1.4	2.1	0.25	200	5.7	3.7	0.65	9.7	9.2	0.95	Asymmetric collapse to E, then to W. Reverse fault trace to E first, then W, both propagating bidirectionally to N & S.

* Vertical roof aspect ratio for elliptical honey chambers taken as roof thickness/long axis of honey chamber (cf. Roche et al. 2000)

E = East; W = West; N = North; S = South

b) Syn- or Post-Tectonic Caldera Collapse

Expt. No.	Title	Initial conditions: Pre-collapse regional displace-ment (cm)	Chamber Long axis (cm)	Chamber short axis (cm)	Horizontal roof aspect ratio	Chamber thickness (cm)	Chamber depth (cm)	Vertical roof aspect ratio*	Final conditions: Collapse duration (mins)	Central zone long axis (cm)	Central zone short axis (cm)	Central zone aspect ratio	Perpipheral zone long axis (cm)	Peripheral zone short axis (cm)	Peripheral zone aspect ratio	Observations/Remarks
1	Mag Cal 1	1	8.8	6.7	0.76	2	1	0.11	600	7	3	0.43	10.7	9.5	0.89	Asymmetric collapse to SE. Reverse fault trace to SE first, then NW.
2	Mag Cal 2	1.5	8.5	6.6	0.78	1	2	0.24	120	6.5	3	0.46	10.4	10	0.96	Asymmetric collapse to NW. Reverse fault trace to NW, later a suggestion to SE.
3	Mag Cal 3	1.7	8.6	6.1	0.71	1.5	1.5	0.17	890 (165**)	6	2.5	0.42	9.8	8	0.82	Asymmetric collapse to SE. Reverse fault trace to SE.
4	Mag Cal 4	1.6	8.6	6.1	0.71	1	3	0.35	300	6.5	1.8	0.28	11.1	9.3	0.84	Symmetric collapse. Reverse fault traces simultaneously appear to SE and NW.
5	Mag Cal 5	1.7	9	6.5	0.72	1.5	2.5	0.28	420	5.5	2.5	0.45	11	9.5	0.86	Asymmetric collapse to NW. Reverse fault trace to NW first, then very late on to SE.
6	Mag Cal 6	1.5	9.6	6.5	0.68	1.5	1.5	0.16	1100 (140**)	6	3.4	0.57	9.1	8.8	0.97	Asymmetric collapse to NW. Reverse fault trace to NW. No RF to SE
7	Mag Cal 7	4	10	5.7	0.57	1.5	1.5	0.15	600	5	5	1.00	7	6.9	0.99	Asymmetric collapse to NW, Reverse fault trace to NW, none to SE. Difficult to measure caldera geometry.
8	Mag Cal 10	1.7	8.5	6.7	0.79	1.5	1.5	0.18	120	5.7	3.6	0.63	9.2	8.7	0.95	
9	Mag Cal 11	1.5	8.8	6.5	0.74	1.5	1.5	0.17	210	6.2	3.7	0.60	9.8	8.2	0.84	Asymmetric collapse to NW. Reverse fault traces to NW, none to SE.
10	Mag Cal 12	1.7	8.5	6.5	0.76	1	3	0.35	300	5.7	3.4	0.60	9.8	8.7	0.89	Slightly asymmetric collapse to SE. Reverse fault to NW first, then later on to SE.
11	Mag Cal 14	1.4	9.5	8	0.84	1.5	2	0.21	50	7.7	5.5	0.71	10.7	9	0.84	Asymmetric collapse to S. Max subsidence adjacent reactivated regional fault. Reverse fault trace to SE.
12	Mag Cal 16	1.5	9.2	6.8	0.74	1.5	2	0.22	70	6.6	3.4	0.52	9.8	7.3	0.74	Symmetric collapse. No reverse fault traces noted, just sag with marginal reactivation of regional faults.
13	Mag Cal 17	1.5	8.9	6.8	0.76	1.5	2	0.22	70	7	4.1	0.59	10.3	8.7	0.84	
14	Mag Cal 18	1.6	9	7	0.78	2	3	0.33	60	4.3	2.1	0.49	10.2	6.7	0.66	Slightly asymmetric collapse to SE. Reverse faults almost simultaneously to NW and SE.
15	Mag Cal 19	1.6	9.1	6.9	0.76	2	3	0.33	75	4.1	2.8	0.68	10.2	6.5	0.64	Asymmetric collapse to SW. Max subsidence adjacent reactivated regional fault. Reverse fault trace to SE.

* Vertical roof aspect ratio for elliptical honey chambers taken as roof thickness/long axis of honey chamber (cf. Roche et al. 2000)
** Time after which motor was switched off in these experiments

E = East; W = West; N = North; S = South

Table 6.2 Experimental data from experiments simulating **(a)** caldera collapse without regional faulting and **(b)** caldera collapse following regional strike-slip faulting.

Experiment	Syn-collapse regional motion (cm)	Reactivation of pre-collapse regional faults at surface?	Position of reactivated faults (central zone vs. peripheral zone)	Reverse faults arrested at corners cut by regional faults?	Displacement transfer from reverse fault to regional fault?
MagCal 5	0.0	Yes, but subtle. R-shear to SW.	- Outside chamber margin (peripheral fault).	Yes. Reverse fault to NW arrested against Y-shear.	Yes. Marginal ridge to SE bends into Y-shear corner.
MagCal 14	0.0	Yes. R-shears to (1) NE and (2) SW.	- (1) Outside chamber margin (peripheral fault). - (2) Outside chamber margin (peripheral fault).	Yes. Reverse fault to NW and SE arrested against R-shear.	Unclear.
MagCal 16	0.0	Yes. Chamber-localised faults to (1) NW and (2) SE.	- (1) Outside chamber margin (peripheral fault). - (2) Outside chamber margin (peripheral fault).	No reverse faults formed (just sag).	N/A
MagCal 17	0.0	Yes. Chamber-localised faults to (1) NW and (2) SE.	- (1) Outside chamber margin (peripheral fault). - (2) Outside chamber margin (peripheral fault).	No. No corners.	N/A
MagCal 18	0.0	Yes. Chamber-localised fault to SW.	- Inside chamber margin (central caldera fault?).	Unclear as cross-sectioned, not excavated.	N/A
MagCal 19	0.0	Yes. Chamber-localised faults to (1) NE and (2) SW.	- (1) Outside chamber margin (peripheral fault). - (2) Outside chamber margin (peripheral fault).	Unclear as cross-sectioned, not excavated.	N/A
MagCal 2	< 0.1	Yes. (1) Chamber-localised graben fault to NE and (2) R-shear to SW.	- (1) Outside chamber margin (peripheral fault). - (2) Inside chamber margin (central caldera fault?)	Yes. Reverse fault to SE arrested against Y- & R-shears	Yes. Marginal ridge to SE on chamber bends sharply into Y-shear corner.
MagCal 3	< 0.1	Yes. (1) Chamber-localised graben fault to NE and (2) R-shear to SW. Note: most re-activation after motor stopped.	- (1) Outside chamber margin (peripheral fault). - (2) Inside chamber margin (central caldera fault).	No. No corners cut.	No.

Table 6.3 Summary of observations on regional-tectonic and volcano-tectonic fault interactions during caldera collapse. Syn-collapse regional motion values were measured not estimated.

7 Summary of Thesis and Outlook

7.1 Summary of main conclusions

To more accurately assess the eruptive threat and economic potential presented by caldera volcanoes, we must better understand the initiation, development, and interrelation of caldera-related structures. The results of the experimental series described in this thesis offer several new insights into the development of caldera structures under a variety of initial conditions related to magma chamber geometry and regional tectonic regime.

7.1.1 The generalized kinematic evolution and geometry of caldera collapse structures

From the experimental results reported in **Chapter 2**, four general and interlinked themes in the structural evolution of calderas are further developed. The first concerns the perceived ‘space problem’ of caldera subsidence, which links to the question of how caldera collapse is structurally accommodated. Documented here from experiment are structures resolving not only the radial component of collapse-related strain (concentric reverse faults, concentric normal faults), but also those accommodating the hitherto-neglected concentric component (radial wrinkle ridges, obliquely trending reverse faults, strike-slip faults and oblique-normal faults). These experimental structures define a three-fold (rather than two-fold) zonation of calderas in plan-view. Evidence for a similar plan-view zonation in nature is provided from observations at Olympus Mons caldera, Mars. Combined with a re-interpretation of previous numerical observations, the results of this study lead to the prediction that the structures identified to accommodate concentric shortening may be more widespread in nature than previously recognized.

The second theme concerns the role of the magma chamber roof’s thickness/diameter ratio in governing the style of deformation. This is further illustrated via the relative development of different structures accommodating both radial and concentric strain components in the models. Overall, deformation of thinner roofs is more ductile (distributed); deformation of thicker roofs is more brittle (localised). With thin chamber roofs (i.e. relatively low thickness/diameter ratios), ductile sagging accommodates a more substantial proportion of model subsidence, and hence more of the required radial shortening, than brittle reverse faulting. With thinner roofs, structures such as radially-trending wrinkle ridges and sub-concentrically-trending strike-slip faults are more prominent and so accommodate more of the concentric shortening; with thicker roofs, concentric shortening is partitioned (localised) outward from the caldera centre and predominantly taken up along obliquely-trending oblique-reverse faults.

The main reverse and normal faults accommodating caldera collapse are also shown to comprise a geometrically coherent system. The models here also indicate that strong variations on the exact geometry and kinematics of these faults may occur with asymmetric subsidence.

Observations in this study also indicate that the reverse ring faults propagate very rapidly upward and normal ring faults propagate downward, as inferred by previous workers, but that the displacement profiles seen on the faults may not always directly reflect their propagation. Instead, the maintenance of geometric coherence as the fault systems evolve may regulate the accumulation of displacement along them.

This study shows that the polygonal geometry of calderas noted by previous workers is seen regardless of exposure level or scale, but also reveals how faulting and land-sliding may act in concert to produce a caldera with a polygonal outline.

The combination of complex extensional faulting in the caldera periphery, plus the formation of multiple reverse faults with relatively thick reservoir roofs, may to a large extent account for piecemeal-like subsidence observed in nature.

7.1.2 A revised view of the caldera collapse continuum

Five end-member styles of caldera subsidence have been previously proposed, each with characteristic structural elements and architectures. A continuum between these collapse end-members has been postulated, but not clearly defined. To shed light on this concept, the results of new and recent physical models of caldera subsidence firstly synthesized in **Chapter 3**. These results are then compared in detail with evidence from well-studied natural calderas and with recent numerical models of caldera subsidence. It is thereby shown that the structural elements characteristic of all five end-member collapse styles may progressively accumulate through overlapping and inter-gradational phases of a single caldera collapse event. It is also illustrated, however, that the relative development of each end-member's structural elements strongly depends on the initial thickness/diameter ratio of the magma chamber roof and on the final subsidence/diameter ratio of the caldera. The postulated continuum between all five idealised end-member caldera collapse styles thus primarily reflects the progressive development of subsidence structures in a way that is regulated by initial depth/diameter ratio and final subsidence/diameter ratio.

7.1.3 The role of elliptical magma chamber geometry in the kinematic evolution and geometry of caldera collapse structures

Experiments detailed in **Chapter 4** demonstrate that the structural development of caldera subsidence into a magma chamber of elliptical outline is inherently more systematic, and hence potentially more predictable, than collapse into circular magma chambers of similar plan view area. Failure during elliptical collapse consistently occurs along reverse faults that first localise near the ends of an elliptical roof's short axis, where shear strain maximises at the onset of reservoir depressurisation and down-warping of the reservoir roof. The experiments also reveal a potential continuum of lateral propagation ('unzipping') patterns for reverse faults during elliptical caldera collapse. This continuum is bound by end-member patterns characteristic of circular (A/B = 1.0) and highly elliptical (A/B = 2.0) plan-view reservoir geometries, with more variable unzipping patterns for intermediate ellipticities (A/B = 1.33 – 1.5). The variation in unzipping patterns with increasing roof ellipticity is related to increased disparity in shear strain around the down-warped elliptical roof as roof ellipticity increases.

In nature, similar patterns of fault initiation and lateral propagation are observed or inferred at several elliptical calderas and at intermediate-scale analogues, such as hydrocarbon reservoirs. The long-enigmatic pattern of ring fracture 'unzipping' inferred at the highly-elliptical Long Valley caldera matches that observed in experimental collapse of roofs with A/B = 2.0. 'Unzipping' at Long Valley is thus explained as a direct consequence of the highly elliptical plan-view shape of the pre-collapse magma chamber roof. Vent positions, vent migration patterns, and reactivations of ring faults at several other elliptical calderas of various dimensions are also consistent with a control from elliptical reservoir geometry. The plan-view ellipticity of a magma chamber roof may thus decisively influence the dynamics of caldera-related faulting and eruption at all scales, and in any volcano-tectonic regime (tumescence, collapse or resurgence).

Geometries of fault systems resulting from caldera collapse into elliptical reservoirs in experiment have been documented in detail and in 3D. Subsidence-controlling reverse faults generally have shallower (~60-70°) outward dips along the short axis of the magma chamber roof, than along the long axis (~70-80°). In addition, peripheral extension penetrates further outward from the reservoir margin and to a deeper level from the surface along the short axis of an elliptical caldera than along the long axis. This is manifested as greater intensity and better development of crevasse, normal faults, and gräben around the ends of the elliptical caldera's short axis. This circumferential variation in the 3D geometry of elliptical caldera faulting is tentatively related to a circumferential variation in the components of horizontal contraction and vertical shear along the edge of an elliptical reservoir during subsidence, with greatest horizontal contraction occurring along the roof's short axis.

This 3D fault architecture reflects a consistent geometric relationship between the limits of the zones of peripheral extension and central contraction at the surface and the outline of the reservoir at depth. The limit of peripheral extension is characteristically less elliptical than the underlying reservoir, whereas the limit of the central zone is typically more elliptical than the reservoir. The model characteristics closely match surface geometric attributes of several calderas in nature, and hence allow the estimation of pre-collapse magma chamber limits and caldera fault geometries at depth.

7.1.4 Influence of regional tectonics on the evolution of caldera structures

Experiments of with two different set-ups investigated the possible influences on the formation of collapse calderas of stresses and structures generated in two different regional tectonic regimes. Rigid-rimmed circular balloons were deflated under orthogonal regional extension and compression (**Chapter 5**), whilst viscous honey chambers were deformed and then evacuated in strike-slip to transtensive tectonics regimes (**Chapter 6**). Results of these experimental sets show some differences relatable to tectonic regime and methodology, but also some commonalities that may be related to general influences of regional tectonics on caldera collapse.

The experiments with balloons indicate that 'distortion' of caldera ring faults may occur through the interaction of regional and local stress fields. This interaction may result in elongation of the caldera in the direction of the regional field's least horizontal compressive stress (ShMin), a frequently observed feature of calderas formed in active tectonic regimes.

The experiments with honey chambers did not allow evaluation of the interaction of regional and local stresses, but instead permitted assessment of the effect on caldera collapse of regional faults delimiting the edge of a magma reservoir. These experiments show that, where regional-tectonic strike-slip faults define corners in the magma chamber margin, they may halt the propagation of volcano-tectonic reverse faults.

Results of both experiment sets experiments show that whilst the magma chamber shape principally influences the development and geometry of volcano-tectonic collapse structures, reactivation of the pre-existing fault systems associated with the regional stress field is a major factor in caldera formation in active tectonic regimes. Some reactivations of regional faults took place within the central zone, but most occurred at the edges of the magma reservoir. Indeed, the experiments indicate on the whole that regional faults may preferentially reactivate where tangential to the collapse area and coincident with the chamber margins. In this case, volcano-tectonic extension in the caldera periphery tends to localise on regional-tectonic faults that lie just outside the chamber margins. In addition, volcano-tectonic reverse faults may link with and reactivate pre-collapse regional-tectonic faults that lie just inside the chamber margins. Truncation and 'capture' of caldera-related peripheral faulting by regional faults can lead to enhancement of the caldera's polygonal morphological expression.

The experiments also highlight the potential difficulties in assessing the relative contributions of volcano-tectonic and regional-tectonic subsidence processes to the final caldera structure seen in the field. Experiments with balloons sometimes showed syn-collapse along pre-existing regional faults. In experiments with honey reservoirs, however, pre-collapse disruption of the caldera floor by regional-tectonic faulting was preserved during coherent volcano-tectonic subsidence to produce a caldera floor of differentially subsided fault blocks. Although the latter result may in part relate to experimental conditions, it merits a cautionary note that without definitive evidence for syn-eruptive growth faulting (as seen at Scafell and Glencoe calderas), thickness changes in caldera fill across such regional-tectonic fault blocks in nature could be mistaken as evidence for piecemeal volcano-tectonic collapse.

7.2 Suggestions for further work

7.2.1 Simulation of caldera formation above elliptical reservoirs with Discrete Element Method software

As shown in this study (and others), physical models can broadly reproduce the structural evolution and final architecture of many calderas. However, even the most carefully scaled models are limited by inaccuracies inherent in the approach - e.g. using essentially non-cohesive granular material to model more rheologically complex solid rock - and so they can offer limited quantitative insight into the exact stress and strain conditions leading to initial reservoir roof failure in nature.

Numerical studies promise to solve this problem by accurately modelling rock rheology. Numerical simulations to date have mostly comprised Boundary Element Models (e.g. Gudmundsson 1998) or Finite Element Models, (e.g. Folch and Marti 2004). These considered the Earth's crust to be an isotropic elastic continuum, in which a magma reservoir was modelled as an over-pressured (inflating), or more realistically for the onset of caldera collapse, an under-pressured (deflating) fluid-filled hole. As faults represent discontinuities, however, it is difficult or impossible to accurately simulate their development in such continuum-based numerical models. These models are typically valid only until the point of fracture, beyond which they can only estimate the initial geometry and mode of caldera faults from calculated stress patterns. Rare numerical models that have produced fractures (Burov and Guillou-Frotier 1999) applied geologically unrealistic boundary conditions or physical mechanisms (e.g. reservoir overpressure). Some analytical studies (e.g. Roche and Druitt 2001) used predefined fault geometries, but this ignores how faults initiate and develop in the first place.

Discrete Element Method (DEM) modelling is a branch of numerical modelling that simulates the deformation of an assemblage of discrete particles interacting with each other according to elastic-frictional contact laws (see Potyondy and Cundall 2004). DEM was first applied to study small-scale processes in rock mechanics in the 1970s. As it is computationally intensive, however, DEM's application to large-scale structural processes, such as accretionary wedge development, basement fault reactivation, and volcanic edifice instability, has had to await recent advances in computer technology. The principle advantage of DEM is that it can not only accurately model the localisation and growth of discontinuities like faults (the strength of previous physical models), but it can also precisely calculate displacements, stresses, and bulk strains in the model based on realistic rock properties (the strength of previous numerical models). The use of DEM to numerically evaluate aspects of the geometry and kinematics of caldera collapse is thus strongly recommended.

7.2.2 Constraining the critical volumetric fraction of magma required to initiate complete failure of elliptical magma chamber roofs

Systematic experimental evaluation and numerical modeling of the critical volumetric fraction of magma required to initiate complete failure of magma chamber roofs of varying plan-view ellipticities, but constant areas, is recommended. Calculations of Roche and Druitt (2001) indicate that elliptical reservoirs may be less stable than the circular plan-view geometries used in most numerical simulations to date (e.g. Gudmundsson 1998; Folch and Marti 2004). Recent experimental work by Geyer et al. has shown that analogue experiments can provide a first-order evaluation of critical volume fractions require to cause circular magma chamber roof failure. A similar study could readily be extended to elliptical reservoirs, and followed up with more quantitative analysis with DEM models. These data could cross check against, and perhaps experimentally constrain, the predictions based on calculations of Roche and Druitt (2001). Such simulations should also test the effect of increased roof thickness, as patterns of elliptical failure and fault propagation were identified as sensitive to roof thickness in this study.

7.2.3 Influence of loading variation induced by high topographic relief

Experiments here simulated a simplified planar or low-relief land surface. Experiments with circular balloons by Lavallée et al. (2004) and Belousov et al. (2004) indicate that pre-collapse topography may play an important role in the development of caldera faults. Numerical evaluation of this factor in caldera collapse into a wider range of magma chamber geometries could be undertaken with DEM models. These models could also investigate the influence of loading variation induced by a conical volcanic, as attempted analytically by Pinel and Jaupart (2005).

7.2.4 Influence of vent position on the evolution of caldera collapse

The experimental results here also indicate that vent position may be important in caldera collapse. Field evidence for a control in nature is ambiguous, however, and previously experimental or numerical studies have not tested this factor. There may also be a complex interplay in nature between initial conduit position, initial roof loading conditions, ellipticity of the reservoir roof, fault propagation, and the opening of new conduits. Further numerical and analogue study of such complex interactions may be a fruitful path for further research.

7.2.5 Regional tectonic influences on caldera formation

Further numerical testing of the influence on caldera formation of interacting local and regional stress fields and of pre-existing regional-tectonic faults is recommended. Again these factors may be readily tested with DEM models.

7.2.6 Physical and numerical modeling of elliptical tumescence and resurgence

As discussed in **Chapter 4**, the mechanics postulated to govern the initiation and propagation of faulting at above elliptical magma reservoirs during collapse should also apply to rocks above elliptical reservoirs during inflation or resurgence. Further work to physically and numerically model elliptical tumescence and resurgence on caldera structures is thus most strongly recommended, in part because it may have the most direct bearing on hazard assessment at elliptical calderas and magmatic centers Most eruptions do not lead to caldera collapse, but many (e.g. the 1994 eruption at Rabaul - Saunders (2001)) are preceded by uplift.

7.2.7 New constraints from geophysical, geodetic, and field studies

The above suggestions for future work all involve further modelling of aspects of caldera collapse and resurgence. The formulation of all models and analysis of their results, however, is inherently dependent on the current state of knowledge of the modelled process in nature, as constrained indirectly by geophysical and geodetic means, and directly by field observations. Observations of a natural process and modelling of that process should ideally proceed in tandem, such that a positive feedback of insight into the natural process is achieved from one approach to the other.

Existing geophysical, geodetic, and field observations of collapse calderas were drawn upon heavily in this study, both in order to find a context for model observations in nature and to find a context for natural observations in the models. The models in turn provide several predictions for the geometry and development of caldera structures, for instance with regard to the accommodation of circumferential shortening during collapse, the kinematics and structural geometry of elliptical calderas, and the influence of regional stresses and structures on caldera collapse. The validity of these predictions for caldera collapse in nature, as well as the results of any future corollary modelling work along the lines suggested in this chapter, should therefore be rigorously tested through further geophysical and geodetic studies, and perhaps most importantly, through detailed field observations at suitably exposed calderas.

8 References

Acocella, V., Salvini F., Funiciello, R. & Faccenna, C. 1999. The role of transfer structures on volcanic activity at Campi Flegrei (Southern Italy). *Journal of Volcanology and Geothermal Research*, **91**, 123–139.

Acocella, V. & Funiciello, R. 1999. The interaction between regional and local tectonics during resurgent doming; the case of the island of Ischia, Italy. *Journal of Volcanology and Geothermal Research*, **88**, 109-123.

Acocella, V., Cifelli, F. & Funiciello, R. 2000. Analogue models of collapse calderas and resurgent domes. *Journal of Volcanology and Geothermal Research*, **104**, 81–96.

Acocella, V., Cifelli, F. & Funiciello, R. 2001. Formation and architecture of nested collapse calderas: insights from analogue models. *Terra Nova*, **13**, 58-63.

Acocella, V., Korme, T., Salvini, F. & Funiciello, R. 2003. Elliptic calderas in the Ethiopian Rift: control of pre-existing structures. *Journal of Volcanology and Geothermal Research*, **119**, 189-203.

Acocella, V., Spinks, K., Cole, J.W. & Nicol, A., 2003. Oblique back-arc rifting of Taupo Volcanic Zone, New Zealand. *Tectonics*, **22**, 1045.

Acocella, V., Funiciello, R., Marotta, E., Orsi, G. & de Vita, S. 2004. The role of extensional structures on experimental calderas and resurgence. *Journal of Volcanology and Geothermal Research*, **129**, 199-217.

Acocella, V. 2006. Caldera types; how end-members relate to evolutionary stages of collapse. *Geophysical Research Letters*, **33**, L18314, doi:10.1029/2006GL027434.

Adam, J., Urai, J.L., Wieneke, B., Oncken, O., Pfeiffer, K., Kukowski, N., Lohrmann, J., Hoth, S., van der Zee, W. & Schmatz, J. 2005. Shear localisation and strain distribution during tectonic faulting; new insights from granular-flow experiments and high-resolution optical image correlation techniques. *Journal of Structural Geology*, **27(2)**, 283-301.

Aldiss, D.T. & Ghazali, S.A. 1984. The regional geology and evolution of the Toba volcano-tectonic depression, Indonesia. *Journal of the Geological Society of London*, **141**, 487-500.

Aldrich, M.J., Chapin, C.E. & Laughlin, A.W. 1986. Stress history and tectonic development of the Rio Grande Rift, New Mexico. *Journal of Geophysical Research,* **91B**, 6199-6211.

Allen, D.R. 1968. Physical changes of reservoir properties caused by subsidence and repressuring operations. *Journal of Petroleum Technology,* **20**, 23-29.

Almond, D.C. 1977. The Sabaloka igneous complex, Sudan. *Philosophical Transactions of the Royal Society of London*, **273**, 595-635.

Amelung, F., Jonsson, S., Zebker H. & Segall, P. 2000. Widespread uplift and “trapdoor” faulting on Galápagos volcanoes observed with radar interferometry. *Nature,* 407, 993–998.

Anderson, E.M. 1936. The dynamics of the formation of cone sheets, ring dikes, and cauldron subsidences. *Proceedings of the Royal Society of Edinburgh*, **56**, 128-163.

Anderson E.M. 1951. *The dynamics of faulting and dyke formation, with applications to Britain,* 2nd Ed. Edinburgh: Oliver & Boyd, 206 pp.

Anderson, A.T., Davis, A.M. & Lu, F. 2000. Evolution of Bishop Tuff rhyolitic magma based on melt and magnetite inclusions, and zoned phenocrysts. *Journal of Petrology*, **41**, 449–473.

Aramaki, S. 1984. Formation of the Aira caldera, southern Kyushu, ~22,000 years ago. *Journal of Geophysical Research*, **89**, 8485-8501.

Basile, C. & Brun, J.P. 1999. Transtensional faulting patterns ranging from pull-apart basins to transform continental margins: an experimental investigation. *Journal of Structural Geology*, **21**, 23-37.

Bellier, O. & Sebrier, M. 1994. Relationship between tectonism and volcanism along the Great Sumatran fault zone deduced by SPOT image analyses. *Tectonophysics*, **233**, 215-231.

Bellier, O., Bellon, H., Sébrier, M., Sutanto & Maury, R.C. 1999. K–Ar age of the Ranau Tuffs: implications for the Ranau caldera emplacement and slip-partitioning in Sumatra (Indonesia). *Tectonophysics*, **312**, 347-359.

Belousov, A., Walter, T.R. & Troll, V.R. 2005. Large scale failures on domes and stratocones situated on caldera ring-faults: sand-box modelling of natural examples from Kamchatka, Russia. *Bulletin of Volcanology*, **67**, 457-468.

Benn, K., Odonne, F. & de Saint Blanquat, M. 1998. Pluton emplacement during transpression in brittle crust; new views from analogue experiments. *Geology*, **26**, 1079-1082.

Bianco, F., Castellano, M., Milano, G., Ventura, G. & Vilardo, G. 1998. The Somma-Vesuvius stress field induced by regional tectonics: evidences from seismological and mesostructural data. *Journal of Volcanology and Geothermal Research*, **82**, 199-218.

Bindeman, I.N., 2006. The secrets of supervolcanoes: Scientific American (June issue), 38-43.

Bosworth, W., Burke, K. & Strecker, M. 2000. Magma chamber elongation as an indicator of intraplate stress field orientation: "borehole break-out mechanism" and examples from the Late Pleistocene to Recent Kenya Rift Valley. *Journal of the Virtual Explorer* (Online - http://virtualexplorer.com.au), **2**.

Bosworth, W., Burke, K. & Strecker, M. 2003. Effect of stress fields on magma chamber stability and the formation of collapse calderas. *Tectonics*, **22**, 1042.

Branney, M.J. & Kokelaar, P. 1994. Volcanotectonic faulting, soft-state deformation, and rheomorphism of tuffs during development of a piecemeal caldera, English Lake District. *Geological Society of America Bulletin*, **106**, 507-530.

Branney, M.J. 1995. Downsag and extension at calderas: new perspectives on collapse geometries from ice-melt, mining, and volcanic subsidence. *Bulletin of Volcanology*, **57**, 303-318.

Burov, E.B. & Guillou-Frottier, L. 1999. Thermomechanical behaviour of large ash flow calderas. *Journal of Geophysical Research*, **104**, 23,081–23,109.

Cailleau, B., Walter, T.R., Janle, P. & Hauber, E. 2003. Modeling volcanic deformation in a regional stress field: Implications for the formation of graben structures on Alba Patera, Mars. *Journal of Geophysical Research*, **108**, 5141.

Carr, W.J. & Quinlivan, W.D. 1968. Structure of Timber Mountain resurgent dome, Nevada Test Site. *Memoir of the Geological Society of America*, **110**, 99-108.

Chesner, C.A. 1998. Petrogenesis of the Toba Tuffs, Sumatra, Indonesia. *Journal of Petrology*, **39**, 397-438.

Cole, J.W., Brown, S.J.A., Burt, R.M., Beresford, S.W. & Wilson, C.J.N., 1998. Lithic types in ignimbrites as a guide to the evolution of a caldera complex, Taupo volcanic centre, New Zealand. *Journal of Volcanology and Geothermal Research*, **80**, 217-237.

Cole, J.W., Milner, D.M. & Spinks, K.D. 2005. Calderas and caldera structures: a review. *Earth Science Reviews*, **69**, 1-26.

Corti, G., Bonini, M., Innocenti, F., Manetti, P. & Mulugeta, G. 2001. Centrifuge models simulating magma emplacement during oblique rifting. *Journal of Geodynamics*, **31**, 557-576.

Corti, G., Moratti, G. & Sani, F. 2005. Relations between surface faulting and granite intrusions in analogue models of strike-slip deformation. *Journal of Structural Geology*, **27**, 1547–1562.

Cruden, A.R. 1998. On the emplacement of tabular granites. *Journal of the Geological Society of London*, **155**, 853-862.

Crumpler, L.S., Head, J.W. & Aubele, J.C. 1996. Calderas on Mars: characteristics, structure, and associated flank deformation. *Geological Society of London Special Publication*, **110**, 307-348.

Crumpler, L.S. & Aubele, J.C. 2000. Volcanism on Venus, in: Sigurdsson, H., Houghton, B.F., McNutt, S.R., Rymer, H. & Stix, J. (Eds.), Encyclopedia of Volcanoes, pp. 727-769. San Diego: Academic Press.

Deplus, C., Bonvalot, S., Dahrin, D., Diament, M., Harjono, H. & Dubois, J. 1995. Inner structure of the Krakatau volcanic complex (Indonesia) from gravity and bathymetry data. *Journal of Volcanology and Geothermal Research*, **64**, 23-52.

Dingwell, D.B. 1999. Granitic melt viscosities. *Geological Society of London Special Publications*, **168**, 27-38.

Donnadieu, F. & Merle, O. 1998. Experiments on the indentation process during cryptodome intrusions; new insights into Mount St. Helens deformation. *Geology*, **26**, 79-82.

Dooley, T. & McClay, K. 1997. Analog modeling of pull-apart basins. *Bulletin of the American Association of Petroleum Geologists*, **81**, 1804-1826.

Druitt, T.H. & Sparks, R.S.J. 1984. On the formation of calderas during ignimbrite eruptions. *Nature*, **310**, 679-681.

Emeleus, C.H., Wadsworth, W.J. & Smith, N.J. 1985. The early igneous and tectonic history of the Rhun Tertiary Volcanic Centre. *Geological Magazine,* **122***,* 451-457.

Emeleus, C.H. 1997. Geology of Rum and the adjacent islands. *Memoir of the British Geological Survey of Scotland*, Sheet 60.

Finlayson, D.M., Gudmundsson, O., Itikarai, I., Nishimura, Y. & Shimamura, H. 2003. Rabaul Volcano, Papua New Guinea; seismic tomographic imaging of an active caldera. *Journal of Volcanology and Geothermal Research*, **124**, 153-171.

Folch, A & Marti, J. 2004 Geometrical and mechanical constraints on the formation of ring-fault calderas. *Earth and Planetary Science Letters*, **221**, 215-225.

Fouqué, F. 1879. *Santorin et ses eruptions*. Paris Masson et cie, 1-440 pp.

Francis, P.W., Hammill, M., Kretzschmar, G. & Thorpe, R. 1978. The Cerro Galan Caldera, North-west Argentina and its tectonic setting. *Nature*, **274**, 749-751.

Francis, P.W., 1993 *Volcanoes: a planetary perspective*, pp. 525, Oxford, Clarendon Press

Freundt, A., Wilson, C.J.N. & Carey, S.N. 2000. Ignimbrites and Block-and-Ash Flow Deposits. In: Sigurdsson, H., Houghton, B.F., McNutt, S.R., Rymer H. & Stix, J. (Eds.), *Encyclopedia of Volcanoes*, pp. 595. San Diego: Academic Press.

Fridrich, C.J., Smith, R.P., DeWitte, E. & McKee, E.H. 1991. Structural, eruptive, and intrusive history of the Grizzly Peak caldera, Sawatch range, Colorado. *Geological Society of America Bulletin*, **103**, 1160-1177.

Friedman, M., Handin, J., Logan, J.M., Min, K.D. & Stearns, D. 1976. Experimental folding of rocks under confining pressure; Part III, Faulted drape folds in multilithologic layered specimens. *Geological Society of America Bulletin*, **87**, 1049 - 1066.

Gambolati, G., Sartoretto, F., Rinaldo, A. & Ricceri, G. 1987. A boundary element solution to land subsidence above 3-D gas/oil reservoirs. *International Journal for Numerical and Analytical Methods in Geomechanics*, **11,** 489-502.

Geist, D., Howard, K. A., Jellinek, A. M. & Rayder, S. 1994. The volcanic history of Volcán Alcedo, Galápagos Archipelago: A case study of rhyolitic oceanic volcanism. *Bulletin of Volcanology*, **86**, 243–260.

Geist, D., Chadwick, W. & Johnson, D. 2006. Results from new GPS and gravity monitoring networks at Fernandina and Sierra Negra Volcanoes, Galápagos, 2000–2002. *Journal of Volcanology and Geothermal Research*, **150**, 79-97.

Geshi, N., Shimano, T., Chiba, T. & Nakada, S. 2002. Caldera collapse during the 2000 eruption of Miyakejima Volcano, Japan. *Bulletin of Volcanology*, **64**, 55-68.

Geyer, A., Folch, A. & Marrti, J. 2006. Relationship between caldera collapse and magma chamber withdrawal; an experimental approach. *Journal of Volcanology and Geothermal Research*, **157**, 375-386.

Girard, G. & van Wyk de Vries, B. 2005. The Managua Graben and Las Sierras-Masaya volcanic complex (Nicaragua); pull-apart localisation by an intrusive complex: results from analogue modelling. *Journal of Volcanology and Geothermal Research*, **144**, 37-57.

Goff, F. & Gardner, J.N. 1994. Evolution of a mineralized geothermal system, Valles Caldera, New Mexico. *Economic Geology*, **89**, 1803-1832.

Goodman, R.E. 1989. *Introduction to rock mechanics*. New York: John Wiley and Sons.

Gudmundsson, A. 1988. Formation of collapse calderas. *Geology*, **16**, 808-810.

Gudmundsson, A. 1998. Formation and development of normal-fault calderas and the initiation of large explosive eruptions. *Bulletin of Volcanology*, **60**, 160-170.

Gudmundsson, A., Marti, J. & Turon, E. 1997. Stress fields generating ring faults in volcanoes. *Geophysical Research Letters*, **24**, 1559-1562.

Guest, J.E., Gaspar, J.L., Cole, P.D., Queiroz, G., Duncan, A.M., Wallenstein, N., Ferreira, T. & Pacheco, J.M. 1999. Volcanic geology of Furnas Volcano, São Miguel, Azores. *Journal of Volcanology and Geothermal Research*, **92**, 1-29.

Hallinan, S. 1993 Nonchaotic collapse at funnel calderas; gravity study of the ring fractures at Guayabo Caldera, Costa Rica , *Geology*, **21**, 367-370.

Hickman, R.G., Dobson, P.F., van Gerven, M., Sagala, B.D. & Gunderson, R.P. 2004. Tectonic and stratigraphic evolution of the Sarulla graben geothermal area, North Sumatra, Indonesia. *Journal of Asian Earth Sciences*, **23**, 435-448.

Hildreth, W. & Mahood, G.A. 1986. Ring-fracture eruption of the Bishop Tuff. *Geological Society of America Bulletin*, **97**, 396-403.

Hildreth, W. & Fierstein, J. 2000. Katmai volcanic cluster and the great eruption 1912. *Geological Society of America Bulletin*, **112**, 1594-1620

Hildreth, W., and Wilson C.J.N., 2007, Compositional zoning of the Bishop Tuff: *Journal of Petrology*, **48**, 951-999.

Holohan, E.P., Troll, V.R., Walter, T.R., Münn, S., McDonnell, S. & Shipton, Z.K. 2005. Elliptical calderas in active tectonic settings: an experimental approach. *Journal of Volcanology and Geothermal Research*, **144**, 119-136.

Holohan, E. Troll, V. Acocella, V. & Walter T., 2006. A reappraisal of the caldera structural continuum; insights into super-volcano formation from field studies and analogue experiments, *Eos, Transactions, American Geophysical Union*, **87** (2006 Fall Meeting)

Holohan, E.P., van Wyk de Vries, B. & Troll, V.R. Analogue models of caldera collapse in strike-slip tectonic regimes, *Bulletin of Volcanology, in press*.

Hon, K.A. 1987. Geologic and petrologic evolution of the Lake City caldera, San Juan Mountains, Colorado. PhD thesis, University of Colorado.

Horsfield, W. 1977. An experimental approach to basement-controlled faulting. *Geologie en Mijnbouw,* **56**, 363-370.

Howells, M.F., Reedman, A. J., & Campbell, S. D. G. 1986. The submarine eruption and emplacement of the Lower Rhyolitic Tuff Formation (Ordovician), N Wales. *Journal of the Geological Society*, **143**, 411-423.

Hubbert, M.K. 1951. Mechanical basis for certain familiar geologic structures. *Geological Society of America Bulletin*, **62**, 355-372.

Hutton, D.H.W. & Reavy, R.J. 1992. Strike-slip tectonics and granite petrogenesis. *Tectonics*, **11**, 960-967.

Jacques, J.M. & Reavy, R.J. 1994. Caledonian plutonism and major lineaments in the SW Scottish Highlands. *Journal of the Geological Society of London*, **151**, 955-969.

Jellinek, A.M. & DePaolo, D.J. 2003. A model for the origin of large silicic magma chambers: precursors of caldera-forming eruptions. *Bulletin of Volcanology*, **65**, 363-381.

John, D.A. 1995. Tilted middle Tertiary ash-flow calderas and subjacent granitic plutons, southern Stillwater Range, Nevada; cross sections of an Oligocene igneous center. *Geological Society of America Bulletin*, **107**, 180-200.

Johnson, R.W. 1969. Volcanic Geology of Mount Suswa, Kenya. *Philosophical Transactions of the Royal Society of London, Series A: Mathematical and Physical Sciences*, **265**, 383-412.

Jones, M.E., Leddra, J., & Potts, D. 1990. Ground motions due to hydrocarbon production from chalk: Chalk, Thomas Telford, London.

Jones, R.H. & Stewart, R.C. 1997. A method for determining significant structures in a cloud of earthquakes. *Journal of Geophysical Research*, **102**, 8245-8254.

Jónsson, S., Zebker, H. & Amelung, F. 2005. On trapdoor faulting at Sierra Negra volcano, Galápagos. *Journal of Volcanology and Geothermal Research*, **144,** 59-71.

Kennedy, B. & Stix, J. 2003. Igneous rock associations 1: Styles and mechanisms of caldera collapse. *Geoscience Canada*, **30**, 59-72.

Kennedy, B., Stix, J., Vallance, J.W., Lavallée, Y. & Longpré, M.-A. 2004. Controls on caldera structure: Results from analogue sandbox modeling. *Geological Society of America Bulletin*, **116**, 515–524.

Kokelaar, P. & Moore, I. 2006. Classical Areas of British Geology: Glencoe caldera volcano, Scotland. *British Geological Survey Memoir*.

Komuro, H., Fujita, Y. & Kodama, K., 1984. Numerical and experimental models on the formation mechanism of collapse basins during Green Tuff orogenesis of Japan. *Bulletin of Volcanology*, **47**, 649-666.

Komuro, H. 1987. Experiments on cauldron formation: a polygonal cauldron and ring fractures. *Journal of Volcanology and Geothermal Research*, **31**, 139-149.

Kovach, R.L. 1974. Source mechanisms for Wilmington Oil Field, California, subsidence earthquakes. *Bulletin of the Seismological Society of America*, **64**, 699-711.

Krantz, R.W. 1995. The transpressional strain model applied to strike-slip, oblique-convergent and oblique-divergent deformation. *Journal of Structural Geology*, **17**, 1125-1137.

Lavallée, Y., Stix, J., Kennedy, B., Richer, M. & Longpré, M.-A. 2004. Caldera subsidence in areas of variable topographic relief: results from analogue modelling. *Journal of Volcanology and Geothermal Research*, **129**, 219-236.

Lécuyer, F., Bellier, O., Gourgaud. A. & Vincent, P.M. 1997. Tectonique active du Nord-Est de Sulawesi (Indonésie) et contrôle structural de la caldeira de Tondano. *Comptes rendus de l'Académie des sciences. Série 2. Sciences de la terre et des planets*, **325**, 607–613.

Legros, F., Kelfoun, K. & Martí, J. 2000. The influence of conduit geometry on the dynamics of caldera-forming eruptions. *Earth and Planetary Science Letters*, **179**, 53-61.

Lipman, P.W. 1984. The roots of ash flow calderas in western North America; windows into the tops of granitic batholiths. *Journal of Geophysical Research*, **89B**, 8801-8841.

Lipman, P.W. 1997. Subsidence of ash-flow calderas; relation to caldera size and magma-chamber geometry. *Bulletin of Volcanology*, **59**, 198-218

Lipman, P.W. 2000. Calderas. In: Sigurdsson, H., Houghton, B.F., McNutt, S.R., Rymer H. & Stix, J. (Eds.), *Encyclopedia of Volcanoes*, pp. 643-662. San Diego: Academic Press.

Longpré, M.-A., Staudacher, T. and Stix J. The November 2002 eruption at Piton de la Fournaise volcano, La Réunion Island: ground deformation, seismicity, and pit crater collapse. *Bulletin of Volcanology*, (in press).

Lopes-Gautier, R. 2000. Volcanism on Io. In: Sigurdsson, H., Houghton, B.F., McNutt, S.R., Rymer H. & Stix, J. (Eds.), *Encyclopedia of Volcanoes*, pp. 709-726. San Diego: Academic Press.

Mandl, G. 1987. Tectonic deformation by rotating parallel faults: the bookshelf mechanism. *Tectonophysics*, **141**, 277-316.

Mandl, G. 1988. Mechanics of Tectonic Faulting: models and basic concepts. Zwart H.J. (Ed.), 407 pp. Amsterdam, Netherlands: Elsevier Science Publishing.

Marrett, R.A., Allmendinger, R.W., Alonso, R.N. & Drake, R.E. 1994. Late Cenozoic tectonic evolution of the Puna Plateau and adjacent foreland, NW Argentine Andes. *Journal of South American Earth Sciences*, **7**, 179-207.

Marti, J., Ablay, G.J., Redshaw, L.T. & Sparks, R.S.J. 1994. Experimental studies of collapse calderas. *Journal of the Geological Society of London*, **151**, 919-929.

Marti, J., Folch, A., Neri, A. & Macedonio, G. 2000. Pressure evolution during explosive caldera-forming eruptions. *Earth and Planetary Science Letters*, **175**, 275–287.

Mason, B.G., Pyle, D.M. & Oppenheimer, C. 2004. The size and frequency of the largest explosive eruptions on Earth. *Bulletin of Volcanology*, **66**, 735-748.

McBirney, A.R. 1990. An historical note on the origin of calderas. *Journal of Volcanology and Geothermal Research*, **42**, 303-306.

Miller, G.F., 2001. The constraints on caldera alignment of Uranius Patera: Regional tectonic stress vs. topographic gradient. *Grosfils Research Letters*, **2**, 17-20.

Milner, D.M., Cole, J.W. & Wood, C.P. 2002. Asymmetric, multiple-block collapse at Rotorua Caldera, Taupo volcanic zone, New Zealand. *Bulletin of Volcanology*, **64**, 134-149.

Miura, D. 1999. Arcuate pyroclastic conduits, ring faults, and coherent floor at Kumano caldera, southwest Honshu, Japan. *Journal of Volcanology and Geothermal Research*, **92**, 271–294.

Molyneux, S.J. & Hutton, D.H.W. 2000. Evidence for significant granite space creation by the ballooning mechanism; the example of the Ardara Pluton, Ireland. *Geological Society of America Bulletin*, **112**, 1543-1558.

Moore, I. & Kokelaar, P. 1998. Tectonically controlled piecemeal caldera collapse; a case study of Glencoe Volcano, Scotland. *Geological Society of America Bulletin*, **110**, 1448-1466.

Moos, D. & Zoback, M.D. 1993. State of stress in the Long Valley caldera, California. *Geology*, **21**, 837-840.

Mori, J. & McKee, C. 1987. Outward-dipping ring-fault structure at Rabaul caldera as shown by earthquake locations. *Science*, **235**, 193-194.

Mouginis-Mark, P.J. & Robinson, M.S. 1992. Evolution of the Olympus Mons Caldera, Mars. *Bulletin of Volcanology*, **54**, 347-360.

Munro, D.C. & Rowland, S.K. 1996. Caldera morphology in the western Galapagos and implications for volcano eruptive behavior and mechanisms of caldera formation. *Journal of Volcanology and Geothermal Research*, **72**, 85-100.

Nairn, I.A., McKee, C.O., Talai, B. & Wood, C.P. 1995. Geology and eruptive history of Rabaul caldera area, Papua New Guinea. *Journal of Volcanology and Geothermal Research*, **69**, 255-284.

Nappi, G., Renzulli, A. & Santi, P. 1991. Evidence of incremental growth in the Vulsinian calderas (central Italy). *Journal of Volcanology and Geothermal Research*, **47**, 13-31.

Newhall, C.G. & Dzurisin, D. 1988. Historical unrest at large calderas of the world. *United States Geological Survey Bulletin*, **1855**, 1108pp.

Odonne, F., Ménard, I., Massonnat, G.J. & Rolando, J.P. 1999. Abnormal reverse faulting above a depleting reservoir. *Geology*, **27**, 111-114.

Orsi G., De Vita S. & Di Vito M. 1996. The restless, resurgent Campi Flegrei nested caldera (Italy): constraints on its evolution and configuration. *Journal of Volcanology and Geothermal Research*, **74**, 179-214.

Park, R.G., 1997. *Foundations of Structural Geology*, 3rd Ed. London: Chapman and Hall.

Patton, T.L. & Fletcher, R.C. 1995. Mathematical block-motion model for deformation of a layer above a buried fault of arbitrary dip and sense of slip. *Journal of Structural Geology*, **17**, 1455-1472.

Petford, N., Cruden, A.R., McCaffrey, K.J.W. & Vigneresse, J.L. 2000. Granite magma formation, transport and emplacement in the Earth's crust. *Nature*, **408**, 669-673.

Pinel, V. & Jaupart, C. 2005. Some consequences of volcanic edifice destruction for eruption conditions. *Journal of Volcanology and Geothermal Research*, **145**, 68-80.

Plescia, J.B. 1994. Geology of the small Tharsis volcanoes; Jovis Tholus, Ulysses Patera, Biblis Patera, Mars. *Icarus*, **111**, 246-269.

Plescia, J.B. & Golombek, M.P. 1986. Origin of planetary wrinkle ridges based on the study of terrestrial analogs. *Geological Society of America Bulletin*, **97**, 1289-1299.

Potyondy, D.O. and Cundall, P.A., 2004. A bonded-particle model for rock. *International Journal of Rock Mechanics and Mining Sciences*, **41**, 1329-1364

Ramberg, H., 1981. *Gravity, Deformation and the Earth's Crust*, 2nd Ed. London: Academic Press, 452 pp.

Ramelow, J., Riller, U., Romer, R. & Oncken, O. 2006. Kinematic link between episodic trapdoor collapse of the Negra Muerta caldera and motion on the Olacapato-El Toro fault Zone, southern central Andes. *International Journal of Earth Science*, **95**, 529-541.

Ramsay, J.G. & Huber, M.I. 1983. *The techniques of modern structural geology. Volume 1: Strain Analysis*. London: Academic Press, 307 pp.

Rampino, M.R. & Self, S. 1992. Volcanic winter and accelerated glaciation following the Toba super-eruption. *Nature*, **359**, 50–52.

Reynolds, R.W., Geist, D. & Kurz, M.D. 1995. Physical volcanology and structural development of Sierra Negra Volcano, Isabela Island, Galapagos Archipelago *Geological Society of America Bulletin*, **107**, 1398 - 1410.

Richey, J.E. & Thomas, H.H. 1932. The Tertiary Ring Complex of Slieve Gullion, Ireland. *Quarterly Journal of the Geological Society of London*, **88**, 653-688.

Riller, U., Petrinovic, I., Ramelow, J., Strecker, M.R. & Oncken, O. 2001. Late Cenozoic tectonism, collapse caldera and plateau formation in the Central Andes. *Earth and Planetary Science Letters*, **188**, 299-311.

Robin, C., Eissen, J.-P. & Monzier, M. 1993. Giant tuff cone and 12-km-wide associated caldera at Ambrym Volcano (Vanuatu, New Hebrides Arc). *Journal of Volcanology and Geothermal Research*, **55**, 225-238.

Roche, O., Druitt, T.H. & Merle, O. 2000. Experimental study of caldera formation. *Journal of Geophysical Research*, **105**, 395-416.

Roche, O. & Druitt, T.H. 2001. Onset of caldera collapse during ignimbrite eruptions. *Earth and Planetary Science Letters*, **191**, 191-202.

Roche, O., van Wyk de Vries, B. & Druitt, T.H. 2001. Sub-surface structures and collapse mechanisms of summit pit craters. *Journal of Volcanology and Geothermal Research*, **105**, 1-18.

Roman-Berdiel, T. 1999. Geometry of granite emplacement in the upper crust: contributions of analogue modelling. *Geological Society of London Special Publications*, **168**, 77-94.

Rose,W. I., & Chesner, C. A., 1990. Worldwide dispersal of ash and gases from Earth's largest known eruption: Toba, Sumatra, 75 ka. *Palaeogeography, Palaeoclimatology, Palaeoecology*, **89**, 269–275.

Sanford, A.L., 1959. Analytical and experimental sturdy of simple geologic structures. *Geological Society of America Bulletin*, **70**, 19-52

Scandone, R., 1990. Chaotic collapse of calderas. *Journal of Volcanology and Geothermal Research*, **42**, 285-302.

Saunders, S.J., 2001, The shallow plumbing system of Rabaul Caldera; a partially intruded ring fault?: *Bulletin of Volcanology*, **63**, 406-420.

Schöpfer, M.P.J. & Steyrer, H.P., 2001. Experimental modeling of strike-slip faults and the self-similar behaviour. *Geolological Society of America Memoir*, **193**, 21-27.

Seggiaro, R.E. & Hongn, F.D. 1999. Tectonic influence in Cenozoic vulcanism in North-Western Argentina. *Acta Geologica Hispanica* (now *Geologica Acta*), **34**, 227-242.

Self, S., Goff, F., Gardner, J.N., Wright, J.V. & Kite, W.M. 1986. Explosive rhyolitic volcanism in the Jemez Mountains; vent locations, caldera development and relation to regional structure. *Journal of Geophysical Research*, **91**, 1779-1798.

Self, S., Rampino, M.R., Newton, M.S. & Wolff J.A. 1984. Volcanological study of the great Tambora eruption of 1815. *Geology*, **12**, 659-663.

Skilling, I.P. 1993. Incremental caldera collapse of Suswa volcano, Gregory Rift Valley, Kenya. *Journal of the Geological Society London*, **150**, 885-896.

Smith, R.L. & Bailey, R.A. 1968. Resurgent cauldrons. *Geological Society of America Memoir*, **116**, 613-662.

Stachel, T., Lorenz, V. & Stanistreet, I.G. 1994. Gross Brukkaros (Namibia) – an enigmatic crater-fill reinterpreted as due to Cretaceous caldera evolution. *Bulletin of Volcanology*, **56**, 386-397.

Spinks, K.D., Acocella, V., Cole, J.W. & Bassett, K.N. 2005. Structural control of volcanism and caldera development in the transtensional Taupo Volcanic Zone, New Zealand. *Journal of Volcanology and Geothermal Research*, **144**, 7-22.

Summerfield, M.A. 1991. *Global geomorphology; an introduction to the study of landforms.* Harlow : Longman Scientific & Technical, 537 pp.

Timoshenko, P. & Woinowsky-Krieger, S. 1959. *Theory of plates and shells*, 2nd Ed. Engineering Societies Monographs, New York: McGraw-Hill.

Troll, V.R., Emeleus, C.H. & Donaldson, C.H. 2000. Caldera formation in the Rum Central igneous complex, Scotland. *Bulletin of Volcanology*, **62**, 301-317.

Troll, V.R., Walter, T.R. & Schminke, H.-U. 2002. Cyclic caldera collapse: Piston or piecemeal subsidence? Field and experimental evidence. *Geology*, **30**, 135-138.

Twiss, R.J. & Moores, E.M. 1992. *Structural Geology*, 1st Ed. New York: W. H. Freeman & Co., 532 pp.

Vallance, J.W. 2000. Lahars, in: Sigurdsson, H., Houghton, B.F., McNutt, S.R., Rymer, H. & Stix, J. (Eds.), Encyclopedia of Volcanoes, pp. 601-616. San Diego: Academic Press.

Varga, R.J. & Smith, B.M. 1984. Evolution of the early Oligocene Bonanza caldera, northeast San Juan, volcanic field, Colorado. *Journal of Geophysical Research*, **89**, 8679-8694.

Varnes, D. 1963. Geology and ore deposits of the South Silverton mining area, San Juan County, Colorado. *U.S. Geological Survey Professional Paper*, **378-A**, 1–56.

Van den Bogaard, P. and Schmincke H.-U., 1984, The eruptive centre of the Late Quaternary Laacher See Tephra: *Geologische Rundschau*, **73**, 933-980.

Van Wyk de Vries, B. & Merle, O. 1996. The effect of volcanic constructs on rift fault patterns. *Geology*, **24**, 643-646.

Van Wyk de Vries, B. & Merle, O. 1998. Extension induced by volcanic loading in regional strike-slip zones. *Geology*, **26**, 983-986.

Verbeek, R.D.M. 1885. *Krakatau*. Batavia: Government Press, 546 pp.

Ventura, G., Vilardo, G., Milano, G. & Pino, N.A. 1999. Relationships among crustal structure, volcanism and strike-slip tectonics in the Lipari-Vulcano volcanic complex (Aeolian Islands, southern Tyrrhenian Sea, Italy). *Physics of the Earth and Planetary Interior*, **116**, 31-52.

Voight, B., Glicken, H., Janda, R.J. & Douglass, P.M. 1981. Catastrophic rockslide avalanche of May 18, in: P. W. Lipman, D. R. Mullineaux (Eds.), The 1980 eruptions of Mount St. Helens, Washington, Prof. Paper US Geological Survey 347-377.

Von Buch, L. 1820. Über die Zusammensetzung der basaltischen Inseln und über Erhebungskrater. Kg. Preuss. Akad. Wiss. Berlin, pp. 51-68.

Walker, G.P.L. 1984. Downsag calderas, ring-faults, caldera sizes, and incremental caldera growth. *Journal of Geophysical Research*, **89**, 8407-8416.

Walker, G.P.L. 1988. Three Hawaiian calderas: an origin through loading by shallow intrusions? *Journal of Geophysical Research*, **93**, 14773–14784.

Wallmann, P.C., Pollard, D.D., Hildreth, W. & Eichelberger, J.C. 1990. New structural limits on magma chamber locations at the Valley of Ten Thousand Smokes, Katmai National Park, Alaska. *Geology*, **18**, 1240-1243.

Walter, T.R. & Troll, V.R. 2001. Formation of caldera periphery faults: an experimental study. *Bulletin of Volcanology*, **63**, 191-203.

Walsh, J. & Watterson, J. 1991. Geometric and kinematic coherence and scale effects in normal fault systems. *Geological Society of London, Special Publications*, **56**, 193-203.

Williams, H. 1941. Calderas and their origin. *University of California Bulletin of Geological Science*, **25**, 239-346.

Wilson, C.J.N., Hildreth, W.H. 1997. The Bishop Tuff; new insights from eruptive stratigraphy. *Journal of Geology*, **105**, 407-439.

Wilson, C.J.N., Houghton, B.F., McWilliams, M.O., Lanphere, M.A., Weaver, S.D. & Briggs, R.M. 1995. Volcanic and structural evolution of Taupo Volcanic Zone, New Zealand: a review. *Journal of Volcanology and Geothermal Research*, **68**, 1-28.

Woodcock, N.H. & Schubert, C., 1994. Continental Strike-Slip Tectonics. In: Hancock, P.L. (Ed.) *Continental Deformation*, pp. 251–263. Oxford: Pergamon Press.

Wolff, J.A., Wörner, G., and Blake, S., 1990, Gradients in physical parameters in zoned felsic magma bodies: implications for evolution and eruptive withdrawal: *Journal of Volcanology and Geothermal Research*, **43**, 37-55.

Wolff, J.A. & Gardner, J.N. 1995. Is the Valles Caldera entering a new cycle of activity? *Geology*, **23**, 411-414.

Yerkes R.F. & Castle R.O. 1970. Surface deformation associated with oil and gas field operations in the United States, In: *Proceedings of the Tokyo Symposium on Land Subsidence, International Association of Scientific Hydrology and UNESCO,* **88**, 55-66.

Yerkes, R.F. & Castle, R.O. 1976. Seismicity and faulting attributable to fluid extraction. *Engineering Geology,* **10**,151-167.

Yoshida, T. 1984. Tertiary Ishizuchi cauldron, southwest Japan: formation by ring fracture subsidence. Journal of Geophysical Research, 89, 8502-8510.

Young, W.C. & Budynas, R.G. 2002. *Roark's Formulas for Stress and Strain*. 7th Ed. New York: Mc Graw-Hill, 852 pp.

Zuber, M.T. & Mouginis-Mark, P.J. 1992. Caldera subsidence and magma chamber depth of the Olympus Mons volcano, Mars. *Journal of Geophysical Research*, **97**, 18,295-18,307.